UNIVERSITÉ SAVOIE MONT BLANC

THÈSE

Pour obtenir le grade de

DOCTEUR DE L'UNIVERSITÉ SAVOIE MONT BLANC

Spécialité : Physique Subatomique & Astroparticules

Arrêté ministériel : 25 Mai 2016

Présentée par

Anthony Downes

Thèse dirigée par **Edwige Tournefier** et
codirigée par **Maximilien Chefdeville**

préparée au sein du **Laboratoire d'Annecy des Physique des Particules**
dans **l'École Doctorale de Physique, Grenoble**

Une étude des désintégrations $B^0_{(s)} \rightarrow J/\psi\eta^{('\,)}$ avec l'experience LHCb

Thèse soutenue publiquement le **28 Septembre 2022**,
devant le jury composé de :

Dr. Lucia Di Ciaccio
Professeure des universités á Laboratoire d'Annecy des Physique des Particules, Présidente

Dr. Isabelle Ripp-Baudot
Directrice de recherche á Institut pluridisciplinaire Hubert Curien, Rapportrice

Dr. Vincent Tisserand
Directeur de recherche á Laboratoire de Physique de Clermont, Rapporteur

Dr. Olivier Deschamps
Maître de conférences á Laboratoire de Physique de Clermont, Examinateur

Dr. Matthew Needham
Professeur assistant á University of Edingburgh, Examinateur

UNIVERSITÉ
SAVOIE
MONT BLANC

A study of $B^0_{(s)} \to J/\psi\eta^{(\prime)}$ decays with the LHCb experiment

Anthony Gavin Downes
of the Laboratoire d'Annecy de Physique des Particules

A dissertation submitted to the Université de Savoie Mont Blanc
for the degree of Doctor of Philosophy

Résumé

L'objectif principal de cette thèse est l'étude des désintégrations de $B^0_{(s)} \to J/\psi\eta^{(\prime)}$ avec l'expérience LHCb au Grand Collsionneur de Hadrons/Large Hadron Collider (LHC) du CERN. Au niveau des quarks, ces désintégrations procèdent par des transitions à l'arbre supprimées de couleur pour les désintégrations de B^0_s ou les transitions $b \to c\bar{c}d$ supprimées par Cabibbo pour les désintégrations B^0. Ces mésons B neutres peuvent osciller entre les états de particule B et d'antiparticule $\bar{B}$. Comme l'état final $J/\psi\ \eta^{(\prime)}$ est accessible aux mésons B comme aux anti-mésons $\bar{B}$, il est possible d'observer une violation des symétries de charge-parité (CP). Cette violation provient de l'interférence dans les désintégrations avec et sans oscillations B^0_s-$\bar{B}^0_s$. Elle peut être mesurée à partir de l'asymétrie temporelle entre les désintégrations de $B^0_s \to J/\psi\eta^{(\prime)}$ et de $\bar{B}^0_s \to J/\psi\eta^{(\prime)}$ qui est liée à la différence de largeur de désintégration $\Delta\Gamma_s$ et à la phase ϕ_s. Une mesure future de ϕ_s dans ces canaux peut alors être utilisée pour tester le Modèle Standard. Cependant, il existe une contribution à cette mesure qui provient de désintégrations à boucles appelées diagrammes pingouins. Il est donc nécessaire de sur-contraindre les paramètres des diagrammes pingouins. C'est en partie ce qui est étudié dans cette thèse à travers les mesures suivantes des rapports d'embranchement des désintégrations $B^0_{(s)} \to J/\psi\eta^{(\prime)}$ et du mélange entre les mésons η et η'. Dans la mesure de ce mélange, il pourrait entrer également une faible contribution d'un meson hypothétique formé de gluons de valence, appelé gluonium ou glueballs. Cela conduit à mesurer deux angles de mélange à partir des différentes fractions de rapports de branchement. L'un des angles est associé au mélange entre les états de quark des mésons η et η' et l'autre pour leur mélange avec l'état gluonium.

La objectif de cette thèse est de mesurer ces rapports de branchement et les angles de mélange en utilisant les états finals $J/\psi \to \mu^+\mu^-$ et les désintégrations des mésons η et η' dans les états finals : $\eta \to \pi^+\pi^-\gamma$, $\eta \to \pi^+\pi^-(\pi^0 \to \gamma\gamma)$, $\eta' \to (\rho^0 \to \pi^+\pi^-)\gamma$ et $\eta' \to \pi^+\pi^-(\eta \to \gamma\gamma)$. Ces mesures exploitent un échantillon de données enregistrées lors de collisions proton-proton à $\sqrt{s} = 7, 8$ et 13 TeV qui correspond à une luminosité intégrée d'environ 9 fb^{-1} qui été collectées lors des périodes d'opération I et II du LHC. Les mesures des états finals η et η' sont compliquées par la présence de photons et l'environnement hadronique. Il a donc été nécessaire d'effectuer également une analyse des performances de la simulation pour calibrer l'efficacité de la reconstruction des photons et des π^0.

Abstract

The main objective of this thesis is the study of the decays of $B^0_{(s)} \to J/\psi\eta^{(\prime)}$ with the LHCb experiment at CERN's Large Hadron Collider. At the quark level, these decays proceed by colour-suppressed $b \to c\bar{c}s$ transitions for the B^0_s decays or Cabibbo-suppressed $b \to c\bar{c}d$ transitions for the B^0 decays. These neutral B mesons can oscillate between the states of particle B and antiparticle $\bar{B}$. As the final state $J/\psi\ \eta^{(\prime)}$ is accessible to both B mesons and $\bar{B}$ anti-mesons, it is possible to observe a violation of charge-parity symmetries (CP). This violation arises from the interference in the decays with and without oscillations B^0_s-$\bar{B}^0_s$. This can be measured from the time asymmetry between the decays of $B^0_s \to J/\psi\eta^{(\prime)}$ and $\bar{B}^0_s \to J/\psi\eta^{(\prime)}$ which is related to the difference in decay width $\Delta\Gamma_s$ and the phase ϕ_s. A future measurement of ϕ_s in these channels can then be used to test the Standard Model. However, there is a contribution to this measurement that comes from loop decays called penguin diagrams. It is therefore necessary to constrain the parameters of the penguin diagrams. This is partly what is studied in this thesis through the following measurements of the branching ratios of the decays $B^0_{(s)} \to J/\psi\eta^{(\prime)}$ and of the mixing between the mesons η and η'. In the measurement of this mixing, there could also enter a small contribution of a hypothetical meson formed by valence gluons, called gluonium or glueballs. This leads to the measurement of two mixing angles from the different branching ratio fractions. One of the angles is associated with the mixing between the quark states of the mesons η and η' and the other for their mixing with the gluonium state.

The objective of this thesis is to measure these branching ratios and mixing angles using the final states $J/\psi \to \mu^+\mu^-$ and the decays of mesons η and η' in the final states: $\eta \to \pi^+\pi^-\gamma$, $\eta \to \pi^+\pi^-(\pi^0 \to \gamma\gamma)$, $\eta' \to (\rho^0 \to \pi^+\pi^-)\gamma$ and $\eta' \to \pi^+\pi^-(\eta \to \gamma\gamma)$. These measurements were performed using a sample of data recorded in proton-proton collisions at $\sqrt{s} = 7, 8$ and 13 TeV which corresponds to an integrated luminosity of about 9 fb^{-1} that were collected during LHC operation periods I and II. The measurements of the final states η and η' are complicated by the presence of photons and the hadronic environment. It was therefore necessary to also perform a simulation performance analysis to calibrate the efficiency of the photon and π^0 reconstruction.

Acknowledgements

There are no achievements in life that can be credited to one person alone. Least of all this. Over the last three years I have relied on amazing academic, scientific, social and emotional support from equally amazing people that I have the privilege to know or have known. Here I would like to attempt to do some justice to you for that.

To Isabelle Ripp-Baudot and Vincent Tisserand, I would like to thank you for taking on the difficult and lengthy task of being reporters in the jury of my thesis. Your comments and discussions have helped my final developments greatly.

Also to Lucia Di Ciaccio, Olivier Deschamps and Matthew Needham for taking on the role of examiners in the jury. Your reading and the subsequent discussion, along with the reporters, was greatly appreciated for allowing me to consider carefully all aspects of the work surrounding my thesis and provided invaluable incite in them.

Many of the finest qualities that I needed to learn and develop in this period came from the superb direction of Maximilien Chefdeville. You went above and beyond the efforts that, I believe, many in your position might. Because of that, this thesis is something I could be truly proud of. I cannot thank you enough for that. I wish you and Ying-Rui the best of luck with your work going forward.

To Edwige Tournefier, I thank you for kindly accepting to be the director of my thesis and providing important experience in driving up the quality of my work chapter by chapter.

Some of the most exciting aspects of this thesis stemmed from the physics itself. Without Daniel Decamp's teachings of these, I doubt I would have truly appreciated them in full. Thank you also for the great length of time you spent ensuring that I had understood concepts and that they were presented with accuracy.

To all of my colleagues in the LHCb group at LAPP, the exchange of expertise has been, not only a vital part of this period, but also a great pleasure. May your valuable work continue to make a lasting impact in the experiment.

Thanks to my friends in LAPP who, by simply sharing a coffee or a pint with, have done wonders to keep me sane throughout a personally and globally difficult period. I will miss that greatly.

To my friends back home, thanks to the internet, I managed to overcome a large part of any homesickness with you virtually with me the whole way.

And finally my family who I missed dearly and I am glad to return to. You are my foundation in every sense of the word.

Contents

Introduction

This thesis covers the comprehensive experimental study of the decays of $B^0_{(s)} \to J/\psi\eta^{(\prime)}$. This primarily includes the updated measurements of the branching ratios of these decays and consequently the mixing between η and η' mesons. The measurement of these decays with $J/\psi \to \mu^+\mu^-$ and multiple $\eta^{(\prime)}$ final states (namely $\eta \to \pi^+\pi^-\gamma$, $\eta \to \pi^+\pi^-\pi^0$ with $\pi^0 \to \gamma\gamma$, $\eta' \to \rho^0\gamma$ with $\rho^0 \to \pi^+\pi^-$ and $\eta' \to \pi^+\pi^-\eta$ with $\eta \to \gamma\gamma$) was a key factor in achieving the most precise measurements of the branching ratios to date.

The improved understanding of the mixing between the η and η' mesons and hence the branching ratios of $B^0_{(s)} \to J/\psi\eta^{(\prime)}$ leads to a clarification of the quark content of these mesons. An extension of the mixing scheme to include non-conventional mesons made of valence gluons, commonly referred to as glueballs or gluonium, can also be investigated. This allows for an inclusion of not just the meson's quark composition but an additional component of glue.

The data samples used were combined from proton-proton collisions in CERN's Large Hadron Collider at the centre of mass energies of 7, 8 and 13 TeV amounting to 9 fb^{-1} collected at the LHCb experiment in the two operating periods spanning over the years 2012 to 2018. Using this combined data set with the multiple final states of the $\eta^{(\prime)}$ mesons allowed for great improvements in the statistical uncertainties of the updated measurements of $B^0_{(s)} \to J/\psi\eta^{(\prime)}$ in comparison to others performed within and without the LHCb Collaboration.

Yet there are unique challenges in measuring final states with photons in the LHCb experiment. There is a necessity in this work, and many others, for simulation data to reproduce the reconstruction and selection of efficiencies of these decays produced within the detector environment. In the case of photons, there are many factors that may produce differences in the measured efficiencies. There is imperfect knowledge of the photon interactions throughout the detector material, the calibration and performance of the Preshower, Scintillating Pad Detector and Electromagnetic Calorimeter is also imperfect, issues with the pile-up of the detector and other factors. The accumulation of these imperfections lead to significant differences in the measured efficiencies of photons that must be corrected for or factorised out of any measurements involving photons.

Therefore this thesis also includes a study of the reconstruction efficiencies of photons and provides a correction for simulation by use of the decays of $B^+ \to \chi_{c1} K^+$ with $\chi_{c1} \to \gamma J/\psi$ (for single photons) and $B^+ \to J/\psi K^{*+}(892)$ with $K^{*+}(892) \to K^+\pi^0$ and $\pi^0 \to \gamma\gamma$ (for two photons originating from a π^0). These decays are then compared to the topologically similar $B^+ \to J/\psi K^+$ to mitigate the effects of the charged particles involved in the decays.

Chapter 1.

Theoretical Motivation

In this chapter the various interesting aspects of physics relevant to this thesis are discussed. These include the Standard Model of Particle Physics in Section 1.1 giving a overview of the Standard Model in the first part and a more in depth look at the Flavour Sector of the Standard Model in the second part. As this thesis studies B_s^0 decays through $b \to c\bar{c}s$ (with a reasonably large yield) it is worthwhile to explore the possibility of future measurements of the time-dependent CP asymmetries that result from the oscillations of the neutral mesons, especially in the B_s^0-$\bar{B}_s^0$ case. The physics of these oscillations and how they relate to the CP phase ϕ_s is therefore discussed in Section 1.2.

After the general discussion of B physics it is necessary to also discuss the physics of the interesting $\eta^{(\prime)}$ mesons in the decay products in Section 1.3. This first requires an understanding of some the interesting sectors of the quark model (Section 1.3.1). In Section 1.3.4, this model is used to describe the physics of the daughter pseudoscalar mesons, the $\eta^{(\prime)}$, and make predictions on an angle that parameterises their mixing with each other. These predictions tend to be less reliable for pseudoscalar mesons (compared to the near-ideal situation of the vector mesons) so a brief description of other predictions made by an Effective Field Theory (EFT) is necessary. This EFT has been shown to provide more successful phenomenological predictions, especially in limits where it becomes difficult to make calculations using Quantum Chromodynamics (QCD). Then it is discussed that there is a possible connection in the mixing of η and η' with a possible bound state of non-$q\bar{q}$ meson states, specifically with valence gluons, commonly called glueballs.

Since the physics of the mesons of interest is described, the application of this physics to the decays of $B_{(s)}^0 \to J/\psi\eta^{(\prime)}$, which this thesis concerns, then follows in Section 1.4. The decay amplitudes and branching ratios of the decays of $B_{(s)}^0 \to J/\psi\eta^{(\prime)}$ will be described in terms of their respective Cabibbo-Kobayashi-Maskawa matrix elements, phase-space, other kinematic quantities and the η-η' mixing angles. This description allows for the determination of these mixing angles through the measurements of various ratios of branching ratios. These different ratios will be measurable many times by considering different $\eta^{(\prime)}$ decay channels to a number of pions and/or photons, namely: $\eta^{(\prime)} \to \gamma\gamma$, $\eta \to \pi^+\pi^-\gamma$, $\eta' \to (\rho^0 \to \pi^+\pi^-)\gamma$, $\eta \to \pi^+\pi^-(\pi^0 \to \gamma\gamma)$ and $\eta' \to \pi^+\pi^-(\eta \to \gamma\gamma)$.

It is worth noting that, throughout this manuscript, the speed of light and reduced Planck constants are both considered unitary, *i.e.* $c = \hbar = 1$.

1.1. The Standard Model

1.1.1. Introduction to the Standard Model

The Standard Model of particle physics (SM) is a description of the fundamental particles and their interactions. It is a successful quantum field theory that provides a common framework for the strong force and unified electroweak force. It has at least 18 free parameters in its simplest form (with massless neutrinos), each relating to the masses of particles and the couplings of interactions between them, as well as the parameters describing the Cabibbo-Kobayashi-Maskawa matrix described in Section 1.1.2. In the Standard Model elementary particles (summarised in Table 1.1) can be categorised into two groups by their spin. Spin-half particles are called fermions and the integer spin particles are bosons, where there are the spin-one gauge bosons and the spin-zero Higgs boson (the only scalar boson currently in the Standard Model). They also have other quantum numbers such as their baryon or lepton numbers and electromagnetic (EM) or colour charges.

There are twelve fermions: six quarks and six leptons along with their associated anti-fermions. With three generations (pairs of quarks and pairs of leptons), of which, most observable matter is made of the first generation. The lepton generations contain charged leptons that define the reference value for electromagnetic charge quantum numbers ($Q = -1$), and their respective neutrinos of zero charge. For quarks these generations are pairs of up-type and down-type quarks with electromagnetic charges of $Q = +2/3$ and $Q = -1/3$ respectively.

Interactions between fermions are mediated by the exchange of gauge bosons responsible for one of the three fundamental interactions of the Standard Model. These bosons and their respective interactions are:

1. **photons (γ)**: electromagnetic force,
2. **gluons (g)**: strong force,
3. **weak bosons ($W^{\pm}$ and Z)**: weak force.

In the Standard Model, these forces have been shown to be successfully described by two gauge theories. Quantum chromodynamics (QCD) is the theory for the strong interaction involving a

Table 1.1.: The Standard Model groupings of fundamental particles and their key quantum numbers [1].

Name	Spin	Baryon No.	Lepton No.	EM Charge	Colour Charge
Quarks					
u, c, t	$\frac{1}{2}$	$\frac{1}{3}$	0	$+\frac{2}{3}$	r, g, b
d, s, b	$\frac{1}{2}$	$\frac{1}{3}$	0	$-\frac{1}{3}$	r, g, b
Leptons					
e, μ, τ	$\frac{1}{2}$	0	1	-1	0
ν_e, ν_μ, ν_τ	$\frac{1}{2}$	0	1	0	0
Gauge bosons					
γ	1	0	0	0	0
$W^{\pm}$,Z	1	0	0	$\pm 1, 0$	0
g (8 types)	1	0	0	0	octet of r, g, b
Scalar bosons					
H	0	0	0	0	0

$SU(3)_C$ symmetry group. The electroweak (EW) theory unifies both the electromagnetic and weak interactions in a $U(1)_Y \otimes SU(2)_L$ symmetry [1].

Quarks couple to all interactions with their electric and colour charges. Up (u) and down (d) quarks are in the first generation, charm (c) and strange (s) in the second, and top (t) and bottom/beauty (b) making the third generation. The mass hierarchy of the generations are such that the down-type quarks are the lightest and up-type quarks are the heaviest with overall mass increasing with generation.

Colour charge is the attribute carried by quarks that allow for strong interactions via gluons. This is categorised as red, green, blue, and their respective anticolours ($r, g, b, \bar{r}, \bar{g}$ and $\bar{b}$). The strong force confines quarks to bound states called hadrons. These hadrons must have no net colour charge (*i.e.* be colour singlets) due to an effect called colour confinement. Mesons (*e.g.* K and π) are quark-antiquark pairs bound with colour and respective anticolour charges $r\bar{r}$, $g\bar{g}$ or $b\bar{b}$. For baryons (*e.g.* protons and neutrons) there are three quarks with one of each type of all colours (rgb) [1]. There have also been observations of rarer baryons considered to be tetraquarks and pentaquarks [2–7]. Tetraquarks are bound states of two quark-antiquark pairs (of which are colour-anticolour pairs) and pentaquarks are five quarks consisting of three quarks in a colour singlet and a quark-antiquark pair.

Similar to quarks, gluons carry colour but simultaneously carry a colour and anticolour pairs. These colour pairs can be represented in an octet to represent the eight gluon types, *e.g.* [8]:

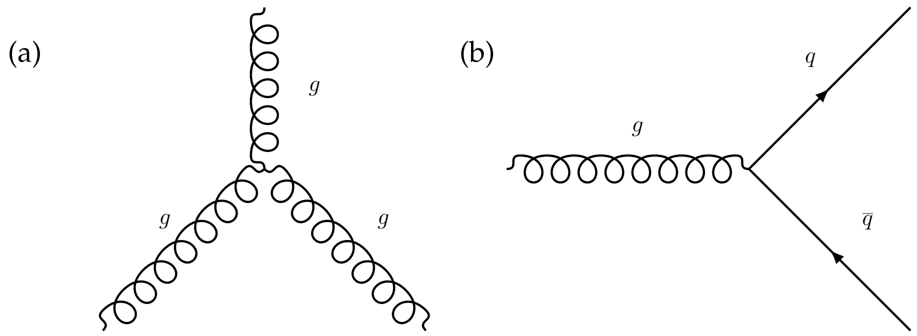

Figure 1.1.: Example diagrams of interactions involving gluons where a) is self-interacting gluons and b) is gluon-fermion interaction.

$$
\begin{aligned}
&\frac{1}{\sqrt{2}}(r\overline{b}+b\overline{r}), && -i\frac{1}{\sqrt{2}}(r\overline{b}-b\overline{r}),\\
&\frac{1}{\sqrt{2}}(r\overline{g}+g\overline{r}), && -i\frac{1}{\sqrt{2}}(r\overline{g}-g\overline{r}),\\
&\frac{1}{\sqrt{2}}(b\overline{g}+g\overline{b}), && -i\frac{1}{\sqrt{2}}(b\overline{g}-g\overline{b}),\\
&\frac{1}{\sqrt{2}}(r\overline{r}-b\overline{b}), && \frac{1}{\sqrt{6}}(r\overline{r}+b\overline{b}-2g\overline{g}).
\end{aligned}
$$

Therefore gluons can both couple to quarks and also self-couple in ways like those displayed in Figure 1.1. These gluons are associated to a gauge field G^a_μ where $a = 1, \ldots 8$ from the $\mathrm{SU}(3)_C$ symmetry group.

Leptons do not carry colour charge so would only interact weakly or electromagnetically for charged leptons. As neutrinos only interact weakly, they are elusive in comparison to other fermions. Each generation is considered to hold a characteristic flavour: first is the electron and electron neutrino; secondly the muon and muon neutrino; and finally the third generation is the tau lepton and tau neutrino. Standard Model neutrinos have zero mass, although experiments have found this to not be the case and have observed their oscillations between these lepton flavours.

With the electroweak interaction there is the three fields W^b_μ where $b = 1, 2, 3$ related to the gauge group $\mathrm{SU}(2)_L$ and one field B_μ from $\mathrm{U}(1)_Y$. This gives us the relation for the field description of the massive charged bosons $W^\pm$:

$$W^\pm_\mu = \frac{1}{\sqrt{2}}(W^1_\mu \mp iW^2_\mu). \tag{1.1}$$

There is then the W_μ^3 and B_μ fields describing the two neutral physical boson states by their mixing with an angle θ_W, called the Weinberg angle:

$$A_\mu = W_\mu^3 \sin\theta_W + B_\mu \cos\theta_W, \tag{1.2}$$

$$Z_\mu = W_\mu^3 \cos\theta_W - B_\mu \sin\theta_W, \tag{1.3}$$

where A_μ and Z_μ are the field descriptions of the massless γ and massive Z boson respectively [9]. The Weinberg angle can be given by a relation between the independent group couplings involved in electroweak interactions

$$g \sin\theta_W = g' \cos\theta_W = e, \tag{1.4}$$

where g and g' are the coupling constants for the W_μ^b and B_μ fields respectively and e is the classical coupling constant for $\mathrm{U}(1)_Y$ fields [1].

Photons mediate the electromagnetic force by coupling to electric charges and Z mediates the neutral current of the weak interaction by coupling to fermion and antifermion pairs. The charged current of the weak interaction is mediated by the $W^\pm$ bosons which is the only case where inter-generational fermions can interact with each other. $W^\pm$ boson interactions are dependent on the chirality of the fermions, as they only interact with left-handed fermions (or right-handed antifermions). This allows for processes where one fermion decays to produce fermions of other generations (*i.e.* flavour changing). This is the primary concern of the Flavour Sector of the Standard Model.

The Standard Model Lagrangian can be expressed in three terms as

$$\mathcal{L} = \mathcal{L}_{kinetic} + \mathcal{L}_{Higgs} + \mathcal{L}_{Yukawa}, \tag{1.5}$$

where the kinetic term describes the interactions between fermions and the gauge fields G_μ^a, W_μ^b and B_μ as

$$\mathcal{L}_{kinetic} = i\overline{\psi}(D_\mu \gamma^\mu)\psi, \tag{1.6}$$

where ψ are the spinor field describing the three fermion generations and $\bar{\psi} \equiv \psi^\dagger \gamma^0$. The covariant derivative D^μ introduces the gauge field interactions as

$$D_\mu = \partial_\mu + ig_s G_\mu^a \lambda^a + igW_\mu^b \sigma^b + ig' B_\mu Y, \tag{1.7}$$

where λ^a and σ^b are the Gell-Mann and Pauli matrices respectively and Y is the hypercharge. The coupling constants of the respective gauge fields are g_s, g and g' [10].

Table 1.2.: Summary of the spinor fields' attributed weak isospin and hypercharge. The electromagnetic charge is related to these quantum numbers by the expression $Q = I_3 + Y/2$.

Name	Weak Isospin (I_3)	Weak Hypercharge (Y)	EM Charge (Q)
Quarks			
$(Q'_L)_i$	$+\frac{1}{2}$(u-type),$-\frac{1}{2}$(d-type)	$+\frac{1}{3}$	$+\frac{2}{3}$(u-type),$-\frac{1}{3}$(d-type)
$(u'_R)_i$	0	$+\frac{4}{3}$	$+\frac{2}{3}$
$(d'_R)_i$	0	$-\frac{2}{3}$	$-\frac{1}{3}$
Leptons			
$(L'_L)_i$	$+\frac{1}{2}(\nu_e,\nu_\mu,\nu_\tau),-\frac{1}{2}(e,\mu,\tau)$	-1	$0(\nu_e,\nu_\mu,\nu_\tau),-1(e,\mu,\tau)$
$(l'_R)_i$	0	-2	-1

The spinor fields contain five ways to represent fermions in the interacting basis. These are categorised by their values of the weak hypercharge Y:

1. $(Q'_L)_i$ for quarks with $Y = +1/3$, containing a $\mathrm{SU}(3)_C$ triplet and left-handed $\mathrm{SU}(2)_L$ doublet.
2. $(u'_R)_i$ for up-type quarks with $Y = +4/3$, containing a $\mathrm{SU}(3)_C$ triplet and right-handed $\mathrm{SU}(2)_R$ singlet.
3. $(d'_R)_i$ for down-type quarks with $Y = -2/3$, containing a $\mathrm{SU}(3)_C$ triplet and right-handed $\mathrm{SU}(2)_R$ singlet.
4. $(L'_L)_i$ for leptons with $Y = -1$, containing a left-handed $\mathrm{SU}(2)_L$ doublet.
5. $(l'_R)_i$ for charged leptons with $Y = -2$, containing right-handed $\mathrm{SU}(2)_R$ singlet.

where i denotes the three fermion generations and L or R signifies left or right-handed chirality. An overview of their respective weak isospin (I_3) and electromagnetic charges ($Q = I_3 + Y/2$) is given in Table 1.2. The left-handed quarks can also be expressed more intuitively as

$$(Q'_L)_i = \begin{pmatrix} u'_g & u'_r & u'_b \\ d'_g & d'_r & d'_b \end{pmatrix}_i . \tag{1.8}$$

This notation represents the $\mathrm{SU}(3)_C$ triplet with colours r, g and b and the $\mathrm{SU}(2)_L$ doublet with up and down-type quarks [10].

The term $\mathcal{L}_{Higgs}$ describes the Higgs field interactions with the strong and electroweak bosons. It introduces an isospin doublet

$$\phi = \begin{pmatrix} \phi^+ \\ \phi^0 \end{pmatrix}, \qquad \tilde{\phi} = \begin{pmatrix} \phi^0 \\ -\phi^- \end{pmatrix}. \tag{1.9}$$

It is this Lagrangian that supplies the W and Z bosons their respective masses as

$$\mathcal{L}_{Higgs} = (D_\mu\phi)^\dagger(D^\mu\phi) - \mu^2\phi^\dagger\phi - \lambda(\phi^\dagger\phi)^2. \tag{1.10}$$

where μ^2 is the negative mass-squared parameter and λ is the positive Higgs self-coupling[1]. The first term shows the interactions of the Higgs scalar and vector boson fields, whereas the second and third terms describe the Higgs potential ($-V_{Higgs}$). The minimisation of V_{Higgs} is at $\langle\phi^\dagger\phi\rangle = v^2/2 = -\mu^2/2\lambda$, where v is the vacuum expectation parameter.

However the generation of the fermion masses arises in the Yukawa term $\mathcal{L}_{Yukawa}$ describing the Yukawa couplings (*i.e.* the coupling between fermions and the Higgs field). This term is

$$\begin{aligned} \mathcal{L}_{Yukawa} &= -Y_{ij}\overline{(\psi_L)}_i\phi(\psi_R)_j + h.c. \qquad (1.11)\\ &= -Y^d_{ij}\overline{(Q'_L)}_i\phi(d'_R)_j - Y^u_{ij}\overline{(Q'_L)}_i\tilde{\phi}(u'_R)_j - Y^l_{ij}\overline{(L'_L)}_i\phi(l'_R)_j + h.c., \qquad (1.12)\end{aligned}$$

where Y_{ij} are the 3×3 Yukawa coupling matrices responsible for the interactions between the different fermion generations [10]. This links the generation of fermion masses in the Standard Model Lagrangian explicitly into the Flavour Sector. This is expanded on in Section 1.1.2.

Discrete symmetries

There are the charge-conjugation (C), parity (P) and time-reversal (T) symmetries that were originally believed to be invariant. Parity transforms are the reversal of spatial dimensions when operating on a space-dependent wavefunction *e.g.*

$$\psi'(\vec{r}) = P\psi(\vec{r}) \equiv \psi(-\vec{r}) \tag{1.13}$$

in the case of an operation on an eigenfunction the only possible eigenvalues are $\eta_P = \pm 1$ *i.e.*

$$P\psi(\vec{r}) \equiv \pm\psi(\vec{r}). \tag{1.14}$$

Parity eigenvalues are explored for mesons in Section 1.3.1. Time-reversal transformations are a similar concept where there is a reversal of the time dimension under the operation on a

[1] Not to be confused with the Wolfenstein parameter λ

time-dependent wavefunction

$$\psi'(t) = T\psi(t) \equiv \psi(-t). \tag{1.15}$$

T transforms would be invariant if processes have the same time evolution in the forward and backward time directions [11].

Charge-conjugation is the operation of transforming particles into their respective antiparticles. It changes the sign a particle's charge and quantum numbers related to its flavour, see Section 1.3.1 for the quark quantum numbers. Neutral particles with no net fermion flavour remain unchanged under a C transform. They are their own antiparticles in this case. Examples of the C transform are:

$$\pi^+ \xrightarrow{C} \pi^- \tag{1.16}$$

$$\nu_e \xrightarrow{C} \overline{\nu}_e \tag{1.17}$$

$$\pi^0 \xrightarrow{C} \pi^0 \tag{1.18}$$

$$\gamma \xrightarrow{C} \gamma. \tag{1.19}$$

Similarly to parity, the only possible eigenvalues of charge-conjugation are $\eta_C = \pm 1$. These symmetries were originally believed to be invariant, which still appears to be the case for the electromagnetic and strong interactions.

First suggestions of parity violation in the weak interaction arose from the observations of two kaon decays $K^+ \to \pi^+\pi^0$ and $K^+ \to \pi^+\pi^-\pi^+$. From the two-pion decay, the parity of the spin-zero kaon would be expected to be the square of the pion parity

$$\eta_P(K) = \eta_P(\pi)^2(-1)^l = (-1)^2(-1)^l, \tag{1.20}$$

and the relative spin of the two pions, l, must be equal to the spin of the kaon so $l = 0$. Therefore the parity of the kaon here must be $\eta_P(K) = +1$. Yet, in the case of the three-pion decay the sum of the relative pion spins, $l_1 + l_2$ would also be zero due to the zero spin of the kaon, *i.e.* $|l_1| = |l_2|$. So the pion parity must be cubed

$$\eta_P(K) = \eta_P(\pi)^3(-1)^{l_1+l_2} = (-1)^3 = -1, \tag{1.21}$$

and it therefore has the opposite parity eigenvalue. As it was assumed by many at the time that parity would be conserved, it was hypothesised that there were two different particles with the kaon mass that each had different parities [12]. It was first suggested by Lee and Yang that parity conservation was not always true, since all experimental data suggested that these two hypothetical kaons had identical masses and lifetimes. They therefore suggested multiple tests of parity conservation using β-decays [13]. The first evidence to provide proof that parity was in fact violated was the experimental study of β-decays of polarised cobalt-60 nuclei (where ${}^{60}Co \to {}^{60}Ni^{*}e^{-}\overline{\nu}_{e}$). The electrons produced in this decay travelled in a preferred direction. This meant that the spin of the electron was always opposite to its momentum, this is referred to as left-handedness [14]. This means that the charged-current weak interaction, that is responsible for these decays, could only couple to left-handed particles (e^{-}) or right-handed antiparticles ($\overline{\nu}_{e}$) [12]. This was also confirmed in an experiment measuring the polarisation and resonant scattering of photons produced in the orbital electron capturing in decays of ^{152}Eu which proved that 100% of the neutrinos produced were left-handed particles [15]. Therefore, symmetry under parity can be violated. Another consequence of this is that charge-conjugation can also be violated in weak decays as a decay involving right-handed antineutrinos operated under a charge conjugation does not occur. It was then posited that the combined *CP* operation would be invariant as nothing about this property of the weak interaction would directly forbid this [1]. Though this was found to not necessarily be true. When studying neutral kaon decays it was found that the long-lived kaon state $|K^0_{\mathrm{L}}\rangle$ with $CP = -1$ could decay to two charged pions with $CP = +1$ [16]. This meant that a small amount of *CP* violation was indeed entering into kaon decays [1].

The combined *CPT* transformation is invariant ($CPT = 1$) for all processes in Quantum Field Theory was first given in Schwinger's work in 1951 [17]. This was later proven as a theorem under general assumptions by Lüders and Pauli in 1954 [18, 19]. This means that particles and their corresponding antiparticles all have equally sized masses, charges, magnetic moments and lifetimes. Hence tests of *CPT* invariance include measuring the mass differences of particles and antiparticles (*e.g.* K^0 and $\bar{K}^0$ where $|m_{K^0} - m_{\bar{K}^0}|/m_{avg} < 6 \times 10^{19}$ [20]) or magnetic momenta of μ^{+} and μ^{-} (such as in $g-2$ experiments [11]). *CPT* invariance implies that, with measurements of *CP* violation, there must also be *T* violation.

1.1.2. Flavour Sector of the Standard Model

The Cabibbo-Kobayashi-Maskawa Matrix

The Cabibbo-Kobayashi-Maskawa (CKM) matrix was an extension from the Cabibbo matrix which was introduced to describe the universality of the weak interaction in the context of two quark families [21]. The extension with a third quark family was necessary to produce a model that can describe *CP* violation [22]. For the purpose of understanding the quark mass terms and their connection to the CKM matrix, the quark terms in $\mathcal{L}_{Yukawa}$ must be expanded on after the spontaneous symmetry breaking of the Higgs field induced by the Higgs potential

$$\phi = \begin{pmatrix} \phi^{+} \\ \phi^{0} \end{pmatrix} \to \begin{pmatrix} G^{+} \\ \frac{1}{\sqrt{2}}(v + H^0 + iG^0) \end{pmatrix}, \tag{1.22}$$

where H^0 is the Higgs boson, $G^{+,0}$ are Goldstone bosons and v is the vacuum expectation parameter related to the Higgs self-coupling and mass. The parameter v gives $W^{\pm}$ and Z bosons their masses defined by $M_W = gv/2$ and $M_Z = \sqrt{g^2 + g'^2}v/2$ [23]. It then follows that the quark terms in $\mathcal{L}_{Yukawa}$ are

$$\mathcal{L}_{Yukawa} = -Y^d_{ij}\overline{(Q'_L)}_i\phi(d'_R)_j - Y^u_{ij}\overline{(Q'_L)}_i\tilde{\phi}(u^I_R)_j + h.c. \tag{1.23}$$

$$= -Y^d_{ij}\overline{(d'_L)}_i\frac{v}{\sqrt{2}}(d'_R)_j - Y^u_{ij}\overline{(u'_L)}_i\frac{v}{\sqrt{2}}(u'_R)_j + h.c. \tag{1.24}$$

$$= -M^d_{ij}\overline{(d'_L)}_i(d^I_R)_j - M^u_{ij}\overline{(u'_L)}_i(u'_R)_j + h.c., \tag{1.25}$$

where $M^{d,u}_{ij} = Y^{d,u}_{ij}v/\sqrt{2}$ are the mass terms which when diagonalised give the masses of the quarks

$$M^d_{diag} \equiv \begin{pmatrix} m_d & 0 & 0 \\ 0 & m_s & 0 \\ 0 & 0 & m_b \end{pmatrix} = \frac{v}{\sqrt{2}}U^\dagger_{d_L}Y^dU_{d_R}, \tag{1.26}$$

$$M^u_{diag} \equiv \begin{pmatrix} m_u & 0 & 0 \\ 0 & m_c & 0 \\ 0 & 0 & m_t \end{pmatrix} = \frac{v}{\sqrt{2}}U^\dagger_{u_L}Y^uU_{u_R}, \tag{1.27}$$

where the unitary matrices U_{u_L}, U_{u_R}, U_{d_L} and U_{d_R} are employed for this purpose [10,23]. These matrices therefore also give a rotation of the quark states from the interacting basis into their respective mass eigenstates

$$(u_L)_i = (U_{u_L})_{ij}(u'_L)_j \qquad (u_R)_i = (U_{u_R})_{ij}(u'_R)_j, \tag{1.28}$$

$$(d_L)_i = (U_{d_L})_{ij}(d'_L)_j \qquad (d_R)_i = (U_{d_R})_{ij}(d'_R)_j. \tag{1.29}$$

Taking just the charged current terms in the Kinetic Lagrangian written in this quark mass basis gives

$$\mathcal{L}_{kinetic,CC} = -\frac{g}{\sqrt{2}}(\overline{u}'_L)_i\gamma^\mu(d'_L)_iW^+_\mu + h.c. \tag{1.30}$$

$$= -\frac{g}{\sqrt{2}}(\overline{u}_L)_i(U_{u_L}U^\dagger_{d_L})_{ij}\gamma^\mu(d_L)_jW^+_\mu + h.c., \tag{1.31}$$

where $(u_L)_i$ and $(d_L)_i$ are the left-handed quarks in the mass basis; and U_{u_L} with U_{d_L} are the respective unitary matrices that rotate the quarks from the interacting basis $(u'_L)_i$ and $(d'_L)_i$ to the mass basis [10,23].

It is from these terms in the lagrangian that the 3×3 unitary matrix arises

$$(V_{CKM})_{ij} \equiv (U_{u_L} U^{\dagger}_{d_L})_{ij}, \tag{1.32}$$

which is the Cabibbo-Kobayashi-Maskawa matrix [21,22]. Conventionally the CKM matrix is only used to rotate the down-type quarks from the weak interacting eigenstates to the mass eigenstates, whereas the up-types are chosen to be equal:

$$\begin{aligned} u'_i &= u_i, \\ d'_i &= (V_{CKM})_{ij} d_j, \end{aligned}$$

i.e.

$$\begin{pmatrix} d' \\ s' \\ b' \end{pmatrix} = V_{CKM} \begin{pmatrix} d \\ s \\ b \end{pmatrix} = \begin{pmatrix} V_{ud} & V_{us} & V_{ub} \\ V_{cd} & V_{cs} & V_{cb} \\ V_{td} & V_{ts} & V_{tb} \end{pmatrix} \begin{pmatrix} d \\ s \\ b \end{pmatrix}. \tag{1.33}$$

The CKM matrix elements V_{ij} are defined by the transitions of quarks from down-type ($j = d, s, b$) to up-type ($i = u, c, t$) or anti-up-type to anti-down-type [10,23]. The complex conjugates V^*_{ij} either describe transitions of up-type to down-type or anti-down-type to anti-up-type. Therefore invariance under a *CP* transformation requires that all $V_{ij} = V^*_{ij}$ (*i.e.* that these elements have no complex phase).

There are two commonly used parameterisations of the the CKM matrix. One is the Chau and Keung notation [24] which introduces Euler angles θ_{ij} for generations i and j. Shortening $\cos\theta_{ij}$ and $\sin\theta_{ij}$ to c_{ij} and s_{ij} respectively allows for the expression of the CKM matrix as

$$V_{CKM} = \begin{pmatrix} c_{12} & s_{12} & 0 \\ -s_{12} & c_{12} & 0 \\ 0 & 0 & 1 \end{pmatrix} \begin{pmatrix} c_{13} & 0 & s_{13}e^{-i\delta_{13}} \\ 0 & 1 & 0 \\ -s_{13}e^{i\delta_{13}} & 0 & c_{13} \end{pmatrix} \begin{pmatrix} 1 & 0 & 0 \\ 0 & c_{23} & s_{23} \\ 0 & -s_{23} & c_{23} \end{pmatrix} \tag{1.34}$$

$$= \begin{pmatrix} c_{12}c_{13} & s_{12}c_{13} & s_{13}e^{-i\delta_{13}} \\ -s_{12}c_{23} - c_{12}s_{23}s_{13}e^{i\delta_{13}} & c_{12}c_{23} - s_{12}s_{23}s_{13}e^{i\delta_{13}} & s_{23}c_{13} \\ s_{12}c_{23} - c_{12}c_{23}s_{13}e^{i\delta_{13}} & -c_{12}s_{23} - s_{12}c_{23}s_{13}e^{i\delta_{13}} & c_{13}c_{23} \end{pmatrix}. \tag{1.35}$$

In this parameterisation the complex phase is introduced by the parameter δ_{13} which is the source of the *CP* violation in the CKM mechanism of the Standard Model. The hierarchy of the small angles is $\sin\theta_{12} \gg \sin\theta_{23} \gg \sin\theta_{13}$. An intuitive approximation can be used to understand the relative importance of each matrix element. This is the Wolfenstein parameterisation [25] that uses powers of $\lambda = \sin\theta_{12} \approx 0.225$, with the higher order substitutions of

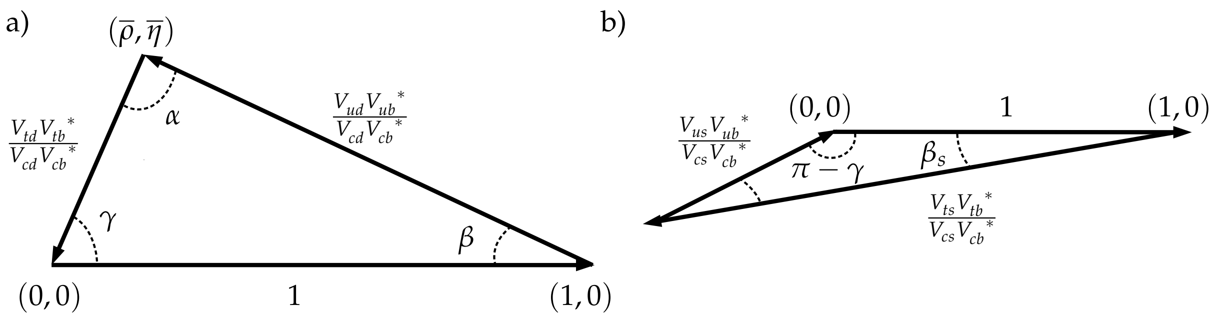

Figure 1.2.: The unitarity triangles formed from the orthogonal relations given by a) equation (1.47) and b) equation (1.48). These triangles introduce the definitions of the angles α, β, γ and β_s.

$A\lambda^2 = \sin\theta_{23}$ and $A\lambda^3(\rho - i\eta) = \sin\theta_{13}e^{-i\delta_{13}}$ to approximate the CKM matrix as

$$V_{CKM} = \begin{pmatrix} 1-\frac{1}{2}\lambda^2 & \lambda & A\lambda^3(\rho-i\eta) \\ -\lambda & 1-\frac{1}{2}\lambda^2 & A\lambda^2 \\ A\lambda^3(1-\rho-i\eta) & -A\lambda^2 & 1 \end{pmatrix} + \mathcal{O}(\lambda^4), \tag{1.36}$$

where A, ρ and the imaginary η are all parameters of order 1. Note that for the CP violation in system of B_s^0-$\overline{B}_s^0$ oscillations (see Section 1.2.2) the matrix element V_{ts} needs to be considered at a higher order of λ:

$$V_{ts} = -A\lambda^2 + \frac{1}{2}\lambda^4(1-2(\rho+i\eta)) + \mathcal{O}(\lambda^6). \tag{1.37}$$

For V_{ts}, the complex term is of order λ^4 (and therefore the CP violation) is small in comparison to that of V_{td} and V_{ub} which are of order λ^3. This has an important consequence for the size of the angles of the unitarity triangles that are introduced in the following part of this thesis.

Unitarity triangles and *CP* violation

As the CKM matrix is a 3×3 unitary matrix ($V_{CKM}^\dagger V_{CKM} = \mathbb{1}$), its elements will have 9 conditions to satisfy. There will be 3 unitary relations and 6 orthogonal relations. These relations arise from

$$V_{CKM}^\dagger V_{CKM} = V_{CKM}V_{CKM}^\dagger \tag{1.38}$$

$$V_{CKM}^\dagger V_{CKM} = \begin{pmatrix} V_{ud} & V_{us} & V_{ub} \\ V_{cd} & V_{cs} & V_{cb} \\ V_{td} & V_{ts} & V_{tb} \end{pmatrix} \begin{pmatrix} V_{ud}^* & V_{us}^* & V_{ub}^* \\ V_{cd}^* & V_{cs}^* & V_{cb}^* \\ V_{td}^* & V_{ts}^* & V_{tb}^* \end{pmatrix} = \begin{pmatrix} 1 & 0 & 0 \\ 0 & 1 & 0 \\ 0 & 0 & 1 \end{pmatrix}, \tag{1.39}$$

which implies that the unitarity relations are

$$V_{ud}V_{ud}^* + V_{us}V_{us}^* + V_{ub}V_{ub}^* = 1, \tag{1.40}$$
$$V_{cd}V_{cd}^* + V_{cs}V_{cs}^* + V_{cb}V_{cb}^* = 1, \tag{1.41}$$
$$V_{td}V_{td}^* + V_{ts}V_{ts}^* + V_{tb}V_{tb}^* = 1, \tag{1.42}$$

and the orthogonal relations neglecting complex conjugates are

$$V_{ud}V_{cd}^* + V_{us}V_{cs}^* + V_{ub}V_{cb}^* = 0, \tag{1.43}$$
$$V_{ud}V_{td}^* + V_{us}V_{ts}^* + V_{ub}V_{tb}^* = 0, \tag{1.44}$$
$$V_{cd}V_{td}^* + V_{cs}V_{ts}^* + V_{cb}V_{tb}^* = 0, \tag{1.45}$$
$$V_{ud}V_{us}^* + V_{cd}V_{cs}^* + V_{td}V_{ts}^* = 0, \tag{1.46}$$
$$V_{ud}V_{ub}^* + V_{cd}V_{cb}^* + V_{td}V_{tb}^* = 0, \tag{1.47}$$
$$V_{us}V_{ub}^* + V_{cs}V_{cb}^* + V_{ts}V_{tb}^* = 0. \tag{1.48}$$

It is from the relations that involve complex phases that the unitarity triangles are formed. For these relations to form triangles and equal 0 there must be complex phases present, as seen in the previous parameterisations. If there are no complex phases present then it is not possible to form triangles, *i.e.* they would be flat in a complex plane.

Considering the unitarity relation from equation (1.47), and dividing by $V_{cd}V_{cb}^*$, can give a unitarity triangle in a complex space (see Figure 1.2) with three sides: 1, $-V_{ud}V_{ub}^*/V_{cd}V_{cb}^*$ and $-V_{td}V_{tb}^*/V_{cd}V_{cb}^*$. This triangle defines the three angles α, β and γ and three vertices at $(0,0)$, $(1,0)$ and $(\overline{\rho},\overline{\eta})$ where

$$\overline{\rho} + i\overline{\eta} \equiv \frac{V_{ud}V_{ub}^*}{V_{cd}V_{cb}^*}. \tag{1.49}$$

which is the apex of the unitarity triangle with a unitary base. The definitions of $\overline{\rho}$ and $\overline{\eta}$, in terms of the Wolfenstein parameters, are

$$\overline{\rho} = \rho(1 - \frac{\lambda^2}{2}) + \mathcal{O}(\lambda^4), \qquad \overline{\eta} = \eta(1 - \frac{\lambda^2}{2}) + \mathcal{O}(\lambda^4). \tag{1.50}$$

The equivalent triangle for a system where the d is replaced by an s introduces the fourth and final angle of interest β_s and is given by equation (1.48) and shown in Figure 1.2. Other triangles can be formed from the other orthogonal relations but this will not introduce any fundamentally new angles.

The formal definitions of these angles are then given as

$$\alpha \equiv arg\left[-\frac{V_{td}V_{tb}{}^{*}}{V_{ud}V_{ub}{}^{*}}\right], \qquad \beta \equiv arg\left[-\frac{V_{cd}V_{cb}{}^{*}}{V_{td}V_{tb}{}^{*}}\right], \qquad \gamma \equiv arg\left[-\frac{V_{ud}V_{ub}{}^{*}}{V_{cd}V_{cb}{}^{*}}\right] \tag{1.51}$$

for the first triangle, and

$$\beta_s \equiv arg\left[-\frac{V_{ts}V_{tb}{}^{*}}{V_{cs}V_{cb}{}^{*}}\right] \tag{1.52}$$

for the second triangle. This angle is of special interest in this thesis and will be practically substituted for the angle

$$\phi_s = -2\beta_s \tag{1.53}$$

from this point forward. The utility of the replacement of β_s with ϕ_s is evident in the parameterisation of the *CP* asymmetries of B_s^0 decays involving $b \to c\bar{c}s$ transitions, which is covered in Section 1.2.2.

It can be intuitive to consider the CKM matrix with the introduced *CP* violating phase angles factorised out:

$$V_{CKM} = \begin{pmatrix} |V_{ud}| & |V_{us}| & |V_{ub}|e^{-i\gamma} \\ -|V_{cd}| & |V_{cs}| & |V_{cb}| \\ |V_{td}|e^{-i\beta} & -|V_{ts}|e^{-i\beta_s} & |V_{tb}| \end{pmatrix} + \mathcal{O}(\lambda^5), \tag{1.54}$$

giving a simple description of V_{CKM} where the sign of the real matrix elements is known along with the complex parts. It is now evident from the Wolfenstein parameterisation of the element V_{ts} (shown in equation (1.37)) that the angle β_s must be considerably smaller than the other angles.

Experimental status of the *CP* violating phases and the CKM matrix elements

The current measurements of the CKM matrix elements V_{ij} are summarised in Table 1.3. The details of the fit are described in [28]. These are values measured and included in the fit shown in Figure 1.3 to aid in the determining of the size of the unitarity triangle sides using a number of observable inputs. Therefore there are available *CP* violating phase angles, that are determined by the fit to be

$$\alpha = (91.98^{+0.82}_{-1.40})^{\circ}, \qquad \beta = (22.42^{+0.64}_{-0.37})^{\circ}, \qquad \gamma = (65.5^{+1.3}_{-1.2})^{\circ}. \tag{1.55}$$

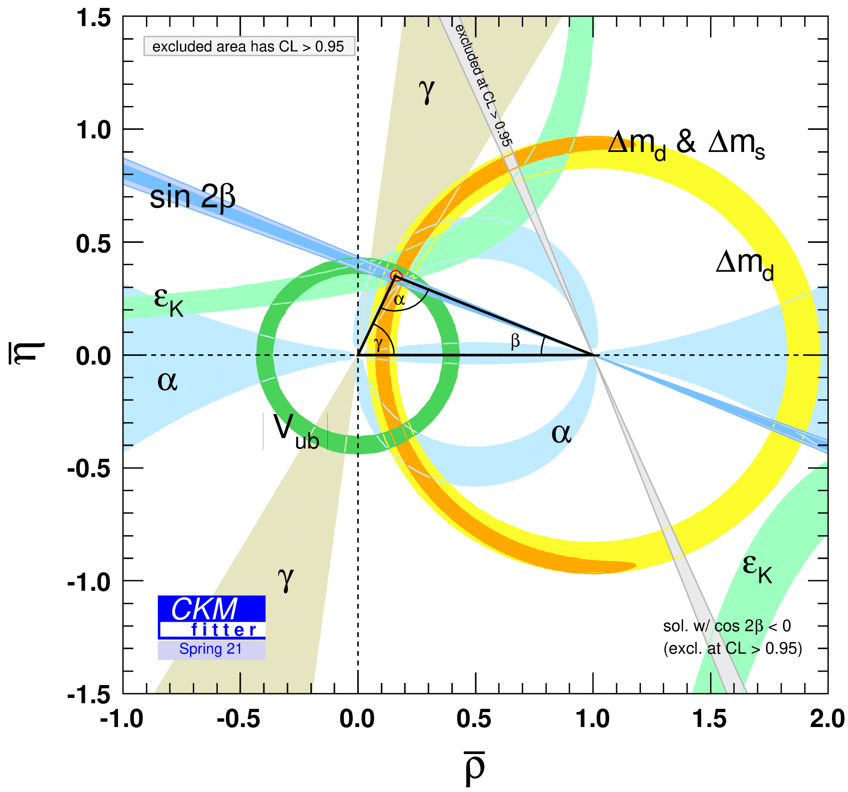

Figure 1.3.: The results of a fit on the measured CKM elements, B^0 and B_s^0 oscillation parameters and the *CP* phases α, β and γ. Results are shown in the $\bar{\rho}$ and $\bar{\eta}$ plane [26].

The angles are constrained by experimental measurements. The most precise measurements of α are determined in isospin analyses via $B \to \rho\pi$, $B \to \pi\pi$ and $B \to \rho\rho$ decays; β is best determined by $B \to J/\psi K$ or $B \to Dh^0$ decays; and γ is usually determined via $B \to DK$ decays [28].

As for the angle ϕ_s, the principle method of determination is through analyses of B_s^0 decays including a $b \to c\bar{c}s$ transition. The most precise modes for these measurements being $B_s^0 \to J/\psi K^+K^-$ and $B_s^0 \to J/\psi \pi^+\pi^-$. The combined averaging from various experimental measurements is shown in Figure 1.4. The averaging method is given in [27]. This determined that the angle measured with $b \to c\bar{c}s$ transitions is

$$\phi_s{}^{c\bar{c}s} = -0.050 \pm 0.019\,\text{rad}. \tag{1.56}$$

The most precise measurements to date come from the LHCb Experiment, for example the latest result (at the point of writing this thesis) is the updated measurement using the most favourable decay mode $B_s^0 \to J/\psi K^+K^-$, sometimes referred to as the Golden Channel for measuring ϕ_s.

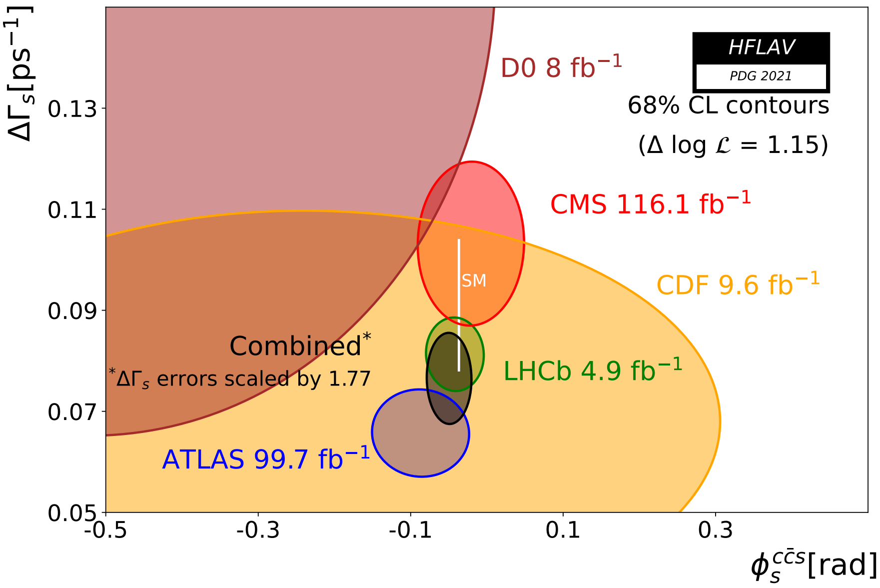

Figure 1.4.: Plot of the results of the fit done on results from the ATLAS, CMS, CDF, D0 and LHCb experiments. These results are shown in the ϕ_s and $\Delta\Gamma_s$ plane [27].

Table 1.3.: The current measurement status for the CKM elements (Spring 2021 global fit) [28]. This includes the type of decay channels that provided the best precision measurements [10].

V_{CKM} element	Best mode	Current measurement
V_{ud}	nuclear β decay rate	$0.974353^{+0.000049}_{-0.000056}$
V_{us}	semileptonic K decays	$0.22500^{+0.00024}_{-0.00021}$
V_{ub}	semileptonic B decays	$0.003667^{+0.000088}_{-0.000073}$
V_{cd}	semileptonic D decays	$0.22487^{+0.00024}_{-0.00021}$
V_{cs}	semileptonic D decays	$0.973521^{+0.000057}_{-0.000062}$
V_{cb}	semileptonic B decays	$0.04145^{+0.00035}_{-0.00061}$
V_{td}	B^0-$\bar{B}^0$ oscillations	$0.008519^{+0.000075}_{-0.00061}$
V_{ts}	B_s^0-$\bar{B}_s^0$ oscillations	$0.04065^{+0.00040}_{-0.00055}$
V_{tb}	$\mathcal{B}(t \to W^+b)/\mathcal{B}(t \to W^+q)$	$0.999142^{+0.000018}_{-0.000023}$

The combination of the studies of this mode gave $\phi_s = -0.081 \pm 0.032$ rad [29,30]. Combining all LHCb (including the additional modes of $B_s^0 \to J/\psi\pi^+\pi^-$, $B_s^0 \to \psi(2S)\phi$ and $B_s^0 \to D_s^+ D_s^-$) results gave $\phi_s = -0.042 \pm 0.025$ [29–35]. These values are currently still compatible with the Standard Model expectation of $\phi_s = -0.0370^{+0.0007}_{-0.0008}$ rad within two standard deviations. Then there is the global fit of [28] (same that gave equation (1.55)) which determines the angle to be

$$\phi_s = -0.0368^{+0.0009}_{-0.0006}\,\text{rad}, \tag{1.57}$$

which has the same compatibility of two standard deviations.

In this thesis, a study of the pseudoscalar to vector and pseudoscalar decays $B_s^0 \to J/\psi\eta^{(\prime)}$ is shown. This decay involves a $b \to c\bar{c}s$ transition so it is necessary to explore the possibility of using this decay channel in an analysis at the LHCb experiment to contribute towards the measurements of $\phi_s{}^{c\bar{c}s}$. This is a mode of particular interest for these kinds of analysis as it has the advantage of not requiring a full angular analysis. This is unlike the previous channels of study such as $B_s^0 \to J/\psi K^+K^-$ and $B_s^0 \to J/\psi\pi^+\pi^-$ which both have contributions of intermediary resonances (dominantly $\phi \to K^+K^-$ and $\rho^0 \to \pi^+\pi^-$) which explicitly involve the decay of the pseudoscalar B_s^0 to two vectors.

1.2. Neutral mesons

As this thesis concerns $B_{(s)}^0$ decays, it is good to note some of the most interesting tests of Standard Model physics available in the decays of these neutral mesons. It may be possible to study the oscillations of the B_s^0 mesons in the $B_s^0 \to J/\psi\eta^{(\prime)}$ decay modes. In this section, the time development of neutral mesons and their decay amplitudes are described with the intention of deriving the *CP* violating asymmetries arising in the interference between the rates of decay of a meson or anti-meson decaying to the same final state. Then it is shown how, in the case of $b \to c\bar{c}s$, these asymmetries relate to the *CP* phase ϕ_s.

1.2.1. Neutral oscillations

The *CP* violating phases of the CKM matrix can be determined by the experimental measurements of the oscillations of neutral mesons. These oscillations occur between a meson P^0 and anti-meson $\bar{P}^0$ where $\overset{(-)}{P^0} \equiv \overset{(-)}{K}{}^0, \overset{(-)}{D^0}, \overset{(-)}{B^0}, \overset{(-)}{B_s^0}$. This is measured in the relative phase difference between the decay amplitudes to a given final state that is a *CP* eigenstate accessible to both the decaying meson and anti-meson. This phase difference originates in the differences of lifetimes to be described in this section. Considering the particle-antiparticle states as oscillating in a state

$$|\psi(t)\rangle = a(t)|P^0\rangle + b(t)|\bar{P}^0\rangle, \tag{1.58}$$

with time-dependent coefficients $a(t)$ and $b(t)$, and considering the Schrödinger equation

$$i\frac{\partial}{\partial t}|\psi(t)\rangle = H|\psi(t)\rangle. \tag{1.59}$$

The Hamiltonian H is a 2×2 matrix in the P^0 and $\bar{P}^0$ basis that can be separated into imaginary and real parts

$$H = M - i\frac{\Gamma}{2}, \tag{1.60}$$

where M and Γ are the 2×2 mass and decay matrices that are both Hermitian.

Under the assumption that CPT is conserved $H_{11} = H_{22}$ and due to the hermiticity of H $H_{21} = H_{12}^*$ so this Hamiltonian can be written as

$$H = \begin{pmatrix} M_{11} - i\Gamma_{11}/2 & M_{12} - i\Gamma_{12}/2 \\ M_{21} - i\Gamma_{21}/2 & M_{22} - i\Gamma_{22}/2 \end{pmatrix} = \begin{pmatrix} M_{11} - i\Gamma_{11}/2 & M_{12} - i\Gamma_{12}/2 \\ M_{12}^* - i\Gamma_{12}^*/2 & M_{11} - i\Gamma_{11}/2 \end{pmatrix}, \tag{1.61}$$

where the diagonal matrix elements describe the propagation of the mesons and the off-diagonal matrix elements are responsible for the transitions between P^0 and $\bar{P}^0$. The on-shell contribution (via real intermediary particles f in $P^0 \to f \to \bar{P}^0$) and off-shell contribution (via box-diagrams with virtual particles) to the oscillations are associated with the $-i\Gamma_{12}^{(*)}/2$ and $M_{12}^{(*)}$ terms respectively. From these transitions a phase can be determined between on-shell and off-shell intermediate states

$$\phi = arg\left[-\frac{M_{12}}{\Gamma_{12}}\right]. \tag{1.62}$$

The mass eigenstates can be determined by the diagonalisation of H to give two states $|P_H\rangle$ and $|P_L\rangle$ [2] with $\Delta m = m_H - m_L > 0$ and $\Delta\Gamma = \Gamma_L - \Gamma_H$. The corresponding eigenvectors are then the states

$$|P_L\rangle = p|P^0\rangle - q|\bar{P}^0\rangle, \tag{1.63}$$

$$|P_H\rangle = p|P^0\rangle + q|\bar{P}^0\rangle \tag{1.64}$$

which, due to the decision that $\Delta m > 0$, gives q/p[3] as a positive value

$$\frac{q}{p} = \sqrt{\frac{M_{12}^* - i\Gamma_{12}^*/2}{M_{12} - i\Gamma_{12}/2}}. \tag{1.65}$$

A relation between the on-shell and off-shell transition phase and the q/p is therefore

$$2\left(1 - \frac{|q|}{|p|}\right) \approx \frac{|\Gamma_{12}|}{|M_{12}|}\sin\phi \approx \frac{\Delta\Gamma}{\Delta m}\tan\phi. \tag{1.66}$$

[2] There is an exception to this notation in the case of $P = K$ where instead of heavy (P_H) and light (P_L) states, the use of short-lived (K_S) and long-lived (K_L) are used. In this notation $\Delta m = m_L - m_S$ and from experimental observation $\Delta\Gamma = \Gamma_S - \Gamma_L > 0$ where $CP|K_L\rangle = -|K_L\rangle$.

[3] In the K case, there is also the historic use of the parameter ϵ instead of p and q where $q/p = (1-\epsilon)/(1+\epsilon)$.

Time dependence

From the mass eigenstate relations in equations (1.63) and (1.64), the flavour states P^0 and $\bar{P}^0$ can be written in terms of the mass states as

$$|P^0\rangle = \frac{1}{2p}(|P_H\rangle + |P_L\rangle), \tag{1.67}$$

$$|\bar{P}^0\rangle = \frac{1}{2q}(|P_H\rangle - |P_L\rangle). \tag{1.68}$$

The evolution of the mass states over time are determined from Schrödinger's equation (1.59) as

$$|P_L(t)\rangle = e^{-im_L t - \Gamma_L t/2}|P_L(0)\rangle = e^{-im_L t - \Gamma_L t/2}(p|P^0\rangle - q|\bar{P}^0\rangle), \tag{1.69}$$

$$|P_H(t)\rangle = e^{-im_H t - \Gamma_H t/2}|P_H(0)\rangle = e^{-im_H t - \Gamma_H t/2}(p|P^0\rangle + q|\bar{P}^0\rangle), \tag{1.70}$$

and by substituting equations (1.69) and (1.70) into equations (1.67) and (1.68) gives the time dependence of the oscillations between particle and antiparticle states

$$|P^0(t)\rangle = g_+(t)|P^0\rangle + \frac{q}{p}g_-(t)|\bar{P}^0\rangle \tag{1.71}$$

$$|\bar{P}^0(t)\rangle = \frac{p}{q}g_-(t)|P^0\rangle + g_+(t)|\bar{P}^0\rangle, \tag{1.72}$$

where the time-dependent functions are

$$g_\pm(t) = \frac{1}{2}(e^{-im_H t - \Gamma_H t/2} \pm e^{-im_L t - \Gamma_L t/2}), \tag{1.73}$$

with a squared modulo

$$|g_\pm(t)|^2 = \frac{e^{-\Gamma t}}{2}\left[\cosh\left(\Delta\Gamma t/2\right) \pm \cos\left(\Delta m t\right)\right] \tag{1.74}$$

and

$$g^*_\pm(t)g_\mp(t) = \frac{e^{-\Gamma t}}{2}\left[-\sinh\left(\Delta\Gamma t/2\right) \pm i\sin\left(\Delta m t\right)\right], \tag{1.75}$$

where $\Gamma = (\Gamma_L + \Gamma_H)/2 = 1/\tau$ is the decay constant.

Then for a particle starting in either the $|P^0\rangle$ or $|\bar{P}^0\rangle$ states, the probability that it is measured as $|P^0\rangle$ or $|\bar{P}^0\rangle$ can be found by projecting equation (1.71) or (1.72) to those states:

$$|\langle P^0|P^0(t)\rangle|^2 = |g_+(t)|^2, \tag{1.76}$$
$$|\langle \bar{P}^0|\bar{P}^0(t)\rangle|^2 = |g_+(t)|^2, \tag{1.77}$$
$$|\langle \bar{P}^0|P^0(t)\rangle|^2 = \left|\frac{q}{p}\right|^2 |g_-(t)|^2, \tag{1.78}$$
$$|\langle P^0|\bar{P}^0(t)\rangle|^2 = \left|\frac{p}{q}\right|^2 |g_-(t)|^2. \tag{1.79}$$

These relations give the different probabilities of net oscillations[4] at a time t from production, depending on the starting state. Therefore the probability that there are zero net oscillations is given in equations (1.76) and (1.77). The probability of oscillations from P^0 to $\bar{P}^0$ is given in equation (1.78), and the probability for $\bar{P}^0$ to P^0 oscillations is in equation (1.79).

Meson decays

With an understanding of the different P^0 and $\bar{P}^0$ states as well as $P^0 - \bar{P}^0$ oscillations, experimental studies of *CP* violation in the meson system also require a time dependent description of the decay rates of these mesons to final state f. The definition of the decay amplitudes are

$$A_f \equiv \langle f|T|P^0\rangle, \qquad \bar{A}_f \equiv \langle f|T|\bar{P}^0\rangle, \tag{1.80}$$

where T is the transition matrix. Including the time dependency that was given in equations (1.71) and (1.72) leads to the decay amplitudes for the starting states P^0 or $\bar{P}^0$ at a time t from production

$$A_{P^0(t)\to f} = g_+(t)A_f + \frac{q}{p}g_-(t)\bar{A}_f, \tag{1.81}$$
$$A_{\bar{P}^0(t)\to f} = \frac{p}{q}g_-(t)A_f + g_+(t)\bar{A}_f. \tag{1.82}$$

[4]By net oscillations, it is meant that the flavour of the meson at the two moments of interest, production and decay, are different (one net oscillation) or the same (zero net oscillations). If there is an even number of meson oscillations it is treated the same as zero oscillations, and inversely if there is an odd number of oscillations they are treated as one oscillation.

By employing the common substitution of $\lambda_f \equiv \frac{q}{p}\frac{\bar{A}_f}{A_f}$ and $\bar{\lambda}_f \equiv \lambda_f^{-1}$, the squared modulo of these decay amplitudes can then give the decay rates as

$$\Gamma_{P^0(t)\to f} = |A_f|^2 \left(|g_+(t)|^2 + |\lambda_f|^2 |g_-(t)|^2 + 2\mathcal{R}e[\lambda_f g_+^*(t) g_-(t)]\right), \tag{1.83}$$

$$\Gamma_{\bar{P}^0(t)\to f} = |A_f|^2 \left|\frac{p}{q}\right|^2 \left(|g_-(t)|^2 + |\lambda_f|^2 |g_+(t)|^2 + 2\mathcal{R}e[\lambda_f g_+(t) g_-^*(t)]\right), \tag{1.84}$$

and considering the antiparticle equivalent final state (*i.e.* *CP* conjugate) similar relations can be inferred:

$$\Gamma_{P^0(t)\to \bar{f}} = |\bar{A}_{\bar{f}}|^2 \left|\frac{q}{p}\right|^2 \left(|g_-(t)|^2 + |\bar{\lambda}_{\bar{f}}|^2 |g_+(t)|^2 + 2\mathcal{R}e[\bar{\lambda}_{\bar{f}} g_+(t) g_-^*(t)]\right), \tag{1.85}$$

$$\Gamma_{\bar{P}^0(t)\to \bar{f}} = |\bar{A}_{\bar{f}}|^2 \left(|g_+(t)|^2 + |\bar{\lambda}_{\bar{f}}|^2 |g_-(t)|^2 + 2\mathcal{R}e[\bar{\lambda}_{\bar{f}} g_+^*(t) g_-(t)]\right), \tag{1.86}$$

The equations with the $|q/p|^2$ or $|p/q|^2$ factors describe the decays with a net oscillation having occurred at the time of measurement. The terms $2\mathcal{R}e[\lambda_f g(t) g^*(t)]$ come from the interference between decays with and without oscillations.

The decay rates can be written in a form (termed master equations) that are obtained by substituting equations (1.74) and (1.75) into equations (1.83) and (1.84):

$$\begin{aligned}\Gamma_{P^0(t)\to f} = |A_f|^2(1+|\lambda_f|^2)\frac{e^{-\Gamma t}}{2}\Big[\cosh\left(\frac{\Delta\Gamma t}{2}\right) - D_f \sinh\left(\frac{\Delta\Gamma t}{2}\right) \\ + C_f \cos(\Delta m t) - S_f \sin(\Delta m t)\Big],\end{aligned} \tag{1.87}$$

$$\begin{aligned}\Gamma_{\bar{P}^0(t)\to f} = |A_f|^2\left|\frac{p}{q}\right|^2(1+|\lambda_f|^2)\frac{e^{-\Gamma t}}{2}\Big[\cosh\left(\frac{\Delta\Gamma t}{2}\right) - D_f \sinh\left(\frac{\Delta\Gamma t}{2}\right) \\ - C_f \cos(\Delta m t) + S_f \sin(\Delta m t)\Big],\end{aligned} \tag{1.88}$$

$$\begin{aligned}\Gamma_{\bar{P}^0(t)\to \bar{f}} = |\bar{A}_{\bar{f}}|^2(1+|\bar{\lambda}_{\bar{f}}|^2)\frac{e^{-\Gamma t}}{2}\Big[\cosh\left(\frac{\Delta\Gamma t}{2}\right) - D_{\bar{f}} \sinh\left(\frac{\Delta\Gamma t}{2}\right) \\ + C_{\bar{f}} \cos(\Delta m t) - S_{\bar{f}} \sin(\Delta m t)\Big],\end{aligned} \tag{1.89}$$

$$\begin{aligned}\Gamma_{P^0(t)\to \bar{f}} = |\bar{A}_{\bar{f}}|^2\left|\frac{q}{p}\right|^2(1+|\bar{\lambda}_{\bar{f}}|^2)\frac{e^{-\Gamma t}}{2}\Big[\cosh\left(\frac{\Delta\Gamma t}{2}\right) - D_{\bar{f}} \sinh\left(\frac{\Delta\Gamma t}{2}\right) \\ - C_{\bar{f}} \cos(\Delta m t) + S_{\bar{f}} \sin(\Delta m t)\Big],\end{aligned} \tag{1.90}$$

where parameters are used to simplify the equations

$$D_f \equiv \frac{2\mathcal{R}e[\lambda_f]}{1+|\lambda_f|^2}, \qquad C_f \equiv \frac{1-|\lambda_f|^2}{1+|\lambda_f|^2}, \qquad S_f \equiv \frac{2\mathcal{I}m[\lambda_f]}{1+|\lambda_f|^2}, \tag{1.91}$$

with $D_f^2 + C_f^2 + S_f^2 = 1$.

The three types of *CP* violation in the context of neutral mesons

In the context of neutral meson decays there is a distinction made between the sources of *CP* violation: the direct *CP* violation of a decay, the case of *CP* violation in the oscillations of neutral mesons and the *CP* violation in the interference between decays that occur with and without prior meson oscillations. Both the cases involving meson mixing are considered to be the indirect cases of *CP* violation.

For direct *CP* violation the rate of decay of the neutral meson P^0 to a final state f is not the same as the rate of the anti-meson $\bar{P}^0$ to $\overline{f}$ (*i.e.* $\Gamma_{P^0 \to f} \neq \Gamma_{\bar{P}^0 \to \overline{f}}$). From equations (1.87) and (1.89) it is therefore implied that $|A_f| \neq |\overline{A}_{\overline{f}}|$. This is the only possible type of *CP* violation to occur in mesons that do not oscillate (*i.e.* in charged meson decays). Over the years of 2007 to 2012 experiments such as BaBar, Belle, CDF and LHCb have precisely measured direct *CP* violation in neutral channels such as $B^0 \to K^+\pi^-$, $B^0 \to \pi^+\pi^-$ and $B_s^0 \to K^+\pi^-$ [36–39]. Although this section is primarily concerning neutral mesons, this type of *CP* violation is also present in the $B^\pm$ system such as found in studies of $B^+ \to K^+\pi^0$ [37] and $B^+ \to D^0K^+$ [40].

For the indirect *CP* violation from mixing the rate of oscillations from neutral meson P^0 to anti-meson $\bar{P}^0$ is not the same as the inverse case ($\Gamma_{P^0 \to \bar{P}^0} \neq \Gamma_{\bar{P}^0 \to P^0}$). This type of *CP* violation occurs if $|q/p| \neq 1$, as is evident in equations (1.88) and (1.90).

When meson decays have the same final state whether or not the mesons were particles or antiparticles at the moment of decay (*i.e.* when $f = \overline{f}$), then the second indirect type of *CP* violation may occur. This is due to the interference between the decay amplitudes of the meson P^0 to a final state f and the decay of $\bar{P}^0$ to the same state f. This interference arises between two amplitudes that contribute to the total decay amplitude. These two amplitudes are for when the decays occur with one or zero net oscillations. Measurement of *CP* violation must be done via studies of the time-dependent decay rate by defining the *CP*-asymmetry as

$$\mathcal{A}^{CP}(t) = \frac{\Gamma_{\bar{P}^0(t) \to f} - \Gamma_{P^0(t) \to f}}{\Gamma_{\bar{P}^0(t) \to f} + \Gamma_{P^0(t) \to f}} = \frac{S_f \sin(\Delta m t) - C_f \cos(\Delta m t)}{\cosh\left(\frac{\Delta\Gamma t}{2}\right) - D_f \sinh\left(\frac{\Delta\Gamma t}{2}\right)}, \tag{1.92}$$

where $|q/p|$ is considered to unitary in this case, which in Section 1.2.2 is shown to be a correct approximation due to the direct *CP* violation being much smaller than the *CP* violation in the interference between the decay amplitudes of P^0 and $\bar{P}^0$. The term proportional to C_f is related to the direct *CP* violation occurring in the decay amplitudes if $\Gamma_{P^0(t) \to f} \neq \Gamma_{\bar{P}^0(t) \to \overline{f}}$ *i.e.* if $|A_f| \neq |\overline{A}_{\overline{f}}|$. That leaves the imaginary term S_f and the real term D_f as the terms describing *CP* violation related to the interference.

1.2.2. Time-dependent *CP* asymmetries for B^0 and B_s^0 decays

Convenient approximations arise in the cases of the B^0 and B_s^0 systems. With negligible *CP* violation expected to arise in the mixing of B^0-$\bar{B}^0$ or B_s^0-$\bar{B}_s^0$, the value of the mixing parameters are supposed to have equal magnitude ($|q/p| \approx 1$). This also means the parameter λ_f can be simplified to $|\lambda_f| \approx |\bar{A}_f/A_f|$. In the B^0 system the difference between the lifetimes of the heavy and light mass eigenstates is negligible meaning that $\Delta\Gamma_d \approx 0$. The decay rates from equations (1.87) and (1.88), when applied to the B_s^0 system, can then be written as

$$\Gamma_{B_s^0(t)\to f} = (|A_f|^2 + |\bar{A}_f|^2)\frac{e^{-\Gamma_s t}}{2}\left[\cosh\left(\frac{\Delta\Gamma_s t}{2}\right) - D_f \sinh\left(\frac{\Delta\Gamma_s t}{2}\right)\right.$$
$$\left. + C_f \cos(\Delta m_s t) - S_f \sin(\Delta m_s t)\right], \tag{1.93}$$
$$\Gamma_{\bar{B}_s^0(t)\to f} = (|A_f|^2 + |\bar{A}_f|^2)\frac{e^{-\Gamma_s t}}{2}\left[\cosh\left(\frac{\Delta\Gamma_s t}{2}\right) - D_f \sinh\left(\frac{\Delta\Gamma_s t}{2}\right)\right.$$
$$\left. - C_f \cos(\Delta m_s t) + S_f \sin(\Delta m_s t)\right]. \tag{1.94}$$

For the *CP*-asymmetry, this yields the same relation as equation (1.92). For the B^0 meson $\Delta\Gamma_d/\Gamma_d = 0.001 \pm 0.010$ [41] so the approximation of $\Delta\Gamma \approx 0$ for the B^0 system is typically used. In this case the decay rates are no longer sensitive to D_f and $\cosh\Delta\Gamma_d/2 \approx 1$ giving

$$\Gamma_{B^0(t)\to f} = (|A_f|^2 + |\bar{A}_f|^2)\frac{e^{-\Gamma_d t}}{2}\left[1 + C_f \cos(\Delta m_d t) - S_f \sin(\Delta m_d)\right], \tag{1.95}$$
$$\Gamma_{\bar{B}^0(t)\to f} = (|A_f|^2 + |\bar{A}_f|^2)\frac{e^{-\Gamma_d t}}{2}\left[1 - C_f \cos(\Delta m_d t) + S_f \sin(\Delta m_d t)\right]. \tag{1.96}$$

with the simpler relation for the *CP*-asymmetry as

$$\mathcal{A}^{CP}(t) = \frac{\Gamma_{\bar{B}^0(t)\to f} - \Gamma_{B^0(t)\to f}}{\Gamma_{\bar{B}^0(t)\to f} + \Gamma_{B^0(t)\to f}} = S_f \sin(\Delta m_d t) - C_f \cos(\Delta m_d t). \tag{1.97}$$

Considering the case of negligible direct *CP* violation ($C_f \approx 0$) the terms for interference become simply $D_f = \mathcal{R}e[\lambda_f]$ and $S_f = \mathcal{I}m[\lambda_f]$. This reduces the *CP*-asymmetries for B^0 and B_s^0 systems to single terms as

$$\mathcal{A}^{CP}(t) = \frac{\Gamma_{\bar{B}^0(t)\to f} - \Gamma_{B^0(t)\to f}}{\Gamma_{\bar{B}^0(t)\to f} + \Gamma_{B^0(t)\to f}} = \mathcal{I}m[\lambda_f]\sin(\Delta m_d t) \tag{1.98}$$

for the B^0, and

$$\mathcal{A}^{CP}(t) = \frac{\Gamma_{\bar{B}_s^0(t)\to f} - \Gamma_{B_s^0(t)\to f}}{\Gamma_{\bar{B}_s^0(t)\to f} + \Gamma_{B_s^0(t)\to f}} = \frac{\mathcal{I}m[\lambda_f]\sin(\Delta m_s t)}{\cosh\left(\frac{\Delta\Gamma_s t}{2}\right) - \mathcal{R}e[\lambda_f]\sinh\left(\frac{\Delta\Gamma_s t}{2}\right)} \tag{1.99}$$

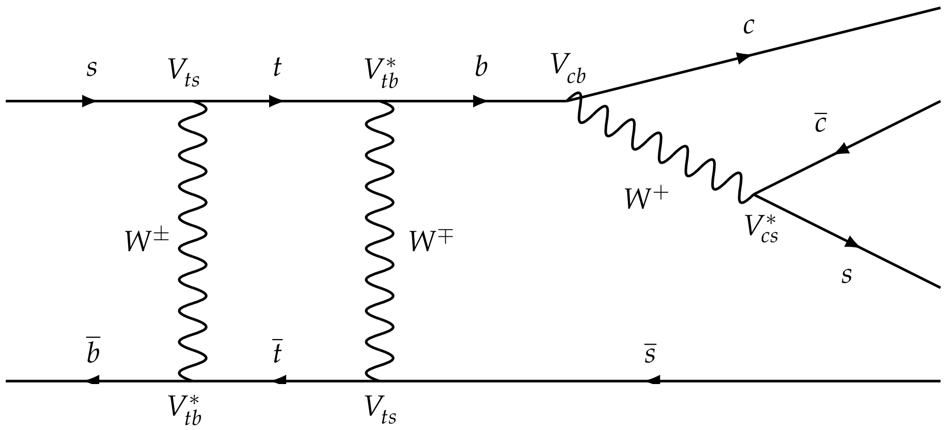

Figure 1.5.: Diagram for the dominant $b \to c\bar{c}s$ decay transition after a single $B^0_s \to \overline{B}^0_s$ oscillation. The virtual t and $\bar{t}$ could also be $u\bar{u}$ or $c\bar{c}$, although these are less common.

for the B^0_s, where the denominator is non-negligible due to $\Delta\Gamma_s/\Gamma_s = 0.128 \pm 0.007$ being much larger than $\Delta\Gamma_d/\Gamma_d$ [41].

Time-dependent *CP* asymmetries in relation to ϕ_s via $b \to c\bar{c}s$ transitions

In $b \to c\bar{c}s$ transitions in the B^0_s system there can be a spectator s. Figure 1.5 shows the dominant process for these transitions with virtual $t\bar{t}$ pairs in the $\overline{B}^0_s$-B^0_s oscillation and the relevant CKM matrix elements describing this. Considering the case where $c\bar{c}$ forms a charmonium J/ψ meson and f is a *CP* eigenstate, the definition of $\lambda_{f=J/\psi s\bar{s}}$ gives

$$\lambda_{J/\psi s\bar{s}} \equiv \left(\frac{q}{p}\right)_{B^0_s} \frac{\overline{A}_{J/\psi s\bar{s}}}{A_{J/\psi s\bar{s}}} = \eta_{CP} \frac{V^*_{tb}V_{ts}}{V^*_{ts}V_{tb}} \frac{V_{cb}V^*_{cs}}{V^*_{cb}V_{cs}}, \tag{1.100}$$

with η_{CP} as the *CP* eigenvalue of the final state equal to $+1$ or -1 for *CP*-odd or *CP*-even states respectively. It is defined by the relation $|\overline{f}\rangle = CP|f\rangle = \eta_{CP}|f\rangle$ which implies that $A_{\overline{f}} = \eta_{CP}A_f$ and $\overline{A}_{\overline{f}} = \eta_{CP}\overline{A}_f$. From the definition of β_s in equation (1.52) and cancelling the real parts of the matrix elements leaves

$$\lambda_{J/\psi s\bar{s}} = \eta_{CP} e^{i2\beta_s} = \eta_{CP} e^{-i\phi_s}. \tag{1.101}$$

It is possible to introduce the *CP*-violating phase ϕ_s into the parameters $D_{J/\psi s\bar{s}}$ and $S_{J/\psi s\bar{s}}$ by considering that

$$D_{J/\psi s\bar{s}} = \eta_{CP}\cos\phi_s, \qquad S_{J/\psi s\bar{s}} = -\eta_{CP}\sin\phi_s \tag{1.102}$$

This now gives the relation between the time-dependent *CP* asymmetry and the mixing angle ϕ_s as

$$\mathcal{A}^{CP}(t) = \frac{\Gamma_{\bar{B}^0_s(t)\to f} - \Gamma_{B^0_s(t)\to f}}{\Gamma_{\bar{B}^0_s(t)\to f} + \Gamma_{B^0_s(t)\to f}} = \frac{-\eta_{CP}\sin\phi_s \sin(\Delta m_s t)}{\cosh\left(\frac{\Delta\Gamma_s t}{2}\right) - \eta_{CP}\cos\phi_s \sinh\left(\frac{\Delta\Gamma_s t}{2}\right)} \tag{1.103}$$

1.3. $\eta^{(\prime)}$ physics

In order to understand the physics underpinning the light (compared with $B^0_{(s)}$) $\eta^{(\prime)}$ mesons, it is necessary to consider their quark content and the descriptive power that comes with this. This is why this section starts with an overall description of the quark model and how it describes and categorises mesons. There is focus on the mixing between zero-isospin mesons which has noticeable impacts on the production and decay rates of these mesons. In this thesis, this mixing is studied by the measurement of various decays of $B^0_{(s)} \to J/\psi\eta^{(\prime)}$. Predictions of the mixing can be made using this quark model but, as will be shown in this section, there are inconsistencies that arise in this model due to the gluon dynamics of theses mesons at low energies. This is why calculations must also be made with the use of an EFT (called chiral perturbation theory) that better describes these mesons in this energy regime.

There is also the discussion of the possible glueball states that enter in the mixing of η-η' mesons and so must also be accounted for in studies of the mixing. These glueball states could possibly be attributed to pseudoscalar meson resonances somewhere in between the masses of the η' and the η_c meson, the lightest charmonium ($c\bar{c}$) state. There are also a large number of other interesting physics tests not explored in the analyses of this thesis. These tests are also summarised at the end of this section to give a broad overview of the prospects for $\eta^{(\prime)}$ mesons in studying Standard Model and Beyond Standard Model physics.

1.3.1. The quark model

Quarks

Hadrons are described by quantum numbers that are directly related to their quark content. This description is called the quark model and considers the hadronic wavefunctions in terms of the valence quarks. The quarks are spin-$\frac{1}{2}$ fermions which are also attributed with the quantum numbers:

1. Q: electric charge ($+2/3$ for up-type quarks and $-1/3$ for down-type quarks),
2. $\mathcal{B}$: baryon number ($1/3$ for all quarks),

3. I: isospin ($+1/2$ for u and d quarks and 0 for s, c, b and t quarks),
4. I_3: third component of isospin ($-1/2$ for d and $= +1/2$ for u),
5. S: strangeness (-1 for the s quark),
6. C: charm ($+1$ for the c quark),
7. B: bottomness ($= -1$ for the b quark),
8. T: topness ($+1$ for the t quark),

The definition of another quantum number of interest can also be determined by the values of some of these other quantum numbers. This is called the strong hypercharge[5] and is calculated as

$$Y_s = \mathcal{B} + S - \frac{1}{3}(C + B + T), \tag{1.104}$$

where $Y_s = 1/3$ for u and d quarks and $Y_s = -2/3$ for the s quark. The electric charge of only the non-zero Y_s quarks (u, d and s) can be determined by the use of the Gell-Mann-Nishijima formula

$$Q = I_3 + \frac{Y_s}{2} \tag{1.105}$$

The sign convention for the charge is therefore the same as the value of the sign of the flavour quantum numbers.

Mesons

Mesons are bound states of quarks and antiquarks ($q\overline{q}$) and can be characterised by their spin J and their charge-conjugation C and parity P eigenvalues. Their spin can be calculated by the equation

$$|l - s| \leq J \leq |l + s|, \tag{1.106}$$

where l is the relative angular momentum between quarks and s is the net spin of the two quarks ($\frac{1}{2} \pm \frac{1}{2} = 1, 0$ for aligned or anti-aligned spins). The numbers l and s also determine the values of C and P as

$$C = (-1)^{l+s}, \qquad P = (-1)^{l+1}. \tag{1.107}$$

The categorisation of mesons can then be given by the multiplets J^{PC}:

[5] Not to confused with the variable introduced earlier as the weak hypercharge.

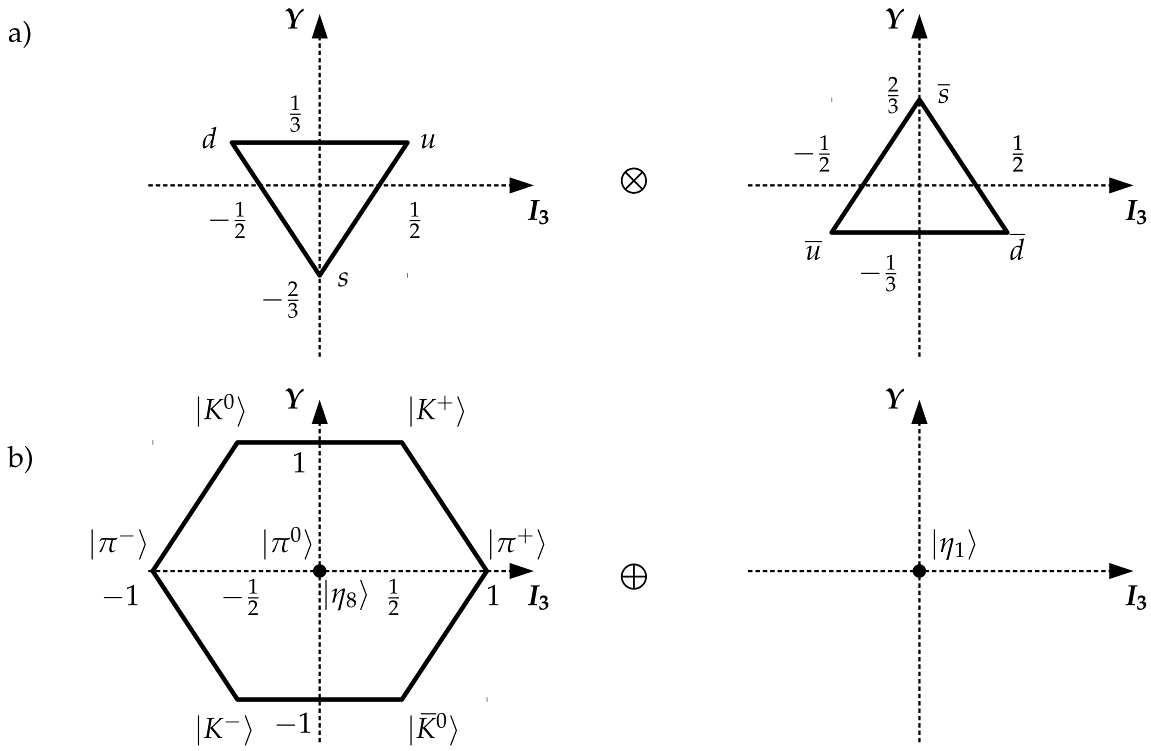

Figure 1.6.: Diagrams of the multiplets for a) the SU(3) triplets ($3 \otimes \bar{3}$) and b) the SU(3) octet and singlet ($8 \oplus 1$) for the pseudoscalar mesons.

1. $J^{PC} = 0^{-+}$ with $l = 0$ and $s = 0$ are the pseudoscalar mesons,
2. $J^{PC} = 1^{--}$ with $l = 0$ and $s = 1$ are the vector meson,
3. $J^{PC} = 0^{++}$ with $l = 1$ and $s = 1$ are scalar mesons,
4. $J^{PC} = 1^{++}(1^{+-})$ with $l = 1$ and $s = 1(0)$ are axial vector mesons,
5. $J^{PC} = 2^{++}$ with $l = 1$ and $s = 1$ are tensor mesons.

The light mesons with just u, d or s quarks can be grouped into a singlet and octet from their fundamental triplet quark combinations:

$$3 \otimes \bar{3} = 1 \oplus 8.$$

This is a $\mathrm{SU}(3)_F$ group representation shown in Figure 1.6, where the various mesons can be represented in the quark flavour basis as an octet with a multiplet structure for their respective isospins. With isospin-1 pions

$$|\pi^+\rangle = |u\bar{d}\rangle, \qquad \text{with } I_3 = 1, Y = 0, \tag{1.108}$$
$$|\pi^-\rangle = |\bar{u}d\rangle, \qquad \text{with } I_3 = -1, Y = 0, \tag{1.109}$$
$$|\pi^0\rangle = \frac{1}{\sqrt{2}}(|u\bar{u}\rangle - |d\bar{d}\rangle), \qquad \text{with } I_3 = 0, Y = 0, \tag{1.110}$$

the isospin-$\frac{1}{2}$ kaons

$$|K^+\rangle = |u\bar{s}\rangle, \qquad \text{with } I_3 = 1/2, Y = 1, \tag{1.111}$$
$$|K^-\rangle = |\bar{u}s\rangle, \qquad \text{with } I_3 = -1/2, Y = -1, \tag{1.112}$$
$$|K^0\rangle = |d\bar{s}\rangle, \qquad \text{with } I_3 = -1/2, Y = 1, \tag{1.113}$$
$$|\bar{K}^0\rangle = |\bar{d}s\rangle, \qquad \text{with } I_3 = 1/2, Y = -1, \tag{1.114}$$

and the isospin-0

$$|\eta_8\rangle = \frac{1}{\sqrt{6}}(|u\bar{u}\rangle + |d\bar{d}\rangle - 2|s\bar{s}\rangle), \qquad \text{with } I_3 = 0, Y = 0. \tag{1.115}$$

The additional singlet state introduces the second isospin-0 pseudoscalar

$$|\eta_1\rangle = \frac{1}{\sqrt{3}}(|u\bar{u}\rangle + |d\bar{d}\rangle + |s\bar{s}\rangle), \qquad \text{with } I_3 = 0, Y = 0, \tag{1.116}$$

where the singlet and octet states of the η and η' mesons represented as η_1 and η_8 respectively.

All $I = 0$ mesons of the same J^{PC} multiplet can mix due to the breaking of SU(3) symmetry which results from the reality that $m_u \neq m_d \neq m_s$. This is why η and η' mix, but also in general terms, f and f' also may mix which can be described with a single mixing angle θ while considering general isospin-zero octet (ψ_8) and singlet (ψ_1) states:

$$\begin{pmatrix} |f'\rangle \\ |f\rangle \end{pmatrix} = \begin{pmatrix} \cos\theta & -\sin\theta \\ \sin\theta & \cos\theta \end{pmatrix} \begin{pmatrix} |\psi_8\rangle \\ |\psi_1\rangle \end{pmatrix}, \tag{1.117}$$

where the octet and singlet wave functions are the same as η_1 and η_8:

$$|\psi_1\rangle = \frac{1}{\sqrt{3}}(|u\bar{u}\rangle + |d\bar{d}\rangle + |s\bar{s}\rangle), \qquad |\psi_8\rangle = \frac{1}{\sqrt{6}}(|u\bar{u}\rangle + |d\bar{d}\rangle - 2|s\bar{s}\rangle). \tag{1.118}$$

There is the case where the state $|f'\rangle = -|s\bar{s}\rangle$ and $|f\rangle = (|u\bar{u}\rangle + |d\bar{d}\rangle)/\sqrt{2}$, which is referred to as the ideal mixing. This angle $\theta_i = 35.3^\circ$ is the ideal mixing angle where $\tan\theta_i = 1/\sqrt{2}$.

Mass formulae

A way to calculate the mixing angle can be found through the diagonalisation of the mass matrix of the two zero-isospin mesons ψ_1 and ψ_8

$$\mathcal{M} = \begin{pmatrix} m_8 & m_{81} \\ m_{18} & m_1 \end{pmatrix}, \tag{1.119}$$

where $m_8 = \langle \psi_8 | \mathcal{H} | \psi_8 \rangle$, $m_1 = \langle \psi_1 | \mathcal{H} | \psi_1 \rangle$ and $m_{81} = m_{18} = \langle \psi_8 | \mathcal{H} | \psi_1 \rangle$. The meson masses m_f and $m_{f'}$ are the eigenvalues of the diagonalisation where $\mathcal{M}|f\rangle = m_f|f\rangle$ and $\mathcal{M}|f'\rangle = m_{f'}|f'\rangle$. This implies that

$$\begin{pmatrix} m_8 & m_{81} \\ m_{18} & m_1 \end{pmatrix} \begin{pmatrix} \cos\theta \\ -\sin\theta \end{pmatrix} = m_{f'} \begin{pmatrix} \cos\theta \\ -\sin\theta \end{pmatrix}. \tag{1.120}$$

So the meson masses can then be given in terms of the mixing angle θ and the masses m_8 and m_{18} as

$$\tan\theta = \frac{m_8 - m_{f'}}{m_{18}}. \tag{1.121}$$

The masses m_8 and m_{18} can be calculated from considering the constituent quark masses for the mesons

$$m_8 = \frac{1}{3}(m_u + m_d + 4m_s) \qquad m_1 = \frac{2}{3}(m_u + m_d + m_s) \tag{1.122}$$

$$m_{18} = \frac{\sqrt{2}}{3}(m_u + m_d - 4m_s). \tag{1.123}$$

Therefore, by assuming $m_u = m_d = m_q$ the masses are

$$m_8 = \frac{1}{3}(4[m_q + m_s] - [m_q + m_q]) = \frac{1}{3}(4m_b - m_a) \tag{1.124}$$

$$m_{18} = \frac{\sqrt{2}}{3}(2[m_q + m_q - 2[m_s + m_q]) = \frac{2\sqrt{2}}{3}(m_a - m_b), \tag{1.125}$$

where m_a and m_b are masses of general mesons (of non-specific J^{PC} multiplets) where $|a\rangle = |q\bar{q}\rangle$ and $|b\rangle = |q\bar{s}\rangle$, where $q = u, d$, giving two relations for the mixing angle in terms of the meson masses

$$\tan\theta = \frac{4m_b - m_a - 3m_{f'}}{2\sqrt{2}(m_a - m_b)}. \tag{1.126}$$

Table 1.4.: The calculated mixing angles for zero-isospin pseudoscalar and vector mesons. This gives the results of using the two mass formulae (1.126) and (1.128) with both linear (lin.) masses and the quadratic (quad.) mass replacements.

				$\theta/^\circ$			
J^{PC}	Meson type	f	f'	(1.126)lin.	(1.128)lin.	(1.126)quad.	(1.128)quad.
0^{-+}	pseudoscalars	η'	η	-11.7	-24.5	-6.3	-11.4
1^{--}	vectors	ω	ϕ	39.0	37.8	44.5	36.0

Another mass formula can be determined by using the unitarity of the mixing matrix instead of considering equation (1.120)

$$\begin{pmatrix} m_8 & m_{81} \\ m_{18} & m_1 \end{pmatrix} = \begin{pmatrix} \cos\theta & \sin\theta \\ -\sin\theta & \cos\theta \end{pmatrix} \begin{pmatrix} m_{f'} & 0 \\ 0 & m_f \end{pmatrix} \begin{pmatrix} \cos\theta & -\sin\theta \\ \sin\theta & \cos\theta \end{pmatrix}. \tag{1.127}$$

This leads to a second mass formula involving both meson masses m_f and $m_{f'}$

$$\tan^2\theta = -\frac{4m_b - m_a - 3m_{f'}}{4m_b - m_a - 3m_f}, \tag{1.128}$$

supplying a second requirement on the mixing angle.

So the meson masses can then be an indicator of the expected mixing angles for $I = 0$ mesons. In the vector case, a calculation can be performed using the neutral $J^{PC} = 1^{--}$ masses $m_a = m_{\rho^0} = (775.26 \pm 0.25)$ MeV, $m_b = m_{K^{*0}} = (891.66 \pm 0.26)$ MeV, $m_{f'} = m_\phi = (1019.461 \pm 0.016)$ MeV and $m_f = m_\omega = (782.65 \pm 0.12)$ MeV [41]. The two calculated angles are $\theta_V = 39.0^\circ$ and $\theta_V = 37.8^\circ$ using equation (1.126) and (1.128) respectively. As these two calculations yield similar results, the model seems to hold well for vector mesons.

For the pseudoscalars the situation becomes different, using the neutral meson masses $m_a = m_{\pi^0} = (134.9768 \pm 0.0005)$ MeV, $m_b = m_{K^0} = (497.611 \pm 0.013)$ MeV, $m_{f'} = m_\eta = (547.862 \pm 0.017)$ MeV and $m_f = m_{\eta'} = (957.78 \pm 0.06)$ MeV [41], gives the η and η' mixing angle as $\theta_P = -11.7^\circ$ or $\theta_P = -24.5^\circ$ for the same respective equations. It is then clear that the naive quark model does not hold when applied to the mixing of pseudoscalars due to SU(3) symmetry breaking. A more suitable model is needed in order to make phenomenological predictions of the mixing between the η and η' mesons. For this Chiral Perturbation Theory with an extension of high number of colours has had phenomenological success.

There is the case where there is a replacement of the masses in equations (1.126) and (1.128) with the square of the masses. This is sometimes theoretically justified by Chiral Perturbation Theory (χ-PT) [41] (see Section 1.3.2) or less stringently by the entry of squared masses in the Klein-Gordon equation [42]. By doing this, there is another set of angles for vectors and pseudoscalars: from the quadratic version of equations (1.126) and (1.128) the vector mixing angles are $\theta_V = 44.5^\circ$ and $\theta_V = 36.0^\circ$ and the pseudoscalar angles are $\theta_P = -6.3^\circ$ and $\theta_P = -11.4^\circ$. All angles are summarised in Table 1.4. In this version of the relations, the two angles for the vector mesons have large disagreement and the pseudoscalars have an improved agreement. This model therefore only holds better, although not perfectly, for the pseudoscalars. This is likely due to the model of χ-PT only being necessary for the description of pseudoscalars as a singlet and octet of pseudo-Goldstone bosons, where the meson mixing is not as near to the ideal mixing as the vector meson case.

An explanation for the pseudoscalar deviation from the ideal angle arises from a perturbation model adding a non-vanishing constant term into the singlet state $|\psi_1\rangle$ mass matrix. This state perturbation arises from the exchange of a state of gluons [42]. According to the Landau-Yang theorem [43, 44], due to the conservation of spin in decays, the vector mesons require at least three intermediary (spin-1) gluons in this type of transition. This is not the case for the pseudoscalars which can transition into a two gluon state [42]. The Okubo-Zweig-Iizuka (OZI) rule [45–47] states that the transitions, with hadronic initial and final states that can be separated into separate diagrams without any quark lines between them, are suppressed relative to decays where this is not the case [12]. Therefore these gluon transitions are expected to be suppressed. Also the transitions with the three gluon states (proportional to the strong coupling cubed α_s^3) is more suppressed than the two gluon case (proportional to α_s^2), by gluon-line counting [41]. This explains why these effects appear more prominently in the pseudoscalar case [42].

1.3.2. Mixing angle calculations from Chiral Perturbation Theory

Due to the strong coupling α_s running at the low energy limit, the common description of QCD begins to lose viability. Therefore it is necessary to apply an effective theory based on chiral symmetries (that is the symmetry of left-handed and right-handed fermions) called chiral perturbation theory to make predictions in this limit. For η and η' mesons, this is the energy range of concern. In this theory the pseudoscalar octet (including η_8) enters as a natural consequence. Yet for the recovery of the singlet η_1, there is a need for an extension to the theory, towards an infinite number of colours [48]. This has some especially interesting phenomenological consequences and, with the right inputs, predictive power for the mixing angle θ_P. In [49] a combination of η and η' phenomenology is studied by exploiting η and η' data leading to the calculation of the value of $\theta_P = (-15.4 \pm 1.0)^\circ$.

1.3.3. Mixing angle calculations from Lattice QCD

There are also some simulations of the η-η' mixing scheme using lattice QCD. The precision of the calculated mixing angles are becoming increasingly competitive [48]. In [50] a phenomenological determination of the η and η' masses and their mixing angle θ_P was performed. This gave $m_\eta = (557 \pm 11\,(\text{stat}) \pm 3(\chi\text{PT}))$ MeV and $m_{\eta'} = (911 \pm 64\,(\text{stat}) \pm 3(\chi\text{PT}))$ MeV for the masses and $\theta_P = (-15.9 \pm 2.2\,(\text{stat})2.4 \pm (\chi\text{PT}))$, where the respective uncertainties are the statistical and the systematic uncertainty related to extrapolation in the chiral limit at discretised lattice spacing.

1.3.4. η-η' meson mixing

The isoscalar pseudoscalar states $|\eta\rangle$ and $|\eta'\rangle$ can be generally described by the mixing singlet and octet states $|\eta_1\rangle$ and $|\eta_8\rangle$:

$$\begin{pmatrix} |\eta\rangle \\ |\eta'\rangle \end{pmatrix} = \begin{pmatrix} \cos\theta_P & -\sin\theta_P \\ \sin\theta_P & \cos\theta_P \end{pmatrix} \begin{pmatrix} |\eta_8\rangle \\ |\eta_1\rangle \end{pmatrix}, \tag{1.129}$$

where the pseudoscalar mixing angle is θ_P. The singlet and octet states can be expressed by their quark components in the same way as equation (1.118).

It is also useful to consider the rotation into the quark flavour basis with mixing angle φ_P. Equation (1.129) can then be written in terms of these angles as

$$\begin{pmatrix} |\eta\rangle \\ |\eta'\rangle \end{pmatrix} = \begin{pmatrix} \cos\varphi_P & -\sin\varphi_P \\ \sin\varphi_P & \cos\varphi_P \end{pmatrix} \begin{pmatrix} |\eta_q\rangle \\ |\eta_s\rangle \end{pmatrix}, \tag{1.130}$$

where flavour basis states are

$$|\eta_q\rangle = \frac{1}{\sqrt{2}}(|u\bar{u}\rangle + |d\bar{d}\rangle), \qquad |\eta_s\rangle = |s\bar{s}\rangle.$$

which is the mixing basis used in the content of this thesis.

The consideration of singular mixing angles θ_P or φ_P does not give a complete explanation of this mixing system. It is important to note that the mixing of $\eta^{(\prime)}$ singlet and octet weak decay constants, $f^{0,8}_{\eta^{(\prime)}}$, has a requirement for two angles:

$$\begin{pmatrix} f^8_\eta & f^0_\eta \\ f^8_{\eta'} & f^0_{\eta'} \end{pmatrix} = \begin{pmatrix} f_8\cos\theta_8 & -f_0\sin\theta_0 \\ f_8\sin\theta_8 & f_0\cos\theta_0 \end{pmatrix}, \tag{1.131}$$

where the pseudoscalar mixing angles are θ_0 and θ_8 for the singlet and octet states and $f_{0,8}$ are basic decay constants. Similarly there is this representation in the flavour basis given as

$$\begin{pmatrix} f_\eta^q & f_\eta^s \\ f_{\eta'}^q & f_{\eta'}^s \end{pmatrix} = \begin{pmatrix} f_q \cos\theta_q & -f_s \sin\theta_s \\ f_q \sin\theta_q & f_s \cos\theta_s \end{pmatrix}, \tag{1.132}$$

with analogous mixing angles φ_q and φ_s [6] [48].

There has been phenomenological success by the use of the assumption that $\varphi_s \approx \varphi_q \equiv \varphi_P$. This is justified by large-N_c χ-PT calculations of both φ_s and φ_q where they are found to be compatible, as well as this being a required approximation for mixing schemes where OZI-breaking effects are neglected [49,51–55]. For example, in [53] the experimentally measured values (circa 2004 [56]) of the decay widths $\Gamma(\eta \to \gamma\gamma)$ and $\Gamma(\eta' \to \gamma\gamma)$ as well as the ratio of J/ψ decay widths $\Gamma(J/\psi \to \eta'\gamma)/\Gamma(J/\psi \to \eta\gamma)$ were used as inputs in a fit of the mixing angles in the large-N_c χ-PT scheme. The values were found to be $\varphi_q = (39.9 \pm 1.3)^\circ$ and $\varphi_s = (41.4 \pm 1.4)^\circ$, in good agreement with each other and the result of the review in [49] of $\varphi_P \equiv \varphi_q = \varphi_s = (39.3 \pm 1.0)^\circ$. These calculated values are also within the range of values found in the linear and quadratic mass equations of (1.126) and (1.128) of $\theta_P = -24.5^\circ$ to -6.3° which corresponds to $\varphi_P = 30.2^\circ$ to 48.4° in the equivalent basis. This establishes the single-angle mixing scheme for the η and η' mesons. It is useful to consider this mixing basis which is relative to the ideal mixing angle at $\tan\theta_i = 1/\sqrt{2}$. This angle θ_i would be the hypothetical angle at which the η is a pure $s\bar{s}$ state.

1.3.5. η and η' masses and the connection to gluonium

For hadrons, the majority of their mass does not equal the sum of the valence quark masses. As quarks are confined in bound states as a result of the strong force mediated by gluons, their mass is increased by the potential of confinement described in QCD. However, a spontaneous chiral symmetry breaking between left-handed and right-handed quarks gives rise to a description of pseudoscalar mesons as Goldstone bosons. This means that there is a proportionality between the squared meson masses and the valence quark masses, without the need of contributions from the gluon dynamics [48]. Yet this model only holds for π^0 and K, for η and η' there are much larger masses measured than the description of pure Goldstone bosons can provide. In this case the gluon dynamics give, not only an increase in their masses, but also noticeable effects in the measured decay or production rates of η and η'.

It is interesting to extend the η-η' mixing model to include a small amount of mixing with a third pseudoscalar zero-isospin state formed of two or three valence gluons $|\eta_G\rangle$, typically called gluonium or glueballs [57]. As a practical approximation, it is assumed that there is

[6] Not to be confused with the CP phase ϕ_s

negligible mixing with the lower mass η ($m_\eta = 547.862 \pm 0.017$ MeV [41]) and only introduce a small mixing angle φ_G in the higher mass η' case ($m_{\eta'} = 957.78 \pm 0.06$ MeV [41]). Since this connection to gluons is the source of the high masses, then the mixing is more prominent in the η'. This leaves two well-identifiable mesons (η and η') and two mixing angles (φ_P and φ_G). Therefore extending the mixing scheme in equation (1.130) gives

$$|\eta\rangle = \cos\varphi_P|\eta_q\rangle - \sin\varphi_P|\eta_s\rangle, \tag{1.133}$$

$$|\eta'\rangle = \cos\varphi_G \sin\varphi_P|\eta_q\rangle + \cos\varphi_G\cos\varphi_P|\eta_s\rangle - \sin\varphi_G|\eta_G\rangle, \tag{1.134}$$

where $|\eta_G\rangle$ is the gluonium state in the flavour basis.

The scalar pseudoscalars have been well studied. Three zero-isospin scalar mesons around this mass are the $f_0(1370)$, $f_0(1500)$ and $f_0(1710)$ observed states [58–60] which are expected to mix heavily with the gluonium state, but not necessarily be the physical state themselves. In fact, at Crystal Barrel there have been various observed decays of these mesons that suggest that $f_0(1370)$ and $f_0(1500)$ are predominantly $u\bar{u} + d\bar{d}$ states. This is due to their dominant decays being to $\pi^0\pi^0$ and $\eta\ \eta$ [61,62] and not $K\bar{K}$ [63]. In CERN's WA102 experiment $f_0(1370)$, $f_0(1500)$ and $f_0(1710)$ decays were observed in their decays to two pions or two kaons. This confirmed that the $f_0(1370)$ and $f_0(1500)$ do decay to $\pi\pi$ states at much higher rate than $K\bar{K}$ and that the inverse is true for the $f_0(1710)$ state [64]. So the $f_0(1710)$ state is predominantly $s\bar{s}$ [42]. Contradictions on this subject have been found though. A fit of WA102 and BES data found that in a mixing scheme of these three mesons with a gluonium component that $f_0(1500)$ has a significantly large gluonium content [65]. There has also been a notable absence of $f_0(1500)$ in $\gamma\gamma$ production at the Belle and LEP experiments, supporting the hypothesis that $f_0(1500)$ could be gluonium as photons would then couple very weakly [42]. Yet more recent studies at BES-III of the $f_0(1710)$ decay rates found a suppression of its decays to $\eta\ \eta'$ which suggested significant glue contributions in this state [66]. At this current epoch of meson spectroscopy our understanding of gluonium remains in relative infancy. There is a great need to better understand the quark and gluon compositions of these mass states.

In the pseudoscalar sector there is less success in searches for gluonium candidates. The observed pseudoscalar states above the $\eta^{(\prime)}$ masses are $\eta(1295)$, $\eta(1405)/\eta(1475)$, $\eta(1760)$ and $\eta(2225)$ as well as $X(1835)$, $X(2120)$, $X(2370)$, $X(2500)$ and perhaps $X(2600)$ [67]. There have been suggestions that the two lowest mass states $\eta(1295)$ and $\eta(1405)/\eta(1475)$ could be either be low-mass gluonium states or simply radial excitations of the η and η', respectively. Generally, it is believed that gluonium states would be above 2 GeV. In a number of Lattice QCD calculations performed over more than two decades, the mass of a gluonium pseudoscalar has been consistently suggested to be over 2 GeV [68–72]. Although there has been a suggestion that this mass would be reduced to about 1700 MeV if the meson is not pure gluonium, but is predominantly gluonium with some mixed $|\eta_q\rangle$ and $|\eta_s\rangle$ contributions [73].

1.3.6. Key physics tests possible with η and η' decays

The decays of the light η and η' mesons can be used to test various aspects of low-energy QCD as well as BSM physics. These are highlighted, in depth, in the review [48]. The review also provides suggestions on the most high-priority of these. This includes looking at η-η' mixing (the focus of this thesis), which can be done in ways that aren't described in the following section. There is also a way of measuring this mixing through the determination of the decay widths of $\eta^{(\prime)} \to \gamma\gamma$. High precision measurement of this is not only useful for mixing measurement, but also plays a major role in understanding the anomalous magnetic moment of the muon. This is because the transition form factors of these decays have important contributions to the hadronic parameters of $(g-2)_\mu$ [48]. This can also be combined with measurements of η decays to three pions in Dalitz plots to allow for a precise measurement of the light-quark mass ratio which could improve matching to EFTs.

For the test of C and CP violation, studies of $\eta \to \mu^+\mu^-$ decays could be used to test the muon polarisation asymmetries. Decays of $\eta^{(\prime)} \to \gamma\gamma\gamma$ could be an interesting decay to search for as it would be a CP conserving but C and P violating decay. Therefore this would be a particularly interesting candidate to probe BSM physics [48].

There is some potential for various dark energy or dark matter searches, such as dark photons, a new leptophobic scalar or axion-like particles (ALPs). In the case of massive dark photons, there could be a resonance in the dilepton resonance of $\eta^{(\prime)} \to \ell^+\ell^-\gamma$ decays which could be a be measured in $\eta^{(\prime)}$ factories. For the measurements of the leptophobic scalar, there could be a scalar appearing in the two-photon resonance in $\eta^{(\prime)} \to \gamma\gamma\pi^0$ decays, as a $\pi\pi$ resonance in $\eta^{(\prime)} \to \pi\pi\pi$ decays or as a dilepton resonance in $\eta^{(\prime)} \to \ell^+\ell^-\pi^0$. There is a need for more theoretical motivation for ALP searches, so a definite proposition of decay modes is not proposed in [48].

1.3.7. Key physics laboratories for $\eta^{(\prime)}$ physics

1.4. $B^0_{(s)} \to J/\psi\eta^{(\prime)}$ decays

In this thesis the study of the decays of $B^0_{(s)} \to J/\psi\eta^{(\prime)}$ are performed with the principle goal of measuring their rates and the angles φ_G and φ_P. These measurements were needed to provide a better understanding of the hadronic structure involved in these decays. An understanding which is necessary for a future study of the CP asymmetries of the B^0_s system using the $B^0_s \to J/\psi\eta^{(\prime)}$ decay channels. In order to do this, an of the underlying physics of mesons in both the context of B^0_s-$\overline{B}^0_s$ oscillations (Section 1.2) and the mixing between the η and η' mesons (Section 1.3) is needed.

1.4.1. Decay amplitudes and η-η' mixing measurement

This section discusses the decays of $B^0_{(s)} \to J/\psi\eta^{(\prime)}$ which are a worthwhile channel to study the mixing between the η and η' mesons and how measurements of their decay rate can be exploited to calculate the mixing angles. For a two-body decay, the differential decay rate can be determined from the expression

$$d\Gamma = \frac{1}{32\pi^2}\frac{|A|^2 p^* d\Omega}{M^2} \tag{1.135}$$

where $|A|$ is the decay amplitude for the decay mode, M is the mass of the parent particle (m_{B^0} or $m_{B^0_s}$), $d\Omega$ is the solid angle of the decay. The momentum of the decay products p^* are equal in the centre of mass frame due to the conservation of momentum and is calculated by considering conservation of energy for the two-body decay

$$M = E_1 + E_2 = \sqrt{p^{*2} + m_1^2} + \sqrt{p^{*2} + m_2^2} \tag{1.136}$$

$$\Rightarrow p^* = \frac{M}{2}\sqrt{\left[1 - \left(\frac{m_1 - m_2}{M}\right)^2\right]\left[1 - \left(\frac{m_1 + m_2}{M}\right)^2\right]} = \frac{\Phi M}{2}, \tag{1.137}$$

E and m are the energies and masses of the two decay products. Φ is introduced as a phase-space factor to simplify the expression. For the specific case of the $B^0_{(s)} \to J/\psi\eta^{(\prime)}$ decays a useful notation to adopt is with $m_1 = m_{J/\psi}$, $m_2 = m_\eta, m'_\eta$ and $M = m_{B^0}, m_{B^0_s}$ so

$$\Phi_d^{\eta^{(\prime)}} = \frac{2p_d^{\eta^{(\prime)}}}{m_{B^0}} = \sqrt{\left[1 - \left(\frac{m_{J/\psi} - m_{\eta^{(\prime)}}}{m_{B^0}}\right)^2\right]\left[1 - \left(\frac{m_{J/\psi} + m_{\eta^{(\prime)}}}{m_{B^0}}\right)^2\right]}, \tag{1.138}$$

$$\Phi_s^{\eta^{(\prime)}} = \frac{2p_s^{\eta^{(\prime)}}}{m_{B^0_s}} = \sqrt{\left[1 - \left(\frac{m_{J/\psi} - m_{\eta^{(\prime)}}}{m_{B^0_s}}\right)^2\right]\left[1 - \left(\frac{m_{J/\psi} + m_{\eta^{(\prime)}}}{m_{B^0_s}}\right)^2\right]}. \tag{1.139}$$

As the decay is a $P \to VP$ transition, where the $P = B^0_{(s)}, \eta^{(\prime)}$ are pseudoscalars and $V = J/\psi$ is the vector, it is isotropic in the centre of mass frame. This would mean that an integration over the solid angle and the substitution of equation (1.136) into equation (1.135) yields

$$\Gamma_{B^0 \to J/\psi\eta^{(\prime)}} = \frac{1}{16\pi}\frac{|A_{B^0 \to J/\psi\eta^{(\prime)}}|^2 \Phi_d^{\eta^{(\prime)}}}{m_{B^0}}, \tag{1.140}$$

$$\Gamma_{B^0_s \to J/\psi\eta^{(\prime)}} = \frac{1}{16\pi}\frac{|A_{B^0_s \to J/\psi\eta^{(\prime)}}|^2 \Phi_s^{\eta^{(\prime)}}}{m_{B^0_s}}. \tag{1.141}$$

For the decays of $B^0 \to J/\psi\eta^{(\prime)}$ and $B_s^0 \to J/\psi\eta^{(\prime)}$ the respective quark transitions are $b \to c\bar{c}d$ and $b \to c\bar{c}s$. This implies that the relevant CKM matrix elements for the transition amplitudes are $V_{cd}V_{cb}^*$ and $V_{cs}V_{cb}^*$ respectively. The decay amplitudes for the four decays can then be found by projecting the η and η' states to $s\bar{s}$ or $d\bar{d}$:

$$|A_{B^0\to J/\psi\eta}| \propto |V_{cd}V_{cb}^*| p_d^{\eta} |F_{B^0\to J/\psi d\bar{d}}| |\langle d\bar{d}|\eta\rangle|, \tag{1.142}$$

$$|A_{B_s^0\to J/\psi\eta}| \propto |V_{cs}V_{cb}^*| p_s^{\eta} |F_{B_s^0\to J/\psi s\bar{s}}| |\langle s\bar{s}|\eta\rangle|, \tag{1.143}$$

$$|A_{B^0\to J/\psi\eta'}| \propto |V_{cd}V_{cb}^*| p_d^{\eta'} |F_{B^0\to J/\psi d\bar{d}}| |\langle d\bar{d}|\eta'\rangle|, \tag{1.144}$$

$$|A_{B_s^0\to J/\psi\eta'}| \propto |V_{cs}V_{cb}^*| p_s^{\eta'} |F_{B_s^0\to J/\psi s\bar{s}}| |\langle s\bar{s}|\eta'\rangle|, \tag{1.145}$$

where $F_{B_q\to J/\psi q\bar{q}}$ are the hadronic form factors for the $B_{(s)}^0$ decays which describe the underlying physics interactions in the decays of $B_q \to J/\psi q\bar{q}$. The proportionality to momenta $p_{(s)}^{\eta^{(\prime)}}$ enters as a consequence of the 4-vector polarisation of the vector J/ψ in a $P \to PV$ transition. These amplitudes can then be substituted into equation (1.140) to give the decay rate in terms of the form factors and CKM matrix elements

$$\Gamma_{B^0\to J/\psi\eta^{(\prime)}} \propto \frac{m_{B^0}}{64\pi}|V_{cd}V_{cb}^*|^2 \left(\Phi_d^{\eta^{(\prime)}}\right)^3 |F_{B^0\to J/\psi d\bar{d}}|^2 |\langle d\bar{d}|\eta^{(\prime)}\rangle|^2, \tag{1.146}$$

$$\Gamma_{B_s^0\to J/\psi\eta^{(\prime)}} \propto \frac{m_{B_s^0}}{64\pi}|V_{cs}V_{cb}^*|^2 \left(\Phi_s^{\eta^{(\prime)}}\right)^3 |F_{B_s^0\to J/\psi s\bar{s}}|^2 |\langle s\bar{s}|\eta^{(\prime)}\rangle|^2. \tag{1.147}$$

Then the decay channel probabilities (*i.e.* Branching Ratios) are

$$\mathcal{B}_{B^0\to J/\psi\eta} = \frac{\tau_{B^0}m_{B^0}}{64\pi}|V_{cd}V_{cb}^*|^2 \left(\Phi_d^{\eta}\right)^3 |F_{B^0\to J/\psi d\bar{d}}|^2 |\langle d\bar{d}|\eta\rangle|^2, \tag{1.148}$$

$$\mathcal{B}_{B_s^0\to J/\psi\eta} = \frac{\tau_{B_s^0}m_{B_s^0}}{64\pi}|V_{cs}V_{cb}^*|^2 \left(\Phi_s^{\eta}\right)^3 |F_{B_s^0\to J/\psi s\bar{s}}|^2 |\langle s\bar{s}|\eta\rangle|^2, \tag{1.149}$$

$$\mathcal{B}_{B^0\to J/\psi\eta'} = \frac{\tau_{B^0}m_{B^0}}{64\pi}|V_{cd}V_{cb}^*|^2 \left(\Phi_d^{\eta'}\right)^3 |F_{B^0\to J/\psi d\bar{d}}|^2 |\langle d\bar{d}|\eta'\rangle|^2, \tag{1.150}$$

$$\mathcal{B}_{B_s^0\to J/\psi\eta'} = \frac{\tau_{B_s^0}m_{B_s^0}}{64\pi}|V_{cs}V_{cb}^*|^2 \left(\Phi_s^{\eta'}\right)^3 |F_{B_s^0\to J/\psi s\bar{s}}|^2 |\langle s\bar{s}|\eta'\rangle|^2. \tag{1.151}$$

As both final states $J/\psi\ \eta$ and $J/\psi\ \eta'$ are *CP*-even the lifetime $\tau_{B_s^0}$ must be for the light mass eigenstate of the B_s^0 meson. The lifetime τ_{B^0} and the masses m_{B^0} and $m_{B_s^0}$ have negligible differences between the mass eigenstates of the respective parent $B_{(s)}^0$ mesons and so do not need this distinction.

From the description of the η and η' states in terms of their flavour states and a gluonium contribution (in equation (1.133)) the projection onto the $s\bar{s}$ and $d\bar{d}$ yields

$$\langle d\bar{d}|\eta\rangle = \frac{1}{\sqrt{2}}\cos\varphi_P, \tag{1.152}$$

$$\langle s\bar{s}|\eta\rangle = -\sin\varphi_P, \tag{1.153}$$

$$\langle d\bar{d}|\eta'\rangle = \frac{1}{\sqrt{2}}\cos\varphi_G\sin\varphi_P, \tag{1.154}$$

$$\langle s\bar{s}|\eta'\rangle = \cos\varphi_P\cos\varphi_G. \tag{1.155}$$

The relations in equation (1.148), (1.149), (1.150) and (1.151) can be used to determine the relationship between ratios of branching ratios and the mixing angles φ_P and φ_G. First considering the ratio of $J/\psi\,\eta'$ and $J/\psi\,\eta$ final states with the same parent $B^0_{(s)}$ meson gives

$$\mathcal{R}_d = \left(\frac{\Phi_d^{\eta}}{\Phi_d^{\eta'}}\right)^3 \frac{\mathcal{B}_{B^0\to J/\psi\eta'}}{\mathcal{B}_{B^0\to J/\psi\eta}} = \cos^2\varphi_G\tan^2\varphi_P, \tag{1.156}$$

$$\mathcal{R}_s = \left(\frac{\Phi_s^{\eta}}{\Phi_s^{\eta'}}\right)^3 \frac{\mathcal{B}_{B_s^0\to J/\psi\eta'}}{\mathcal{B}_{B_s^0\to J/\psi\eta}} = \cos^2\varphi_G\cot^2\varphi_P, \tag{1.157}$$

The determination of both angles φ_P and φ_G can be done using the four branching ratios by

$$\mathcal{R}_d\mathcal{R}_s = \cos^4\varphi_G, \qquad \frac{\mathcal{R}_d}{\mathcal{R}_s} = \tan^4\varphi_P. \tag{1.158}$$

So with the measurement of these branching ratios it is possible to also measure the mixing angles φ_G and φ_P.

There are two other ways to measure φ_P with these sets of branching ratios. This can be done by defining another two fractions $\mathcal{R}_\eta$ and $\mathcal{R}_{\eta'}$

$$\mathcal{R}_\eta = \left(\frac{\Phi_s^{\eta}}{\Phi_d^{\eta}}\right)^3 \frac{\mathcal{B}_{B^0\to J/\psi\eta}}{\mathcal{B}_{B_s^0\to J/\psi\eta}} = \frac{\tau_{B^0}m_{B^0}}{\tau_{B_s^0}m_{B_s^0}}\left|\frac{V_{cd}}{V_{cs}}\right|^2\left|\frac{F_{B^0\to J/\psi d\bar{d}}}{F_{B_s^0\to J/\psi s\bar{s}}}\right|^2\frac{\cot^2\varphi_P}{2}, \tag{1.159}$$

$$\mathcal{R}_{\eta'} = \left(\frac{\Phi_s^{\eta'}}{\Phi_d^{\eta'}}\right)^3 \frac{\mathcal{B}_{B^0\to J/\psi\eta'}}{\mathcal{B}_{B_s^0\to J/\psi\eta'}} = \frac{\tau_{B^0}m_{B^0}}{\tau_{B_s^0}m_{B_s^0}}\left|\frac{V_{cd}}{V_{cs}}\right|^2\left|\frac{F_{B^0\to J/\psi d\bar{d}}}{F_{B_s^0\to J/\psi s\bar{s}}}\right|^2\frac{\tan^2\varphi_P}{2} \tag{1.160}$$

Neglecting breaking of the $\mathrm{SU}(3)_F$ symmetry, the approximation that $F_{B^0\to J/\psi d\bar{d}} = F_{B_s^0\to J/\psi s\bar{s}}$ can be employed to simplify these relations:

$$\mathcal{R}_\eta = \left(\frac{\Phi_s^\eta}{\Phi_d^\eta}\right)^3 \frac{\mathcal{B}_{B^0\to J/\psi\eta}}{\mathcal{B}_{B_s^0\to J/\psi\eta}} = \frac{\tau_{B^0} m_{B^0}}{\tau_{B_s^0} m_{B_s^0}} \left|\frac{V_{cd}}{V_{cs}}\right|^2 \frac{\cot^2\varphi_P}{2}, \tag{1.161}$$

$$\mathcal{R}_{\eta'} = \left(\frac{\Phi_s^{\eta'}}{\Phi_d^{\eta'}}\right)^3 \frac{\mathcal{B}_{B^0\to J/\psi\eta'}}{\mathcal{B}_{B_s^0\to J/\psi\eta'}} = \frac{\tau_{B^0} m_{B^0}}{\tau_{B_s^0} m_{B_s^0}} \left|\frac{V_{cd}}{V_{cs}}\right|^2 \frac{\tan^2\varphi_P}{2}. \tag{1.162}$$

With the lifetimes and masses known to good precision in [41] and the CKM matrix elements are given in Table 1.3, it is possible to determine φ_P in a second and third way. Yet it is important to note that $\mathcal{R}_{\eta'}/\mathcal{R}_\eta \equiv \mathcal{R}/\mathcal{R}_s$.

η-η' mixing in relation to the rate of $B^0 \to J/\psi\pi^0$

Another way to calculate these mixing angles is to measure the fraction of the branching ratios of the decays $B^0 \to J/\psi\eta^{(\prime)}$ and $B^0 \to J/\psi\pi^0$. The branching ratio of $B^0 \to J/\psi\pi^0$ is similar to that of $B^0 \to J/\psi\eta$ in equation (1.148), so can be written as

$$\mathcal{B}_{B^0\to J/\psi\pi^0} = \frac{\tau_{B^0} m_{B^0}}{64\pi} |V_{cd}V_{cb}^*|^2 \left(\Phi^{\pi^0}\right)^3 |F_{B^0\to J/\psi d\bar{d}}|^2 |\langle d\bar{d}|\pi^0\rangle|^2, \tag{1.163}$$

where the flavour state of the π^0 is $\frac{1}{\sqrt{2}}(|u\bar{u}\rangle - |d\bar{d}\rangle)$ which implies that $|\langle d\bar{d}|\pi^0\rangle|^2 = 1/2$. This allows the introduction of the ratio dependent only on φ_P [74,75]

$$\mathcal{R}_0 = \left(\frac{\Phi_d^{\pi^0}}{\Phi_d^\eta}\right)^3 \frac{\mathcal{B}_{B^0\to J/\psi\eta}}{\mathcal{B}_{B^0\to J/\psi\pi^0}} = \cos^2\varphi_P, \tag{1.164}$$

and another two-angle relation with $B^0 \to J/\psi\eta$

$$\mathcal{R}_{0'} = \left(\frac{\Phi_d^{\pi^0}}{\Phi_d^{\eta'}}\right)^3 \frac{\mathcal{B}_{B^0\to J/\psi\eta'}}{\mathcal{B}_{B^0\to J/\psi\pi^0}} = \cos^2\varphi_G \sin^2\varphi_P. \tag{1.165}$$

It is worth noting that these relations are now proportional to $\cos^2\varphi_P$ and $\sin^2\varphi_P$ instead of $\tan^2\varphi_P$ and $\cot^2\varphi_P$ in the respective relations for $\mathcal{R}$, $\mathcal{R}_s$, $\mathcal{R}_\eta$ and $\mathcal{R}_{\eta'}$. This means that $\mathcal{R}_0$ and $\mathcal{R}_{0'}$ are more sensitive to any uncertainties in the measured branching ratios of $B^0 \to J/\psi\eta^{(\prime)}$ and $B^0 \to J/\psi\pi^0$.

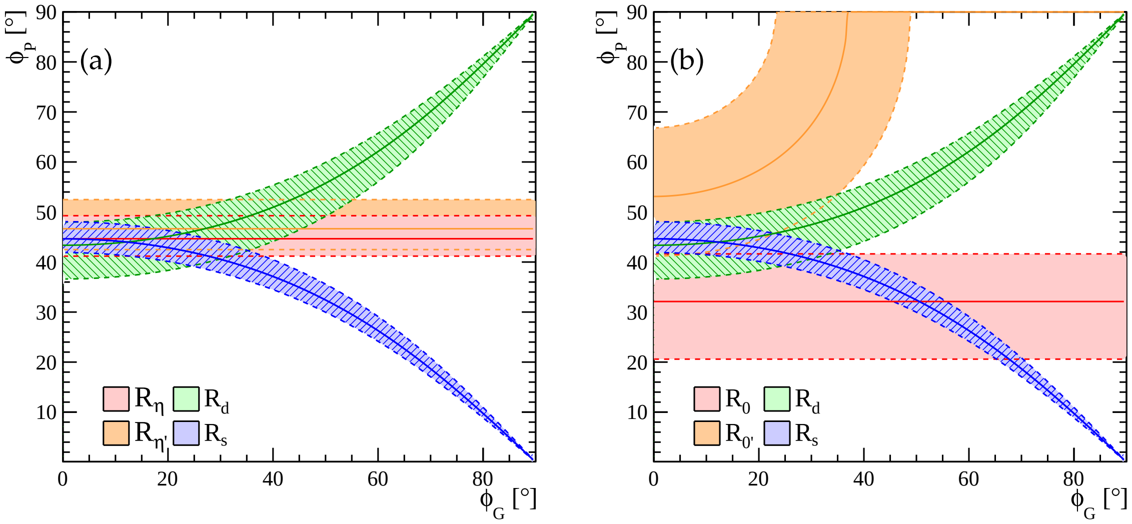

Figure 1.7.: The exclusion plot for the mixing angles φ_P and φ_G determined by the Particle Data Group [41] averages of the relevant branching ratios substituted into the ratios $\mathcal{R}_{d,s}$, a) $\mathcal{R}_{\eta^{(\prime)}}$ and b) $\mathcal{R}_{0^{(\prime)}}$.

Current experimental averages

The relevant branching ratios for the calculation of the mixing angles are averaged in [41] as

$$\mathcal{B}_{B^0\to J/\psi\pi^0} = (1.66 \pm 0.10) \times 10^{-5}, \tag{1.166}$$

$$\mathcal{B}_{B^0\to J/\psi\eta} = (1.08 \pm 0.23) \times 10^{-5}, \tag{1.167}$$

$$\mathcal{B}_{B^0\to J/\psi\eta'} = (7.6 \pm 2.4) \times 10^{-6}, \tag{1.168}$$

$$\mathcal{B}_{B_s^0\to J/\psi\eta} = (4.0 \pm 0.7) \times 10^{-4}, \tag{1.169}$$

$$\mathcal{B}_{B_s^0\to J/\psi\eta'} = (3.3 \pm 0.4) \times 10^{-4}. \tag{1.170}$$

Which can be used to determine the values of each ratio $\mathcal{R}$, $\mathcal{R}_s$, $\mathcal{R}_\eta$ and $\mathcal{R}_{\eta'}$, $\mathcal{R}_0$ and $\mathcal{R}_{0'}$. So substituting these into equations (1.156-1.157,1.161-1.162,1.164-1.165) gives the averages:

$$\mathcal{R} = 0.89 \pm 0.34 = \cos^2\varphi_G \tan^2\varphi_P, \tag{1.171}$$

$$\mathcal{R}_s = 1.03 \pm 0.22 = \cos^2\varphi_G \cot^2\varphi_P, \tag{1.172}$$

$$\mathcal{R}_\eta = 0.057 \pm 0.016 = \frac{\tau_{B^0} m_{B^0}}{\tau_{B_s^0} m_{B_s^0}} \left|\frac{V_{cd}}{V_{cs}}\right|^2 \frac{\cot^2\varphi_P}{2}, \tag{1.173}$$

$$\mathcal{R}_{\eta'} = 0.050 \pm 0.017 = \frac{\tau_{B^0} m_{B^0}}{\tau_{B_s^0} m_{B_s^0}} \left|\frac{V_{cd}}{V_{cs}}\right|^2 \frac{\tan^2\varphi_P}{2}, \tag{1.174}$$

$$\mathcal{R}_0 = 0.72 \pm 0.16 = \cos^2\varphi_P, \tag{1.175}$$

$$\mathcal{R}_{0'} = 0.64 \pm 0.21 = \cos^2\varphi_G \sin^2\varphi_P. \tag{1.176}$$

These ratios can then be shown as exclusion plots in the plane of the two angles φ_P and φ_G as done in Figure 1.7.

$B_s^0 \to J/\psi\eta^{(\prime)}$ as a laboratory for ϕ_s measurements

The decays of $B_s^0 \to J/\psi\eta^{(\prime)}$ can provide an interesting testing ground for measurements of ϕ_s. This would be analogous to the use of $B_s^0 \to J/\psi\phi$ but with the added advantage of being a decay of a pseudoscalar (B_s^0) to a vector (J/ψ) and pseudoscalar ($\eta^{(\prime)}$), as opposed to a second vector (ϕ). This study would therefore remove the complication of performing an angular analysis but at the expense of statistics, the branching ratios of $B_s^0 \to J/\psi\eta^{(\prime)}$ are about one third of that of the $B_s^0 \to J/\psi\phi$.

An important application of the measurements of φ_P and φ_G is determining whether a future ϕ_s measurement is in agreement with the Standard Model or not. The different possible decay topologies can restrict the precision at which a measurement of ϕ_s can be used to determine if there is evidence of new physics. The amplitudes of these topologies include a dependency on mixing angles φ_P and φ_G. It is therefore suggested in [74] to use the fraction of the branching ratios of $B^0 \to J/\psi\eta^{(\prime)}$ and $B_s^0 \to J/\psi\eta^{(\prime)}$ to give a constraint on these parameters and provide an important prediction on the precision at which a future ϕ_s measurement can be made. It is also suggested in [74] to use a measurement of the effective lifetime of these decays to constrain $\Delta\Gamma_s$.

1.5. Concluding remarks

The study of the $B_{(s)}^0 \to J/\psi\eta^{(\prime)}$ decays opens up opportunities for an improved understanding of interesting aspects of meson physics, from the oscillations of B mesons to the mixing of

$\eta^{(\prime)}$ mesons. By studying their decay rates, and therefore the mixing between η and η' it is possible to test the reliability of the quark model, QCD and χ-PT calculations. A second but no less important consequence of these measurements is their quality of being a foundation for future measurements of the *CP* violation in oscillations of B_s^0-$\bar{B}_s^0$. In the following chapters, the measurements of the $B_{(s)}^0 \to J/\psi\eta^{(\prime)}$ decays at the LHCb experiment will be shown. These measurements are an update and broader extension of previous analyses performed at LHCb, one being a measurement of the absolute branching ratio of $B_s^0 \to J/\psi\eta^{(\prime)}$ decays with data taken in 2011 [76] and another analysis of both data taken in 2011 and 2012 that studied the mixing of η and η' with measurements of $B_s^0 \to J/\psi\eta^{(\prime)}$ and $B^0 \to J/\psi\eta^{(\prime)}$ [77]. This thesis shows the reanalysis of these two results with full Run-1 (data-taken in 2011 and 2012) and Run-2 (2015 to 2018), as well as more final states of the η and η' decays. This greatly increased the available statistics in the measurement of the absolute branching fractions of $B_{(s)}^0 \to J/\psi\eta^{(\prime)}$ as well as the ratios of branching fractions $\mathcal{R}_d$, $\mathcal{R}_s$, $\mathcal{R}_\eta$ and $\mathcal{R}_{\eta'}$, while also providing the first direct measurement of the ratios $\mathcal{R}_0$ and $\mathcal{R}_{0'}$.

Chapter 2.

The LHCb experiment

The data samples used in the analyses of this thesis originated in the LHCb experiment. This chapter describes this experiment by first introducing the source of the decays, the Large Hadron Collider, then describing the various systems of the LHCb experiment: tracking, calorimetry, triggering and particle identification. There is also a section that covers the reconstruction and identification algorithms used for neutral particles as this is of particular interest to this thesis as the efficiency of these processes were studied.

2.1. The Large Hadron Collider

The CERN Large Hadron Collider (LHC) is a circular synchrotron particle accelerator and collider with a 26.7 km circumference making it the largest particle accelerator in the world. It primarily collides protons and has so far reached centre of mass energies ($\sqrt{s}$) up to 13 TeV. It is built with two rings that accelerate beams in opposite directions through separate magnetic fields and vacuum chambers. As the proton beams are accelerated in a synchrotron they pass through the following sections of the ring: they are accelerated linearly by Radio Frequency (RF) electric field cavities, focused by superconducting quadrupole magnets and bent into a circular orbit by superconducting dipole magnets.

Before injection into the LHC, proton beams are initially accelerated up to 450 GeV via a chain of accelerators from the Linac2 to Proton Synchrotron Booster to Proton Synchrotron and finally the Super Proton Synchrotron. These accelerators were specifically tuned and upgraded to reach the required 450 GeV for injection into the LHC. Each LHC proton beam contains 2808 sets of protons (bunches) that each carry 1.15×10^{11} protons [78].

In the data-taking years of 2010 to 2012 (called Run-1), these protons were accelerated up to 3.5 TeV and later 4 TeV, and in the data-taking years of 2015 to 2018 (Run-2) this reached 6.5 TeV. Once they have reached these energies they would then collide at interaction points which are where the two beams intersect. These intersections are the locations of the four largest

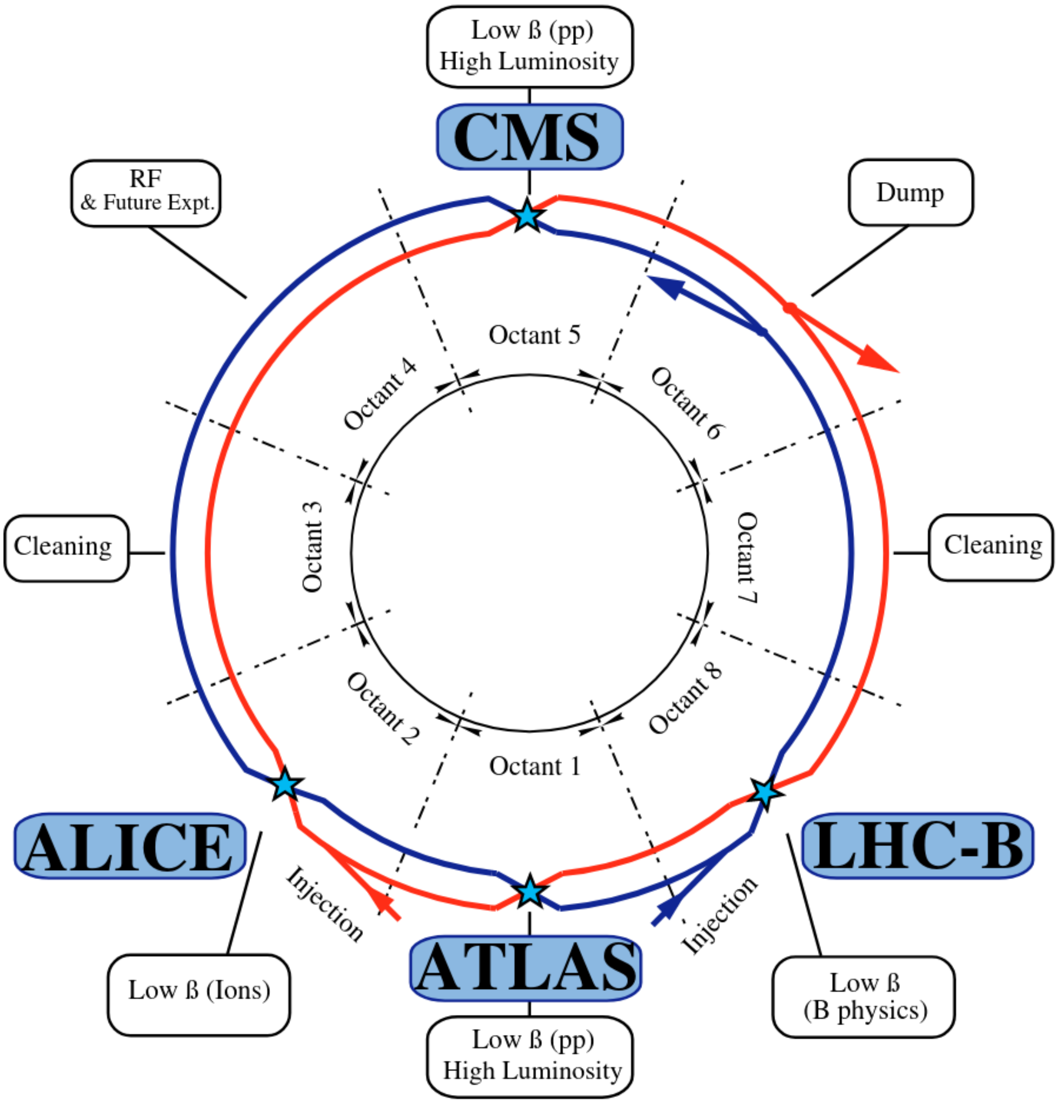

Figure 2.1.: Diagram of the LHC, its beams, and the locations of the main experiments. [78]

experiments: ATLAS, CMS, LHCb and ALICE. Figure 2.1 shows the a view of the beams of the LHC and the locations of the four main experiments.

ATLAS and CMS are two general purpose detectors aimed at studying Higgs and Beyond Standard Model (BSM) physics. For this task they exploit the maximum luminosity capabilities of the LHC. In contrast, ALICE and LHCb experiments operate at a reduced luminosity. ALICE takes advantage of data from heavy-ion collisions to probe physics in the quark-gluon plasma state of matter. The LHCb experiment is the apparatus that concerns this thesis. Designed for the measurement of Heavy Flavour physics, in particular, CP violating decays, LHCb targets high precision measurements by operating at a near-constant instantaneous luminosity of $\mathcal{L} = 10^{32}\,\mathrm{cm}^2\,\mathrm{s}^{-1}$ [78]. The instantaneous luminosity is kept levelled by the slight mis-alignement of the two proton beam axes to lower the rate of proton collisions adjusted for the control of pile-up, this is shown in Figure 2.2.

At intersection points the instantaneous number of events generated by proton collisions is given by

$$N = \sigma\mathcal{L}, \tag{2.1}$$

where σ is the cross-section of particular collision modes and $\mathcal{L}$ is the instantaneous luminosity which is dependent on a number of beam conditions. The measured luminosity over the data-taking years are included in Table 2.1. These events correspond to luminosity values integrated over the time of operation of the LHCb experiment during its first two Runs (see Figure 2.3) and to the cross-sections of $b\bar{b}$ pairs produced within the acceptance of the detectors $\sigma(pp \to b\bar{b}X) = (72.0 \pm 0.3\,(\mathrm{stat}) \pm 6.8\,(\mathrm{syst}))\,\mu\mathrm{b}$ and $(144 \pm 1\,(\mathrm{stat}) \pm 21\,(\mathrm{syst}))\,\mu\mathrm{b}$ for collision energies of 7 TeV and 13 TeV respectively [79]. Throughout this thesis (stat) and (syst) label the statistical and systematical uncertainties respectively.

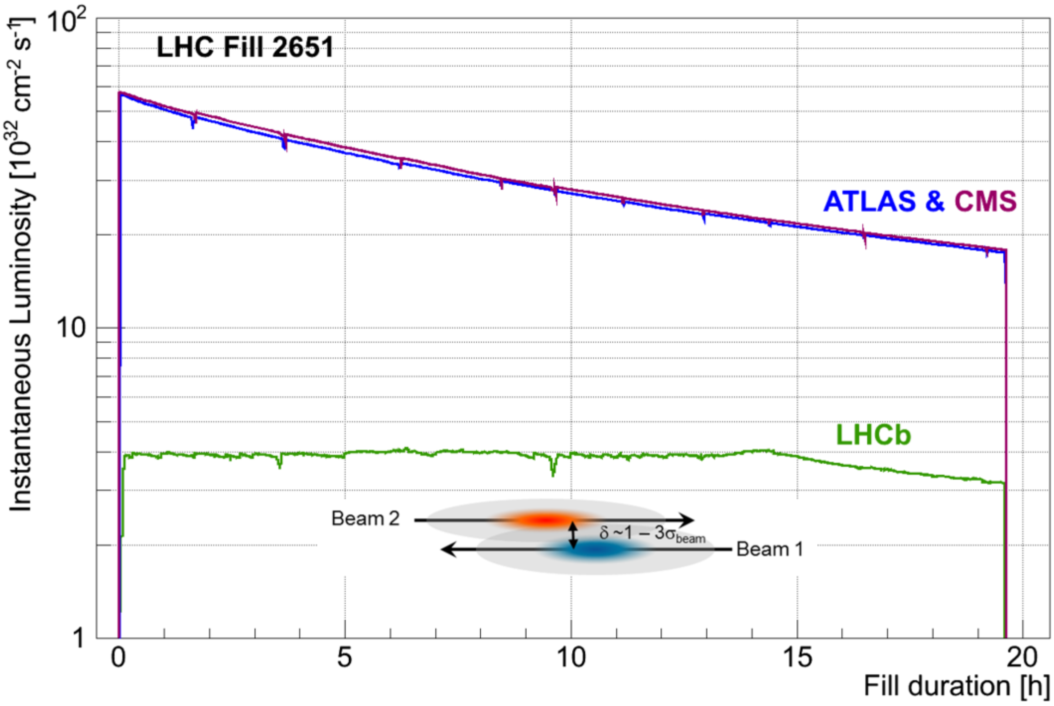

Figure 2.2.: The collected luminosity over time by ATLAS, CMS and LHCb during an LHC fill. The LHCb luminosity is kept roughly constant for the first 15 hours of filling due to the tuning of the alignment of the two beams [80].

Table 2.1.: An Overview of the data-taking years and their respective beam energies; cross-section for $b\bar{b}$ production and expected number of $b\bar{b}$ produced in the LHCb acceptance.
*: Estimated as a linear interpolation of 3.5 TeV and 6.5 TeV results.

Year	(lumi) / fb^{-1}	E_{BEAM} / TeV	$\sigma(pp \to b\bar{b}X)$ / µb	$N(b\bar{b})$ / $\times 10^9$
2010	0.04	3.5	$72.0 \pm 0.3 \pm 6.8$	$2.88 \pm 0.01 \pm 0.27$
2011	1.11	3.5	$72.0 \pm 0.3 \pm 6.8$	$79.9 \pm 0.3 \pm 7.6$
2012	2.08	4.0	$84.0 \pm 0.3 \pm 6.8$*	$174.7 \pm 1 \pm 14$
2015	0.33	6.5	$144 \pm 1 \pm 21$	$47.5 \pm 0.3 \pm 6.9$
2016	1.67	6.5	$144 \pm 1 \pm 21$	$240.5 \pm 2 \pm 35$
2017	1.71	6.5	$144 \pm 1 \pm 21$	$246.2 \pm 2 \pm 36$
2018	2.19	6.5	$144 \pm 1 \pm 21$	$315 \pm 2 \pm 46$

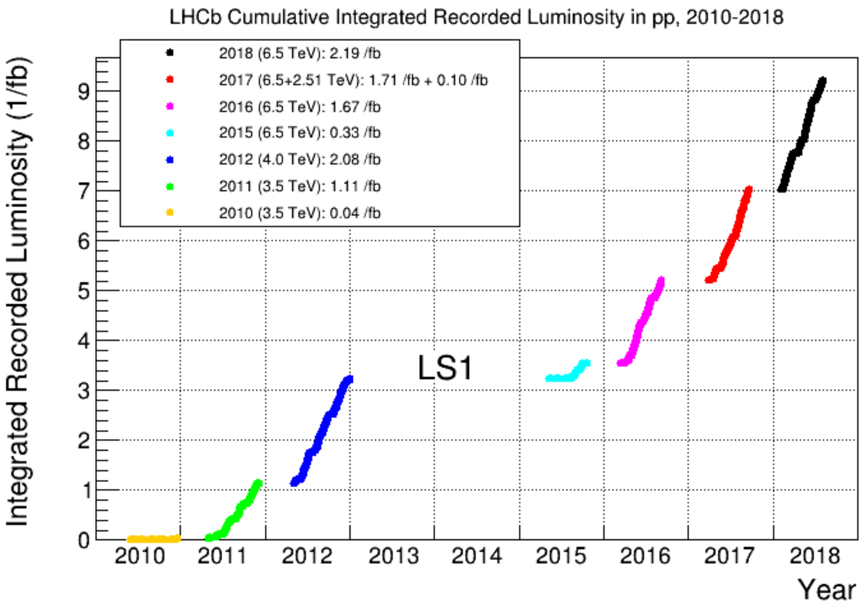

Figure 2.3.: The yearly cumulative gain of integrated luminosity from proton-proton collisions at LHCb. Run-1 corresponds to 2010 to 2012 and Run-2 corresponds to 2015 to 2018 [81].

2.2. The LHCb detector

The LHCb experiment is the LHC's primary flavour physics experiment with a special focus on precise measurements of beauty and charm physics. The experiment attempts to search for new physics indirectly by precisely comparing Standard Model predictions of flavour parameters to their measured values. In the sector of beauty decays there has been $\sim 1 \times 10^{12}$ $b\bar{b}$ pairs within the acceptance of the experiment in the first two data-taking periods (*i.e.* in Run-1 and Run-2). The full estimations of the number of $b\bar{b}$ pairs are given in Table 2.1.

First the identity of the b hadrons has to be established, this requires the identification of its displaced vertex. The b hadron flies from production at the proton-proton collision point, the Primary Vertex (PV), until it decays at its Secondary Vertex (SV). The compatibility of reconstructed vertices to measured decay products is determined by the impact parameter (IP) (the distance of closest approach between the PV and the trajectory of the decay products) and the decay time. Combined with sufficient energy and momentum resolutions of the decay products, this information provides measurements of the invariant mass at high enough resolution to precisely locate the studied B resonances (called signal) and discriminate against backgrounds in the distribution that arising from other decays with similar-enough topology or combinatorial events.

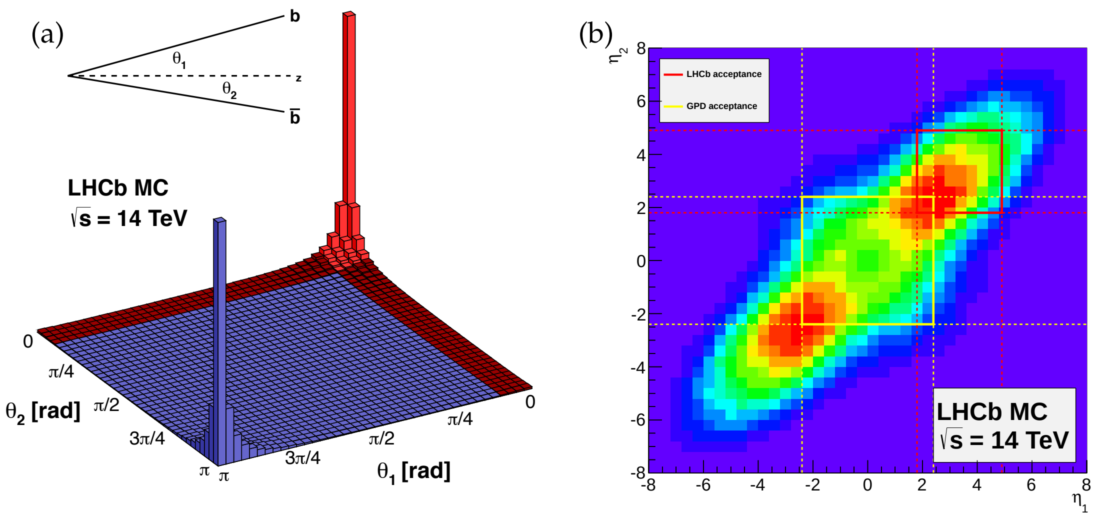

Figure 2.4.: The production rates of $b\bar{b}$ at the LHC as a function of 2-D a) polar angles and b) pseudorapidity (defined in Section 2.2). These plots are made from Monte Carlo (MC) simulated data. (b) compares the acceptance of LHCb (red square) to General Purpose Detectors (yellow square) such as ATLAS and CMS [82].

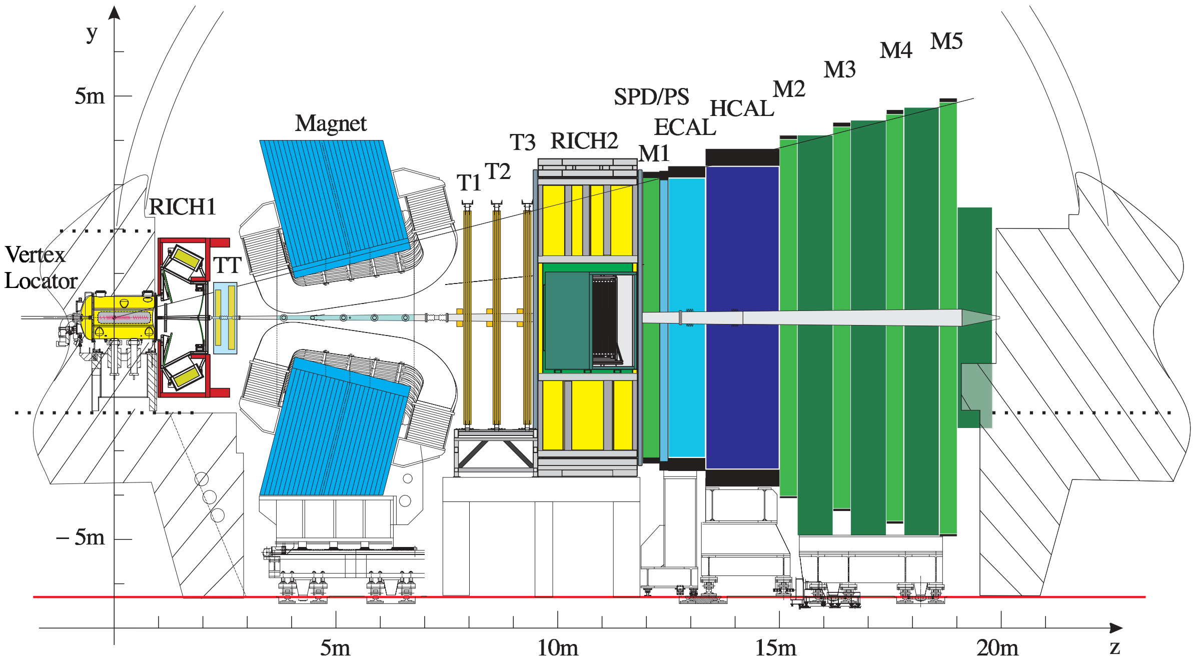

Figure 2.5.: Cross-section view of LHCb, cut in the non-bending y–z plane. [84]

The detector needs to be capable of reconstructing a wide enough range of decay products including electrons, muons, photons, neutral mesons (usually via photon reconstruction) charged mesons and other long-lived hadrons. The extraction of useful information from the high-intensity environment of proton collisions is made possible with the dedicated Trigger selection and data acquisition systems.

Unlike the general purpose detectors on the LHC, LHCb is a forward single-arm spectrometer that covers a relatively narrow angular coverage of 10 mrad to 300(250) mrad in the horizontal(vertical) plane. This geometry is capable of capturing almost half of the b-hadron decays because the hadrons are produced by parton collisions with asymmetric energies and are therefore boosted at a trajectory that is close to the beamline [83]. This can be seen in a figure of the $b\bar{b}$ production rate for different angles in Figure 2.4.

The detector has a geometry system defined relative to the interaction point where the positive z-axis is in the direction of the beamline into the detector. The x and y-axes are situated along the horizontal and vertical directions respectively. Positive x is directed such that the detector has a left-handed geometry. Throughout this thesis a transverse plane will be referred to, this corresponds to the x-y plane (*i.e.* transverse to the beamline), this is especially useful in the context of the energy or momentum of particles that may be boosted in the direction of the beam line. The definition of the transverse momentum (p_{T}) of particles is related to its Cartesian momentum via a polar angle in the transverse plane (ϕ) and the angle from the transverse plane, *i.e.* the pseudorapidity (η). The definitions are as follows:

$$p_x = p_\mathrm{T} \cos\phi \tag{2.2}$$
$$p_y = p_\mathrm{T} \sin\phi \tag{2.3}$$
$$p_z = p_\mathrm{T} \sinh\eta. \tag{2.4}$$

These coordinates are convenient to use for trajectories close to the beamline as seen in LHCb. The layout of the detector is shown in Figure 2.5, as a cross-section on the y–z plane.

The bending dipole magnet allows for the measurement of particle momenta from the deflection of charged particles in the horizontal (or bending) plane. This magnet has an integrated field of 4 T m. The terms upstream and downstream will be relative to this magnet throughout this manuscript. There is the Vertex Locator (VELO) around the point of interaction which is made of silicon modules arranged to give the coordinates of the primary and secondary vertices. There are three main sets to the tracking system: the Tracker Turicensis (TT) located upstream of the bending magnet; the three downstream Inner Tracking (IT) stations, T1-T3; and an Outer Tracker (OT). The TT and IT stations all employ silicon microstrip sensors, unlike the OT which uses layers of Kapton straw trackers filled with 70% Argon and 30% CO_2. The tracking system is described in Section 2.2.1.

For charged hadron identification (K-π separation) there are the two Ring Imaging Cherenkov detectors (RICH1 and RICH2). The system covers a momentum range of about $[2, 100]$ GeV, where the upstream RICH1 is suited to lower momentum values up to 60 GeV and the downstream RICH2 for the higher momenta from 15 GeV [80, 83].

The multipurpose calorimeter system is aimed at the detection of charged and neutral hadrons, electrons and photons. It determines their identities, energies and positions using four layers of sub-detectors: the Scintillating Pad Detector (SPD), the Preshower (PS) scintillator, the electromagnetic calorimeter (ECAL) and the hadronic calorimeter (HCAL). The SPD is responsible for separation of electron and photon signatures where typically neutrals would not be detected, whereas charged electrons and muons would. The PS separates electrons and charged pions due to differing deposited energy distributions. Between the SPD and PS detectors is a 15 mm thick layer of lead corresponding to $2.5X_0$ (radiation lengths) where electron and photon showers will begin [83]. The calorimeters are described in more detail in Section 2.2.2

For the detection of muons there are five stations (M1-M5). M1 is upstream of the calorimeters and its inner section is the only triple Gas Electron Multiplier (GEM) detector. The outer section of the M1 and the rest of the stations (M2-M5) are rectangular Multi-Wire Proportional Chambers (MWPC) and make the furthest downstream detector system.

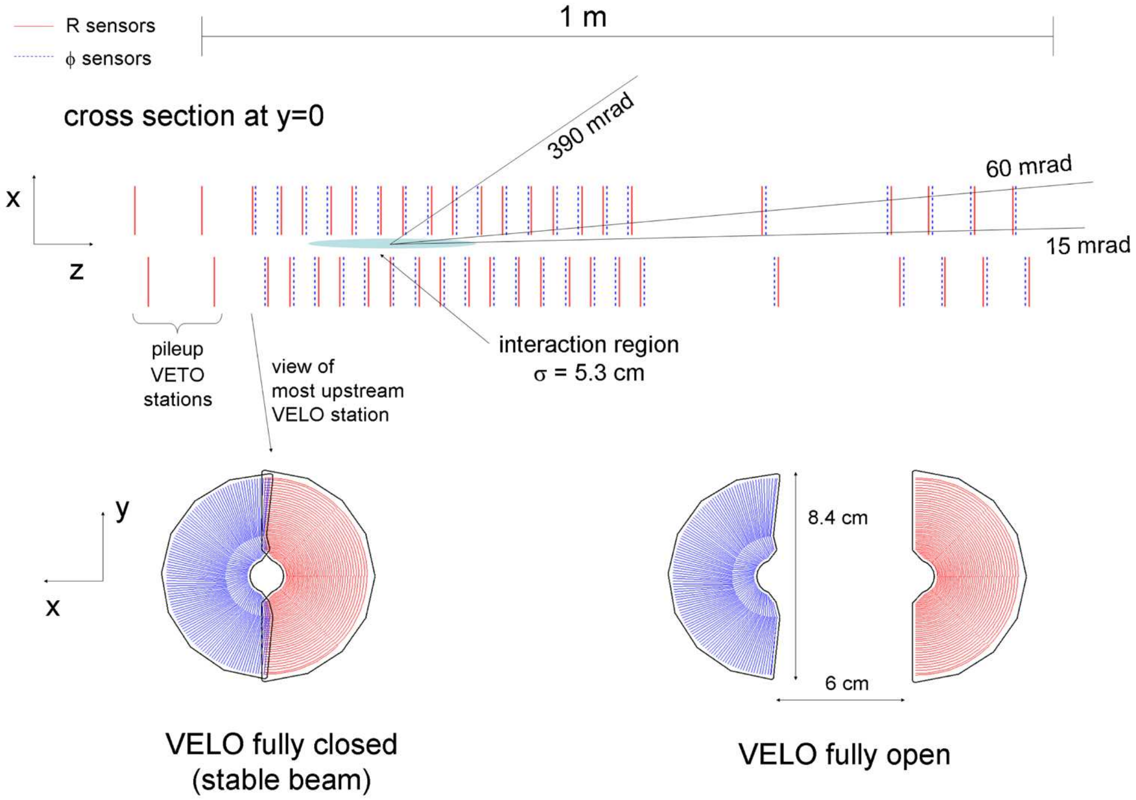

Figure 2.6.: Schematic view of the cross-section in the x–z (above) and x–y (below) plane of the Vertex Locator stations [83].

2.2.1. Tracking

Vertex Locator

The VELO precisely measures a track close to the interaction point. One of its principal aims is to identify decays of b-hadrons by locating their displaced secondary vertex. In cylindrical polar coordinates, the radial and angular measurements are determined by silicon detectors for the specific purpose of being R and Φ sensors. For the purpose of measuring signal, there are 42 of each type of sensor with an addition of four R sensors for vetoing pile-up events. These sensors are all kept within a vacuum enclosed in a thin aluminium wall chosen to minimise the amount of detector material (and so multiple scattering) close to the interaction point.

The reconstruction of the displaced vertices is important for analyses at LHCb to reduce backgrounds. This provides the lifetime measurement and impact parameter of the hadrons decaying in flight, in turn, giving useful information to be used in the High Level Trigger (HLT, described in Section 2.2.3) and offline signal selections.

The angular coverage of the VELO with hits in at least three silicon stations ranges from 15 mrad to 300 mrad covering the acceptance of the LHCb experiment. This corresponds to the pseudorapidity range of $1.6 < \eta < 4.9$ for vertices created up to z values of 10.6 cm. The VELO system was constructed with two halves that overlap slightly in order to proactively avoid issues with possible detector misalignment. [83] In Figure 2.6 the overall layout of the VELO is shown as a cross-section in x–z plane along with an illustration of the two halves of the VELO in the x–y plane.

Silicon Trackers

The TT and IT (the inner part of the T1-T3 trackers also called the T system) are both $\sim 200\,\mu m$ pitch silicon strip detectors. The IT is located upstream of the magnet and covers the LHCb acceptance with an area corresponding to a width of 150 cm and height of 130 cm. Downstream of the dipole magnet are the three stations of the TT which covers an inner subsection of the LHCb acceptance with a width of 120 cm and height of 40 cm. These trackers are designed to give spacial resolutions at the level of $50\,\mu m$ [83].

A variable detector granularity was adopted to account for the differing potential occupancies in different regions of the detector. This is achieved by changing the strip lengths for the inner and outer (close and far from the beamline) regions, in line with the charged particle densities. Excellent time resolution is necessary to reduce the pile-up of events from the high collision rate around the interaction area. Therefore the front-end amplifiers have to have a time shape of the same order as the proton bunch crossing time interval of 25 ns [83]. A maximised signal-to-noise ratio (S/N) allows for the maintenance of a good single-hit efficiency for each module of the tracker system. This was calculated as the most probable signal amplitude for an ionising particle divided by the root-mean-square (RMS) of the modules noise distribution. The detector was designed to keep this ratio over 12, with the expected radiation damage accounted for [83].

As particles travel through detector material there is an increasing effect of multiple scattering on the global resolution of the detectors. It is for this reason that the minimisation of detector material is adopted in its design. This is why, most of the detector supports and front-end electronics are positioned to be outside of the LHCb acceptance and do not contribute to these effects. In the case of the IT, this was not possible due to its positioning relative to the OT. Therefore the components of the IT had a specially chosen design to use less material in the construction of the system supports and front-end electronic cooling systems.

Outer Trackers

To measure momentum in the outer region of the LHCb acceptance where there is less particle occupancy, the use of drift-time detectors was adopted. These detectors make up the outer trackers (OT), the part of the T system (T1-T3). This design used layered straw drift-tubes filled with a gas admixture of 70% Argon and 30% CO_2. This design allowed for a drift time lower than 50 ns and spatial resolution of 200 μm [83].

The individual modules were specifically designed to have a mechanical stability that is sufficient to ensure the desired precision of 100 μm and 500 μm in the x and z direction are maintained. This included the requirement that the centrality of the anode wire was not compromised across the length of the straw tubes and that any gas leakage under the pressure of 10 mbar does not exceed 0.8 ml s^{-1} [83].

Similar to the silicon tracking system, the minimisation of multiple scattering effects in the OT was ensured by keeping detector material below a few percent of X_0 [83]. The minimisation of noise and crosstalk caused by electromagnetic interference in the drift-tubes was ensured by keeping the tubes firmly grounded and forming a Faraday cage around all of the modules and their electronics.

Track Reconstruction and Performance

There are five track categories that can be reconstructed with the LHCb tracking system depending on the combination of the tracking sub-detectors they are formed from. These are demonstrated in Figure 2.7 and defined as:

1. **VELO Tracks**: tracks reconstructed in the VELO system and used for vertex reconstruction. These typically travel outside of the acceptance of the other trackers due to a large polar angle.

2. **Long Tracks**: tracks originating in the VELO and passing the TT and IT systems.

3. **Downstream Tracks**: tracks reconstructed only using the TT and IT systems. These are reconstructed from decays that occur outside of the VELO acceptance.

4. **Upstream Tracks**: tracks that do not reach the T systems but do originate in the VELO and reach the TT. These usually have momentum low enough to be deflected by the magnet to outside of the detector.

5. **T Tracks**: tracks just from the T trackers. These are unlikely to be produced in a signal decay from proton-proton collisions.

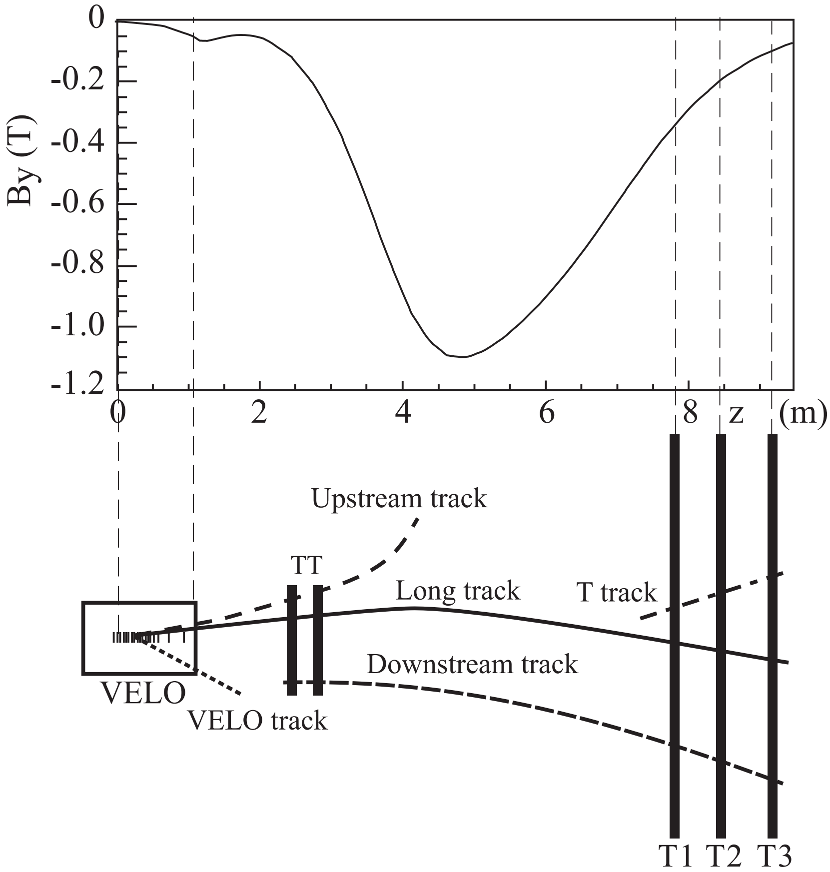

Figure 2.7.: Graph of the vertical magnetic field (B_y) against the z position. A z–scaled illustration of the tracking system and the different types of tracks reconstructed at LHCb [83].

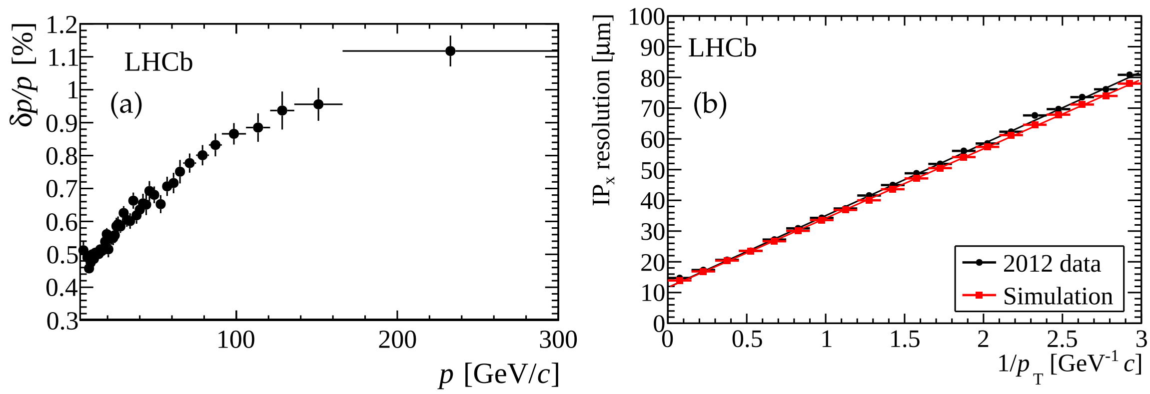

Figure 2.8.: The resolution of a) the track momentum as function of particle momentum and b) Impact parameter as a function of $1/p_{\mathrm{T}}$ [80].

Early simulations of $B^0 \to J/\psi K^0_{\mathrm{S}}$ have determined that there is an average of 72 reconstructed tracks per $b\bar{b}$ event. This amounts to 26 VELO tracks, 26 long tracks, 11 upstream tracks, 4 downstream tracks and 5 T tracks [83].

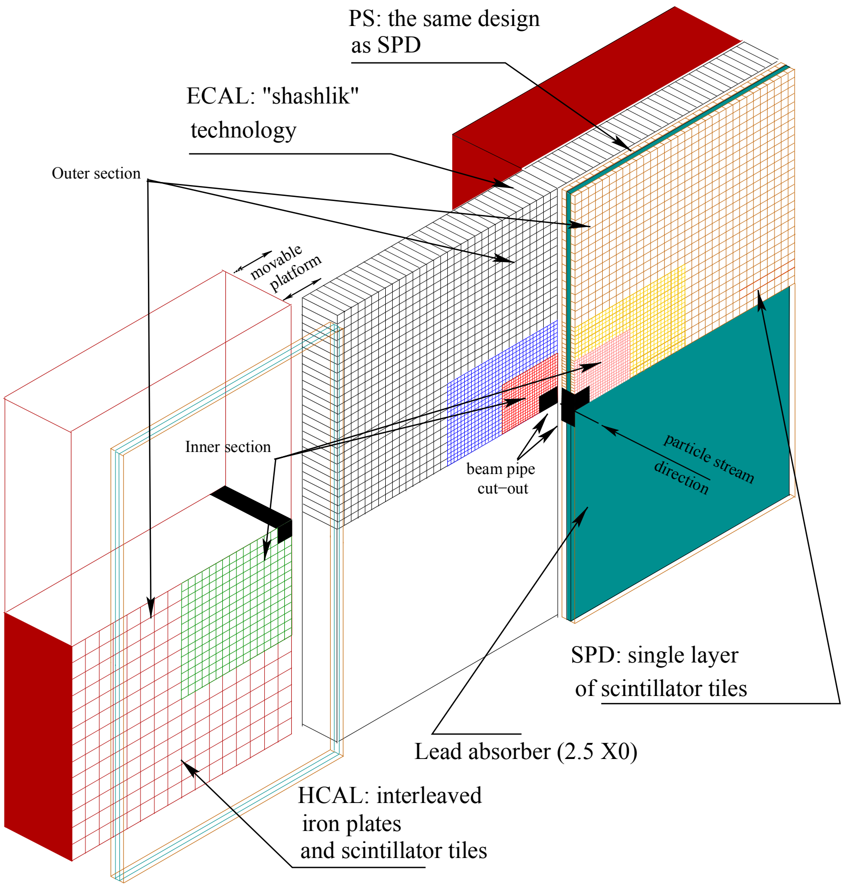

Figure 2.9.: The layout of the LHCb Calorimeters highlighting the PS, SPD, ECAL and HCAL structures [85].

The tracker momentum resolution over particle momentum had achieved $\sigma_p/p = 0.05\%$ at momenta below 20 GeV and as high as 1% as momentum reaches 200 GeV. For the impact parameter (IP) of tracks (*i.e.* the tracks distance of closest approach to the primairy vertex), there is a linear dependence with respect to $1/p_{\mathrm{T}}$. It ranges from about 15 μm to 80 μm in the $1/p_{\mathrm{T}}$ range from $0\,\mathrm{GeV}^{-1}$ to $3\,\mathrm{GeV}^{-1}$ [80]. Both resolutions are given in Figure 2.8.

2.2.2. Calorimeters

Overview

The primary goal of the calorimeter system is to tag the transverse energies (E_{T}) of hardware trigger (L0 described in Section 2.2.3) candidates as well as particle identification. These candidates are separated by four low-level categories: electrons (e), photons (γ), neutral pions

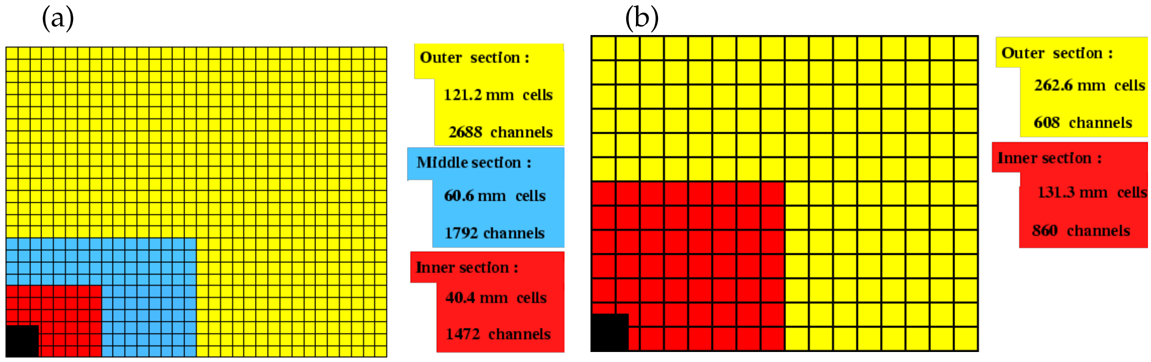

Figure 2.10.: The layout of one quarter of the calorimeter cell structures for the a) three sections of the SPD, ps and ECAL and b) the two HCAL sections [83].

(π^0) and charged hadrons (h). At the level of data analysis the accurate reconstruction of these photons and neutral hadrons (*e.g.* $\eta/\pi^0 \to \gamma\gamma$) is an important feature of the detector system.

The LHCb calorimeter system takes a four-layered approach with the ECAL and then HCAL layers typical of particle physics detectors along with two layers to aid in PID and background rejection, the PS and SPD detectors. Each of these detectors are subdivided into cells that are in the x–y plane. These cells have different sizes depending on the regions, of which there are two sections for the HCAL and three for the others. The smaller cells are located nearer to the beamline in order to give higher detector granularity to accommodate for the larger particle flux in these regions. An overview of this design layout with the cell sizes for the respective regions is given in Figure 2.9 and Figure 2.10.

Each of the four detectors are scintillators with layers of either lead or iron in between the scintillating layers. When interacting particles traverse the scintillators, they produce light that passes through wavelength-shifting (WLS) fibres to either photomultiplier tubes (PMT) for the ECAL and HCAL or multi-anode photomultiplier tubes (MA-PMT) for the SPD and PS. The PMT and MA-PMTs then give electrical signals to the Front-End electronics located on a platform above the calorimeters.

The SPD and PS detectors are used for particle identification where the PS separates electrons from pions while the SPD helps separate charged and neutral particles. The SPD also provides information on the charged particle multiplicity in events which can help remove events that have higher detector occupancy and will be too slow to reconstruct. The measurement of the energy of electrons and photons comes from the combined energy deposited in the PS and the ECAL. The HCAL provides energy measurements for charged hadrons. All four detectors combined are used for offline PID.

The SPD and PS detectors have very similarly designed cells of scintillators with WLS fibre coils inside for light collection leading to the MA-PMT output modules. These two are separated by the lead wall of $2.5X_0$ as the absorber for the PS.

The ECAL is a shashlik detector of successive scintillator-lead layers. The overall thickness of this detector is $25X_0$ which allows for a complete energy measurement from electromagnetic showers and good energy resolution. The ECAL and the LHCb outer tracker are designed to have equal angular acceptances. The energy resolution has been measured by a test beam of electrons and is given by

$$\frac{\sigma(E)}{E} = \frac{(9.0 \pm 0.5)\%}{\sqrt{E}} \oplus (0.8 \pm 0.2)\% \oplus \frac{0.003}{E \sin\theta} \quad , \tag{2.5}$$

where E is the energy of the measured particle in GeV and θ is the polar angle relative to the z–axis [86].

The HCAL is made from scintillator-iron layers of total thickness equal to 5.6 interaction lengths. This uses the same PMT modules and has an energy resolution determined by use of a pion test beam to give

$$\frac{\sigma(E)}{E} = \frac{(67 \pm 5)\%}{\sqrt{E}} \oplus (9 \pm 2)\% \, , \tag{2.6}$$

where E is the energy of the measured particle in GeV [87].

SPD Calibration

Precalibration of the SPD was performed to ensure that its performance was correct before the beginning of data taking. Then during data-taking further calibration was necessary to account for the ageing of the PMTs caused by radiation damage to the photocathodes and scintillator material. To calibrate the SPD, the reconstructed track of a charged particle is matched with hits in the SPD. The ratio of events with clear hits at the expected point from a track's trajectory and the total number of tracks that should lead to the SPD gives the efficiency of the SPD. This can be measured as a function of the threshold energy per cell corresponding to a single Minimum Ionising Particle (MIP) and compared to a theoretical efficiency. The initial calibration of the SPD detector was done by measuring cosmic rays in coincidence of the ECAL and HCAL. This gave the initial global correction to the gain of the detector.

In the data-taking year of 2010 at $\sqrt{s} = 7\,\text{TeV}$ scans of threshold energy values from 0.3 to 2.1 MIP energies were performed. The theoretically expected efficiency was fitted for each of the SPD cells at these energies. This allowed for the extraction of correction factors from these fits that could then be applied periodically. This was repeated in Run-1 in June 2011, April

2012 and November 2012. The radiation ageing corresponded to an average SPD efficiency decreased from 95% to 88% by the end of the first LHCb run [85].

During the long shutdown between Run-1 and Run-2 annealing effects improved the SPD efficiency by about 3% at the beginning of Run-2 (October 2015) compared to the end of Run-1. In the beginning of the 2017 data-taking there was a re-calibration effort to fit new efficiency distributions. This meant up-to-date effects of ageing were taken into account and new corrections could be calculated. With new regular monitoring methods using fast streams of calibration data the average cell efficiency was 94% after 2017 recalibration [85,88].

PS Calibration

The calibration of the PS was done using charged particle tracks that are extrapolated to the cells. The first calibration was done by use of cosmic rays and then partially reconstructed proton-proton collision data were used to improve the corrections. Completely reconstructed MIP tracks that traverse the PS were used to ensure the cell responses were equal across the detector. A corrective multiplicative factor was applied to the high voltage gain of the electronics. Each calibration performance is determined by fitting the energy distribution of each cell and determining the MIP variance. This is done for each data-taking period.

ECAL Calibration

The calibration of the ECAL was done by changing the PMT High Voltage (HV) gains. The precalibration of the PMTs was performed using fixed amplitude LEDs. These LEDs were built for each readout channel for monitoring the gain of the PMTs.

In Run-1 a method of calibration was employed to update the PMT gains to compensate for ageing effects. The ageing effects arise from two principle sources: radiation damage to the scintillator tiles and fibres and the degradation of the PMTs due to the high current integrated over time. The method of correction was a fine calibration approach to ensure the fitted π^0 mass was equal to the nominal π^0 mass. In the original design there was a plan to use LED responses for monitoring the gain corrections over data-taking but the LED clear fibres themselves experienced strong ageing effects and were not reliable for use. Therefore in Run-1 LED monitoring was not used to follow the ageing effect. Checks of the π^0 mass were then used to monitor the age per zone.

For Run-2, in order to use the originally planned LED monitoring system, the replacement of the LED clear fibres with radiation hard ones was necessary. This meant that the calibration methodology was partially altered. In the data-taking years of 2015 and 2016, the gain changes to compensate for ageing effects was calculated and applied manually. For the subsequent

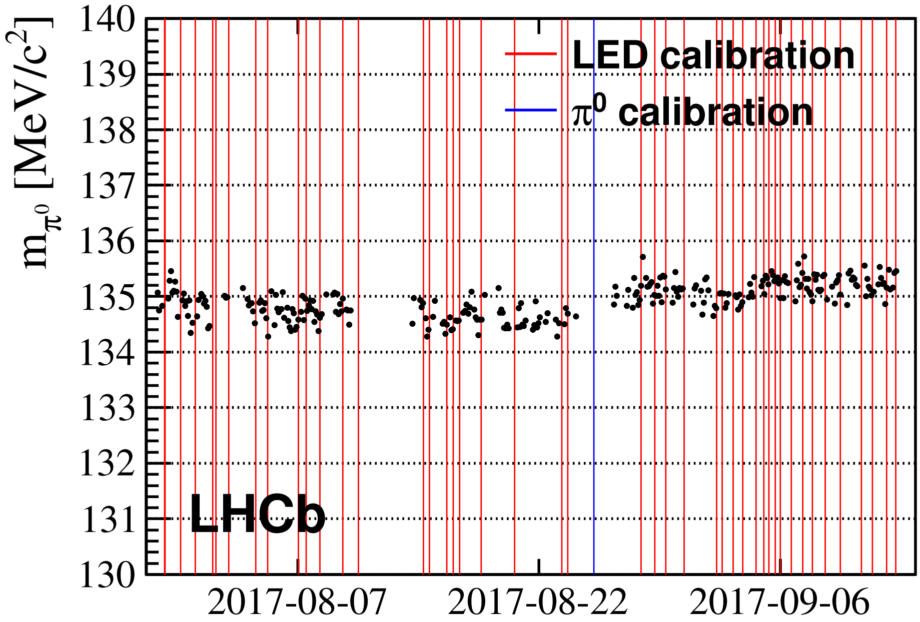

Figure 2.11.: The measured mass of the π^0 determined by a fit on summer 2017 data over time. The red lines give the times of the LED calibration and the blue line gives a date when the π^0 mass is finely calibrated for each cell [85].

data-taking years these were then automatised. The HV gains were then altered so that the LED signal was matching with an LED reference value.

The second method of calibration was finely calibrating the reconstructed π^0 mass to match the nominal value. This was performed by the reconstruction of $\pi^0 \rightarrow \gamma\gamma$ for pairs of cells so that the calibration of each cell was dependent on the calibration of others. For this reason, an iterative approach was required to calibrate every cell multiple times so that the PMT gain correction factors cause the π^0 mass to converge to the nominal value for each cell. This is done in a total of 7 iterations to ensure the new set of corrections is robust. The results of this calibration can be seen in Figure 2.11. This is repeated once per data-taking month (a total of 6 times per year) by 2018 [85].

HCAL Calibration

To calibrate the HCAL two ^{137}Cs sources are used. These sources are attached to each half of the subdetector and are attached by a hydraulic system that moves across each cell to measure the PMT responses. Taking into account the activity of the sources, this system can determine the proportionality between the sensitivity of the cells and the PMT response.

The ageing of the detector becomes apparent when comparing the hadron trigger efficiencies over time for the same selection thresholds. These changes would arise from the difference in the sensitivity of cells and a correction must be applied over time. The method to apply a correction is to calculate a correction factor to the voltage gain of the PMTs. The largest corrections would have to be applied to the central region of the detector due to the higher particle fluency in data taking periods. It is also the case that the most downstream layers of the HCAL are not affected by ageing. Most of the corrections are based either on LEDs or Caesium source information.

2.2.3. Trigger

The LHCb trigger system is how the experiment does its earliest selection requirements. This is achieved by a three-level system including one hardware stage Level-0 trigger (L0) and two software stages, the High Level Trigger 1 and 2 (HLT1 and HLT2). The L0 trigger system is connected to the Decision Unit (DU) where information is collected and determines whether to reject events or not. This stage initially reduces the incoming event rate from the 40 MHz bunch crossing rate to a 1 MHz readout rate. Both HLT1 and HLT2 use C++ algorithms to partially or fully reconstruct events where HLT1 determines what data is saved to local machines and in turn sent to the HLT2 for further selection of events to be stored offline. This reduces the rate of events going to storage to 5(12.5) kHz for Run-1(Run-2).

The hardware trigger

Events are initially selected based on the algorithms of the combined hardware and software trigger systems summarised in Figure 2.12. This limits the rate of data-taking and stores data from decays of interest.

The hardware or L0 trigger makes use of the energy deposited into the calorimeters and makes decisions based on 2×2 clusters of energy in the ECAL and HCAL. This is normally using transverse energy as to be independent of the boosting that arises in the asymmetry of proton-proton collisions and keep the distributions within a standard energy range. These energies are then given as

$$E_T = \Sigma_i E_i \sin\theta_i, \tag{2.7}$$

where E_i and θ_i are the energies and polar angles (relative to the z-axis) of individual cells i. The energies will correspond to either hadrons, photons or electrons depending on their signatures in the PS/SPD system. An electron will cause a registered hit in the SPD, whereas a photon would not.

For triggering on muons, a track is searched for in the muon stations. The transverse momentum is calculated from interpolating this track to the interaction point with the dipole

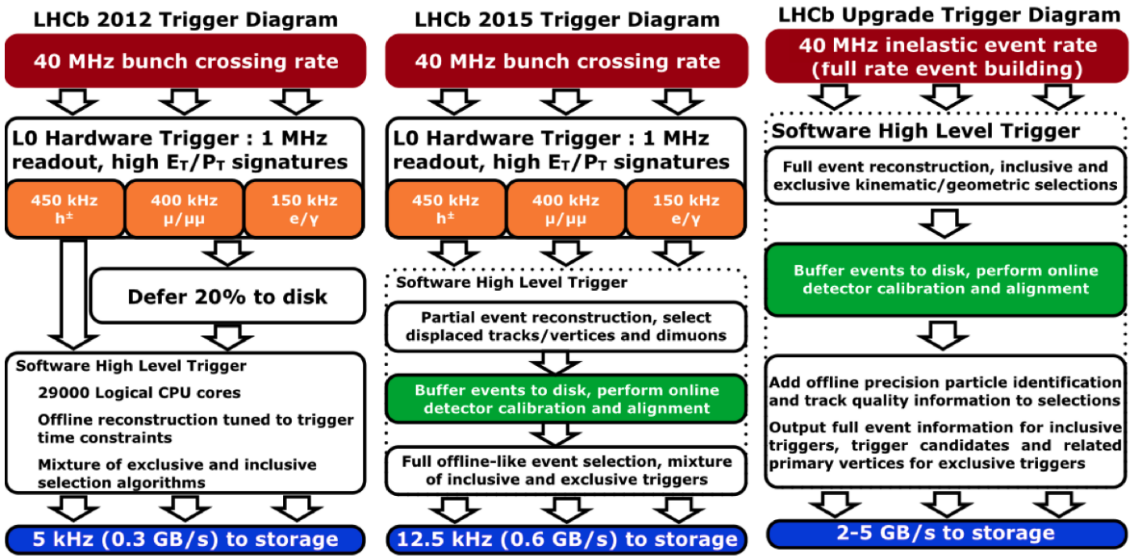

Figure 2.12.: The LHCb trigger system for Run-1 (2012), Run-2 (2015) and the Run-3 Upgrade [89].

bending magnet causing its change in direction. The transverse momentum of a muon measured in this way then needs to be above the threshold which is configured for the L0Muon trigger decision algorithm or the product of two muon momenta must be above the threshold for L0DiMuon. The configuration of L0 thresholds is varied over data-taking to ensure the output is a high as possible for different beam configurations.

The high level trigger

The events accepted by the hardware stage are then fed into the Event Filter Farm (EFF) which processes the software level triggering algorithms (HLT). The first level of this stage is the HLT1 which performs a partial reconstruction of the events. This involves the reconstruction of tracks of particles that pass through the full tracking system with sufficiently high transverse momentum (above 500 MeV) and the precise measurement of the primary vertices. At this stage the only PID algorithm that is used is the identification of muons [90].

The next stage is the full reconstruction of events with the HLT2 algorithms. This stage will perform full reconstruction of tracks that do not necessary pass through the full tracking system, reconstruct neutrals, and make use of PID algorithms. In the Run-1 the reconstruction of HLT2 is different from offline reconstruction, but in Run-2 it is the same methodology.

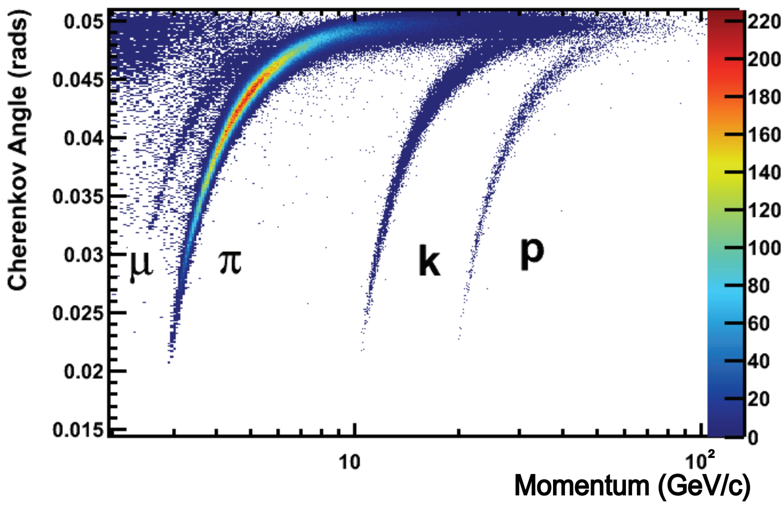

Figure 2.13.: The RICH1 reconstructed Cherenkov angles versus charged particle momenta [91].

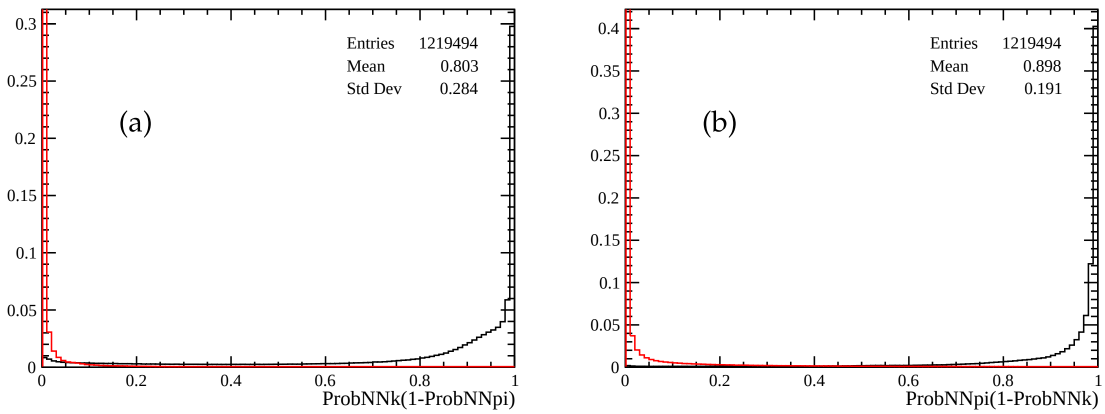

Figure 2.14.: The ANN PID variable distributions in the particle hypothesis of a) kaons and b) pions. Black is the correct hypothesis and red is a kaon-pion swap.

2.2.4. Charged particle identification

The identification of charged particles comes from a combination of information from the calorimeters, muon systems and RICH detectors. The primary goal of the RICH systems is to identify hadron type as the leptons and neutral particles are all well separated by the other subdetectors at LHCb. The distribution of the angle of the Cherenkov light against particle momentum is distinct for different particle identities, see Figure 2.13. The system is composed of two detectors: RICH1 which is upstream of the magnet and just downstream of the VELO and RICH2 which is downstream of the magnet just before M1 and the calorimeters. Each RICH detector covers a different momentum range with RICH1 designed for lower momenta (about $1-60\,\text{GeV}$) and RICH2 for high momenta (over $15\,\text{GeV}$) [83].

The information is combined by use of artificial neural networks as multivariate analysis tools. These then create a variable (ProbNN$_x$) for each particle hypothesis ($x \equiv K, \pi, e, \mu, p$) which functions as a probability density function from 0 to 1. Combinations of ProbNN$_K$ and ProbNN$_\pi$ are shown in Figure 2.14 to illustrate the rejection capabilities of these variables when used as a function with each other.

Specifically for the identification of muons are the muon stations (M1-M5). These produce a binary signal that gives the position of the muons relative to the interaction point. M2-M5 and the outer part of the M1 station are MWPCs with anode wires and cathode pads that include layers of 80 cm iron absorbers. Whereas the inner part of M1 is a triple GEM detector with an anode pad. These all have a fast gas mixture with 4 gas gaps for M2-M5 and 2 for M1. A 6 GeV muon that hits all 5 stations penetrates about 20 interaction lengths including the iron layers and the rest of the detector. There is a binary selection variable based on hits on these stations called IsMuon. The average efficiency of selecting muons is about 98% with 0.5% for mis-identification [92].

2.2.5. Dataflow

After events are selected by the trigger systems the raw data are stored. The reconstruction takes all of the information from detector hits and creates physics objects to be stored and ready for further selections. The next stage of selections are called the Stripping selections which target certain decays of interest. These are offline selections that use the data of fully reconstructed events and categorise them by decay and use loose selections requirements to remove common backgrounds. This thesis concerns analyses of decays involving the $J/\psi \to \mu^+\mu^-$ decay. There is a specific Stripping line (called "StrippingFullDSTDiMuonJpsi2MuMuDetachedLine") used that broadly targets events in the full datasets that have this decay.

2.2.6. Software

LHCb simulation is handled by the software framework called GAUDI [93] which handles the data processing applications with the aid of external libraries. The measurement of selection and reconstruction efficiencies is determined by simulated Monte Carlo (MC) data. The MC proton-proton collisions are generated initially by use of the physics modelling simulation packages PYTHIA 6 [94] or PYTHIA 8 [95]. The EVTGEN package [96] adds decay and time information using B-physics modelling and is of key importance to measuring time-dependent CP asymmetries. For the simulation of photons, there must be corrections made to replicate the leading-order processes and photon behaviour, this is ensured by the use of the PHOTOS package [97]. Together these packages are handled by the GAUSS application which generates the initial events and simulates the particle propagation through the detector [98]. Another principle part of the simulation software is the simulation of the detector and its interactions as particles traverse the experiment which is performed by the GEANT4 [99]. This data is then digitised by BOOLE [100] to replicate the responses of the detector electronics and the L0 trigger hardware. This final stage leaves data-types identical between real and simulated data.

For the reconstruction of both the simulation output of BOOLE and real collision data the software package BRUNEL [100,101] is used. This application then produces the Data Summary Tapes (DSTs) for the use in analysis with DAVINCI [100,101]. It also produces data files with less information than full DSTs, called reduced DSTs (rDSTs), to be processed in the stripping selection stage. DAVINCI is the analysis framework used for the selections of physics events through the manipulation and analysis of physics objects.

2.3. Neutral reconstruction and identification at LHCb

2.3.1. Neutral reconstruction

For the measurement of photons the energy and momentum are determined by the deposits in the cells. To do this the cells of the ECAL are clusterised by the Cellular Automaton algorithm [102]. In the ECAL these are formed from 3×3 cell clusters around a local maximum (*i.e.* the cell with the largest proportion of deposited photon energy), this is called the seed cell. There are requirements that the seed cells have at least 50 MeV of transversal energy deposited and are separated by at least one cell. When there is overlap between two clusters, then the energy in the concerned cell is divided between the two clusters proportionally to their total energy. This is an iterative process, repeated five times to ensure that the total energy converges. All 3×3 clusters can be attributed three parameters based on each constituent cell i with central coordinates of (x_i, y_i): firstly a cluster energy

$$E_{ECAL} = \Sigma_i E_i,$$

its transverse barycentre (*i.e.* energy weighted position)

$$\vec{P}_{ECAL} = \frac{1}{E_{ECAL}}(\Sigma_i E_i x_i, \Sigma_i E_i y_i) = (x_b, y_b),$$

and the transverse dispersion

$$\mathcal{S}_{ECAL} = \frac{1}{E_{ECAL}} \begin{pmatrix} \Sigma_i E_i (x_i - x_b)^2 & \Sigma_i E_i (x_i - x_b)(y_i - y_b) \\ \Sigma_i E_i (x_i - x_b)(y_i - y_b) & \Sigma_i E_i (y_i - y_b)^2 \end{pmatrix}. \tag{2.8}$$

Table 2.2.: The measured photon energy reconstruction calibration parameters in 2012.

Parameter	Photon type	ECAL Section		
		Inner	Middle	Outer
α	non-converted	1	1	1
	converted	1.0144	1.0306	1.0002
β	non-converted	10.23	10.06	7.92
	converted	13.43	11.16	10.27
γ	non-converted	175	125	90
	converted	446	222	205

In order to determine that these clusters are reconstructed from neutral particles there needs to be a check that there are no tracks in the event that are pointed towards the cluster. Therefore the reconstructed track trajectories are extrapolated to the ECAL and are assigned to the best-matching clusters. The goodness of the matching is determined by

$$\chi^2_{2D}(\vec{P}) = (\vec{P}_{tr} - \vec{P})\mathcal{C}_{tr}^{-1}(\vec{P}_{ECAL} - \vec{P}) + (\vec{P}_{ECAL} - \vec{P})^{\mathrm{T}}\mathcal{S}_{ECAL}^{-1}(\vec{P}_{ECAL} - \vec{P}), \quad (2.9)$$

where the extrapolated position of the track is $\vec{P}_{tr}$, with a covariance matrix $\mathcal{C}_{tr}$. The selection of clusters and their positions are determined by the minimisation of χ^2_{2D}. A selection criteria of $\chi^2_{2D} > 4$ is used to remove most of the clusters from charged particles [85, 103].

The photon energy E_c is calculated by the relation

$$E_c = \alpha E_{ECAL} + \beta E_{PS} + \gamma, \quad (2.10)$$

where E_{ECAL} and E_{PS} are the energy deposits measured in the ECAL and PS with α and β are factors to correct for energy leakages in the respective subdetectors [103].

The factor α is the product of many corrections:

$$\alpha = \alpha_G \times \alpha_E \times \alpha_B \times \alpha_X \times \alpha_Y \times \alpha_P \quad (2.11)$$

where

1. α_G: the global ECAL correction factor
2. α_E: corrects for longitudinal leakage
3. α_B: corrects for transverse leakage
4. α_X: accounts for dead module material in the x–direction

5. α_Y: accounts for dead module material in the y–direction
6. α_P: for PS energy dependency

The α factors are obtained by a sample of photons with small PS deposits. Then β is determined given that value of α. There are sets of α, β and γ for converted and non-converted photons in each ECAL region. The measured values of these parameters are in Table 2.2.

The energy of the ECAL had to be subtracted by the pile-up energy E_{pileup} which was modelled as having a linear dependence on the number of hits in the SPD (nSPDHits) which is indicative of the event occupancy. This means $E_{ECAL} = E_{3\times3} - E_{pileup}(\text{nSPDHits})$ where $E_{3\times3}$ is the raw energy of a 3×3 cluster of cells.

For the reconstruction of the photon momentum, an assumption that the photon originates from the primary vertex to the cluster barycenter is used by default. For the measurement of the z_c longitudinal position, a penetration depth correction (L-correction) must be performed. This is given as

$$z_c = z_{ECAL} + a \ln E_c + b(E_{PS}).$$

This energy dependent correction normally gives the penetration depth as $\sim 10 - 20\,\text{cm}$. This is called the L-correction.

A second correction to the transversal barycenter coordinates is necessary to account for the non-linearity of the transversal profile of the shower shape (S-correction). This correction assumes the energy profile of the cluster in the transversal plane can be modelled as an exponential ($E(r) = E_0 e^{-r/b}$), the correction gives the x and y–coordinates from a single parameter function $\mathcal{S}_0(b)$:

$$(x_c, y_c) = \mathcal{S}_0[(x_b, y_b), b] = b \sinh^{-1}\left[\frac{(x_b, y_b)}{\Delta} \cosh \frac{\Delta}{b}\right],$$

where Δ is half the size of a cell and b is the decay constant of the exponential. Further corrections to this were necessary to account for the non-spherical shower shape. The total S-correction is therefore

$$(x_c, y_c) = \mathcal{S}_0[(x_b, y_b), b] + \mathcal{S}_1[(x_b, y_b)] + \mathcal{S}_2[(x_b, y_b)],$$

where $\mathcal{S}_1$ corrects for the residual S-shape and $\mathcal{S}_2$ corrects for the geometrical asymmetries [103]. These corrections are determined from MC simulations.

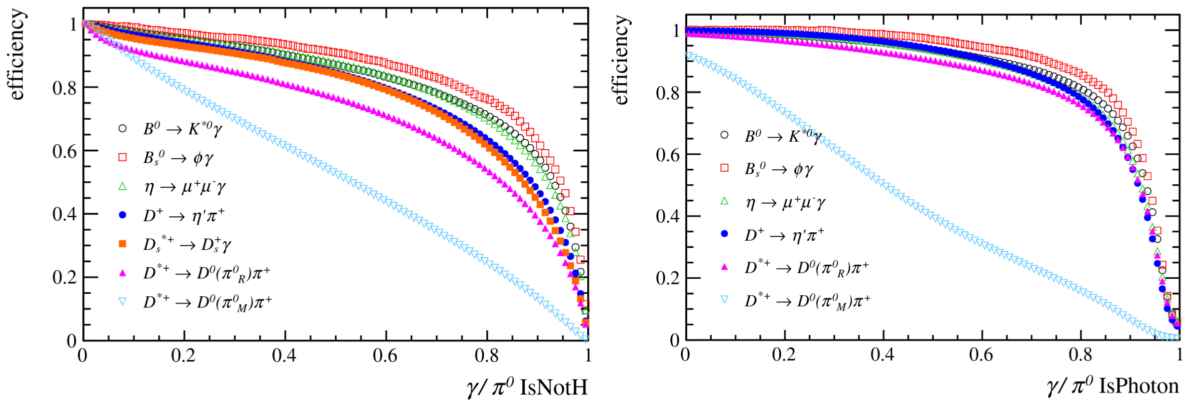

Figure 2.15.: The efficiencies of the photon PID variables for various photon samples [104].

2.3.2. Neutral particle identification

In this thesis, a crucial part of the analyses performed is the identification of the final state photons. The identity of photons are ensured by the use of Neural Networks based on discriminating variables. The variables IsNotH and IsPhoton are multivariates trained on simulated signal and background categories with a set of input variables that are chosen for their distinction between the two categories. IsNotH is used for the separation of photons from hadrons and IsPhoton is for the separation of photons from merged π^0. Therefore signal category is chosen as reconstructed photon candidates that match those generated, the background for IsNotH is the reconstructed photons that are matched as non-electromagnetic particles (*e.g.* hadrons) and for IsPhoton these are merged π^0 ($\pi^0 \to \gamma\gamma$ where both photons are so close to each other that they are reconstructed as one cluster).

There are input variables used in the training of IsNotH including:

- The χ^2_{2D} of the cluster.
- The energy deposits in the PS.
- The ratio of the energy in the seed cell and the total energy in the 3×3 cluster in the ECAL.
- The ratio of the energy in the seed cell and the total energy in the 3×3 cluster in the PS.
- The ratio of the energy in the HCAL over the ECAL.
- The 2×2 PS cells with the highest energy upstream of the ECAL cluster.
- The total number of PS cells with hits upstream of the ECAL cluste.r

- The multiplicity of the 3×3 SPD cells upstream of the ECAL.
- The showershape matrix elements shown in equation (2.8) [105].

In the training of IsPhoton a different set of variables is used:

- The showershape matrix elements shown in equation (2.8) are used to create a number of variables. The first is

$$r2 = < r^2 > = (S_{ECAL})_{11} + (S_{ECAL})_{22}. \tag{2.12}$$

- Another is related to the tails

$$r24 = 1 - \frac{< r^2 >^2}{< r^4 >}. \tag{2.13}$$

- A variable κ is related to the ratio of eigenvalues of the showershape matrix

$$\kappa = \sqrt{1 - 4\frac{\det S}{\mathrm{Tr}^2 S}}. \tag{2.14}$$

- Another is related to the asymmetry of the shower shape and is parameterised as

$$\mathrm{asym} = \frac{(S_{ECAL})_{12}}{\sqrt{(S_{ECAL})_{11}(S_{ECAL})_{22}}} \tag{2.15}$$

- The ratio of the seed cell and the total cluster energies is used, as well as the ratio of the sum of the seed and second most energetic cell over the total cluster energies.
- Then the multiplicities at different energy deposit thresholds were also included [106].

These variables are then combined to produce the single variables IsNotH and IsPhoton using a multi-layer perceptron. The performance of the IsPhoton and IsNotH are shown in Figure 2.15 where the discriminators perform very similarly for the different single photon channels, slightly poorer for resolved $\pi^0 \to \gamma\gamma$ and noticeably poor for merged π^0. To illustrate the effectiveness of the IsNotH variable to remove non-photon backgrounds, Monte-Carlo simulation of real photons can be compared to photon candidates which are not real photons, as shown in Figure 2.16.

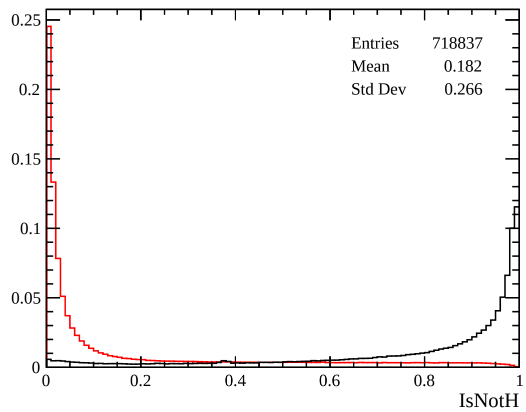

Figure 2.16.: The normalised distribution of IsNotH for real (black) and fake (red) photons. This is a comparison of photons from $B^+ \to \chi_{c1} K^+$ where $\chi_{c1} \to J/\psi\gamma$ and fake photons of $B^+ \to J/\psi K^+$ reconstructed and selected as $B^+ \to \chi_{c1} K^+$ (samples used in the analysis of Chapter 4).

Chapter 3.

Measuring B decays to charmonia at the LHCb experiment

In this thesis there is the presentation of two analyses performed on data taken at the LHCb experiment. One is a physics analysis to measure the branching ratios of $B^0_{(s)} \to J/\psi\eta^{(\prime)}$ normalised to the previously well studied branching ratio of $B^0 \to J/\psi\rho^0$ (where ρ^0 is ρ^0 (770)) and the mixing angles between η and η' calculated in the ratios of the $B^0_{(s)} \to J/\psi\eta^{(\prime)}$ decays. The final states of the $\eta^{(\prime)}$ decays include two charged pions and either one or two photon, yet the ρ^0 nearly always decays to just two pions. Therefore in the measurement of the branching ratios there would be no cancellation of the photon reconstruction efficiencies. This meant that another dedicated performance analysis was needed in order to understand these efficiencies and make corrections such that the efficiencies estimated by Monte Carlo simulated data are as expected in data. These corrections are calculated by a similar method as that employed in the measurement of branching ratios, using the measurement of $B^+ \to \chi_{c1}K^+$ with $\chi_{c1} \to J/\psi\gamma$ for single photons and $B^+ \to J/\psi K^{*+}$ with $K^{*+} \to K^+\pi^0$ for photons originating from $\pi^0 \to \gamma\gamma$ decays.

As both of these analyses make use of B decays to charmonia (*i.e.* $B \to J/\psi X$) there were also commonalities in the overall selections, corrections and systematic uncertainties. This chapter is intended to introduce both analyses in Section 3.1 for the physics analysis and Section 3.2 for the performance analysis, as well as give an overview of the data samples used (Section 3.3), the common basic selections (Section 3.4), the corrections made to simulation for the estimation of efficiencies (Section 3.5), the Multivariate Analysis methods used for further selections after applying those corrections (Section 3.6), and the fitting strategy used to extract signal yields (Section 3.7).

3.1. Analysis strategy for the measurement of the Branching Ratios of $B^0_{(s)} \to J/\psi\eta^{(\prime)}$ and η-η' mixing

This study is intended to determine the the η-η' mixing angles and the absolute branching ratios of $B^0_{(s)} \to J/\psi\eta^{(\prime)}$ decays by measurement of $J/\psi \to \mu^+\mu^-$ final states that are triggered and reconstructed at high efficiencies and with good purity. Throughout this thesis, the charge conjugates of all decays are implied. In previous LHCb analyses of these decays [76,77] a limiting factor in measured parameters was the low amount of statistics. This is partly due to the studies measuring just a few final states. For the mixing measurements (and consequently the $B^0 \to J/\psi\eta^{(\prime)}$), only the $\eta \to \pi^+\pi^-(\pi^0 \to \gamma\gamma)$ and $\eta' \to \pi^+\pi^-(\eta \to \gamma\gamma)$ final states were measured. In order to improve on the precision by increasing statistics, a combination was performed with the $\eta^{(\prime)}$ final states of $\pi^+\pi^-\gamma$, $\pi^+\pi^-\gamma\gamma$ and $\gamma\gamma$. Explicitly these states are produced in the η decays $\eta \to \pi^+\pi^-\gamma$ and $\eta \to \pi^+\pi^-(\pi^0 \to \gamma\gamma)$ as well as the respective η' modes of $\eta' \to (\rho^0 \to \pi^+\pi^-)\gamma$ and $\eta' \to \pi^+\pi^-(\eta \to \gamma\gamma)$. By measuring four final states of the $\eta^{(\prime)}$, this analysis provides the most comprehensive view of $B^0_{(s)} \to J/\psi\eta^{(\prime)}$ decays yet.

To determine the ratios of branching ratios from measurements at LHCb, the number of recorded signal events $N^{\mathrm{s}}_{B^0_{(s)} \to X}$ of the various decays are to be determined by maximum likelihood fits of the invariant mass distributions of the B^0 and B^0_s. These yields can be related to the branching ratios by the following formula:

$$N^{\mathrm{s}}_{B^0_{(s)} \to J/\psi\pi^+\pi^-X^0} = 2 \times f_{d,s} \times \sigma(b\bar{b}) \times \mathcal{L}_{\mathrm{int}} \times \varepsilon^{\mathrm{data}}_{B^0_{(s)} \to J/\psi\pi^+\pi^-X^0} \times \mathcal{B}_{B^0_{(s)} \to J/\psi\pi^+\pi^-X^0}\,, \tag{3.1}$$

where the fragmentation fractions f_d and f_s are the probabilities that a b hadronises to a B^0 or B^0_s meson respectively. The cross-section $\sigma(b\bar{b})$ and integrated luminosity $\mathcal{L}_{\mathrm{int}}$ provide the number of $b\bar{b}$ pairs produced in the proton-proton collisions at the LHCb experiment. The data efficiencies $\varepsilon^{\mathrm{data}}_{B^0_{(s)} \to J/\psi\pi^+\pi^-X^0}$ and $\mathcal{B}_{B^0_{(s)} \to J/\psi\pi^+\pi^-X^0}$ are decay-dependent where X^0 are either the single photons, $\pi^0 \to \gamma\gamma$ or $\eta \to \gamma\gamma$ final states. In this study the normalisation channel would not include that X^0.

For measuring the absolute branching ratios of the $B^0_{(s)} \to J/\psi\eta^{(\prime)}$ decays, it was necessary to use a normalisation channel that is similar in topology, previously well-studied (*i.e.* having low uncertainty on its measured branching ratio), and can also be measured precisely with high statistics at LHCb. The chosen channel that fits these criteria was the $B^0 \to J/\psi\rho^0$ where the decays of $J/\psi \to \mu^+\mu^-$ and $\rho^0 \to \pi^+\pi^-$ provide the same final state tracks as the signal channels. The principal difference between the final states are the single or two additional photons in the signal channels. Therefore, most systematic uncertainties will be minimised in the double ratios of Monte-Carlo efficiencies and real collision data signal yields. The Monte-Carlo photon reconstruction efficiencies and their associated uncertainties were also accounted for in the correction factors found using $B^+ \to \chi_{c1} K^+$ and $B^+ \to J/\psi K^{*+}$ normalised to $B^+ \to J/\psi K^+$ determined in the study of the next chapter.

Table 3.1.: The branching ratios of the η and η' decay modes as well as the $\pi^0 \to \gamma\gamma$. The values are averages from PDG [41].

Channel	$\mathcal{B}/\%$
$\eta \to \pi^+\pi^-\gamma$	4.22 ± 0.08
$\eta \to \pi^+\pi^-\pi^0$	22.92 ± 0.28
$\pi^0 \to \gamma\gamma$	98.823 ± 0.034
$\eta' \to \rho^0\gamma$	29.5 ± 0.4
$\rho^0 \to \pi^+\pi^-$	~ 100
$\eta' \to \pi^+\pi^-\eta$	42.5 ± 0.5
where $\eta \to \gamma\gamma$	39.41 ± 0.20

The calculation of the absolute branching ratios would therefore be determined by the double ratio of the signal channels over the normalisation channel as

$$\frac{\mathcal{B}_{B^0\to J/\psi\eta^{(\prime)}}}{\mathcal{B}_{B^0\to J/\psi\rho^0}} = \frac{N^s_{B^0\to J/\psi\eta^{(\prime)}}}{N^s_{B^0\to J/\psi\rho^0}} \frac{\varepsilon^{MC}_{B^0\to J/\psi\rho^0}}{\varepsilon^{MC}_{B^0\to J/\psi\eta^{(\prime)}}} \frac{1}{\mathcal{B}_{\eta^{(\prime)}\to X}}, \tag{3.2}$$

$$\frac{\mathcal{B}_{B^0_s\to J/\psi\eta^{(\prime)}}}{\mathcal{B}_{B^0\to J/\psi\rho^0}} = \frac{N^s_{B^0_s\to J/\psi\eta^{(\prime)}}}{N^s_{B^0\to J/\psi\rho^0}} \frac{\varepsilon^{MC}_{B^0\to J/\psi\rho^0}}{\varepsilon^{MC}_{B^0_s\to J/\psi\eta^{(\prime)}}} \frac{1}{\mathcal{B}_{\eta^{(\prime)}\to X}} \frac{f_d}{f_s}, \tag{3.3}$$

where the intermediary branching ratios of the $\eta^{(\prime)}$ decays to final states are included as $\mathcal{B}_{\eta^{(\prime)}\to X}$ and $\mathcal{B}_{\rho^0\to\pi^+\pi^-} \sim 1$. In the case of the B^0_s decays versus B^0 channels there are the different production fractions for these mesons at LHCb referred to as the fragmentation fractions f_s/f_d. These are proton-proton centre of mass energy dependent factors that were measured precisely in [107] to be 0.2390 ± 0.0076, 0.2385 ± 0.0075 and 0.2539 ± 0.0079 at 7 TeV, 8 TeV and 13 TeV respectively. The precision of these measurements and the average of previous measurements of $\mathcal{B}_{B^0\to J/\psi\rho^0} = (2.55^{+0.18}_{-0.16})$ and the intermediary decay channels in Table 3.1 (from the Particle Data Group [41]) are considered as external systematic uncertainties on the results.

3.2. Analysis strategy for the measurement of the photon reconstruction efficiencies using decays involving charmonia

In physics analyses at LHCb the reconstruction and selection efficiencies are calculated using Monte-Carlo (MC) simulations. As these simulations are imperfect, the discrepancies between collision and Monte-Carlo simulated data must be well understood. These discrepancies arise from many factors, including mis-modelling of the detector material and imperfect reconstruction. For instance, when reconstructing photons in the electromagnetic calorimeter (ECAL). A number of analyses at LHCb work with neutral particles in the final state normalised to modes without neutrals [76, 109, 110] including the primary analysis of this thesis. It is therefore important to provide the reconstruction efficiencies of these neutrals, as well as correction factors to be applied to the reconstruction and selection efficiency for the mode with a photon or neutral pion in the final state.

In this thesis a detector performance study provided these efficiencies and correction factors for π^0 and γ. These were calculated by performing a data-driven comparison of decay modes with similar final states where there is one additional photon or π^0 in the modes with neutrals. The decay modes $B^+ \to \chi_{c1} K^+$ (where $\chi_{c1} \to J/\psi\gamma$) and $B^+ \to J/\psi K^+$ are used for the γ reconstruction study; and similarly $B^+ \to J/\psi K^{*+}$ (where $K^{*+} \to K^+\pi^0$ and $\pi^0 \to \gamma\gamma$) and $B^+ \to J/\psi K^+$ for the π^0 reconstruction study. The decay $B^0 \to J/\psi K^{*0}$ (where $K^{*0} \to K^+\pi^-$) is also measured as a background control channel. Doing this allows for the reduction in the systematic uncertainty on this background contribution that appears in both the $B^+ \to \chi_{c1} K^+$ and $B^+ \to J/\psi K^{*+}$ studies. These decay modes were all studied using the decays of $J/\psi \to \mu^+\mu^-$ as this is a well triggered and reconstructed mode. This similarity with the measurement of the $B^0_{(s)} \to J/\psi\eta^{(\prime)}$ meant that there was a significant overlap in the analysis strategy: selections, reweighting, signal yield extraction from collision data, Monte-Carlo efficiency estimation and resulting systematic uncertainties. Therefore the primary concern of this chapter is the common analysis strategy of the two analyses and the following chapters will describe the specifics of each and the respective results.

For both analyses, these decay mode choices allow for the reduction of various sources of systematic uncertainty by cancellation in the double ratio of their yields and efficiencies. This is due to their similar topology along with their selection requirements being well aligned

Table 3.2.: The branching ratios of the signal and normalisation modes. The values are averages from PDG [41]. The branching ratio of $B^+ \to \chi_{c1} K^+$ is a more recent average to be published in [108].

Channel	$\mathcal{B}$
$B^+ \to J/\psi K^+$	$(1.020 \pm 0.019) \times 10^{-3}$
$B^+ \to \chi_{c1} K^+$	$(4.74 \pm 0.22) \times 10^{-4}$
$\chi_{c1} \to J/\psi\gamma$	$(34.3 \pm 1.0)\%$
$B^+ \to J/\psi K^{*+}$	$(1.43 \pm 0.08) \times 10^{-3}$
$K^{*+} \to K^+\pi^0$	$1/3$
$\pi^0 \to \gamma\gamma$	$(98.823 \pm 0.034)\%$

where possible. Therefore the selections for the common particles in all of the channels remains the same. The chosen selection strategy includes the use of boosted decision trees (BDTs) for multivariate analysis (MVA) by use of the the package [111]. These BDTs were trained individually per signal and normalisation channel. The input variables used in training were chosen to be as close as possible between the modes. This ensures the selections are as close as possible between these modes. This leaves the principle difference as the reconstruction of the additional γ and π^0 for the respective signal decay channels to be directly measured using $B^+ \to \chi_{c1} K^+$ and $B^+ \to J/\psi K^{*+}$ normalised to $B^+ \to J/\psi K^+$, and applied as multiplicative factors to the Monte-Carlo efficiencies of $B^0_{(s)} \to J/\psi \eta^{(\prime)}$ channels when they are normalised to $B^0 \to J/\psi \rho^0$. Other smaller discrepancies are controlled as systematic uncertainties or are corrected for as factors applied to the efficiencies measured by Monte-Carlo. The event yields for the respective decays are counted by performing a binned maximum likelihood fit to the reconstructed B^+ invariant mass distributions with kinematic constraints. In LHCb the yields for decays of B^+ mesons are calculated similarly to $B^0_{(s)}$ mesons as shown in equation (3.1), and correspond to

$$N^{\mathrm{s}}_{B^+\to X} = 2 \times f_u \times \sigma(b\bar{b}) \times \mathcal{L}_{\mathrm{int}} \times \varepsilon^{\mathrm{data}}_{B^+\to X} \times \mathcal{B}_{B^+\to X} \,, \tag{3.4}$$

where f_u is the fragmentation fraction for a u quark; $\sigma(b\bar{b})$ is the cross section for the production of $b\bar{b}$ pairs at LHCb; $\mathcal{L}_{\mathrm{int}}$ is the integrated luminosity for the respective data-sets; $\varepsilon^{\mathrm{data}}$ is the total measurement efficiency of the respective decays in collision data; and $\mathcal{B}$ is the total branching fraction of those decays.

To measure the reconstruction correction factors we take the ratio of the yields for and by using Equation 3.4, this gives

$$\frac{N^{\mathrm{s}}_{B^+\to J/\psi K^+}}{N^{\mathrm{s}}_{B^+\to (J/\psi\gamma)_{\chi_{c1}} K^+}} = \frac{\varepsilon^{\mathrm{data}}_{B^+\to J/\psi K^+}}{\varepsilon^{\mathrm{data}}_{B^+\to (J/\psi\gamma)_{\chi_{c1}} K^+}} \times \frac{\mathcal{B}_{B^+\to J/\psi K^+}}{\mathcal{B}_{B^+\to \chi_{c1} K^+} \times \mathcal{B}_{\chi_{c1}\to J/\psi\gamma}} \,, \tag{3.5}$$

doing this cancels the common factors in the ratios, including the branching fraction of $J/\psi \to \mu^+\mu^-$.

The data efficiencies are unknown and estimated by using MC simulated data. The ratio of efficiencies are expected to allow for the cancellation of many discrepancies between MC simulated and real collision data due to the common particles in the final state and similar kinematics. Yet some discrepancies remain and are either corrected for or accounted for as systematic uncertainties on the final result. Controlling for all of these factors will leave only the photon reconstruction correction factor applied to $\varepsilon^{\mathrm{MC}}_{B^+\to \chi_{c1} K^+}$ as

$$\frac{\varepsilon^{\mathrm{data}}_{B^+\to J/\psi K^+}}{\varepsilon^{\mathrm{data}}_{B^+\to (J/\psi\gamma)_{\chi_{c1}} K^+}} = \frac{\varepsilon^{\mathrm{MC}}_{B^+\to J/\psi K^+}}{\varepsilon^{\mathrm{MC}}_{B^+\to (J/\psi\gamma)_{\chi_{c1}} K^+} \times \mathcal{R}^{\mathrm{corr}}_{\gamma}} \,. \tag{3.6}$$

This can be substituted into equation (3.5) $\mathcal{R}^{\text{cor}}_{\gamma}$ is the photon reconstruction correction factor measured as

$$\mathcal{R}^{\text{cor}}_{\gamma} = \frac{N^{\text{s}}_{B^+\to(J/\psi\gamma)_{\chi_{c1}}K^+}}{N^{\text{s}}_{B^+\to J/\psi K^+}} \times \frac{\varepsilon^{\text{MC}}_{B^+\to J/\psi K^+}}{\varepsilon^{\text{MC}}_{B^+\to(J/\psi\gamma)_{\chi_{c1}}K^+}} \times \frac{\mathcal{B}_{B^+\to J/\psi K^+}}{\mathcal{B}_{B^+\to\chi_{c1}K^+} \times \mathcal{B}_{\chi_{c1}\to J/\psi\gamma}} \,. \tag{3.7}$$

Similarly the π^0 reconstruction correction factor is

$$\mathcal{R}^{\text{cor}}_{\pi^0} = \frac{N^{\text{s}}_{B^+\to J/\psi K^{*+}}}{N^{\text{s}}_{B^+\to J/\psi K^+}} \times \frac{\varepsilon^{\text{MC}}_{B^+\to J/\psi K^+}}{\varepsilon^{\text{MC}}_{B^+\to J/\psi(K^+\pi^0)_{K^{*+}}}} \times \frac{\mathcal{B}_{B^+\to J/\psi K^+}}{\mathcal{B}_{B^+\to J/\psi(K^+\pi^0)_{K^{*+}}} \times \mathcal{B}_{K^{*+}\to K^+\pi^0} \times \mathcal{B}_{\pi^0\to\gamma\gamma}} \,, \tag{3.8}$$

where the branching ratios from PDG [41] are given in Table 3.2. These values give the double ratio of decay rates for $B^+ \to \chi_{c1}K^+$ and $B^+ \to J/\psi K^+$ as

$$\frac{\mathcal{B}_{B^+\to J/\psi K^+}}{\mathcal{B}_{B^+\to\chi_{c1}K^+} \times \mathcal{B}_{\chi_{c1}\to J/\psi\gamma}} = 6.27 \pm 0.36 \,. \tag{3.9}$$

This contributes an uncertainty on the overall correction factor of 5.8%. The same ratio for $B^+ \to J/\psi K^{*+}$ and $B^+ \to J/\psi K^+$ is

$$\frac{\mathcal{B}_{B^+\to J/\psi K^+}}{\mathcal{B}_{B^+\to J/\psi K^{*+}} \times \mathcal{B}_{K^{*+}\to K^+\pi^0} \times \mathcal{B}_{\pi^0\to\gamma\gamma}} = 2.17 \pm 0.13 \,, \tag{3.10}$$

corresponding to an uncertainty of 5.9% on the π^0 correction factor.

3.3. Collision data samples

This physics analysis uses data collected in the Run-1 (2011 and 2012) and Run-2 (2015 to 2018) data taking periods of the LHCb experiment. These data sets correspond to a total integrated

Table 3.3.: List of the stripping versions used for the respective data-taking periods and the corresponding centre of mass energies and integrated luminosities.

Period	Stripping	$\sqrt{s}$(TeV)	$\int \mathcal{L}$(fb^{-1})
2011	v21r1	7	1.11
2012	v21	8	2.08
2015	v24r2	13	0.33
2016	v28r2	13	1.67
2017	v29r2	13	1.71
2018	v34	13	2.19

luminosity of $\int \mathcal{L} = 9.09\,\text{fb}^{-1}$, of which $\int \mathcal{L} = 1.11\,\text{fb}^{-1}$ was taken in 2011 at $\sqrt{s} = 7\,\text{TeV}$, $\int \mathcal{L} = 2.08\,\text{fb}^{-1}$ was taken in 2012 at $\sqrt{s} = 8\,\text{TeV}$, and the remaining $\int \mathcal{L} = 5.90\,\text{fb}^{-1}$ was taken over the years from 2015 to 2018 at $\sqrt{s} = 13\,\text{TeV}$.

For each data set, referred to by their year of data-taking, the Stripping software versions used for the processing of data are given in Table 3.3. Typically in LHCb software project releases are categorised by a version numbering system vXrY, where X signifies a fundamental software version and Y is a major update to this software version. This nomenclature is used for the different Stripping versions. Each Stripping release comes with list of different sets of selection criteria called Stripping lines. The Stripping line used for all channels in this analysis is `FullDSTDiMuonJpsi2MuMuDetached` for the selections of decays involving $J/\psi \to \mu^+\mu^-$ as described previously in Section 2.2.5. The specific selection criteria contained within this line is described in Section 3.4.1. This is used for the earliest level of selections of the signal decay channels in both analyses.

3.4. Event selection of $B \to J/\psi X$ decays

In this section the criteria for selecting the signal channels and reducing backgrounds are described. The backgrounds are originating from either combinatorial backgrounds or decays of similar topology to signal, referred to as physics backgrounds. All of which include $J/\psi \to \mu^+\mu^-$ decays. The principal aim of selections is to have the highest possible efficiency of the signal modes while reducing backgrounds to a level where the uncertainty on measured signal yields is as low as possible. To minimise systematic uncertainties on the double ratios of signal yields and efficiencies, it was also necessary to keep selections as close as possible between the complementary decay modes with the same number of photons as well as between the signal modes and the normalisation channels. All differences in selections are then corrected for (Section 3.5), or are analysed as contributions to the systematic uncertainties summarised at the end of the two following analysis-specific chapters.

This section describes these selections at different stages as performed chronologically on the simulated data samples as the data efficiencies are estimated with simulation. At the level of generation, all of the Monte Carlo samples are required to be within the acceptance of the LHCb experiment, this is ensured by requiring that the azimuth angle of all tracks is within $0.005\,\text{rad} < \phi < 0.4\,\text{rad}$ and that all photons are within the ECAL by the requirements that $p_x/p_z < 0.36$ and $p_y/p_z < 0.28$. Hence the generation efficiencies should typically correspond to the acceptance of the experiment. This was then followed by the offline Stripping selections (Section 3.4.1), the online trigger selections (Section 3.4.2) and other offline selections, referred to here as preselections (Section 3.4.3). Corrections are then made to the MC in order to give the best agreement between real collision and simulated data (Section 3.5). This was a necessary

Table 3.4.: `FullDSTDiMuonJpsi2MuMuDetached` selections for all Stripping versions $J/\psi \to \mu^+\mu^-$ selections. *: Only in Stripping v21 and v21r1 for Run-1.

	Variable	Requirement
$J/\psi \to \mu^+\mu^-$	Best PV $\lvert$DLS$\rvert$	> 3
	Min. $\Delta \log \mathcal{L}_{\mu-\pi}$	> 0
	Min. $p_{\mathrm{T}}(\mu)$	$> 500\,\mathrm{MeV}$
	Max. $\chi^2_{\mathrm{tr}}/\mathrm{ndf}(\mu)$*	< 5
	$\chi^2_{\mathrm{vtx}}/\mathrm{ndf}$	< 20
	$\lvert m(\mu^+\mu^-) - m(J/\psi)\rvert$	$< 100\,\mathrm{MeV}$

prior step before performing a multivariate analysis (Section 3.6), which uses Boosted Decision Trees to combine multiple variables into one variable that maximises discrimination between chosen signal and background categories.

3.4.1. Stripping selections

The $J/\psi \to \mu^+\mu^-$ candidates were selected offline using the Stripping line `FullDSTDiMuon-Jpsi2MuMuDetached` for all decay channels. This included a set of requirements highlighted in Table 3.4. These selections were kept mostly the same for all data-sets, the only exception is a requirement that the maximum muon χ^2/ndf of the track fit ($\chi^2_{\mathrm{tr}}/\mathrm{ndf}$) was no greater than 5 that was removed in the Stripping versions used after Run-1 (*i.e.* only in Stripping v21 and v21r1). The selections that were common for Stripping versions used in both Run-1 and Run-2 included a requirement that the muon p_{T} was greater than 500 MeV and the PID requirement that the difference in the log-likelihood that they are muons or pions is greater than zero ($\Delta \log \mathcal{L}_{\mu-\pi} > 0$). There were also requirements that in the muon combination, the measured invariant mass of $J/\psi \to \mu^+\mu^-$ is within 100 MeV of the nominal J/ψ mass, the J/ψ decay vertex fit had $\chi^2_{\mathrm{vtx}}/\mathrm{ndf} < 20$ with the magnitude of the decay flight significance $\lvert$DLS$\rvert > 3$.

3.4.2. Trigger requirements

Events selected for this analysis were only required to trigger on either the single or two muon trigger algorithms at the hardware stage (*i.e.* using only the L0 trigger). This trigger has built in selection requirements that the transverse momenta of the muons and the number of hits in the SPD detector are sufficiently large. The thresholds for these quantities have been varied throughout data-taking periods. The sets of selections are categorised by their Trigger Configuration Keys (TCKs). Yet, in simulation only one TCK was used per year. All

Table 3.5.: Summary of preselections on all decay modes. In this table the selections for $J/\psi \to \mu^+\mu^-$ and $B \to J/\psi X$ were applied on all signal and normalisation channels.

	Variable	Requirement
$B \to J/\psi X$	DIRA	> 0.9995
	IP	$< 0.2\,\mu\text{m}$
	χ^2_{IP}	< 20
	$\chi^2_{\text{vtx}}/\text{ndf}$	< 10
$J/\psi \to \mu^+\mu^-$	$\chi^2_{\text{IP}}(\mu^\pm)$	> 4
	$p_{\text{T}}(\mu^\pm)$	$> 550\,\text{MeV}$

of the TCKs and their contributions in the $B^+ \to J/\psi K^+$ samples are shown in Section A.3. Therefore the trigger selections in simulation and real collision data are different and the data efficiencies are in disagreement. This difference was expected to be similar between decay channels, meaning this difference should have partially cancelled in the ratio of efficiencies. It was important to make p_{T}^{μ} and nSPD dependent corrections for each channel per year.

3.4.3. Preselections

With the principal aim of keeping the selection criteria across channels as equal as possible the general selections on the $\mu^+\mu^-$ pairs, J/ψ and B were kept the same. Selections were kept as similar as possible for the channels that have the same number of photons (*i.e.* between the two cases where $X^0 = \gamma$ and between the cases where $X^0 \to \gamma\gamma$). With these constraints on selection criteria taken into account, this section describes the full preselections as summarised in Table 5.6.

There were requirements to ensure that the endvertex of the B in $B \to J/\psi X$ was reconstructed with good compatibility with its daughters and that the B itself came from an identified primary vertex. To do this there was a lower limit on the cosine of the angle between the direction of the B in flight and the total momentum of its daughters (DIRection Angle, DIRA > 0.9995). The minimum distance of the B to the primary vertex, called the Impact Parameter (IP), has an upper limit to ensure good compatibility between the B and the PV IP $< 0.2\,\mu$m. This is along with requirements that there is good confidence in that compatibility by use of the cut $\chi^2_{\text{IP}} < 20$ for the fit between the B and the primary vertex and $\chi^2_{\text{vtx}}/\text{ndf} < 10$ for the end vertex of the B and its daughters.

For the selection of the oppositely charged muon daughters in the $J/\psi \to \mu^+\mu^-$ decays, the decay vertex fit quality was ensured by requiring that $\chi^2_{\text{IP}} > 4$ for the two muons. The two muons were also required to have a high transverse momentum greater than 550 MeV.

For all decay channels, the B candidates were reconstructed with a kinematic fit called Decay Tree Fitter (DTF) [112], making useful kinematic assumption to improve the resolution of the measured mass of the B, giving improved measurements of parameters in the mass fits. This fit constrains the B mesons to the primary vertex and sets the masses of narrow intermediary resonances to their expected mass based on the particle identity hypothesis. For all decay channels the $J/\psi \rightarrow \mu^+\mu^-$ resonance was set to the mass of the J/ψ meson at 3096.900 MeV. The X mesons were all set to their expected masses, specifically $m(K^{*+}) = 891.66$ MeV, $m(\eta) = 547.862$ MeV, $m(\eta') = 957.78$ MeV and all π^0 mesons were set to $m(\pi^0) = 134.9768$ MeV. For the $B^+ \rightarrow \chi_{c1}K^+$ decay, χ_{c1} mass is constrained to the expected mass $m(\chi_{c1}) = 3510.67$ MeV. These are the final requirements on the B candidates applied after the other selections to be used primarily in the extraction of signal yields via fits to the collision data. In the case of two photon channels with the additional resonances of $\pi^0 \rightarrow \gamma\gamma$ or $\eta \rightarrow \gamma\gamma$, there was an additional selection on the DTF $\chi^2/\text{ndf} > 2.5$ which effectively removed events that had the largest disagreement with the mass hypotheses and primary vertex positioning with respect to the B.

The rest of the preselections were analysis-specific and so are highlighted in Section 4.2.1 for the photon reconstruction efficiency study and in Section 5.2.1 for the branching ratio and η-η' mixing studies with $B^0_{(s)} \rightarrow J/\psi\eta^{(\prime)}$ decays.

3.5. Monte Carlo corrections

Monte Carlo simulations are used throughout this analysis for background yield estimation (affecting the signal yields); modelling the shapes of various decay signatures in the B mass spectrum; and calculating the MC efficiencies for all decay channels. As a key component to the measurements made in this analysis are the ratios of efficiencies determined from the simulation, it is important that the MC samples are calibrated to be in agreement with the real collision data as they do not provide a perfect description. This calibration had to be performed separately for each data-taking year to ensure that the changing event conditions are take into account. In order to achieve this an approach of reweighting distributions using Boosted Decision Trees is used, this method is named Gradient Boosted Reweighting (GBR) [113]. This is done by choosing common variables in good agreement across the signal and normalisation channels. A control channel with good statistics and a high purity signal is then used to train a reweighting machine learning algorithm for each year. This is followed by corrections made to the particle identification variables $\text{ProbNN}_{K/\pi}$ by use of calibration samples to compute the cut efficiencies directly from data.

3.5.1. Gradient Boosted Reweighting

There are distinct differences between MC and collision data so it is necessary to provide corrections to MC by applying weights to the distributions calculated from the comparison of certain variable distributions. This is done by employing a method of reweighting using Boosted Decision Trees. This method uses background-subtracted collision data for particular control modes to provide representative data distributions. This can then be compared with MC in order to correct differences between the event occupancy, kinematics and vertex fit quality of the collision data and simulation. For the photon reconstruction analysis, the normalisation channel $B^+ \to J/\psi K^+$ has high statistics and so is an ideal control channel for use with the reweighting procedure. In the case of the η-η' mixing and $B^0_{(s)} \to J/\psi \eta^{(\prime)}$ branching ratio measurements, the normalisation channel $B^0 \to J/\psi \rho^0$ has much fewer statistics due to being a more Cabibbo-suppressed channel. To compensate for this, $B^0 \to J/\psi K^{*0}$ with $K^{*0} \to K^+\pi^-$ is used as a proxy. This channel has the same number of tracks and a similar available phase space so functioned perfectly as the control channel given that no varaibles related the the charged pions or the kaon were used.

The reweighting procedure is employed to directly correct key variables which well represent the signal kinematics and vertex quantities as well as underlying event occupancy and kinematics. Through variable correlations, corrections on these key variables will cause the incidental correction of other important variables, especially those used in the next stage of selections, the inputs for the multivariate analysis. Each variables intended purposes are for the alignment of:

1. the signal kinematics: the transverse momentum of the B, $p_{\mathrm{T}}(B)$,
2. the signal vertex: the impact parameter of the J/ψ, $\mathrm{IP}(J/\psi)$,
3. the underlying event occupancy: the number of tracks and primary vertices, nTracks and nPVs,
4. the underlying event kinematics: charged cone isolation variables calculated in a comparison of the B track with all other tracks inside of a cone centred on the B track. The radius of which is $\sqrt{\phi^2 + \eta^2} = 1.80$, where ϕ is the azimuthal angle and η is the pseudorapidity around the $B^0_{(s)}$. The variables used are the total tracks' transverse momenta calculated as a sum of 3-momenta, called vPT, and the asymmetry in the z-component of the momentum between the $B^0_{(s)}$ and the other tracks in the cone calculated as $p_z^{asy} = [p_z(B) - \Sigma p_z(cone)]/[p_z(B) + \Sigma p_z(cone)]$.

These variables are also chosen for their representative use in those key purposes and for the alignment between decay channels of the MC-data discrepancies.

The weights produced in this method were used firstly in the training of the multivariate analysis described in Section 3.6. The alignment of the MVA input variable distributions gave good confidence in its performance in real data and in the corrected Monte Carlo efficiencies. The sum of the weights could then be used to calculate the efficiencies of every selection stage of the analyses after this point.

3.5.2. Particle identification corrections

In order to calibrate the efficiencies of the charged PID requirements of $\text{ProbNN}_{K/\pi}$ for kaons and pions the use of a calibration sample for data driven corrections were used. These samples were $D^{*+} \to D^0\pi^+$ where $D^0 \to K^+\pi^-$ for the kaon and π [114]. The samples are chosen for their high statistics and low background leading to the calculation of sWeights with confidence. The systematic uncertainty that arises from these sWeights are to be determined.

The efficiencies were found by estimating the signal yields for the decay with and without the PID requirement in the calibration samples. These signal yields were calculated as the sum of sWeights determined using the sPlot method [115]. Efficiencies are determined in bins of charged hadron momentum (p) and pseudorapidity (η) as well as the number of tracks in the event (nTracks). This is so that each event in the MC samples could then be assigned an efficiency determined by the location of the event in the respective bins.

These efficiencies are used as a multiplicative factor to the efficiencies estimated by the Gradient Boosted Reweighted Monte Carlo samples. Therefore the selections on the particle identification variables were removed in the estimation of the Monte Carlo efficiencies before performing this calculation.

3.6. Multivariate Analysis

The final step in selections for the isolation of signal from backgrounds as well as improving the separation of the $B^0 \to J/\psi\eta^{(\prime)}$ and $B^0_s \to J/\psi\eta^{(\prime)}$ signals was to train Boosted Decision Trees (BDTs) with the TMVA toolkit [116]. The BDTs combine a group of variables, that are well-discriminating when comparing the combinatorics and the signal channels, into one powerful discriminator.

As the primary aim of the BDTs were to remove combinatorial backgrounds, therefore the chosen sample for the background category was the side-bands of the J/ψ mass resonance defined as being $\pm 60\,\text{MeV}$ from the nominal J/ψ mass, corresponding to about 4.5 times the measured width of the J/ψ mass. This region ensures that, in this category, there was no inclusion of any signal or physics background contributions (of which all would include a J/ψ

resonance) which are typically signal-like and can reduce the background rejection power of the BDTs. The Monte Carlo samples of the respective signal and normalisation modes were used for the signal category. GBR weights were used to correct all of the distributions used in the training of the BDTs to ensure that the responses of signal MC and real signal candidates in collision data were the same.

The input variables used for the training of the BDTs were:

1. γ: The p_{T}^{γ} for the single photon final states or the minimum and maximum p_{T}^{γ} for the two-photon final states.
2. B: p_{T}, $\chi^2_{\mathrm{vtx}}/\mathrm{ndf}$, the smallest $\Delta\chi^2$ of the decay fit when adding another track candidate to the fit, the number of vertex fits with $\chi^2 < 9$ when performing a swap in track candidates, DIRA IP.
3. J/ψ: p_{T} and IP.
4. $\mu^{\pm}$: minimum p_{T} and maximum IP.
5. Charged cone isolation: the multiplicities within the cone normalised by the number of photons in the event, p_z^{asy}, the p_{T} of the vector sum of all tracks in the cone, and the differences in the pseudorapidities $\Delta\eta = \eta^{B_s^0} - \eta^{cone}$ and polar angles $\Delta\phi = \phi^{B_s^0} - \phi^{cone}$.

There was good separation of the two categories for the various distributions. The combination of information from the input variables led to BDT responses with clear separation of signal and background that is much more effective than any of the inputs alone. The determination of the BDT cuts were done with different aims for each analysis so are described separately in Chapters 4 and 5.

3.7. Data fitting strategy

A binned maximum likelihood fit is used to describe histograms of the Decay Tree Fitted invariant B mass distributions using probability density functions PDFs. The integral of the signal PDF determined the signal yields. This was accomplished using the package for mathematical and statistical methods for data modelling called RooFit [117], which is a toolkit for the ROOT analysis framework [118]. The two analyses had signal yields that greatly differed in statistics. The $B_s^0 \to J/\psi\eta^{(\prime)}$ yields were of order of a thousand events in all of Run 2, whereas $B^+ \to J/\psi K^+$ had a yield of up to the order of one million for each of the last three years of data-taking. This meant that the signal PDFs that were appropriate for the smaller yield channels were not able to well describe higher yield channels. Therefore two different signal PDFs were used for the two analyses.

3.7.1. Fit models for signal

The peaking structures of signal channels in their B DTF mass distributions are modelled using a double-sided Crystal Ball function (introduced in [119]) for the lower yield $B^0_{(s)} \to J/\psi\eta^{(\prime)}$ and $B^0 \to J/\psi\rho^0$ decays. The Crystal Ball function depends on four parameters, two of which are related to the energy calibration and resolution (μ and σ) and the other two can be referred to as tail-shape parameters (a and n). a functions as a threshold parameter where the tail of the distribution becomes modelled by a power-law. The PDF as a function of x is given as

$$f(x|\mu,\sigma,a,n) = \begin{cases} Ae^{-\frac{1}{2}(\frac{\mu-x}{\sigma})^2} & \text{for } a \geq \frac{\mu-x}{\sigma} \\ A\frac{\left(\frac{n}{a}\right)^n e^{-\frac{1}{2}a^2}}{\left(\frac{\mu-x}{\sigma}+\frac{n}{a}-a\right)^n} & \text{for } a < \frac{\mu-x}{\sigma}, \end{cases}$$

where

$$A^{-1} = \sigma\left(\frac{n}{a}\frac{1}{n-1}e^{-\frac{1}{2}a^2} + \sqrt{\frac{\pi}{2}}\left[1+\text{erf}\left(\frac{a}{\sqrt{2}}\right)\right]\right). \tag{3.11}$$

This gives a shape with a Gaussian core and one non-Gaussian tail, meaning that for the measurement of channels with non-Gaussian tails on both sides of the peak, there must be the use of two of these functions added together with equal event population. For modelling the tail of the left-hand side of the distribution, the parameter a is set to a positive number and for the right-hand side it is set to negative number.

For dealing with the larger yields of the channels in the photon reconstruction analysis, the more sophisticated double-sided Hypatia function (based on [120]) was used. This is a function that extends the Crystal Ball to better fit the non-Gaussian core of higher yield decays. This then treats the resolution as a generalised hyperbolic instead of Gaussian, giving a core function of

$$G(x|\mu,\sigma,\lambda,\zeta,\beta) \equiv \left((x-\mu)^2 + A_\lambda^2(\zeta)\sigma^2\right)^{\frac{1}{2}\lambda-\frac{1}{4}} e^{\beta(x-\mu)} K_{\lambda-\frac{1}{2}}\left(\zeta\sqrt{1+\left(\frac{x-\mu}{A_\lambda(\zeta)\sigma}\right)^2}\right), \tag{3.12}$$

where

$$A_\lambda^2(\zeta) = \frac{\zeta K_\lambda(\zeta)}{K_{\lambda+1}(\zeta)} \tag{3.13}$$

and $K_\lambda(\zeta)$ are the special Bessel functions of the third kind. The full PDF of the double-sided Hypatia function uses this core with two power-law tails using threshold and power-law parameters a_l, n_l, a_r and n_r.

$$f(x|\mu,\sigma,\lambda,\zeta,\beta,a_l,n_l,a_r,n_r) = \begin{cases} \frac{G(\mu-a_l\sigma,\mu,\sigma,\lambda,\zeta,\beta)}{\left(1-\frac{x}{n_l G(\ldots)/G'(\ldots)-a_l\sigma}\right)^{n_l}} & \text{if } a_l < \frac{\mu-x}{\sigma} \\ G(x,\mu,\sigma,\lambda,\zeta,\beta) & \text{otherwise} \\ \frac{G(\mu+a_r\sigma,\mu,\sigma,\lambda,\zeta,\beta)}{\left(1-\frac{x}{-n_r G(\ldots)/G'(\ldots)-a_r\sigma}\right)^{n_r}} & \text{if } -a_r > \frac{\mu-x}{\sigma}. \end{cases} \tag{3.14}$$

In both analyses the parameters of the tail-shape ($a_{L,R}$, $n_{L,R}$) and, in the Hypatia case, the core-shape parameters (λ, ζ and β) are determined by fits of the models to Monte Carlo data samples. The determined parameter values are then fixed as constants in the fits to real collision data. This leaves the different μ parameters in different peaking structures of the same mass distribution to be shifted by a common calibration from MC to the true distribution means and their resolutions σ to be scaled, by a common multiplicative factor, to the true resolutions achieved by the detector. This means only two free parameters associated with the peaking structures of distributions (other than the data yields) were typically required in the fits to collision data.

3.7.2. Treatment of backgrounds

A common background found in all data samples is the combinatorial background, the reconstruction of events with one or more particle originating from the underlying event, *i.e.* not the decay of interest. To account for this background every collision data fit included an exponential model with a free slope parameter that can typically be well measured with a high-mass side-band that is clear of any peaking structures.

Physics backgrounds, if their shape permit, were fit with the same PDF as the signal, otherwise a better fitting model was used. Therefore the overall fitting strategy can be kept the same: shape-parameters fixed to values obtained with MC with the same calibration shifts and resolution scaling factors applied as those used for the signal. The yields of backgrounds N^b were constrained relative to the signal yields N^s, where the expected yield was calculated using the scaling factor

$$f = \frac{N^b}{N^s} = \frac{\varepsilon^b}{\varepsilon^s} \times \frac{\mathcal{B}^b}{\mathcal{B}^s}, \tag{3.15}$$

where ε^b and ε^s are the MC efficiencies of the background and signal respectively; and $\mathcal{B}^b$ and $\mathcal{B}^s$ are the product total of the current PDG averaged branching ratios [41] of the background and signal decays. The background yields measured in real collision data were constrained using a Gaussian function with the expected yield ratio of equation (3.15) set as the Gaussian mean and the Gaussian width as the propagated uncertainty from the efficiencies and branching ratios used in the calculation.

3.7.3. Signal yield measurement

In the combined model used to fit the data, typically, the parameter of interest were the signal yields. The other free parameters would therefore be the energy calibration and resolution, the exponential slope of the combinatorial background, and the Gaussian-constrained yields of the various peaking backgrounds. The uncertainty from the fit is therefore dominated by, not just the statistics of the signal decay, but also from the quality of the fit and the variation of the other parameters in the fit.

Chapter 4.

Photon Reconstruction Efficiency

This chapter gives the specifics of the analysis to determine the reconstruction efficiencies for both individual photons produced radiatively and via $\pi^0 \to \gamma\gamma$ decays. These efficiencies are then used to calculate year-by-year correction factors to Monte-Carlo efficiencies involving photons that could then be applied to the result of $\mathcal{B}\,(B^0_{(s)} \to J/\psi\eta^{(\prime)})$, with final state photons, normalised to $\mathcal{B}\,(B^0 \to J/\psi\rho^0)$, a channel with no photons in the final state. The overall analysis strategy was given in the previous chapter. This chapter includes the samples used (Section 4.1), all of the signal selections unique to this analysis (Section 4.2), corrections to Monte Carlo (Section 4.3), the specifics of the MVA in this case(Section 4.4), mass fits (Section 4.5) used to extract the signal yields and the corrections to the MC efficiencies of reconstructing photons (Section 4.6).

4.1. Simulation samples

Monte-Carlo samples were used for $B^+ \to J/\psi K^+$, $B^+ \to \chi_{c1}K^+$, $B^+ \to J/\psi K^{*+}$ and $B^0 \to J/\psi K^{*0}$. It was important that the simulation conditions of these Monte Carlo samples were kept the same to ensure that any significant biases in simulation would cancel in the ratios of Monte Carlo efficiencies as shown in the Equations 3.7 and 3.8. This was ensured by using

Table 4.1.: Summary of generator level selections on the two signal decay modes for the photon reconstruction study. *: applies only to $B^+ \to \chi_{c1}K^+$.

Particle	Variable	Requirement
$\mu^\pm$	p_{T}	$> 500\,\mathrm{MeV}$
	p	$> 6\,\mathrm{GeV}$*
K^+	$p_{\mathrm{T}}(K^+)$	$> 150\,\mathrm{MeV}$
γ	$p_{\mathrm{T}}(\gamma)$	$> 150\,\mathrm{MeV}$
J/ψ	$p_{\mathrm{T}}(J/\psi)$	$> 500\,\mathrm{MeV}$

Table 4.2.: List of the stripping versions used for each Monte Carlo signal and normalisation data-set and the corresponding number of events generated.

Decay Channel	Event type	Year	Magnet Polarity	Stripping	N(events)
$B^+ \to \chi_{c1} K^+$	12243204	2011	Up	v21r1	506371
		2011	Down	v21r1	509254
		2012	Up	v21	963741
		2012	Down	v21	1038948
		2016	Up	v28r2	1464803
		2016	Down	v28r2	1459632
		2017	Up	v29r2	1572574
		2017	Down	v29r2	1687717
		2018	Up	v34	1854499
		2018	Down	v34	1868496
$B^+ \to J/\psi K^{*+}$	12143403	2011	Up	v21r1	509170
		2011	Down	v21r1	600109
		2012	Up	v21	915330
		2012	Down	v21	923901
		2016	Up	v28r2	1003095
		2016	Down	v28r2	1092842
		2017	Up	v29r2	1000868
		2017	Down	v29r2	1081467
		2018	Up	v34	1002217
		2018	Down	v34	1002619
$B^+ \to J/\psi K^+$	12143001	2011	Up	v21r1	5026583
		2011	Down	v21r1	5006996
		2012	Up	v21	5001199
		2012	Down	v21	5002830
		2016	Up	v28r2	4993938
		2016	Down	v28r2	4960561
		2017	Up	v29r2	4997838
		2017	Down	v29r2	5008348
		2018	Up	v34	5005409
		2018	Down	v34	5009929

Table 4.3.: List of the stripping versions used for each Monte Carlo control and background data-set and the corresponding number of events generated.

Decay Channel	Event type	Year	Magnet Polarity	Stripping	N(events)
$B^0 \to J/\psi K^{*0}$	11144001	2011	Up	v21r1	5031100
where $K^{*0} \to K^+\pi^-$		2011	Down	v21r1	5001989
		2012	Up	v21	5000741
		2012	Down	v21	5003370
		2016	Up	v28r2	5064565
		2016	Down	v28r2	5008395
		2017	Up	v29r2	5003787
		2017	Down	v29r2	5007707
		2018	Up	v34	5000153
		2018	Down	v34	5000010
$B^+ \to J/\psi K_1^+$	12143440	2012	Up	v21	1003782
		2012	Down	v21	1006999
		2016	Up	v28r2	2019437
		2016	Down	v28r2	1987778

samples of the most up-to-date simulation software version. A summary of the signal and normalisation channels and their statistics is given in Table 4.2 and the control channel along with a background which appears in the DTF B mass spectrum of $B^+ \to J/\psi K^{*+}$ is given in Table 4.3.

4.2. Event selection

At the level of Monte-Carlo generation, all samples had selections applied to ensure that the events generated were in the acceptance of LHCb. As $B^+ \to \chi_{c1} K^+$ and $B^+ \to J/\psi K^{*+}$ are decays with large photon (or neutral pion for $B^+ \to J/\psi K^{*+}$) combinatorial backgrounds, they required tighter than typical selections at the point of generation in order to ensure the samples contained decays with well-reconstructed tracks at the expense of statistics. These selections are summarised in Table 4.1. This was aimed at improving sample statistics by a factor of ~ 2 for the same expenditure of computer resources. These same selections were applied across all channels for both real and simulated data. These tight cuts were applied to the true variable values for the simulated data and to the variable values determined by reconstruction for the real collision data samples. The selections required for the decay $J/\psi \to \mu^+\mu^-$ included a lower bound on the transverse momentum of $p_{\mathrm{T}} > 500\,\mathrm{MeV}$ for the J/ψ and the muons, whereas the K^+ and photons were required to have a $p_{\mathrm{T}} > 150\,\mathrm{MeV}$. In the case of the $B^+ \to \chi_{c1}K^+$ samples, the muons also had a lower bound on the total momentum of $p > 6\,\mathrm{GeV}$.

4.2.1. Preselection

With the selections of B candidates and $J/\psi \to \mu^+\mu^-$ described in Section 3.4 this section focuses on the analysis-specific selections. These selections include the selections on the K^+ for all decay channels, the single photon and $\chi_{c1} \to J/\psi\gamma$ resonance selections for $B^+ \to \chi_{c1}K^+$, the selections of the $\pi^0 \to \gamma\gamma$ and $K^{*+} \to \pi^+\pi^0$ for $B^+ \to J/\psi K^{*+}$, and the π^- of $K^{*0} \to K^+\pi^-$ selections of the control mode $B^0 \to J/\psi K^{*0}$. All particles are selected using stripping containers with implicit selection criteria summarised in Table 4.4. The summary of the preselections described in this section are given in Tables 4.5 (PID and p_{T} selections) and 4.6 (reconstructed mass requirements).

Kaons were selected using stripping container `StdLooseKaons`. In order to ensure that the kaon is correctly identified, an Artificial Neural Network (ANN) designed to determine particle identification (PID) probabilities was used. These were ProbNN_K and ProbNN_π for the charged kaon and pion respectively. The requirements applied are $\mathrm{ProbNN}_K > 0.1$ and $\mathrm{ProbNN}_K(1 - \mathrm{ProbNN}_\pi) > 0.2$. For $B^0 \to J/\psi K^{*0}$ charged pions were selected using similar selections with `StdLoosePions` and the inverse of the kaon PID selections.

For the $B^+ \to J/\psi K^{*+}$ and $B^+ \to \chi_{c1}K^+$ decays, the stripping container `StdLooseAllPhotons` selected the photon candidates. The transverse momentum requirement of $p_{\mathrm{T}}^{\gamma} > 500\,\mathrm{MeV}$ was applied to the single photon in $\chi_{c1} \to J/\psi\gamma$ to decrease the combinatorial background. To identify the photons and to separate them from neutral hadrons another ANN based variable was used, isNotH, with a common cut of isNotH > 0.05. The invariant mass of the decay $\chi_{c1} \to J/\psi\gamma$ was required to be within approximately $3\sigma = 90\,\mathrm{MeV}$ of the nominal χ_{c1} mass. For resolved π^0 (using stripping containers `StdLoosePi02gg`) in $B^+ \to J/\psi K^{*+}$ decays with $K^{*+} \to K^+\pi^0$ and $\pi^0 \to \gamma\gamma$ cuts to p_{T} need to be tight enough for the π^0 to be well identified with $p_{\mathrm{T}} > 1000\,\mathrm{MeV}$. The K^+ and π^0 are required to have a invariant mass compatible with a K^{*+} within 75 MeV of the expected mass of 891.66 MeV [41].

4.2.2. Mass vetoes

A significant background for $B^+ \to \chi_{c1}K^+$, $B^+ \to J/\psi K^{*+}$ and $B^0 \to J/\psi K^{*0}$ is the $B^+ \to J/\psi K^+$ where the J/ψ and K^+ are combined with photons from the underlying event. These backgrounds form a large structure in the high mass side-band of the B mass distributions of the signal modes. For $B^+ \to \chi_{c1}K^+$ the fit was performed in a narrow range so this background does not appear in the distribution. For $B^+ \to J/\psi K^{*+}$ and $B^0 \to J/\psi K^{*0}$ the DTF 4-momenta

Table 4.4.: Summary of Stripping containers used for the selection of all the particle candidates in the decay modes of interest.

Stripping container	Variable	Requirement
`StdLooseKaons`	$p_{\mathrm{T}}(K^+)$	$> 250\,\mathrm{MeV}$
	χ^2_{IP}	> 4
`StdLoosePions`	$p_{\mathrm{T}}(K^+)$	$> 250\,\mathrm{MeV}$
	χ^2_{IP}	> 4
`StdLoosePhotons`	$p_{\mathrm{T}}(\gamma)$	$> 200\,\mathrm{MeV}$
`StdLoosePi02gg`	$\lvert m(\pi^0) - m(\gamma\gamma)\rvert$	$< 60\,\mathrm{MeV}$

Table 4.5.: Summary of preselections on all decay modes for the photon reconstruction study. In this table these selections are in addition to those described in Section 3.4

	Variable	Requirement
K^+	$p_{\mathrm{T}}(K^+)$	$> 150\,\mathrm{MeV}$
	$\mathrm{ProbNN}_K(1-\mathrm{ProbNN}_\pi)$	> 0.2
γ in $\chi_{c1} \to J/\psi\gamma$	$p_{\mathrm{T}}(\gamma)$	$> 500\,\mathrm{MeV}$
	IsNotH	> 0.05
$\pi^0 \to \gamma\gamma$	$p_{\mathrm{T}}(\gamma)$	$> 200\,\mathrm{MeV}$
	IsNotH	> 0.05
	$p_{\mathrm{T}}(\pi^0)$	$> 1\,\mathrm{GeV}$
π^- in $K^{*0} \to K^+\pi^-$	$\mathrm{ProbNN}_\pi(1-\mathrm{ProbNN}_K)$	> 0.2

Table 4.6.: Summary of mass windows on all decay modes, counted as preselections.

Channel	Mass range	
$B^+ \to J/\psi K^+$	$m(J/\psi K^+)$	$\in [5200, 5500]\,\mathrm{MeV}$
$B^+ \to \chi_{c1} K^+$	$m(J/\psi K^+\gamma)$	$\in [5200, 5400]\,\mathrm{MeV}$
$\chi_{c1} \to J/\psi\gamma$	$\lvert m(J/\psi\gamma) - m(\chi_{c1})\rvert$	$< 90\,\mathrm{MeV}$
$B^+ \to J/\psi K^{*+}$	$m(J/\psi K^+\gamma\gamma)$	$\in [5000, 6000]\,\mathrm{MeV}$
$K^{*+} \to K^+\pi^0$	$\lvert m(K^+\gamma\gamma) - m(K^{*+})\rvert$	$< 75\,\mathrm{MeV}$
$B^0 \to J/\psi K^{*0}$	$m(J/\psi K^+\pi^-)$	$\in [5200, 5600]\,\mathrm{MeV}$
$K^{*0} \to K^+\pi^-$	$\lvert m(K^+\pi^-) - K^{*0}\rvert$	$< 75\,\mathrm{MeV}$

of the muons and kaon are used to calculate the $J/\psi K^+$ invariant mass allowing the rejection of events within 30 MeV of the B^+ mass (5280 MeV), effectively removing the background.

4.3. Monte Carlo corrections

4.3.1. Gradient Boosted Reweighting

As described in Section 3.5.1, Gradient Boosted Decision Trees were employed to create event-by-event weights that were defined by the matching of distributions with similar shapes in all modes, as shown in Figure 4.2. This matching was performed using $B^+ \to J/\psi K^+$ background-subtracted collision data (using sPlot, see Figure 4.1) and Monte Carlo simulation per data-taking year due to this decay mode having a good signal purity and statistics. The performance of the weights in improving the training variables directly is shown in Figure 4.3, leading to excellent agreement between Monte Carlo and real collision data. As this is performed before the training of the Boosted Decision Trees (as described in Section 3.6), the performance of the weights needed to be validated for the variable distributions used in that training. Therefore these distributions are also checked before (Figure 4.4) and after (Figure 4.5) applying these weights.

All but one of the variables reach excellent agreement, the only exception is the charged cone multiplicities normalised to the number of photons in the event (labelled cc multiplicities/nPhotons in the figures). This is due to the number of photons in the event being well described in MC before correcting the number of tracks (nTracks). Therefore, as the occupancy variables are typically correlated, the correction of one poorly described occupancy variable will degrade the MC to real data agreement of a better described variable. As this is a small effect, and considering the improvement achieved in the other fourteen BDT input variables, this reweighting strategy does improve the expected reliability of the Monte Carlo efficiencies for the BDT. This is also in parallel with the improvement of the number of tracks, which is an

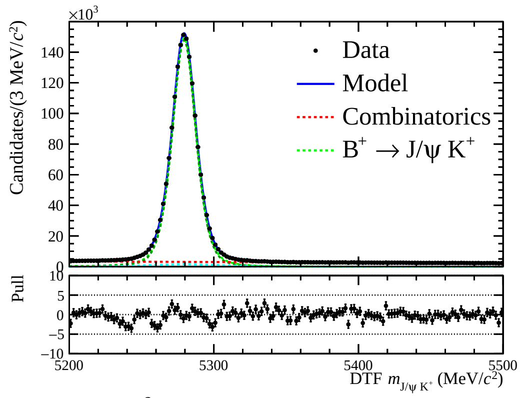

Figure 4.1.: Fit to the decay tree fitted B^0 mass distribution of the collision data sample of the reconstructed signal $B^0 \to J/\psi K^{*0}$ for 2018. This is the fit that was used in the sPlotting [115] for the background-subtracted data used in the training of the Gradient Boosted Reweighter.

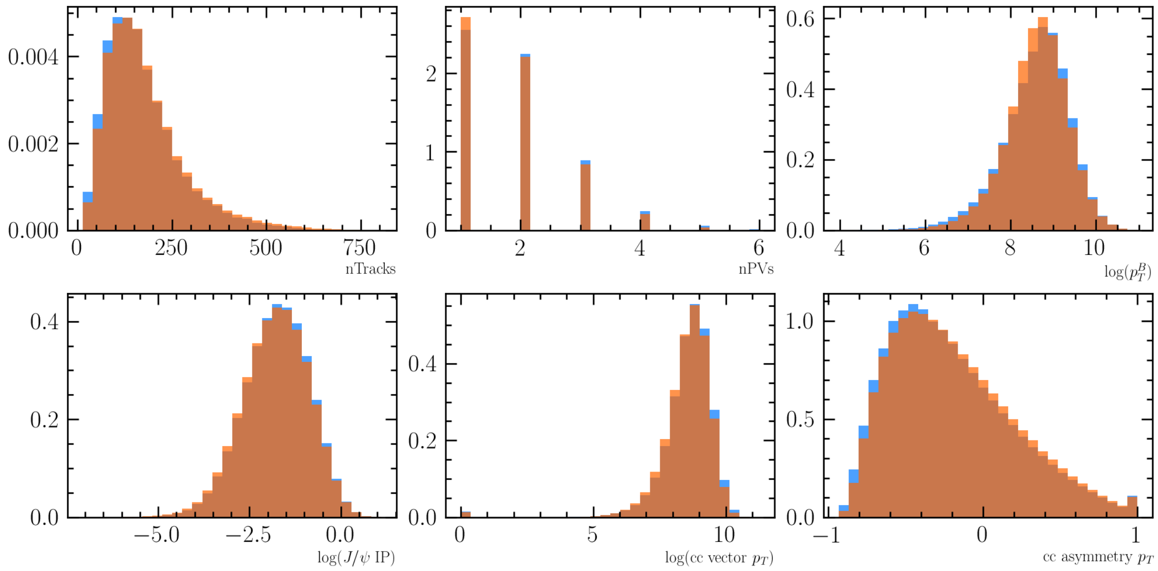

Figure 4.2.: The distributions of the input variables and expressions used for the training of the Gradient Boosted Reweighter. The orange distribution is the background-subtracted $B^+ \to J/\psi K^+$ 2018 collision data used as a target. The blue distribution is the original $B^+ \to J/\psi K^+$ 2018 MC data.

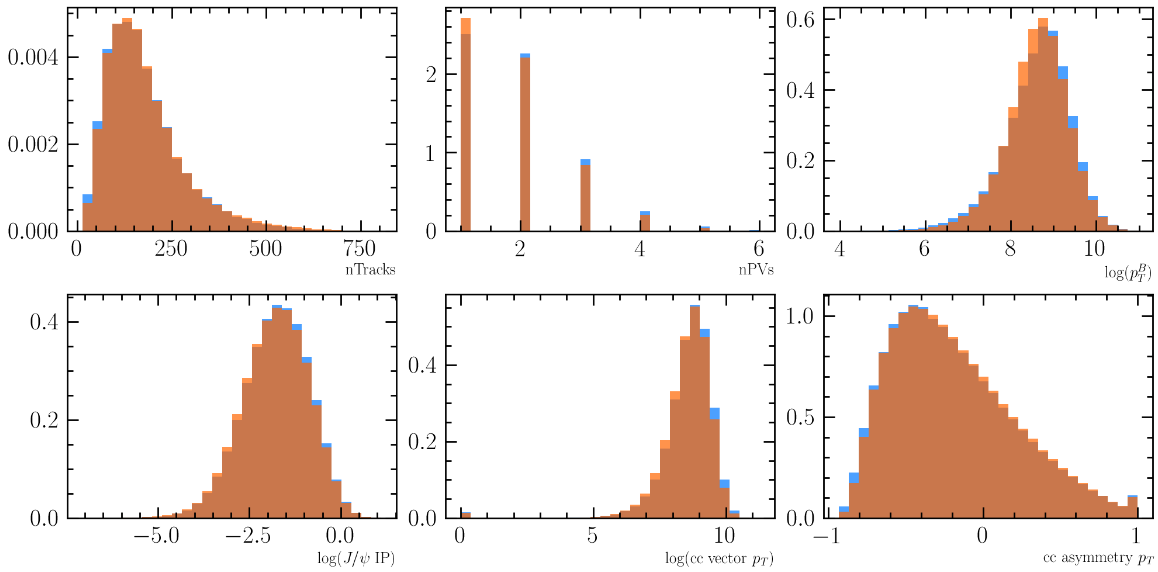

Figure 4.3.: The distributions of the input variables and expressions used for the training of the Gradient Boosted Reweighter. The orange distribution is the background-subtracted $B^+ \to J/\psi K^+$ 2018 collision data used as a target. The blue distribution is the $B^+ \to J/\psi K^+$ 2018 MC data after applying the event-by-event weights that were calculated by the reweighter.

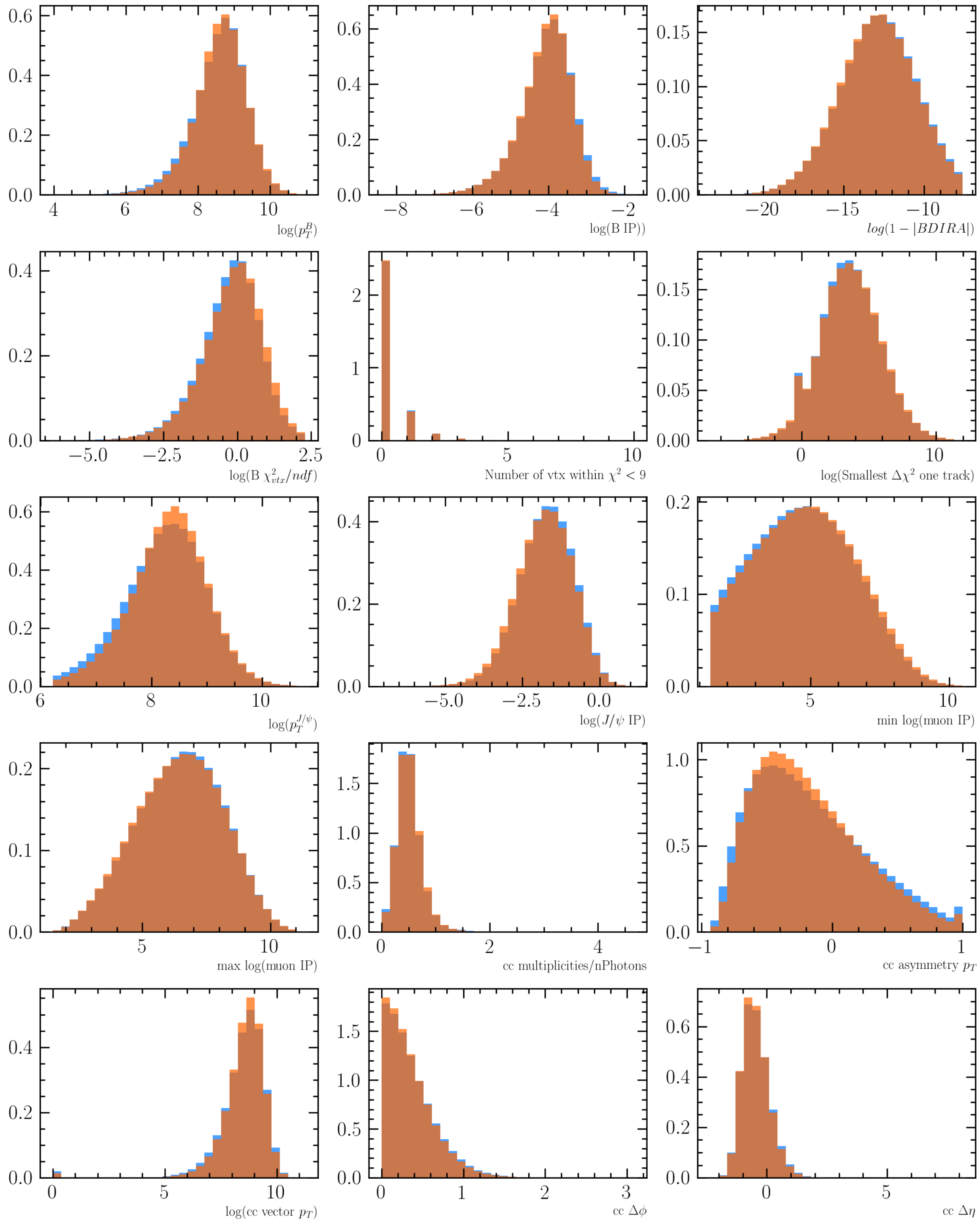

Figure 4.4.: The distributions of the variables and expressions used in the training of the MVA (omitting those unavailable to $B^+ \to J/\psi K^+$ decays) as well as occupancy variables. The orange distribution is the background-subtracted $B^+ \to J/\psi K^+$ 2018 collision data used as a target. The blue distribution is the original $B^+ \to J/\psi K^+$ 2018 MC data.

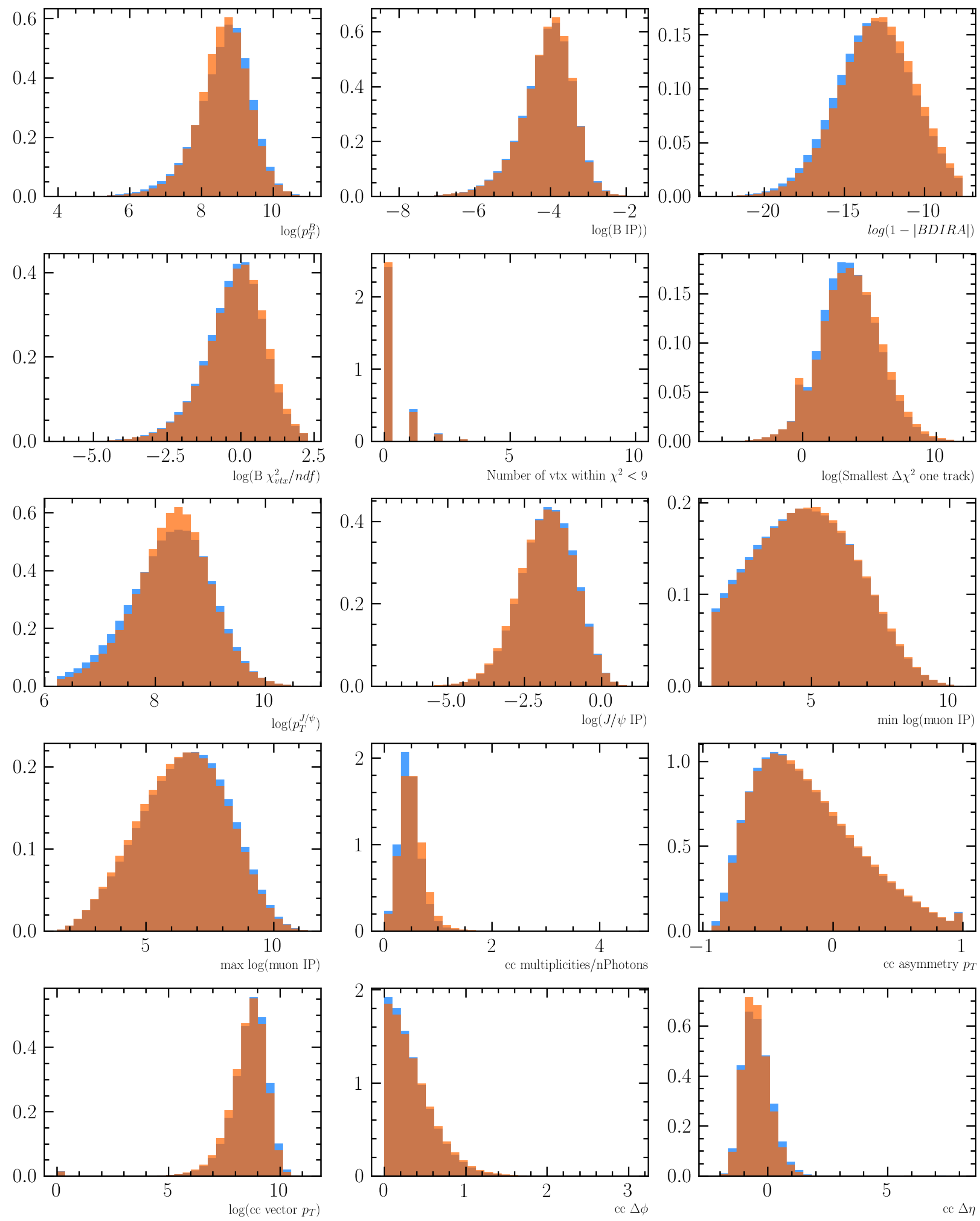

Figure 4.5.: The distributions of the variables and expressions used in the training of the MVA (omitting those unavailable to $B^+ \to J/\psi K^+$ decays) as well as occupancy variables. The orange distribution is the background-subtracted $B^+ \to J/\psi K^+$ 2018 collision data used as a target. The blue distribution is the $B^+ \to J/\psi K^+$ 2018 MC data after applying weights calculated by the reweighter.

samples to allow for corrections to all reconstruction and selection efficiencies in a consistent way.

4.3.2. Corrections to the underlying event photon efficiencies

Table 4.7.: The correction factors to the underlying event photon background used in the DTF B invariant mass fits to collision data.

Year	$\mathcal{R}_{\gamma}^{bkg}/\%$	$\mathcal{R}_{\pi^0}^{bkg}/\%$
2011	90.8 ± 0.5	62.5 ± 2.1
2012	89.32 ± 0.36	57.9 ± 1.3
2016	80.05 ± 0.26	61.4 ± 1.1
2017	80.35 ± 0.27	62.1 ± 1.1
2018	81.76 ± 0.27	63.4 ± 1.1

The most significant background in the B^+ DTF mass distributions of the signal channels $B^+ \to J/\psi K^{*+}$ and $B^+ \to \chi_{c1} K^+$ were originating from incorrectly reconstructed signal decays with the true signal tracks and swapping a number of true signal photons with underlying event photons that do not originate from the signal decay. This kind of background needed to be calibrated for a better understanding of its yield. This is especially important as this background peaked at the mean mass of the B^+, and so the measured signal yields were particularly sensitive to this backgrounds yield. Therefore a study of the reconstruction and identification efficiencies for these photons was necessary. To do this, the $B^+ \to J/\psi K^+$ normalisation channel was reconstructed and selected as the two signal channels to give the rate of combining signal tracks with underlying event photons. This gave the perfect data set for the study of photons from the underlying event that pass $B^+ \to J/\psi K^{*+}$ and $B^+ \to \chi_{c1} K^+$ selections because all of the tracks originate from the large $B^+ \to J/\psi K^+$ data sets so the only effects that do not cancel are from the photons and the selections of the signal channels.

To find these corrections, the yields of fits of $J/\psi K^+$ reconstructed using the DTF 4-vectors were found. Therefore the determination of the $B^+ \to J/\psi K^+$ yield was done using the data sets of the signal channels and the $B^+ \to J/\psi K^+$ data sample. The ratio of the yields of $B^+ \to J/\psi K^+$ reconstructed and selected as the two signal channels and as $B^+ \to J/\psi K^+$ gave the rate at which signal tracks were combined with underlying event photons in real data. Taking the ratio of Monte Carlo efficiencies found using the $B^+ \to J/\psi K^+$ sample reconstructed and selected as $B^+ \to \chi_{c1} K^+$ or $B^+ \to J/\psi K^{*+}$ and as $B^+ \to J/\psi K^+$ gave that rate in Monte Carlo. An example of these fits is given in Figure 4.6. The ratio of these rates in real data and in MC gave a correction factor for the yields of the mis-reconstructed backgrounds which were determined from MC. These correction factors are shown in table Table 4.7 In the final fits

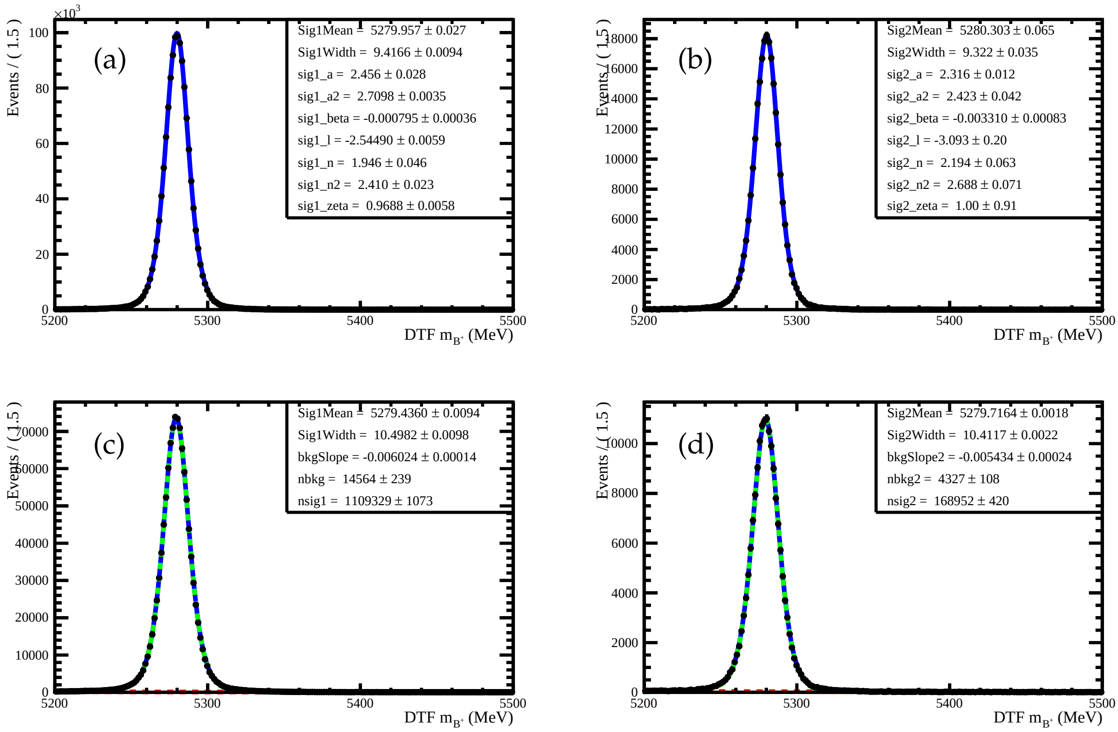

Figure 4.6.: The fits of the DTF $J/\psi K^+$ mass used to produce the corrections for the photon mis-reconstructed background. The fits of the 2018 MC samples of $B^+ \to J/\psi K^+$ reconstructed and selected as a) $B^+ \to J/\psi K^+$ and b) $B^+ \to \chi_{c1} K^+$. The fits of the 2018 real data samples of $B^+ \to J/\psi K^+$ reconstructed and selected as c) $B^+ \to J/\psi K^+$ and d) $B^+ \to \chi_{c1} K^+$. The fits in (a) and (b) gave the Hypatia shape parameters of (c) and (d).

to real data, this background is then Gaussian constrained with the corrected expected yield relative to the signal peaks as the central value, and the combined statistical uncertainty of these corrections and of the Monte Carlo samples used to estimate the efficiency of these backgrounds as the Gaussian width.

4.3.3. Particle identification corrections

In Section 3.5.2 the method of determining the real data efficiencies for the kaon particle identification selections of $\text{ProbNN}_K > 0.1$ and $\text{ProbNN}_K(1 - \text{ProbNN}_\pi) > 0.2$ is described. The statistical uncertainty of the calibration samples are quoted with the efficiencies given in Section 4.6. Other systematic uncertainties of this method come from the binning of the samples. This includes the compatibility between the Monte Carlo and calibration samples, and negative sWeights in the calibration samples due to low statistics in one bin. These are all shown in Section 4.7.2.

4.3.4. L0 trigger efficiency corrections

Table 4.8.: The TIS and TOS efficiencies of the $B^+ \to J/\psi K^+$ simulated and real collision data reweighted to the muon kinematics and event occupancy of the signal and normalisation channels.

Channel	Year	$\varepsilon^{MC}_{TISTOS}/\%$	$\varepsilon^{RD}_{TISTOS}/\%$	$\frac{\varepsilon^{RD}_{TISTOS}}{\varepsilon^{MC}_{TISTOS}}/\%$
$B^+ \to J/\psi K^+$	2011	91.92 ± 0.09	91.72 ± 0.28	99.78 ± 0.32
	2012	88.05 ± 0.10	88.96 ± 0.18	101.03 ± 0.23
	2016	85.93 ± 0.09	85.79 ± 0.14	99.83 ± 0.20
	2017	89.89 ± 0.09	86.43 ± 0.14	96.15 ± 0.19
	2018	86.00 ± 0.10	83.03 ± 0.13	96.55 ± 0.19
$B^+ \to \chi_{c1} K^+$	2011	93.71 ± 0.09	93.30 ± 0.25	99.57 ± 0.28
	2012	91.07 ± 0.10	91.50 ± 0.16	100.47 ± 0.21
	2016	88.99 ± 0.09	87.56 ± 0.12	98.39 ± 0.17
	2017	91.82 ± 0.12	88.27 ± 0.12	96.13 ± 0.19
	2018	89.18 ± 0.10	86.02 ± 0.12	96.45 ± 0.17
$B^+ \to J/\psi K^{*+}$	2011	92.11 ± 0.09	91.92 ± 0.25	99.80 ± 0.29
	2012	88.60 ± 0.10	89.27 ± 0.16	100.75 ± 0.21
	2016	86.73 ± 0.09	85.98 ± 0.12	99.13 ± 0.17
	2017	90.24 ± 0.12	86.50 ± 0.12	95.85 ± 0.19
	2018	86.81 ± 0.10	83.57 ± 0.11	96.27 ± 0.17

Table 4.9.: The correction factors to the L0 trigger efficiency ratios used in the calculation of the correction factors $\mathcal{R}_\gamma$ and $\mathcal{R}_{\pi^0}$.

Year	$\mathcal{R}_\gamma/\%$	$\mathcal{R}_{\pi^0}/\%$
2011	100.22 ± 0.43	99.98 ± 0.43
2012	100.57 ± 0.31	100.28 ± 0.32
2016	101.47 ± 0.27	100.71 ± 0.27
2017	100.02 ± 0.28	100.31 ± 0.28
2018	100.10 ± 0.26	100.29 ± 0.26

The trigger configurations of each real collision data set changes over the data-taking periods with the simulation kept constant. This leads to small differences between the Monte Carlo efficiencies and the real data efficiencies. To provide precise corrections for these differences the $B^+ \to J/\psi K^+$ data samples were reweighted using GBR to align the $J/\psi \to \mu^+\mu^-$ kinematics and the overall event occupancy with that of the signal channels. Since the trigger requirements involve selections on just the transverse momenta of the muons and the number of SPD hits, the GBR was trained on these variables. With weights that match these quantities between $B^+ \to J/\psi K^+$ and the signal channels it is possible to estimate the trigger efficiencies more precisely, exploiting the larger statistics of the $B^+ \to J/\psi K^+$ samples. The method used to estimate these efficiencies was the TISTOS method [121] which calculates the trigger efficiency as

$$\varepsilon_{TISTOS} = \frac{N_{TIS\&TOS}}{N_{TIS\&\overline{TOS}} + N_{TIS\&TOS}} \tag{4.1}$$

where $N_{TIS\&TOS}$ is the number of events that pass both the selection highlighted in Section 3.4.2 (TOS) and also a global L0 requirement that accepts any hardware-level triggering independently of signal (TIS). This calculation is performed with both real data and Monte Carlo to give the efficiencies and ratio of efficiencies in Table 4.8. As the correction factors for photon and π^0 reconstruction were a double ratio of signal yields and efficiencies, then the respective double ratio of the $B^+ \to J/\psi K^+$ efficiency ratio over that of the $B^+ \to \chi_{c1} K^+$ and $B^+ \to J/\psi K^{*+}$ would give the L0 trigger efficiency corrections. The resulting corrections to final result are given in Table 4.9. The uncertainty on these corrections is assigned as a systematic uncertainty on the final result.

4.4. Multivariate Analysis

The methodology of the training of the Boosted Decision Trees is described in Section 3.6, with all of the input variables corrected with the GBR technique. Individual BDTs were trained for the signal and normalisation channels ($B^+ \to \chi_{c1} K^+$, $B^+ \to J/\psi K^{*+}$ and $B^+ \to J/\psi K^+$), their common input variables in the signal and background categories for 2018 data are shown in Figures 4.7, 4.8 and 4.9, while the photon p_{T} inputs for the signal modes are shown in Figures 4.10 and 4.11. Individually these variables gave good separation between the two categories making them ideal input variables for a powerful discriminator. The other positive aspect of using variables only related to the B, J/ψ, muons and the underlying event is that there is strong agreement of these distributions between the signal and normalisation channels. This means, as targeted, there was a minimisation of differences in their selections and greater confidence in the ratio of their Monte Carlo efficiencies. The responses of the BDT for the signal and background category is shown in Figure 4.12. The responses show excellent separation of the two categories for the signal channels, but the already pure normalisation channel with no photons available for input variables has less discriminating power. The BDT of the normalisation channel has a decreased ability to separate signal and background, and a noticeable signal contamination in the background category. The large statistics of $B^+ \to J/\psi K^+$ causes a non-negligible (of 1.5% efficiency) amount of the high-mass radiative tail of the J/ψ that is outside of the $\pm 60\,\mathrm{MeV}$ veto window for the J/ψ mass.

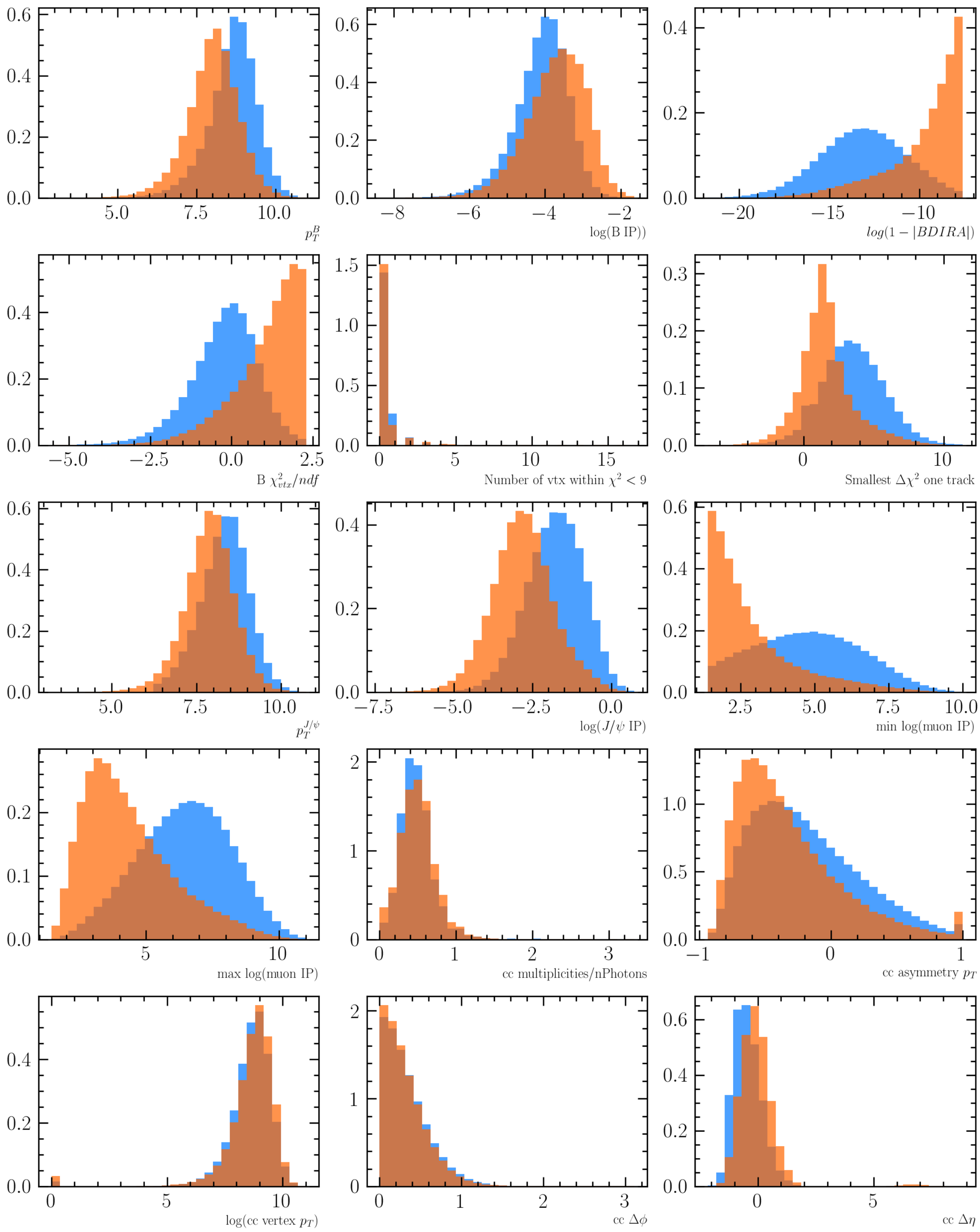

Figure 4.7.: The distributions of the variables and expressions used in the training of the MVA (omitting those unavailable to $B^+ \to J/\psi K^+$ decays) as well as occupancy variables. The orange distribution is the background category $B^+ \to J/\psi K^+$ 2018 collision data when the difference between the measured $\mu^+\mu^-$ mass and nominal mass of the J/ψ is greater than 60 MeV. The blue distribution is the signal category $B^+ \to J/\psi K^+$ 2018 MC data with weights from GBR.

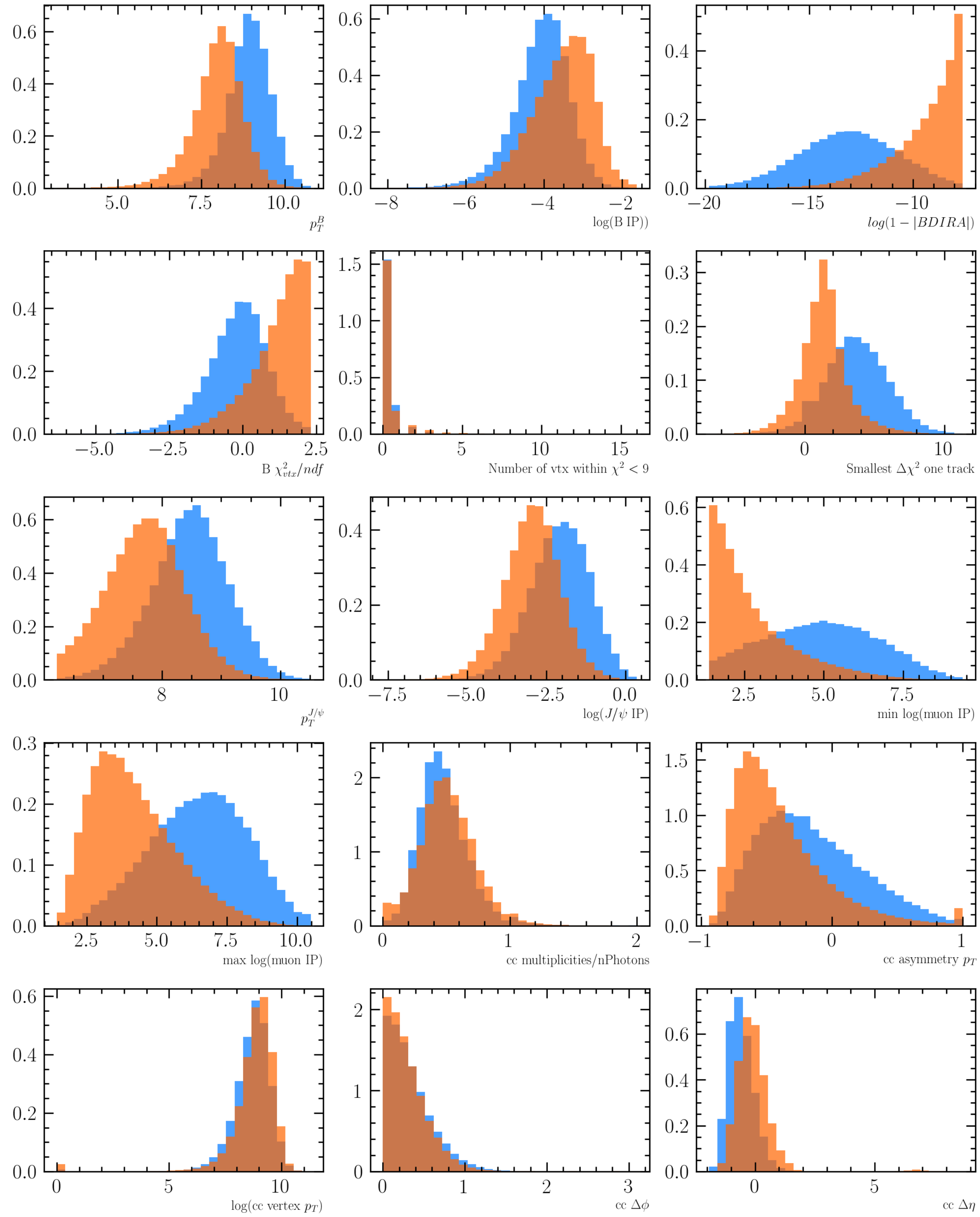

Figure 4.8.: 15 of the 16 distributions of the variables and expressions used in the training of the MVA (omitting those unavailable to $B^+ \to \chi_{c1}K^+$ decays) as well as occupancy variables. The orange distribution is the background category $B^+ \to \chi_{c1}K^+$ 2018 collision data when the difference between the measured $\mu^+\mu^-$ mass and nominal mass of the J/ψ is greater than 60 MeV. The blue distribution is the signal category $B^+ \to \chi_{c1}K^+$ 2018 MC data with weights from GBR.

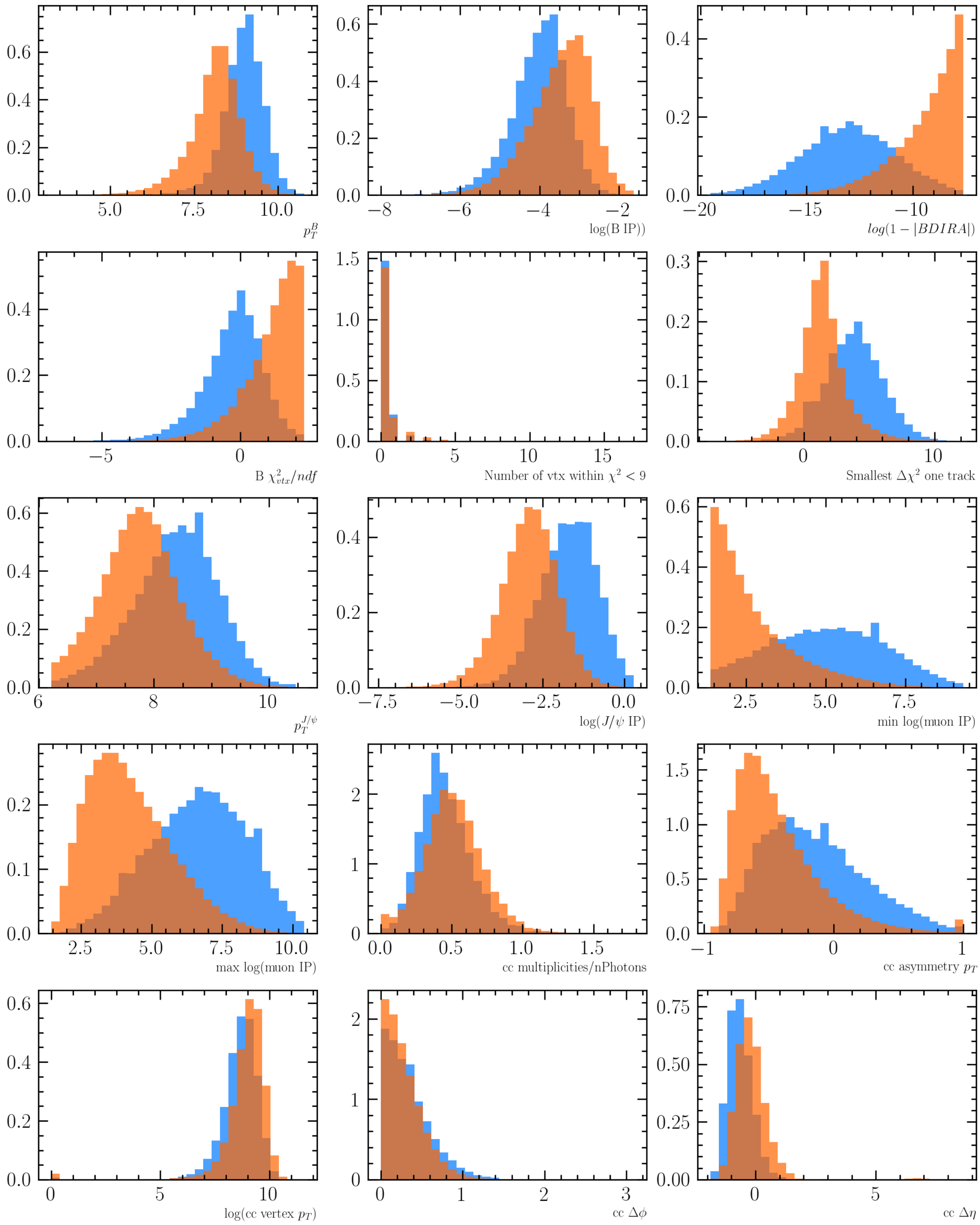

Figure 4.9.: 15 of the 17 distributions the variables and expressions used in the training of the MVA (omitting those unavailable to $B^+ \to J/\psi K^{*+}$ decays) as well as occupancy variables. The orange distribution is the background category $B^+ \to J/\psi K^{*+}$ 2018 collision data when the difference between the measured $\mu^+\mu^-$ mass and nominal mass of the J/ψ is greater than 60 MeV. The blue distribution is the signal category $B^+ \to J/\psi K^{*+}$ 2018 MC data with weights from GBR.

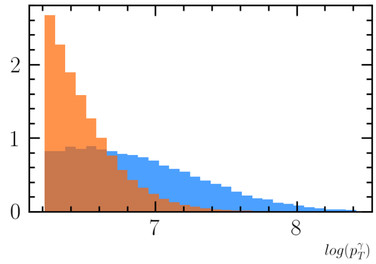

Figure 4.10.: The remaining distribution of the variables and expressions used in the training of the MVA (omitting those unavailable to $B^+ \to \chi_{c1} K^+$ decays) as well as occupancy variables. The orange distribution is the background category $B^+ \to \chi_{c1} K^+$ 2018 collision data when the difference between the measured $\mu^+\mu^-$ mass and nominal mass of the J/ψ is greater than 60 MeV. The blue distribution is the signal category $B^+ \to \chi_{c1} K^+$ 2018 MC data with weights from GBR.

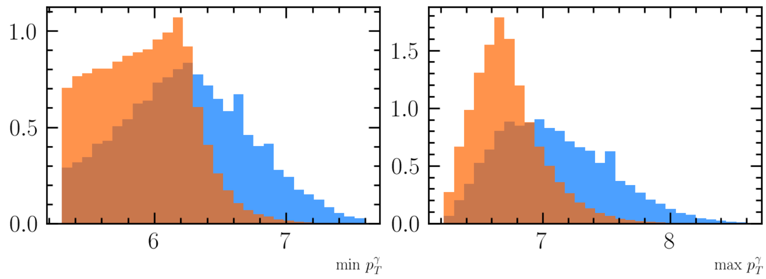

Figure 4.11.: The remaining distributions of the variables and expressions used in the training of the MVA (omitting those unavailable to $B^+ \to J/\psi K^{*+}$ decays) as well as occupancy variables. The orange distribution is the background category $B^+ \to J/\psi K^{*+}$ 2018 collision data when the difference between the measured $\mu^+\mu^-$ mass and nominal mass of the J/ψ is greater than 60 MeV. The blue distribution is the signal category $B^+ \to J/\psi K^{*+}$ 2018 MC data with weights from GBR.

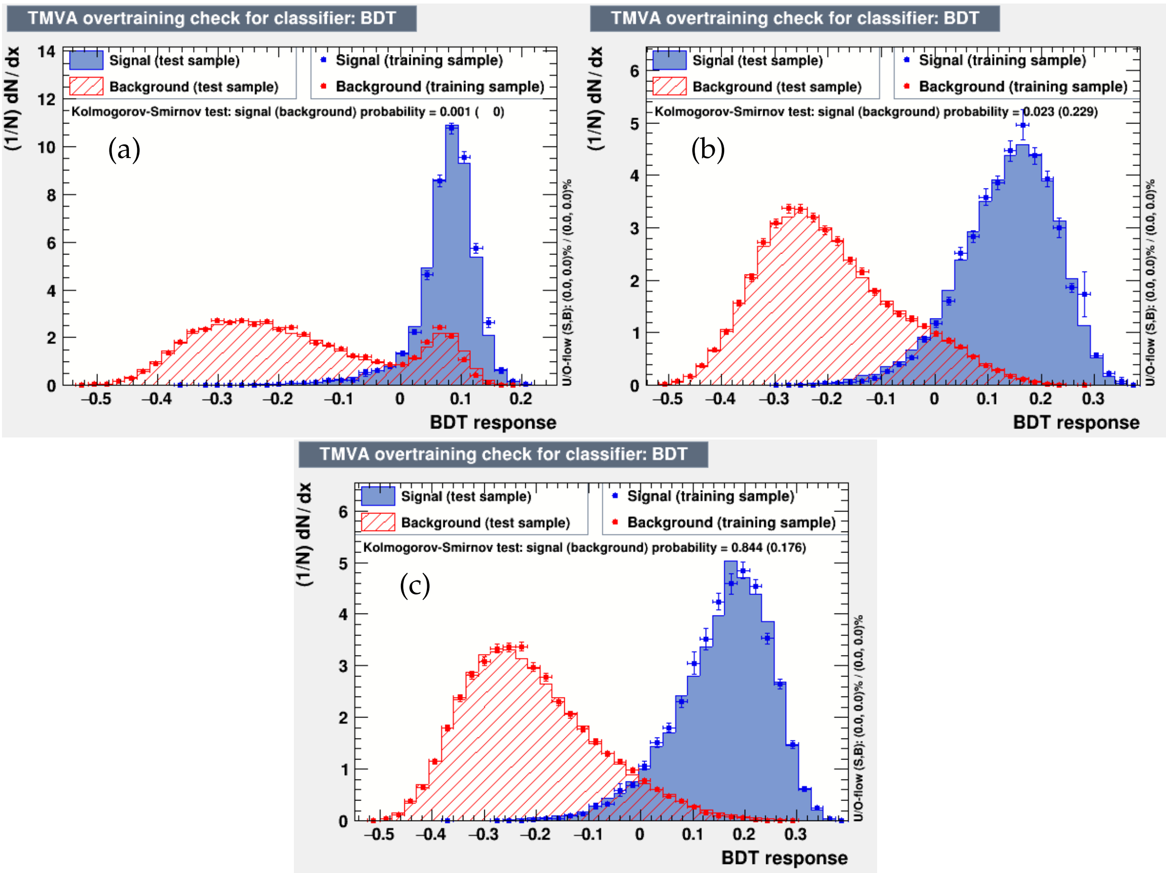

Figure 4.12.: The response of the BDT for a) $B^+ \to J/\psi K^+$, b) $B^+ \to \chi_{c1} K^+$ and c) $B^+ \to J/\psi K^{*+}$. The red distribution is the background category 2018 collision data when the difference between the measured $\mu^+\mu^-$ mass and nominal mass of the J/ψ is greater than 60 MeV. The blue distribution is the signal category 2018 MC data with weights from GBR.

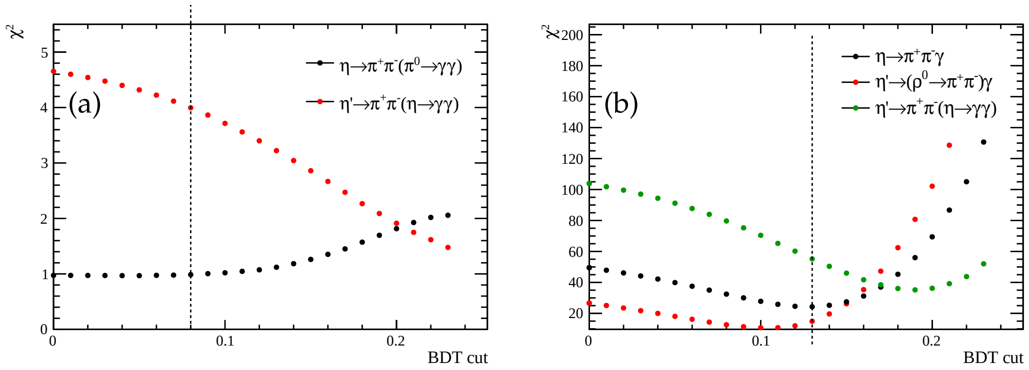

Figure 4.13.: The χ^2 values for the a) $B^+ \to \chi_{c1} K^+$ and b) $B^+ \to J/\psi K^{*+}$ photon p_T distributions over cuts of the BDT. In (a) the test is performed between the minimum and maximum photon p_T histograms of $B^+ \to J/\psi K^{*+}$ and $B^0_s \to J/\psi\eta[\pi^+\pi^-\pi^0]$ in black or $B^0_s \to J/\psi\eta'[\pi^+\pi^-\eta]$ in red. In (b) the test is performed between the photon p_T histograms of $B^+ \to \chi_{c1} K^+$ and $B^0_s \to J/\psi\eta[\pi^+\pi^-\gamma]$ in black, $B^0_s \to J/\psi\eta'[\rho^0\gamma]$ in red, or $B^0_s \to J/\psi\eta'[\pi^+\pi^-\eta]$ in green. The dashed lines show the optimal selection choices for the two decay channels.

As the corrections of the photon reconstruction efficiencies were produced for the measurement of the $B^0_{(s)} \to J/\psi\eta^{(\prime)}$ branching ratios, the optimum cut on the BDT was chosen to best align the photon kinematics of the single photon in $\chi_{c1} \to J/\psi\gamma$ channel with the photons in $\eta \to \pi^+\pi^-\gamma$, $\eta' \to \rho^0\gamma$ and the individual photons of $\eta' \to \pi^+\pi^-\eta[\gamma\gamma]$. Therefore the minimisation of the χ^2 value between the photon p_T distributions of the decay channels for different cuts of the BDT was performed to decide on the cut applied. In the case of the decays including a $\pi^0 \to \gamma\gamma$ resonance, the χ^2 test was performed in two dimensions for the minimum and maximum photon p_T. The implementation of the χ^2 test was that of ROOT [118] based on [122]. The χ^2 distributions are shown in Figure 4.13 where it can be seen that only in the extreme of the BDT cuts (with very low statistics) would the diphoton p_T of the $\pi^0 \to \gamma\gamma$ be in good agreement with $\eta \to \gamma\gamma$. In the comparison of the two cases of $\pi^0 \to \gamma\gamma$ ($B^+ \to J/\psi K^{*+}$ and $B^0_s \to J/\psi\eta[\pi^+\pi^-\pi^0]$) good agreement is found by default with looser cuts of the BDT. Therefore the use of the $B^+ \to J/\psi K^{*+}$ sample to find diphoton reconstruction correction factors is only applicable to $\pi^0 \to \gamma\gamma$ and not $\eta \to \gamma\gamma$. This is the reason why the single photon correction factor with $B^+ \to \chi_{c1} K^+$ decays is applied not just to the two channels with single photon in the final state but also to the two photons of $\eta \to \gamma\gamma$, with a squared correction. The cuts chosen are therefore 0.08 for the $B^+ \to J/\psi K^{*+}$ BDT, the highest cut with good agreement of the π^0, and 0.13 for the $B^+ \to \chi_{c1} K^+$ BDT as a cut that gives good agreement between the photon p_T distributions in all of the use-cases.

For the selections of $B^+ \to J/\psi K^+$ there were two cuts chosen to achieve similar BDT efficiencies with the two signal modes for the respective efficiency corrections. The cuts chosen were 0.7 for the alignment with $B^+ \to J/\psi K^{*+}$ and 0.4 for $B^+ \to \chi_{c1} K^+$. The respective efficiencies and their ratios are given in Tables 4.22 and 4.23 of Section 4.6.

4.5. Mass fits and extraction of signal yields

4.5.1. Fit models

As described in Section 3.7 the signal model used to describe the shape of the signal channels in the Decay Tree Fitted B mass distributions was the double-sided Hypatia PDF. The core (λ, ζ and β) and tail ($a_{L,R}$, $n_{L,R}$) shape parameters are determined in fits of the PDF to the Monte Carlo samples and then fixed to these values in the fits to the real data samples. With the exceptionally high statistics yielded from the normalisation ($B^+ \to J/\psi K^+$) and control ($B^0 \to J/\psi K^{*0}$) channels, an additional component was added when fitting to the real collision data. An extra Gaussian PDF with the same mean as the double-sided Hypatia was used to help fit the tails of the distributions. While the model of the double-sided Hypatia worked well to fit the Monte Carlo samples, there was a failure of this same model in its application of the high statistics real data, which would have led to large pulls.

4.5.2. Backgrounds impacting the $B^+ \to J/\psi K^+$ mode

- $B^+ \to J/\psi \pi^+$: Similar to $B^0 \to J/\psi(\rho^0 \to \pi^+\pi^-)$ in $B^0 \to J/\psi K^{*0}$, the pion could be misidentified as a kaon and could have appeared in the invariant mass spectrum as a small contribution to the high mass tail of $B^+ \to J/\psi K^+$. Yet, along with the suppression of the kaon PID requirement, there is Cabibbo suppression leading to a negligible contribution well below the precision of the measured signal yields of $B^+ \to J/\psi K^+$.

4.5.3. Backgrounds impacting the $B^+ \to J/\psi K^{*+}$ mode

Table 4.10.: The ratio of Monte Carlo efficiencies of the underlying event photon background over the signal efficiencies.

Year	$N^b_\gamma/N^s(B^+ \to \chi_{c1}K^+)\%$	$N^b_\gamma/N^s(B^+ \to J/\psi K^{*+})\%$	$N^b_{\gamma\gamma}/N^s(B^+ \to J/\psi K^{*+})\%$
2011	13.56 ± 0.0025	43.07 ± 0.005	7.034 ± 0.19
2012	14.08 ± 0.0019	47.57 ± 0.0044	9.073 ± 0.17
2016	14.57 ± 0.0015	50.33 ± 0.0041	9.921 ± 0.16
2017	13.34 ± 0.0013	51.31 ± 0.0042	9.352 ± 0.15
2018	11.65 ± 0.0012	51.00 ± 0.0043	9.617 ± 0.16

- mis-combined photons or neutral pions: There are also contributions where one or both of the γ combined to the decay of resolved π^0 can instead have come from the underlying event occupancy. For this background it is particularly important that the yield relative to the signal is well understood as it peaks at the same point in the B^+ mass distribution as the signal. It is necessary to use MC for $B^+ \to J/\psi K^{*+}$ to try to model this type of background. The ratio of the yields of the combinatorial γ/π^0 background and the $B^+ \to J/\psi K^{*+}$ signal are Gaussian constrained in the data fit with the mean value as the estimated yield determined by the ratio of efficiencies in the combined MC sample, see the last two columns of Table 4.10. This background category is sensitive to the occupancy and the PID efficiencies of neutrals, this is why the corrections made in Section 4.3 were necessary. The width of the gaussian is then determined to be the combined uncertainty of the MC sample statistics and the uncertainty on the corrections.

- $B^0 \to J/\psi K^{*0}$: In the decay $K^{*0} \to K^+\pi^-$ the π^- may be replaced in reconstruction with a random π^0 in the event and pass signal selections. The fit model and yield for this background was determined using MC simulation. As this is a contamination involving a π^0 from the underlying event, the same correction factor for this type of background was applied.

- $B \to J/\psi K\pi\pi$: This background is a partially reconstructed background where in the dominant case the additional π^0 from the decay ${K^+}_1 \to K^{*+}\pi^0$ is expected to be lost. Although there were numerous contributions with different combinations of photons from the two π^0 or from the underlying event. To approximate with MC, samples of specifically $B^+ \to J/\psi({K^+}_1(1270) \to K^{*+}(892)\pi^0)$ were used. It was therefore necessary in this fit to use multiple PDFs to fit different types of shapes dependent on the origins of the two π^0 mesons. For the dominant case of a partially reconstructed background, a common PDF to use is an Argus function convoluted with a normal distribution to model the resolution of the detector. For the other photon combinations, a Crystal Ball function was used to aid in the modelling of a wide Gaussian-like distribution with a large tail entering the signal region. The shape parameters of the Crystal Ball and Argus were fixed on MC, along with their relative prominence. The widths were scaled, and the Crystal Ball mean and Argus threshold were shifted with other peaking backgrounds and the signal.

- Non-resonant contribution: Assuming isospin symmetry between K^{*+} and K^{*0}, the expected contribution of the non-resonant component will be the same for both $B^0 \to J/\psi K^{*0}$ and $B^+ \to J/\psi K^{*+}$ resonances, therefore the same contribution calculated from the fits of $B^0 \to J/\psi K^{*0}$ and $K^{*0} \to K^+\pi^-$ are used to correct for this background category. This is described in more detail in Section 4.5.5 where Table 4.11 shows the factors used.

4.5.4. Backgrounds impacting the $B^+ \to \chi_{c1} K^+$ mode

- Mis-combined photons: This is along with an incorrectly combined photon background similar to $B^+ \to J/\psi K^{*+}$ with resolved π^0. The ratio of the yields (from integration of the PDFs) of the combinatoric photon background and the $B^+ \to \chi_{c1} K^+$ signal are Gaussian constrained in the data fit on the corrected value observed by the combined MC sample, as shown in Table 4.10. This is done in the same way as this type of background in $B^+ \to J/\psi K^{*+}$. In the use of the Decay Tree Fitter the $J/\psi\gamma$ distribution is constrained to χ_{c1} mass which causes the shape of this background to be triangular in the $J/\psi\gamma K^+$ mass distribution.

- $B^+ \to \chi_{c2} K^+$: Because this decay has the same final state as the signal it is a fully reconstructed background. Yet due to its $\mathcal{B}$ being about 1% of the size of the signal $\mathcal{B}$, it has a very low yield in the B^+ invariant mass distribution. It is an irreducible background because of the small difference between the χ_{c1} and χ_{c2} masses, $\Delta m = 45.50\,\text{MeV}$. It appears as a peak well within the B^+ mass signal region and is well within the χ_{c1} mass window. Due to the DTF constraining the reconstructed mass of the χ_{c2} to the mass of a χ_{c1}, there is a skewed shape to the B^+ mass distribution. Therefore there was a need for two double-sided Hypatia functions with different means in the fit.

- $B^+ \to J/\psi K^{*+}$: There are two contributions to the background originating from this decay mode. One is when the π^0 is completely missed in reconstruction and an occupancy photon in the event is mis-combined to appear as a signal event. The other is when the photon is one of the photons in the decaying $\pi^0 \to \gamma\gamma$ cascading from $B^+ \to J/\psi K^{*+}$. Both of these backgrounds have broad distributions with different shapes, yet appear in the low mass region with only the tail in the fitting region, and are accounted for in the same PDF as the combinatorial.

- $B^0 \to J/\psi K^{*0}$: When this mode decays as $K^{*0} \to K^+\pi^-$ the π^- can be missed and an occupancy photon is mis-identified as a signal photon similar to the $B^+ \to J/\psi K^{*+}$ background. Therefore they have a very similar shape due to the closeness in masses of B^0 and B^+ and of π^0 and π^-. There is a 4% uncertainty on the branching fraction of $B^0 \to J/\psi K^{*0}$, any estimation of the yield of this background using this branching ratio would have a large contribution to the uncertainty on the signal yield. Therefore, by fully reconstructing this decay, a more precise estimation of its contribution can be made. The yield of this decay as a background for $B^+ \to \chi_{c1} K^+$ was equal to the yield of the full reconstruction scaled by the ratio of MC efficiencies when partially reconstructed as a background over the fully reconstructed MC efficiency. To do this, a fit of the $B^0 \to J/\psi K^{*0}$ in the DTF $m(J/\psi K^+\pi^-)$ was necessary. This fit is performed with an MVA trained on $B^+ \to \chi_{c1} K^+$ with just the photon p_{T} removed. Using this MVA would cancel out the most of the uncertainty related to using the MVA. Scaling the yield from this fit by the

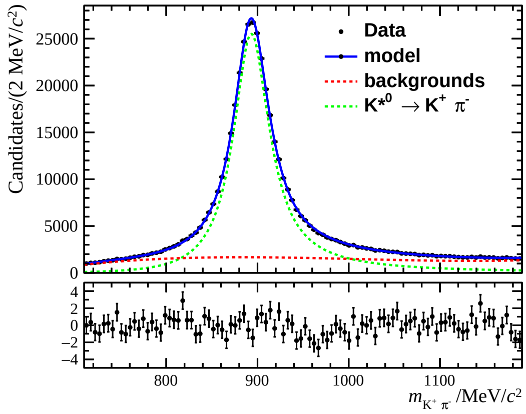

Figure 4.14.: Fit to the $K^{*0} \to K^+\pi^-$ mass distribution of the collision data sample of the reconstructed signal $B^0 \to J/\psi K^{*0}$ for 2018.

ratio of efficiencies of the full reconstruction and partial reconstruction as a background contribution gives a well estimated yield for the fits of this background in the $B^+ \to \chi_{c1}K^+$ invariant masses.

4.5.5. Backgrounds impacting the $B^0 \to J/\psi K^{*0}$ mode

Table 4.11.: The correction factors to the underlying event photon background used in the DTF B invariant mass fits to collision data.

Year	$f(K^{*0} \to \pi^+\pi^-)/\%$
2011	71.9 ± 0.6
2012	72.9 ± 0.5
2016	71.04 ± 0.41
2017	72.89 ± 0.41
2018	73.32 ± 0.38

- $B^0 \to J/\psi(\rho^0 \to \pi^+\pi^-)$: When one of the charged pions originating from the decay $\rho^0 \to \pi^+\pi^-$ is misidentified as a charged kaon, the tail of the combined mass of the two pions (with one under a kaon mass hypothesis) can be within the $K^+\pi^-$ mass requirement. Yet due to the ANN used in the selections for PID, and particularly its Cabibbo suppression, this background is well suppressed. No visible peak could be seen in the B^+ mass spectra. The inclusion of this background was found to have a negligible impact on the measured signal yield of the $B^0 \to J/\psi K^{*0}$ fit.
- Non-resonant contribution: There will be contributions to the $J/\psi K^+\pi^-$ mass spectrum from the direct decay $B^+ \to J/\psi K^+\pi^-$ (S-wave). This decay appears as signal in the

$J/\psi K^+\pi^-$ invariant mass spectrum so must be controlled by studying the $K^{*0} \to K^+\pi^-$ resonance. Signal will appear as a peak in the $K^+\pi^-$ spectrum, whereas the S-wave would not. Therefore we fit for the shape parameters in MC and then fit the collision data, see Figure 4.14. So to estimate this contribution, the high mass region of the $K^+\pi^-$ is selected as being in the range $[1100, 1190]$ MeV. Then using this region, the peaking structure at the B^0 mass will primarily be the non-resonant $J/\psi K^+\pi^-$ component. So using the yield in the B^0 mass fit, the non-resonant component within the signal region can be extrapolated to the signal region (± 75 MeV around the nominal K^{*0} mass). This allowed for the non-resonant contribution to the signal yield to be calculated as a fraction that could be used as a correction factor to the signal yield.

- $B_s^0 \to J/\psi K^{*0}$ For the contribution of the decay with the same final state but originating from a B_s^0 meson, the fit model used was the same as the signal but with the mean increased by the difference in the masses of B_s^0 and B^0 mesons. The width was kept the same as any difference would have a small effect on the overall fit and would not impact the signal yield due to good separation of the B^0 and B_s^0 peaks. The yield of this contribution was kept free in the invariant mass fit.
- $B^0 \to J/\psi K^0{}_1$: Although this background appears in an analogous way to $B^+ \to J/\psi K^+{}_1$ in $B^+ \to J/\psi K^{*+}$, and due to isospin symmetry is likely to be just as prominent, it is not included in the fit. This is because the reconstructed $J/\psi K^+\pi^-$ DTF mass resonance is much narrower than that of the $J/\psi K^+\pi^0$ $[\gamma\gamma\ ]$ resonances. Therefore by using the relatively narrow fit range of $m(J/\psi K^+\pi^-) \in [5200, 5600]$ MeV, the need to include this background in the fit is avoided.

4.5.6. Combined model fit to collision data

The signal fits to real collision data all had similar sets of free or fixed parameters. In all cases the parameters that determine the overall shape of the PDFs were fixed on Monte Carlo, but with a free shift from the Monte Carlo mean position to that of the real data and a free scale factor of the width of the PDF from the MC size to that of the real data. These factors, within a B DTF mass distribution, are kept in common for all signal and physics background contributions. Therefore there were always at least two free parameters related to the energy calibration and resolution. Another free nuisance parameter used in all distributions was the slope of an exponential used to model the combinatorics. All other observable parameters were the yields of the signal channels, the combinatorial background, and the typically Gaussian constrained physics background yields. One of the two physics backgrounds without Gaussian constrained yields were the $B_s^0 \to J/\psi K^{*0}$ in $B^0 \to J/\psi K^{*0}$ (in Figure 4.15), as this background was distinct from the signal and unnecessary to constrain due to the simplicity of the fitting procedure for a fully reconstructed background with no neutrals. The other background

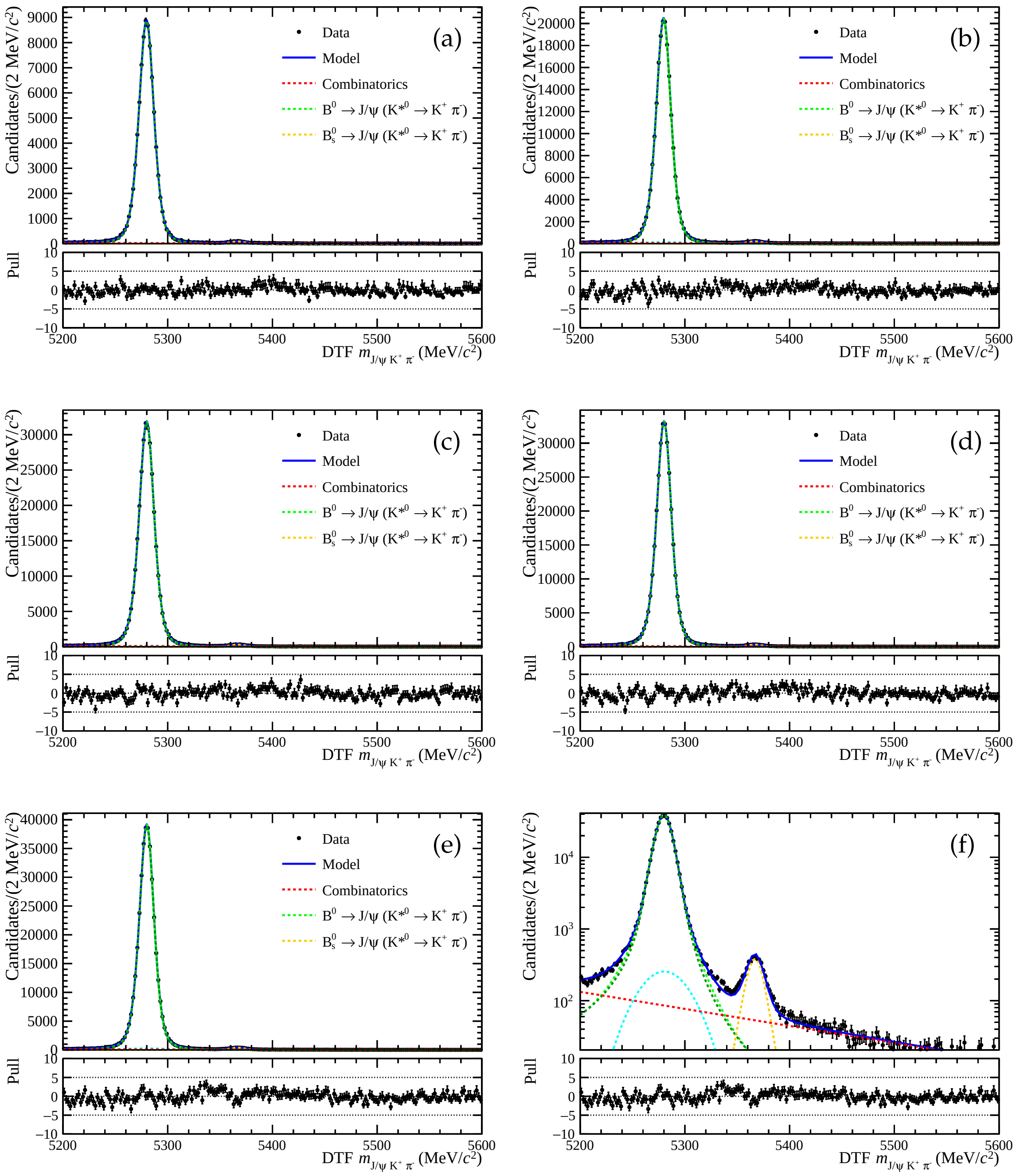

Figure 4.15.: Fit to the decay tree fitted B^+ mass distribution of the collision data sample of the reconstructed signal $B^0 \to J/\psi K^{*0}$ for a) 2011, b) 2012, c) 2016, d) 2017, e) 2018 and f) 2018 in logarithmic scale. The cyan component is the additional Gaussian to improve the fit of the tails.

without a constraint on its yield was the $B \to J/\psi K\pi\pi$ decays in $B^+ \to J/\psi K^{*+}$ (in the low mass of Figure 4.19), as it is a poorly understood background with potentially many contributions of different decays involving strange mesons designated as $K^+{}_1$ or K^*. These totalled to 7 free parameters in the fit to $B^+ \to J/\psi K^+$ data (Figures 4.16 and 4.17 which included an extra

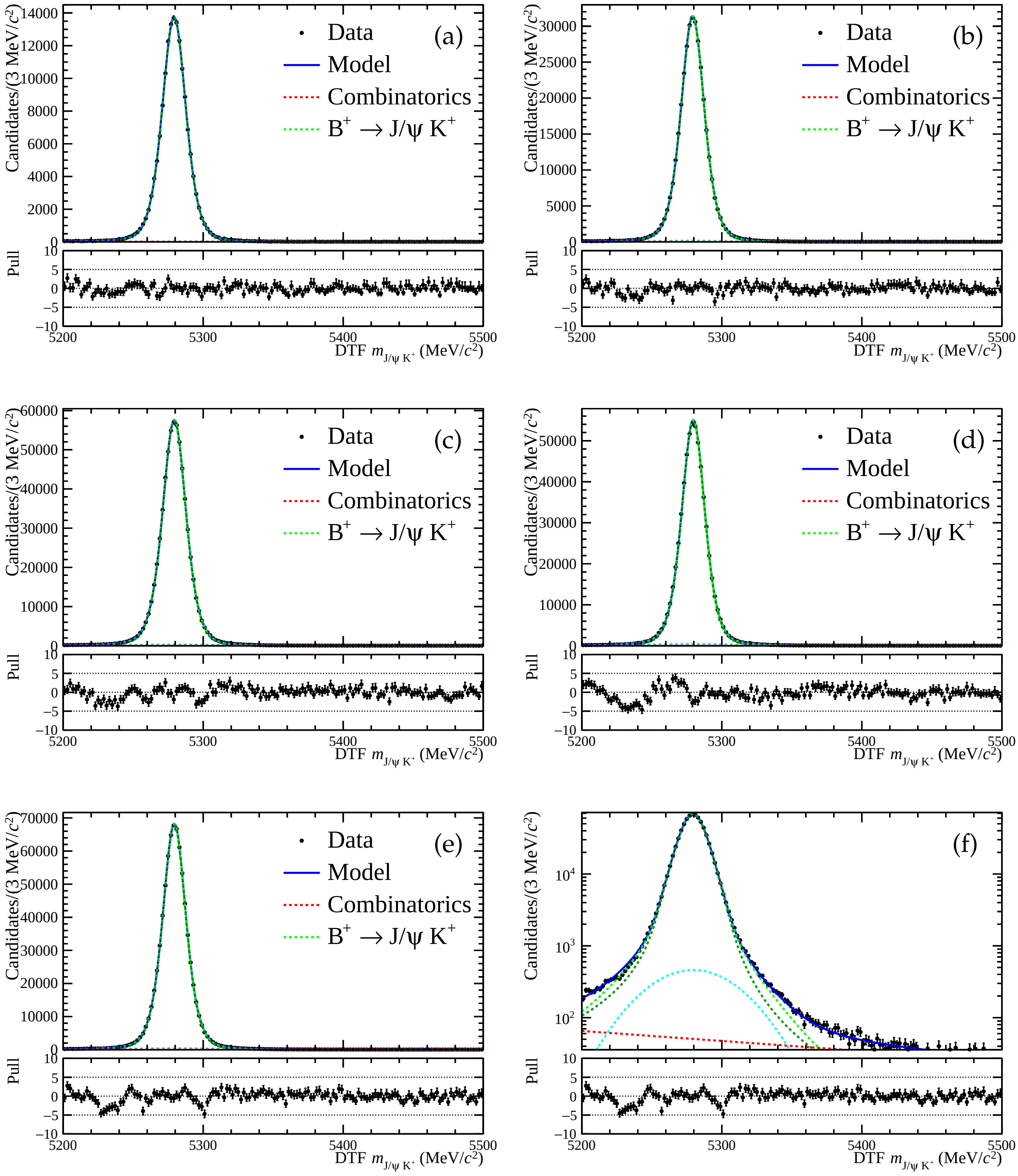

Figure 4.16.: Fit to the decay tree fitted B^+ mass distribution of the collision data sample of the reconstructed signal $B^+ \to J/\psi K^+$ with the MVA selections of $B^+ \to \chi_{c1} K^+$ for a) 2011, b) 2012, c) 2016, d) 2017, e) 2018 and f) 2018 in logarithmic scale. The cyan component is the additional Gaussian to improve the fit of the tails.

Gaussian width and relative contribution), 6 for $B^0 \to J/\psi K^{*0}$ (Figure 4.15), 7 for $B^+ \to J/\psi K^{*+}$ (Figure 4.19) and 8 for $B^+ \to \chi_{c1} K^+$ (Figure 4.18). See Table 4.12 and Table 4.13 for tables summarising the yields of the signal channels $B^+ \to \chi_{c1} K^+$ and $B^+ \to J/\psi K^{*+}$ as well as the normalisation channel $B^+ \to J/\psi K^+$ with both signal BDT cuts applied. There are also the

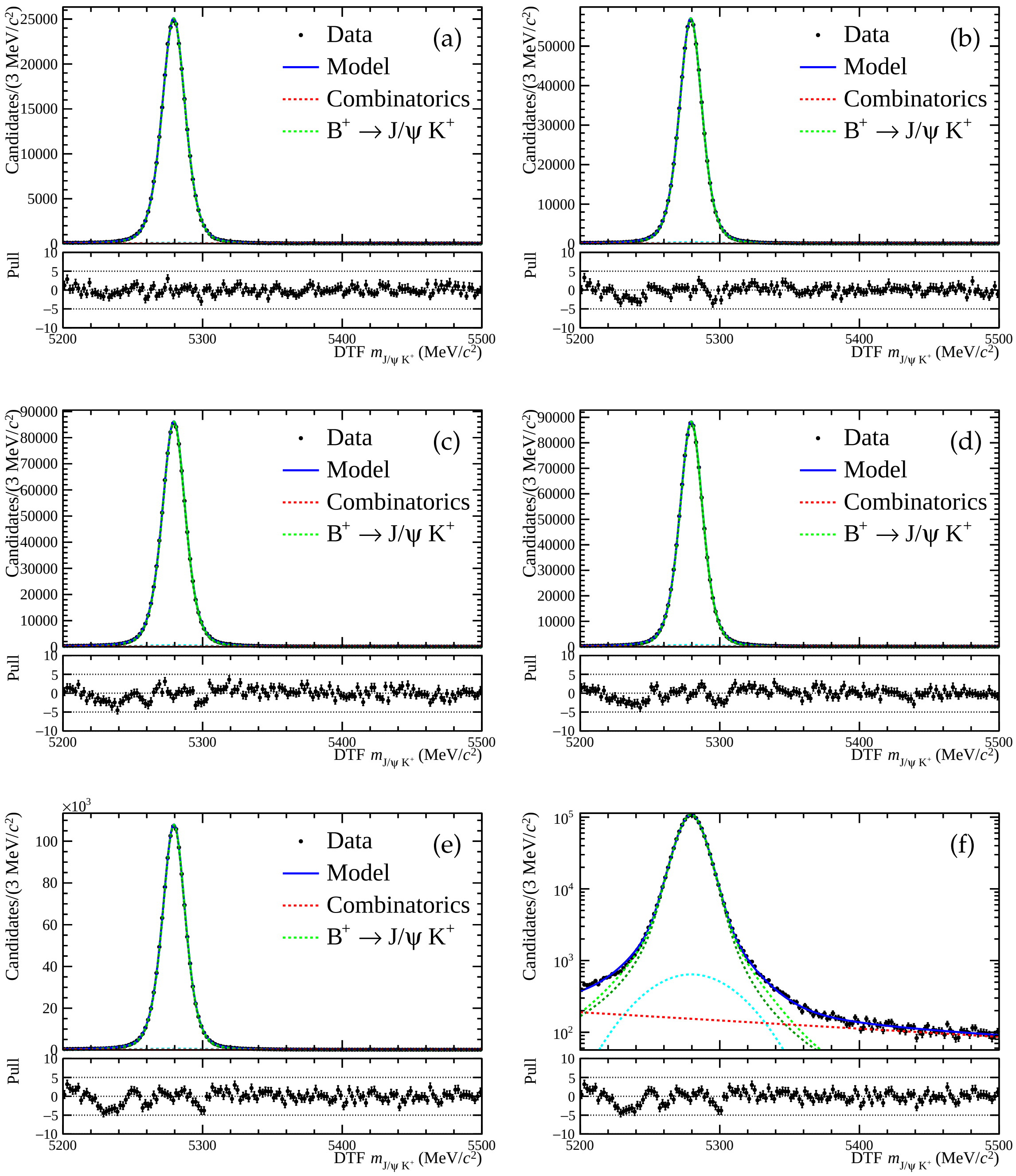

Figure 4.17.: Fit to the decay tree fitted B^+ mass distribution of the collision data sample of the reconstructed signal $B^+ \to J/\psi K^+$ with the MVA selections of $B^+ \to J/\psi K^{*+}$ for a) 2011, b) 2012, c) 2016, d) 2017, e) 2018 and f) 2018 in logarithmic scale. The cyan component is the additional Gaussian to improve the fit of the tails.

fit parameters related to the shapes of the fit models and background yields are in Tables 4.14-4.21.

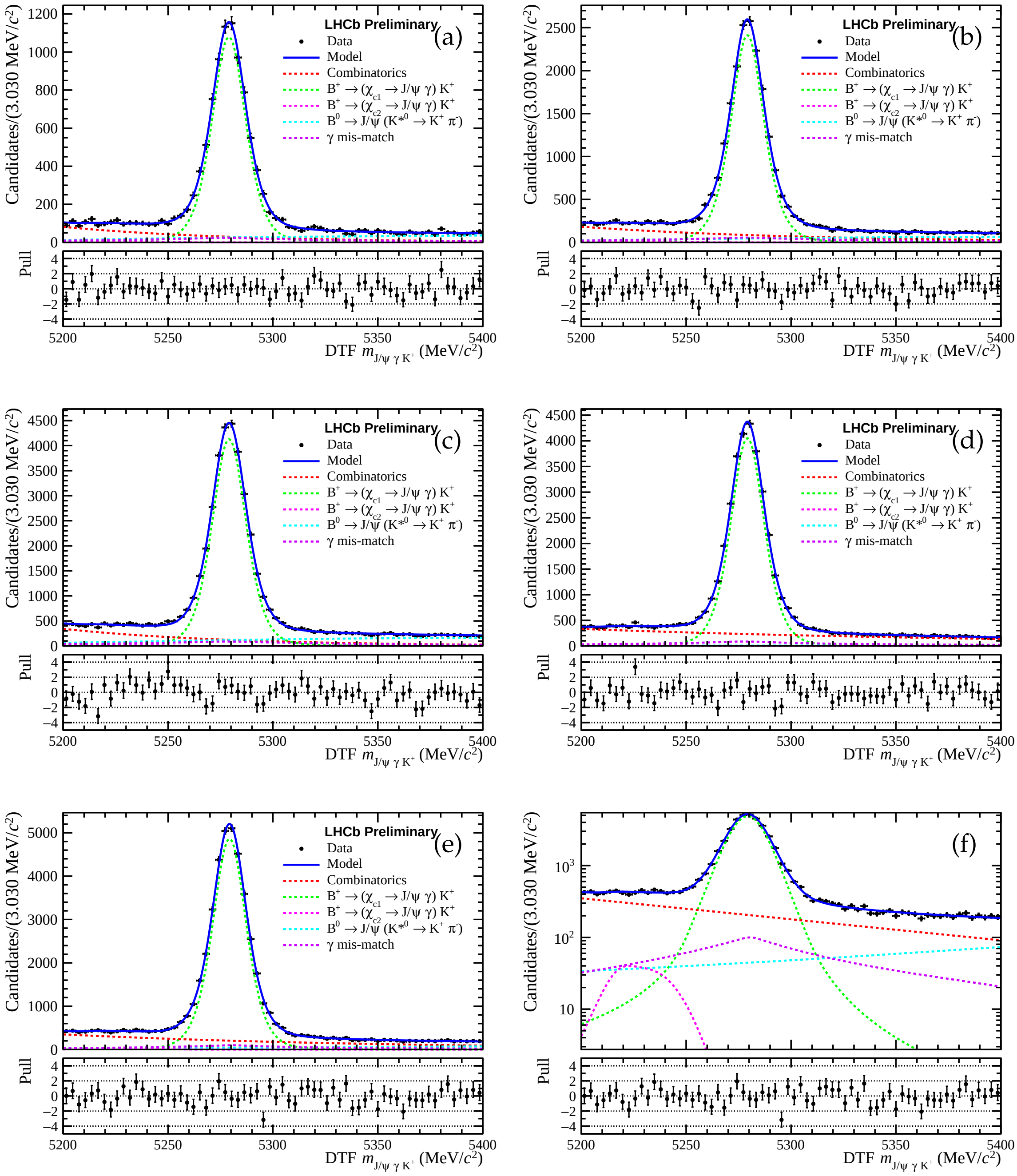

Figure 4.18.: Fit to the decay tree fitted B^+ mass distribution of the collision data sample of the reconstructed $B^+ \to \chi_{c1} K^+$ for a) 2011, b) 2012, c) 2016, d) 2017 and, e) 2018 and f) 2018 in logarithmic scale.

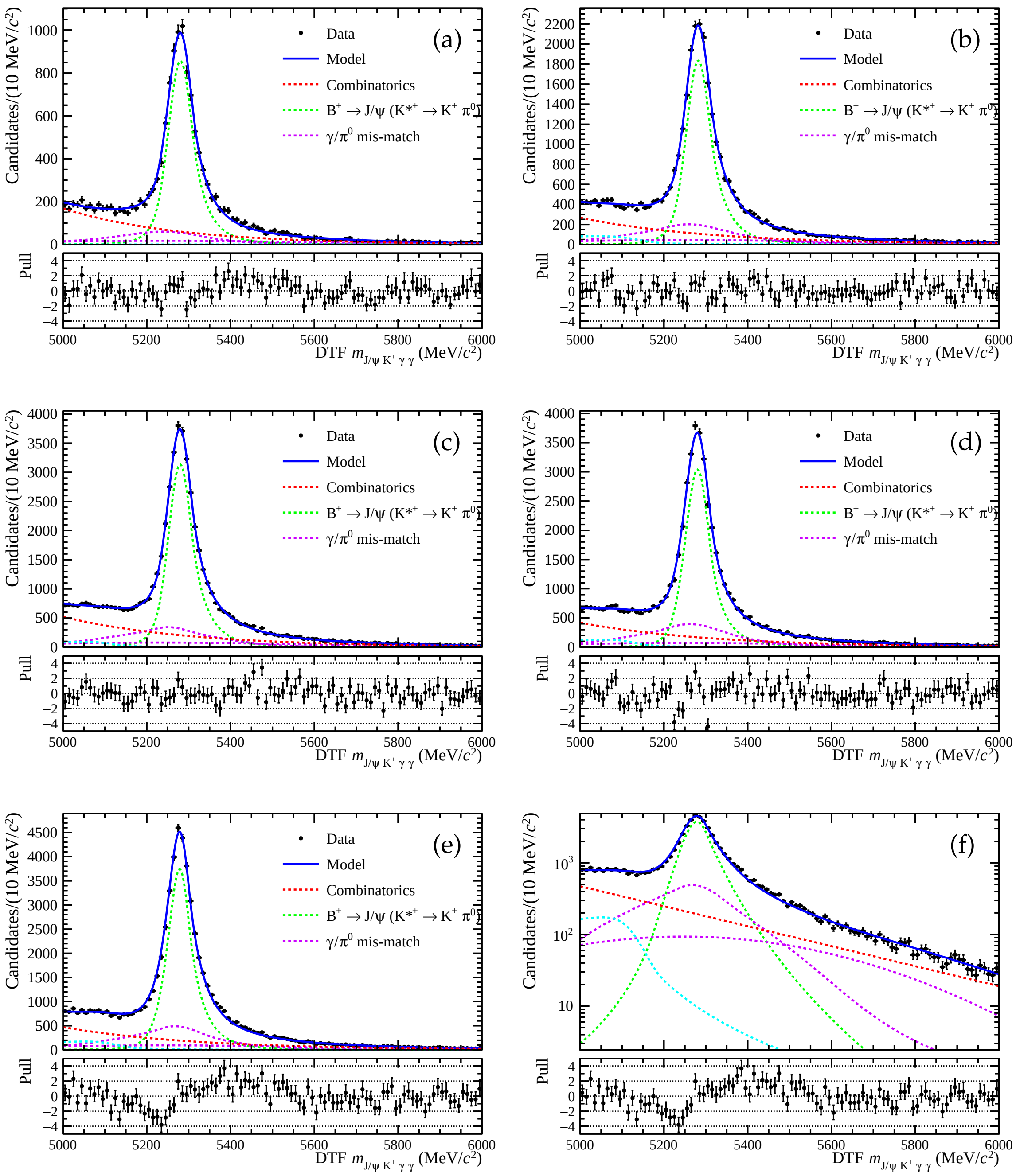

Figure 4.19.: Fit to the decay tree fitted B^+ mass distribution of the collision data sample of the reconstructed $B^+ \to J/\psi K^{*+}$ for a) 2011, b) 2012, c) 2016, d) 2017, e) 2018 and f) 2018 in logarithmic scale.

Table 4.12.: The signal yields of the $B^+ \to \chi_{c1}K^+$ and $B^+ \to J/\psi K^+$ with the BDT selections of a similar efficiency as $B^+ \to \chi_{c1}K^+$.

Year	$N^s_{B^+\to J/\psi K^+}$	$N^s_{B^+\to \chi_{c1}K^+}$	$N^s_{B^+\to \chi_{c1}K^+} / N^s_{B^+\to J/\psi K^+}$ / %
2011	157294 ± 409	7718 ± 88	4.91 ± 0.06
2012	353695 ± 607	16997 ± 130	4.806 ± 0.038
2016	659970 ± 668	29662 ± 172	4.494 ± 0.026
2017	626166 ± 1015	28794 ± 170	4.598 ± 0.028
2018	771941 ± 1506	34728 ± 186	4.499 ± 0.026

Table 4.13.: The signal yields of the $B^+ \to J/\psi K^{*+}$ and $B^+ \to J/\psi K^+$ with the BDT selections of a similar efficiency as $B^+ \to J/\psi K^{*+}$.

Year	$N^s_{B^+\to J/\psi K^+}$	$N^s_{B^+\to J/\psi K^{*+}}$	$N^s_{B^+\to J/\psi K^{*+}} / N^s_{B^+\to J/\psi K^+}$ / %
2011	250659 ± 512	7428 ± 208	2.96 ± 0.08
2012	559671 ± 765	16002 ± 105	2.859 ± 0.019
2016	902206 ± 1004	27003 ± 357	2.993 ± 0.039
2017	911225 ± 1020	26235 ± 380	2.879 ± 0.042
2018	$(1.1107 \pm 0.0011) \times 10^6$	31949 ± 452	2.876 ± 0.041

Table 4.14.: The fit parameters of the $B^+ \to J/\psi K^+$ BDT selections of for $B^+ \to \chi_{c1}K^+$.

Year	$\Delta\mu$ / MeV	$f(\sigma)$	$p_0^{\text{exponential}}$
2011	0.574 ± 0.025	1.1554 ± 0.0034	$(-2.4 \pm 0.8) \times 10^{-3}$
2012	0.614 ± 0.017	1.1097 ± 0.0028	$(-3.23 \pm 0.36) \times 10^{-3}$
2016	0.547 ± 0.011	1.117 ± 0.005	$(-2.7 \pm 1.5) \times 10^{-3}$
2017	0.366 ± 0.007	1.106 ± 0.005	$(-2.1 \pm 2.3) \times 10^{-3}$
2018	0.525 ± 0.009	1.0921 ± 0.0024	$(-3.4 \pm 1.0) \times 10^{-3}$

Table 4.15.: The fit parameters of the $B^+ \to J/\psi K^+$ BDT selections of for $B^+ \to \chi_{c1}K^+$.

Year	$\sigma(Gaus.)$ / MeV	$f(Gaus.)$ /%	$N^b_{\text{exponential}}$
2011	28 ± 5	0.6421 ± 0.0017	$(1.24 \pm 0.11) \times 10^3$
2012	20.6 ± 0.6	1.5940 ± 0.0021	$(3.46 \pm 0.13) \times 10^3$
2016	27.9 ± 3.8	1.698 ± 0.005	$(5.1 \pm 1.2) \times 10^3$
2017	27 ± 6	1.9752 ± 0.0037	$(4.7 \pm 1.4) \times 10^3$
2018	28.0 ± 3.7	2.071 ± 0.005	$(6.5 \pm 1.2) \times 10^3$

Table 4.16.: The fit parameters of the $B^+ \to J/\psi K^+$ BDT selections of for $B^+ \to J/\psi K^{*+}$.

Year	$\Delta\mu$ / MeV	$f(\sigma)$	$p_0^{\text{exponential}}$
2011	0.570 ± 0.020	1.1466 ± 0.0031	$(-2.51 \pm 0.39) \times 10^{-3}$
2012	0.620 ± 0.013	1.1068 ± 0.0022	$(-2.82 \pm 0.25) \times 10^{-3}$
2016	0.524 ± 0.011	1.1105 ± 0.0019	$(-3.34 \pm 0.22) \times 10^{-3}$
2017	0.355 ± 0.008	1.1131 ± 0.0019	$(-2.0 \pm 0.7) \times 10^{-3}$
2018	0.544 ± 0.009	1.0929 ± 0.0016	$(-3.18 \pm 0.24) \times 10^{-3}$

Table 4.17.: The fit parameters of the $B^+ \to J/\psi K^+$ BDT selections of for $B^+ \to J/\psi K^{*+}$.

Year	$\sigma(Gaus.)$ / MeV	$f(Gaus.)$ /%	$N^b_{\text{exponential}}$
2011	20.5 ± 0.7	1.1424 ± 0.0022	$(3.02 \pm 0.12) \times 10^3$
2012	20.0 ± 0.5	1.6985 ± 0.0017	$(6.93 \pm 0.12) \times 10^3$
2016	23.1 ± 0.7	2.2994 ± 0.0014	$(1.191 \pm 0.032) \times 10^4$
2017	28.0 ± 3.8	1.9227 ± 0.0043	$(1.05 \pm 0.13) \times 10^4$
2018	27.0 ± 0.9	2.1297 ± 0.0010	$(1.418 \pm 0.044) \times 10^4$

Table 4.18.: The fit parameters of the $B^+ \to \chi_{c1} K^+$ DTF B^+ mass fits to collision data per year.

Year	$\Delta\mu$ / MeV	$f(\sigma)$	$p_0^{\text{exponential}}$
2011	0.54 ± 0.12	1.157 ± 0.018	$(-1.28 \pm 0.27) \times 10^{-2}$
2012	0.41 ± 0.08	1.138 ± 0.012	$(-7.5 \pm 1.3) \times 10^{-3}$
2016	0.55 ± 0.06	1.135 ± 0.009	$(-9.09 \pm 0.29) \times 10^{-3}$
2017	0.51 ± 0.06	1.125 ± 0.008	$(-4.50 \pm 0.27) \times 10^{-3}$
2018	0.371 ± 0.005	1.135 ± 0.008	$(-7.0 \pm 0.8) \times 10^{-3}$

Table 4.19.: The background fractions or yields in the $B^+ \to \chi_{c1} K^+$ DTF B^+ mass fits to collision data per year.

Year	$f(\text{rand. } \gamma)$	$N^b_{B^0 \to J/\psi K^{*0}}$	$N^b_{exponent}$
2011	0.1479 ± 0.0021	$(1.75 \pm 0.25) \times 10^3$	$(1.96 \pm 0.30) \times 10^3$
2012	0.1915 ± 0.0017	$(2.3 \pm 0.6) \times 10^3$	$(6.3 \pm 0.7) \times 10^3$
2016	0.1168 ± 0.0012	$(6.07 \pm 0.07) \times 10^3$	$(1.026 \pm 0.019) \times 10^4$
2017	0.1072 ± 0.0011	$(3.61 \pm 0.16) \times 10^2$	$(1.459 \pm 0.043) \times 10^4$
2018	0.0953 ± 0.0010	$(3.4 \pm 0.9) \times 10^3$	$(1.27 \pm 0.10) \times 10^4$

Table 4.20.: The fit parameters of the $B^+ \to J/\psi K^{*+}$ DTF B^+ mass fits to collision data per year.

Year	$\Delta\mu$ / MeV	$f(\sigma)$	$p_0^{\text{exponential}}$
2011	-1.5 ± 0.6	1.151 ± 0.032	$(-3.67 \pm 0.12) \times 10^{-2}$
2012	-2.43 ± 0.42	1.158 ± 0.016	$(-3.17 \pm 0.23) \times 10^{-3}$
2016	0.59 ± 0.31	1.123 ± 0.012	$(-3.33 \pm 0.13) \times 10^{-3}$
2017	0.70 ± 0.28	1.108 ± 0.012	$(-3.21 \pm 0.15) \times 10^{-3}$
2018	-2.00 ± 0.29	1.192 ± 0.015	$(-3.30 \pm 0.15) \times 10^{-3}$

Table 4.21.: The background fractions or yields in the $B^+ \to J/\psi K^{*+}$ DTF B^+ mass fits to collision data per year.

Year	$f(\text{rand. }\gamma)$	$f(\text{rand. }\gamma\gamma)$	$N^b_{B\to J/\psi K\pi\pi}$	$N^b_{exponent}$
2011	0.244 ± 0.032	0.150 ± 0.005	0 ± 25	$(4.45 \pm 0.23) \times 10^3$
2012	0.400 ± 0.041	0.1774 ± 0.0043	$(1.5 \pm 0.6) \times 10^3$	$(7.8 \pm 1.0) \times 10^3$
2016	0.348 ± 0.028	0.1841 ± 0.0042	$(1.3 \pm 0.5) \times 10^3$	$(1.516 \pm 0.036) \times 10^4$
2017	0.442 ± 0.031	0.1746 ± 0.0041	$(1.9 \pm 0.5) \times 10^3$	$(1.27 \pm 0.10) \times 10^4$
2018	0.398 ± 0.029	0.1837 ± 0.0043	$(3.0 \pm 0.7) \times 10^3$	$(1.34 \pm 0.12) \times 10^4$

4.6. Monte Carlo efficiencies

The Monte Carlo efficiencies, with the exception of the PID efficiencies, are determined as the sum of the weights determined by GBR (Section 4.3.1) after an analysis stage. The uncertainties are therefore assumed to follow Poissonian statistics. These efficiencies are divided into the different analysis stages: the Acceptance is the efficiency of the generation stage which primarily involves the ensuring that the generated simulation samples were within the acceptance of the LHCb, the Reconstruction and preselection stage which has the selections highlighted in Section 4.2.1 as well as the efficiency for the reconstruction of events, the trigger selection which were corrected by the factors given in Section 4.9, the BDT selection giving the efficiency of the BDT cut which was intended to be similar between the signal and normalisation channels and the PID selection efficiency which is given last due to the efficiency being determined from calibration samples and therefore being an external factor to be applied.

In general the acceptance increases with the collision energy, hence the increases from 2011 to 2012 and 2012 to Run-2. This is due to the higher collision energies giving a smaller opening angle for the B^+ decay products and so are more likely to be withing the forward acceptance of the LHCb detector. These changes are seen across all channels yet it appears that the neutral modes see a larger effect. In the reconstruction and preselection stage the efficiencies remained flat for all channels across years. As would be expected this efficiency decreases for every additional photon being reconstructed. Typically the BDT efficiencies seemed to be higher for Run-2 than Run-1 for all channels. There seemed to be more fluctuation in the PID efficiencies of different years as the response of the ProbNN variables are different for every year.

4.7. Systematic uncertainties

Due to the analysis strategy adopted in this study, the avoidance of many sources of systematic uncertainties was made possible. This is done by the alignment of selections between signal and normalisation channels, through the corrections of the Monte Carlo distributions before the training and application of the BDTs, along with using real collision data to determine the PID efficiencies and calibrating the efficiency of measuring backgrounds with one or more photon originating from the underlying event. There were also systematic uncertainties that were accounted for in the statistical uncertainties, this includes the uncertainties on the background signal yields due to their expectation being calculated using MC efficiencies and branching ratios. By applying Gaussian constrains, with the statistical uncertainties and the uncertainties on previous measurements of branching ratios as the width of the Gaussian, these uncertainties were accounted for in the fit uncertainties on the signal yields.

Table 4.22.: The reconstruction and selection efficiencies for the signal $B^+ \to \chi_{c1} K^+$ and $B^+ \to J/\psi K^+$ Monte-Carlo simulated data for all data-taking periods.

Year	$\varepsilon^{MC}_{B^+\to J/\psi K^+}/\%$	$\varepsilon^{MC}_{B^+\to (J/\psi\gamma)_{\chi_{c1}} K^+}/\%$	$\varepsilon^{MC}_{B^+\to (J/\psi\gamma)_{\chi_{c1}} K^+}/\varepsilon^{MC}_{B^+\to J/\psi K^+}/\%$
		Acceptance	
2011	15.968 ± 0.027	9.601 ± 0.018	60.13 ± 0.15
2012	16.273 ± 0.025	9.859 ± 0.017	60.58 ± 0.14
2016	17.361 ± 0.041	10.682 ± 0.027	61.53 ± 0.21
2017	17.338 ± 0.033	10.721 ± 0.026	61.83 ± 0.19
2018	17.346 ± 0.033	10.672 ± 0.025	61.52 ± 0.18
		Reconstruction and preselection	
2011	23.298 ± 0.015	10.272 ± 0.045	0.4409 ± 0.0020
2012	21.908 ± 0.015	9.522 ± 0.030	0.4346 ± 0.0014
2016	23.601 ± 0.015	10.542 ± 0.027	0.4467 ± 0.0012
2017	23.479 ± 0.015	10.551 ± 0.025	0.4494 ± 0.0011
2018	23.438 ± 0.015	10.654 ± 0.024	0.4545 ± 0.0011
		Trigger requirements	
2011	92.42 ± 0.06	93.28 ± 0.42	1.009 ± 0.005
2012	88.11 ± 0.06	90.33 ± 0.31	1.0251 ± 0.0036
2016	82.50 ± 0.06	85.77 ± 0.24	1.0396 ± 0.0030
2017	87.23 ± 0.06	89.18 ± 0.23	1.0223 ± 0.0027
2018	82.37 ± 0.06	86.07 ± 0.21	1.0450 ± 0.0026
		BDT selection	
2011	52.74 ± 0.05	56.93 ± 0.34	1.079 ± 0.007
2012	52.97 ± 0.05	55.79 ± 0.25	1.053 ± 0.005
2016	64.65 ± 0.06	63.09 ± 0.22	0.9759 ± 0.0035
2017	61.23 ± 0.05	60.07 ± 0.20	0.9811 ± 0.0033
2018	62.19 ± 0.06	59.23 ± 0.19	0.9524 ± 0.0031
		PID selection	
2011	86.96 ± 0.29	88.07 ± 0.34	1.013 ± 0.005
2012	86.14 ± 0.14	87.46 ± 0.17	1.0152 ± 0.0026
2016	88.94 ± 0.06	90.72 ± 0.06	1.0200 ± 0.0009
2017	85.27 ± 0.05	87.65 ± 0.06	1.0279 ± 0.0009
2018	85.32 ± 0.05	88.00 ± 0.05	1.0315 ± 0.0009
		Total	
2011	1.577 ± 0.006	0.4612 ± 0.0033	0.2924 ± 0.0023
2012	1.4335 ± 0.0029	0.4137 ± 0.0021	0.2886 ± 0.0015
2016	1.9437 ± 0.0023	0.5527 ± 0.0019	0.2844 ± 0.0011
2017	1.8541 ± 0.0021	0.5311 ± 0.0018	0.2865 ± 0.0010
2018	1.7770 ± 0.0020	0.5101 ± 0.0016	0.2871 ± 0.0010

Table 4.23.: The reconstruction and selection efficiencies for the signal $B^+ \to J/\psi K^{*+}$ and $B^+ \to J/\psi K^+$ Monte-Carlo simulated data for all data-taking periods.

Year	$\varepsilon^{MC}_{B^+\to J/\psi K^+}$ /%	$\varepsilon^{MC}_{B^+\to J/\psi (K^+\pi^0)_{K^{*+}}}$ /%	$\varepsilon^{MC}_{B^+\to J/\psi (K^+\pi^0)_{K^{*+}}} / \varepsilon^{MC}_{B^+\to J/\psi K^+}$ /%
		Acceptance	
2011	15.968 ± 0.027	6.511 ± 0.012	40.77 ± 0.10
2012	16.273 ± 0.025	6.690 ± 0.013	41.11 ± 0.10
2016	17.361 ± 0.041	7.293 ± 0.018	42.01 ± 0.14
2017	17.338 ± 0.033	7.298 ± 0.019	42.09 ± 0.13
2018	17.35 ± 0.033	7.278 ± 0.019	41.96 ± 0.13
		Reconstruction and preselection	
2011	23.298 ± 0.015	2.738 ± 0.016	11.75 ± 0.07
2012	21.908 ± 0.015	2.826 ± 0.012	12.90 ± 0.06
2016	23.601 ± 0.015	3.021 ± 0.012	12.80 ± 0.05
2017	23.479 ± 0.015	2.966 ± 0.012	12.63 ± 0.05
2018	23.438 ± 0.015	3.007 ± 0.012	12.83 ± 0.05
		Trigger requirements	
2011	92.42 ± 0.06	91.9 ± 0.6	99.5 ± 0.6
2012	88.11 ± 0.06	87.88 ± 0.41	99.7 ± 0.5
2016	82.50 ± 0.06	84.30 ± 0.36	102.18 ± 0.45
2017	87.23 ± 0.06	88.23 ± 0.38	101.15 ± 0.44
2018	82.37 ± 0.06	83.95 ± 0.37	101.9 ± 0.5
		BDT selection	
2011	79.04 ± 0.06	80.9 ± 0.5	102.4 ± 0.7
2012	78.47 ± 0.06	82.56 ± 0.43	105.2 ± 0.5
2016	84.44 ± 0.07	83.11 ± 0.39	98.4 ± 0.5
2017	84.15 ± 0.06	81.43 ± 0.39	96.8 ± 0.5
2018	84.74 ± 0.07	82.53 ± 0.40	97.4 ± 0.5
		PID selection	
2011	87.27 ± 0.30	91.79 ± 0.27	105.2 ± 0.5
2012	86.68 ± 0.15	91.60 ± 0.13	105.67 ± 0.23
2016	89.45 ± 0.06	94.26 ± 0.05	105.38 ± 0.09
2017	86.23 ± 0.06	92.73 ± 0.05	107.54 ± 0.09
2018	86.36 ± 0.05	93.085 ± 0.043	107.79 ± 0.08
		Total	
2011	2.372 ± 0.008	0.1218 ± 0.0009	5.134 ± 0.041
2012	2.1367 ± 0.0041	0.1256 ± 0.0007	5.879 ± 0.033
2016	2.5534 ± 0.0027	0.1455 ± 0.0007	5.698 ± 0.028
2017	2.5768 ± 0.0027	0.1442 ± 0.0007	5.597 ± 0.027
2018	2.4507 ± 0.0025	0.1411 ± 0.0007	5.759 ± 0.029

There were a few remaining statistical uncertainties that needed to be determined individually. These included the uncertainties on the choice of the PDFs used in the fits as they would not necessarily perfectly describe the DTF B mass distributions in reality. Therefore an uncertainty could be determined by refitting and extracting the signal yield with a different PDF. This was done twice, once with different signal PDF choices and again with different combinatorial background PDF choices. Another source of uncertainty can arise from the requirements that the signal must have triggered either `L0Muon` or `L0DiMuon` algorithms. The trigger algorithms are varied within each data-taking period and contain different thresholds for the muon transverse momenta and the number of SPD hits. Each algorithm and hence their associated thresholds are assigned a Trigger Configuration Key (TCK) for their identification. Yet in simulation only the most common TCK was used so the Monte Carlo efficiencies for the trigger are different from those of the collision data. In principle, this difference would be the same for all samples if the $J/\psi \to \mu^+\mu^-$ kinematics and event occupancy were similar. Corrections were found using the $B^+ \to J/\psi K^+$ sample and the uncertainty on this correction was assigned as a systematic uncertainty.

There were also variations made in the B mass fitting boundaries to check the stability of the fit models over wider or narrower ranges. This tests the effect on the free background yields and hence the signal yields. The mass windows used would not cancel in the ratio of the signal channels over the normalisation and so must be tested. Therefore these were also varied to check their effect on the signal yield and efficiency ratios to determine how well estimated the Monte Carlo efficiencies were. Another efficiency that may not cancel in the ratios were the BDT efficiencies, so they were evaluated with and without the application of the GBR weights and their difference in Monte Carlo efficiencies were assigned as a systematic.

4.7.1. Fit model choice

Table 4.24.: The systematic uncertainties on the measured yields of the binned maximum likelihood fits due to the choice of signal PDF.

Year	Unc. on $N^s_{B^+\to J/\psi K^+}$ /%	Unc. on $N^s_{B^+\to (J/\psi\gamma)_{\chi_{c1}} K^+}$ /%	Unc. on $N^s_{B^+\to J/\psi (K^+\pi^0)_{K^{*+}}}$ /%
11	0.11	0.17	0.7
12	0.01	0.23	0.4
16	0.11	0.05	0.4
17	0.23	0.13	0.8
18	0.25	0.11	2.7

Table 4.25.: The systematic uncertainties on the measured yields of the binned maximum likelihood fits due to the choice of combinatorial background PDF.

Year	Unc. on $N^{s}_{B^+ \to J/\psi K^+}$ /%	Unc. on $N^{s}_{B^+ \to (J/\psi\gamma)_{\chi_{c1}} K^+}$ /%	Unc. on $N^{s}_{B^+ \to J/\psi (K^+\pi^0)_{K^{*+}}}$ /%
11	0.09	0.14	0.7
12	0.20	0.19	0.8
16	0.08	0.90	1.4
17	0.09	0.18	0.7
18	0.02	0.18	0.3

There is imperfect knowledge of the $B^0_{(s)}$ mass descriptions of the signal and background distributions. The models used may come with their own biases that needed to be tested for. The associated systematic uncertainty of this was determined by performing all of the fits with a different signal model PDF. The Monte Carlo simulated samples were fit with the alternative model, fixing the tail parameters and using the same methodology as the nominal fitting procedure to measure the signal yields. A systematic is assigned as the difference between the nominal and newly measured signal yields. The chosen alternative model was the double-sided Crystal Ball function. This is a similar function with asymmetric tails, usually preferred for fits of lower statistics than found in this analysis. The resulting uncertainties on the signal yields are shown in Table 4.24

In the fits of collision data it is assumed that the combinatorial background is well estimated by the model of an exponential function. In a similar method to the one used for the systematic on the signal PDFs, the fits to collision data are repeated using alternative models, a second order and a third order Chebychev polynomial. The systematic uncertainty is assigned as the RMS uncertainty of the nominal fit and the two alternatives. This gives uncertainties on the signal yields summarised in Table 4.25.

4.7.2. PID calibration binning scheme

There was the issue that the binning scheme of the calibration, for some events, could not produce a PID efficiency. This sometimes occurred when the sWeights in the calibration sample were produced in a region where too low statistics are found and therefore could create a negative weight and so efficiency. More commonly, this occurred when the Monte Carlo samples used in this analysis had a small number of outlier events outside of the binning range. In both of these cases there needed to be an additional systematic uncertainty on the efficiency equal to the fraction of events that fell into these two categories. These are shown in

Table 4.26.: The systematic uncertainties on the binning of the PID calibration samples.

Year	Unc. on $\varepsilon^{MC}_{B^+\to J/\psi K^+}$ /%	Unc. on $\varepsilon^{MC}_{B^+\to (J/\psi\gamma)_{\chi_{c1}} K^+}$ /%	Unc. on $\varepsilon^{MC}_{B^+\to J/\psi (K^+\pi^0)_{K^{*+}}}$ /%
11	0.42	0.20	0.05
12	0.64	0.23	0.08
16	0.92	0.37	0.05
17	0.92	0.35	0.07
18	0.93	0.34	0.08

Table 4.26. The probability that the kaon had a momentum larger than the binning sample was higher for $B^+ \to J/\psi K^+$ due to its higher available phase-space, leading to a larger uncertainty.

4.7.3. Varying the DTF B mass boundaries in data fits

Table 4.27.: The systematic uncertainties on the measured yields of the binned maximum likelihood fits due to the fitting boundaries.

Year	Unc. on $N^s_{B^+\to J/\psi K^+}$ /%	Unc. on $N^s_{B^+\to (J/\psi\gamma)_{\chi_{c1}} K^+}$ /%	Unc. on $N^s_{B^+\to J/\psi (K^+\pi^0)_{K^{*+}}}$ /%
11	0.22	0.87	1.0
12	0.21	0.51	1.1
16	0.07	0.60	1.0
17	0.26	0.74	0.32
18	0.26	0.51	0.23

The mass fit results may have been dependent on the DTF B mass ranges used, it was important that the variation in the measured signal yields due to the variation of these boundaries be assessed. This uncertainty is indicative of how well modelled the combinatorial background is, or if there are missing background components close to the fit boundaries. Therefore the boundaries were either widened or tightened symmetrically by 50 MeV to estimate the scale of this variation. Therefore the variations of the signal yields are incidental to the changes in the resulting amplitude of the combinatorial background around the signal region. The uncertainties assigned in Table 4.27 were determined at the RMS uncertainty of the nominal, wider and narrower fit ranges. It is clear that he effect was more significant from 2011 to 2016 in the fits of $B^+ \to J/\psi K^{*+}$ data, this is likely due to the low mass partially reconstructed background of $B^+ \to J/\psi K^+{}_1$ which had a free yield in fits.

4.7.4. Varying the mass windows in data fits

Table 4.28.: The systematic uncertainties on the ratio of measured yields of the binned maximum likelihood fits over the Monte Carlo efficiencies due to the mass windows.

Year	Unc. on $\left(\frac{N^s}{\varepsilon^{MC}}\right)_{\chi_{c1}\to J/\psi\gamma}$ /%	Unc. on $\left(\frac{N^s}{\varepsilon^{MC}}\right)_{K^{*+}\to K^+\pi^0}$ /%	Unc. on $\left(\frac{N^s}{\varepsilon^{MC}}\right)_{\pi^0\to\gamma\gamma}$ /%
11	0.69	0.64	1.20
12	0.58	0.74	1.06
16	0.61	1.56	0.44
17	0.31	0.78	1.57
18	0.27	0.17	1.59

For the mass windows used, there may be a difference in the real collision data and Monte Carlo simulation efficiencies. Since these are some of the largest differences in the selections of signal and normalisation channels it was important that the variation in the ratio of signal yields and Monte Carlo efficiencies be determined for changes in these selections. For $\chi_{c1} \to J/\psi\gamma$ and $K^{*+} \to K^+\pi^0$ windows, a roughly $\pm 3\sigma$ mass requirement was used in the nominal result, so the variation chosen was to use tighter $\pm 2.5\sigma$ selections and looser $\pm 3.5\sigma$ selections. For the $\pi^0 \to \gamma\gamma$ window, the mass requirement was $\pm 60\,\text{MeV} \sim \pm 6\sigma$ therefore tighter selections of $\pm 3\sigma$ and $\pm 2.5\sigma$ were used in the assessment of systematic uncertainty. The RMS uncertainties of the ratio of signal yields and MC efficiencies were calculated for the three selections and assigned as the systematic uncertainty on the mass windows as shown in Table 4.28.

4.7.5. BDT efficiencies

Table 4.29.: The systematic uncertainties on the ratio of measured yields of the binned maximum likelihood fits over the Monte Carlo efficiencies due to the mass windows.

Year	Unc. on $\varepsilon^{MC}_{B^+\to J/\psi K^+}$ /%	Unc. on $\varepsilon^{MC}_{B^+\to (J/\psi\gamma)_{\chi_{c1}} K^+}$ /%	Unc. on $\varepsilon^{MC}_{B^+\to J/\psi (K^+\pi^0)_{K^{*+}}}$ /%
11	1.9	3.9	2.1
12	2.0	2.5	1.7
16	0.9	0.8	0.5
17	1.1	0.9	0.1
18	1.3	2.6	0.8

A principal aim of the reweighting of the Monte Carlo was to align the BDT input variables to improve the reliability of the measured BDT efficiencies. To determine the systematic on these efficiencies the relative difference in the Monte Carlo efficiencies with and without reweighting was used. These relative differences are assigned as uncertainties shown in Table 4.29. From the efficiencies given in Tables 4.22 and 4.23, it can be seen that the Run-1 BDT efficiencies were typically lower than that of the Run-2, this seemed to cause larger variation in the efficiency differences and so a typically larger uncertainty on the results.

4.7.6. Total of systematic uncertainties

Table 4.30.: The sources of systematic uncertainty for the measurement of each of the correction factors and their contributions as a percentage.

Year	Unc. on $\mathcal{R}_{\gamma}/\%$	Unc. on $\mathcal{R}_{\pi^0}/\%$
11	4.6	3.4
12	3.5	3.3
16	2.0	2.7
17	1.9	2.4
18	3.2	2.5

Under the assumption that the uncertainties assessed in this section, taking the quadratic sum of all uncertainties summarised in this section, as well as the uncertainty on the trigger efficency corrections given in Section 4.3.4, supplies the uncertainty for the correction factors shown in Table 4.30. These uncertainties were well below the external uncertainty supplied by the previously measured branching ratios of the signal and normalisation channels. Therefore the overall control of uncertainties were sufficient for the precision limit of this analysis.

Table 4.31.: The photon reconstruction efficiencies calculated from data signal yields.

Year	$\varepsilon(\gamma)/\%$	$\varepsilon(\pi^0)/\%$
2011	$30.8 \pm 0.4(stat) \pm 1.8(\mathcal{B})$	$4.56 \pm 0.18(stat) \pm 0.27(\mathcal{B})$
2012	$30.1 \pm 0.2(stat) \pm 1.7(\mathcal{B})$	$4.46 \pm 0.04(stat) \pm 0.26(\mathcal{B})$
2016	$28.2 \pm 0.2(stat) \pm 1.6(\mathcal{B})$	$4.55 \pm 0.08(stat) \pm 0.27(\mathcal{B})$
2017	$28.9 \pm 0.2(stat) \pm 1.7(\mathcal{B})$	$4.49 \pm 0.09(stat) \pm 0.26(\mathcal{B})$
2018	$28.2 \pm 0.2(stat) \pm 1.6(\mathcal{B})$	$4.53 \pm 0.09(stat) \pm 0.27(\mathcal{B})$

Table 4.32.: The photon reconstruction efficiencies calculated from Monte Carlo efficiencies.

Year	$\varepsilon(\gamma)/\%$	$\varepsilon(\pi^0)/\%$
2011	$29.24 \pm 0.23(stat)$	$5.134 \pm 0.041(stat)$
2012	$28.86 \pm 0.15(stat)$	$5.879 \pm 0.033(stat)$
2016	$28.44 \pm 0.11(stat)$	$5.698 \pm 0.028(stat)$
2017	$28.65 \pm 0.10(stat)$	$5.597 \pm 0.027(stat)$
2018	$28.71 \pm 0.10(stat)$	$5.759 \pm 0.029(stat)$

4.8. Photon reconstruction efficiencies and correction factors

With the signal yields extracted from the B^+ DTF mass fits, and the branching ratios of the signal and normalisation channels, the reconstruction efficiency of a photon measured with these selections is calculated as

$$\varepsilon^{\text{data}}(\gamma) = \frac{N^s_{B^+\to\chi_{c1}K^+}}{N^s_{B^+\to J/\psi K^+}} \frac{\mathcal{B}_{B^+\to J/\psi K^+}}{\mathcal{B}_{B^+\to\chi_{c1}K^+}\mathcal{B}_{\chi_{c1}\to\gamma J/\psi}}, \tag{4.2}$$

and the reconstruction efficiency of a π^0 is calculated as

$$\varepsilon^{\text{data}}(\pi^0) = \frac{N^s_{B^+\to J/\psi K^{*+}}}{N^s_{B^+\to J/\psi K^+}} \frac{\mathcal{B}_{B^+\to J/\psi K^+}}{\mathcal{B}_{B^+\to J/\psi K^{*+}}\mathcal{B}_{K^{*+}\to K^+\pi^0}\mathcal{B}_{\pi^0\to\gamma\gamma}}, \tag{4.3}$$

where the signal yields are given in Tables 4.12 and 4.13. These calculations result in the efficiencies summarised in Table 4.31.

The Monte Carlo efficiencies in Tables 4.22 and 4.23 can be used to determine the same reconstruction efficiencies as

$$\varepsilon^{\text{MC}}(\gamma) = \frac{\varepsilon^{MC}_{B^+\to\chi_{c1}K^+}}{\varepsilon^{MC}_{B^+\to J/\psi K^+}}, \tag{4.4}$$

and

$$\varepsilon^{\text{MC}}(\pi^0) = \frac{\varepsilon^{MC}_{B^+\to J/\psi K^{*+}}}{\varepsilon^{MC}_{B^+\to J/\psi K^+}}, \tag{4.5}$$

leading to the photon and π^0 efficiencies as seen in Table 4.32.

From these two efficiencies the γ correction factor is calculated as

$$\mathcal{R}_{\gamma} = \frac{N^{s}_{B^{+}\to\chi_{c1}K^{+}}}{N^{s}_{B^{+}\to J/\psi K^{+}}} \times \frac{\varepsilon^{MC}_{B^{+}\to J/\psi K^{+}}}{X^{PID}_{\gamma}\varepsilon^{MC}_{B^{+}\to\chi_{c1}K^{+}}} \times \frac{\mathcal{B}_{B^{+}\to J/\psi K^{+}}}{\mathcal{B}_{B^{+}\to\chi_{c1}K^{+}} \times \mathcal{B}_{\chi_{c1}\to J/\psi\gamma}}, \tag{4.6}$$

which is used to calculate the correction factors for the data-taking years as

$$\mathcal{R}^{corr}_{\gamma}(2011) = (105.3 \pm 1.5(stat) \pm 4.8(syst) \pm 6.1(\mathcal{B}))\%\,, \tag{4.7}$$
$$\mathcal{R}^{corr}_{\gamma}(2012) = (104.5 \pm 1.0(stat) \pm 3.7(syst) \pm 6.0(\mathcal{B}))\%\,, \tag{4.8}$$
$$\mathcal{R}^{corr}_{\gamma}(2016) = (99.2 \pm 0.7(stat) \pm 2.0(syst) \pm 5.7(\mathcal{B}))\%\,, \tag{4.9}$$
$$\mathcal{R}^{corr}_{\gamma}(2017) = (100.7 \pm 0.7(stat) \pm 1.9(syst) \pm 5.8(\mathcal{B}))\%\,, \tag{4.10}$$
$$\mathcal{R}^{corr}_{\gamma}(2018) = (98.3 \pm 0.6(stat) \pm 3.1(syst) \pm 5.7(\mathcal{B}))\%\,. \tag{4.11}$$

The π^0 correction factors for each year are

$$\mathcal{R}^{corr}_{\pi^0}(2011) = (88.8 \pm 3.5(stat) \pm 3.0(syst) \pm 5.2(\mathcal{B}))\%\,, \tag{4.12}$$
$$\mathcal{R}^{corr}_{\pi^0}(2012) = (75.8 \pm 1.8(stat) \pm 2.5(syst) \pm 4.5(\mathcal{B}))\%\,, \tag{4.13}$$
$$\mathcal{R}^{corr}_{\pi^0}(2016) = (79.9 \pm 1.5(stat) \pm 2.1(syst) \pm 4.7(\mathcal{B}))\%\,, \tag{4.14}$$
$$\mathcal{R}^{corr}_{\pi^0}(2017) = (80.2 \pm 1.6(stat) \pm 1.9(syst) \pm 4.7(\mathcal{B}))\%\,, \tag{4.15}$$
$$\mathcal{R}^{corr}_{\pi^0}(2018) = (78.6 \pm 1.6(stat) \pm 1.6(syst) \pm 4.6(\mathcal{B}))\%\,. \tag{4.16}$$

4.9. Discussion of results

There was a previous study of the photon reconstruction efficiencies at LHCb performed using Run-1 data [123]. In this study there were a number of differences in the analysis strategy, the biggest difference being that they did not use $B^+ \to \chi_{c1}K^+$ to analyse single photon efficiencies but made the assumption that the square root of the π^0 correction would suffice. In the selection requirements this thesis uses a multivariate analysis to remove combinatorial backgrounds to a level where physics backgrounds became more noticeable. In the fitting strategy of $B^+ \to J/\psi K^{*+}$ there was most noticeably no measurement of the background where signal tracks were combined with underlying event photons. A background that the signal yields were very sensitive to due to its mean position underneath the signal. There was also a different strategy for Monte Carlo corrections, where weights were found using histogram division with just the B^+ transverse momentum and pseudorapidity. There were no corrections for the non-resonant component of $B^+ \to J/\psi K^+\pi^0$ which is a significant background when considering that, in the calculation of the correction factors, the precise $B^+ \to J/\psi K^{*+}$ and $K^{*+} \to K^+\pi^0$ branching ratios are explicitly used. All of these factors together lead to strikingly large differences in the central value of the results where they have the corrections as

$$\mathcal{R}_{\pi^0}(2011) = (103.2 \pm 2.6\,(\text{stat}) \pm 2.3\,(\text{syst}) \pm 6.7(\mathcal{B}))\%, \tag{4.17}$$
$$\mathcal{R}_{\pi^0}(2012) = (105.6 \pm 1.8\,(\text{stat}) \pm 1.6\,(\text{syst}) \pm 6.7(\mathcal{B}))\%, \tag{4.18}$$

which are incompatible to more than two σ when considering just the statistical and systematic uncertainties, as the branching fractions are the same. The uncertainties in this thesis are particularly due to the inclusion of the uncertainty on the mass windows and and boundaries. These were not investigated in the older study and have been shown to have large effects on the overall result.

Another important test was performed in this analysis, to determine if the reconstruction efficiencies of the π^0 were simply the square of the photon reconstruction efficiencies. This is an assumption that was made in [123] which would have fortunately meant that, in the conversion of π^0 efficiency corrections to single photon corrections, the uncertainties would be reduced by a factor $\sqrt{2}$. Yet in this thesis the results suggest that, by directly measuring the single photon reconstruction efficiencies independently from the π^0 reconstruction efficiencies, this assumption does not hold well. The square root of the π^0 corrections are

$$\sqrt{\mathcal{R}^{\text{corr}}_{\pi^0}(2011)} = (94.2 \pm 1.8(stat) \pm 1.5(syst) \pm 2.6(\mathcal{B}))\%\,, \tag{4.19}$$
$$\sqrt{\mathcal{R}^{\text{corr}}_{\pi^0}(2012)} = (87.1 \pm 0.4(stat) \pm 1.8(syst) \pm 2.3(\mathcal{B}))\%\,, \tag{4.20}$$
$$\sqrt{\mathcal{R}^{\text{corr}}_{\pi^0}(2016)} = (89.4 \pm 0.8(stat) \pm 1.1(syst) \pm 2.4(\mathcal{B}))\%\,, \tag{4.21}$$
$$\sqrt{\mathcal{R}^{\text{corr}}_{\pi^0}(2017)} = (89.6 \pm 0.8(stat) \pm 0.9(syst) \pm 2.3(\mathcal{B}))\%\,, \tag{4.22}$$
$$\sqrt{\mathcal{R}^{\text{corr}}_{\pi^0}(2018)} = (88.7 \pm 0.8(stat) \pm 0.8(syst) \pm 2.3(\mathcal{B}))\%\,. \tag{4.23}$$

These values have a consistent average difference across all years of about 12 MeV which is about a 2σ disagreement. Therefore corrections to the single photon reconstruction efficiencies should use the result of using $B^+ \to \chi_{c1} K^+$ and so will be subject to the larger uncertainties seen in this direct result. These are chiefly originating from the uncertainty on the branching fractions of $\mathcal{B}\,(B^+ \to \chi_{c1} K^+)$ and $\mathcal{B}\,(\chi_{c1} \to J/\psi\gamma)$. Therefore the prospects for improved precision on these corrections are dependent on a better understanding of these two branching fractions. The most precise measurements so far originate from studies from the BaBar collaboration in 2008 [124] and the Belle collaboration in 2011 [125]. Therefore Belle II would be in a good position to continue producing precise measurements of B to charmonia branching fractions, which remain very competitive due to the experiment having much lower backgrounds in e^+e collisions when compared to the LHCb experiment.

Chapter 5.

Measuring the Branching Ratios of $B^0_{(s)} \to J/\psi\eta^{(\prime)}$ and η-η' Mixing

With the efficiency corrections for photon and π^0 reconstruction, the efficiencies of the reconstruction of the photons in $B^0_{(s)} \to J/\psi\eta^{(\prime)}$ with the final states $\eta \to \pi^+\pi^-\gamma$, $\eta \to \pi^+\pi^-\pi^0$, $\eta' \to \rho^0\gamma$ and $\eta' \to \pi^+\pi^-\eta[\gamma\gamma]$ could be well known. These efficiencies are particularly important in the measurement of the absolute branching ratios of $B^0_{(s)} \to J/\psi\eta^{(\prime)}$ normalised to $B^0 \to J/\psi\rho^0$ where the differences in simulated and real data efficiencies would not cancel. This chapter describes both the measurement of these absolute branching fractions of $B^0_{(s)} \to J/\psi\eta^{(\prime)}$ and the mixing of η-η' mesons, as was introduced in Section 3.1. In a similar structure to the previous chapter this chapter summarises the event selections specifically for the $\eta^{(\prime)}$ mesons and their decay products in Section 5.2, the corrections made to the simulation samples in Section 5.3, the specifics of the fits to simulated and collision data to determine signal yields in Section 5.5.6 and the corrected Monte Carlo efficiencies separated by analysis stage (in the same way as the previous chapter) in Section 5.6. All of these sections then lead to the results of Section 5.8.

5.1. Simulation samples

Similarly to the photon reconstruction study, the simulation samples were required to be of a sufficiently up-to-date simulation version. This is to ensure the major properties of the simulation were produced under similar conditions. Separate simulation samples were used for the $B^0 \to J/\psi\eta^{(\prime)}$ and $B^0_s \to J/\psi\eta^{(\prime)}$ to ensure that the subtleties of the difference in resolution for the B^0 and B^0_s reconstruction are taken into account, as well as the difference in efficiencies, principally caused by the different available phase-spaces of the two decays. Note that only 2016 MC samples are used for this analysis, as shown in Tables 5.1 and 5.3. For the normalisation ($B^0 \to J/\psi\rho^0$ with $\rho^0 \to \pi^+\pi^-$) and control channel used in the reweighting procedure ($B^0 \to J/\psi K^{*0}$ with $K^{*0} \to K^+\pi^-$) see Table 5.4. In the decay of $B^0_{(s)} \to J/\psi\eta'$ with

Table 5.1.: List of the stripping versions used for each Monte Carlo $B^0_s \to J/\psi\eta^{(\prime)}$ signal data-set and the corresponding number of events generated.

Decay Channel	Gen. Cuts	Year	Magnet Polarity	Stripping	N(events)
$B^0_s \to J/\psi\eta$					
$\eta \to \pi^+\pi^-\gamma$	Acc.	2012	Up	v21	504999
		2012	Down	v21	503000
		2016	Up	v28r2	505000
		2016	Down	v28r2	509915
$\eta \to \pi^+\pi^-\pi^0$	Acc.	2015	Up	v24r2	569758
		2015	Down	v24r2	500034
		2016	Up	v28r1	1517485
		2016	Down	v28r1	1528126
		2016	Up	v28r2	527835
		2016	Down	v28r2	527835
		2017	Up	v29r2	1003363
		2017	Down	v29r2	1104122
		2018	Up	v34	1079621
		2018	Down	v34	1141007
$B^0_s \to J/\psi\eta'$					
$\eta' \to \rho^0\gamma$	Acc.	2012	Up	v21	1510492
		2012	Down	v21	1561350
		2015	Up	v24r2	505109
		2015	Down	v24r2	506538
		2016	Up	v28r2	1525642
		2016	Down	v28r2	1502633
		2017	Up	v29r2	2007219
		2017	Down	v29r2	2006185
		2018	Up	v34	2123957
		2018	Down	v34	2001632
$\eta' \to \pi^+\pi^-\eta$	Acc.	2015	Up	v24r2	535353
		2015	Down	v24r2	569714
		2016	Up	v28r2	1507152
		2016	Down	v28r2	1507024

Table 5.2.: List of the stripping versions used for each Monte Carlo $B^0_s \to J/\psi\eta^{(\prime)}$ signal data-set and the corresponding number of events generated.

Decay Channel	Gen. Cuts	Year	Magnet Polarity	Stripping	N(events)
$B^0_s \to J/\psi\eta$					
$\eta \to \pi^+\pi^-\gamma$	Acc., Tight	2011	Up	v21r1	383000
		2011	Down	v21r1	377921
		2012	Up	v21	376999
		2012	Down	v21	380618
		2015	Up	v24r2	275046
		2015	Down	v24r2	276773
		2016	Up	v28r2	381000
		2016	Down	v28r2	375000
		2017	Up	v29r2	752268
		2017	Down	v29r2	750099
		2018	Up	v34	772667
		2018	Down	v34	760622
$\eta \to \pi^+\pi^-\pi^0$	Acc., Tight	2011	Up	v21r1	250747
		2011	Down	v21r1	256201
		2012	Up	v21	507663
		2012	Down	v21	503901
$B^0_s \to J/\psi\eta'$					
$\eta' \to \rho^0\gamma$	Acc., Tight	2011	Up	v21r1	380333
		2011	Down	v21r1	377965
$\eta' \to \pi^+\pi^-\eta$	Acc., Tight	2011	Up	v21r1	376468
		2011	Down	v21r1	378927
		2012	Up	v21	630419
		2012	Down	v21	628835
		2017	Up	v29r2	632199
		2017	Down	v29r2	638004
		2018	Up	v34	625624
		2018	Down	v34	629138

Table 5.3.: List of the stripping versions used for each Monte Carlo $B^0 \to J/\psi\eta^{(\prime)}$ signal data-set and the corresponding number of events generated.

Decay Channel	Gen. Cuts	Year	Magnet Polarity	Stripping	N(events)
$B^0 \to J/\psi\eta$					
$\eta \to \pi^+\pi^-\gamma$	Acc.	2012	Up	v21	500902
		2012	Down	v21	507000
		2016	Up	v28r2	500997
		2016	Down	v28r2	500999
$\eta \to \pi^+\pi^-\pi^0$	Acc.	2016	Up	v28r2	1001793
		2016	Down	v28r2	1048622
		2017	Up	v29r2	1000301
		2017	Down	v29r2	1143677
		2018	Up	v34	1043178
		2018	Down	v34	1004731
$B^0 \to J/\psi\eta'$					
$\eta' \to \rho^0\gamma$	Acc.	2012	Up	v21	505000
		2012	Down	v21	503000
		2016	Up	v28r2	502998
		2016	Down	v28r2	501795
$\eta' \to \pi^+\pi^-\eta$	Acc.	2012	Up	v21	501000
		2012	Down	v21	503000
		2016	Up	v28r2	503846
		2016	Down	v28r2	503000

Table 5.4.: List of the stripping versions used for each Monte Carlo $B^0 \to J/\psi\rho^0$ normalisation and $B^0_s \to J/\psi K^{*0}$ control data-set and the corresponding number of events generated.

Decay Channel	Gen. Cuts	Year	Magnet Polarity	Stripping	N(events)
Normalisation					
$B^0 \to J/\psi\rho^0$	Acc.	2011	Up	v21r1	1025668
		2011	Down	v21r1	1000677
		2012	Up	v21	1006701
		2012	Down	v21	1160031
		2015	Up	v24r2	501947
		2015	Down	v24r2	500074
		2016	Up	v28r2	5004032
		2016	Down	v28r2	5070415
		2017	Up	v29r2	6154606
		2017	Down	v29r2	5000342
		2018	Up	v34	5151574
		2018	Down	v34	5524075
Control					
$B^0_s \to J/\psi K^{*0}$	Acc.	2011	Up	v21r1	5031100
		2011	Down	v21r1	5001989
		2012	Up	v21	5000741
		2012	Down	v21	5003370
		2015	Up	v24r2	5002796
		2015	Down	v24r2	5007891
		2016	Up	v28r2	5064565
		2016	Down	v28r2	5008395
		2017	Up	v29r2	5003787
		2017	Down	v29r2	5007707
		2018	Up	v34	5000153
		2018	Down	v34	5000010

Table 5.5.: List of the stripping versions used for each Monte Carlo $B^0 \to J/\psi\phi$, $B^0 \to J/\psi X$ and $B^+ \to J/\psi X$ background data-set and the corresponding number of events generated.

Decay Channel	Gen. Cuts	Year	Magnet Polarity	Stripping	N(events)
$B^0 \to J/\psi\phi$	Acc.	2016	Up	v28r2	1016673
		2016	Down	v28r2	1009219
		2017	Up	v29r2	2003827
		2017	Down	v29r2	2005935
		2018	Up	v34	1975214
		2018	Down	v34	2004996
$B^0 \to J/\psi X$	Acc.	2016	Up	v28r2	4950339
		2016	Down	v28r2	4986926
$B^+ \to J/\psi X$	Acc.	2016	Up	v28r2	5956066
		2016	Down	v28r2	5052491

$\eta' \to \rho^0\gamma$ there were physics backgrounds present before the tight selections that required modelling in the optimisation process (see Section 5.4.2) and their samples are given in Table 5.5.

Unlike the samples used in the photon reconstruction study, the selections applied at the level of Monte Carlo generation only required that all particles were within the acceptance of the LHCb experiment. Therefore the efficiencies at generation were larger and are indicative of only the acceptance of the experiment itself.

5.2. Event selection

5.2.1. Preselections

With the principal aim of keeping the selection criteria across channels as equal as possible the general selections on the $\pi^+\pi^-$ pairs, $\mu^+\mu^-$ pairs, J/ψ and $B^0_{(s)}$ were kept the same across the different decay channels. Again, all of the selections on the $J/\psi \to \mu^+\mu^-$ and B that are summarised in Section 3.4 were also applied to this analysis. Selections on the $\eta^{(\prime)} \to \pi^+\pi^-X^0$ were kept as similar as possible for the same number of photons (*i.e.* between the two cases where $X^0 = \gamma$ and between the cases where $X^0 \to \gamma\gamma$). With these constraints on selection criteria taken into account, this section describes the full preselections which are summarised in Table 5.6.

The pions were selected in the same way as $B^0 \to J/\psi K^{*0}$ with $K^{*0} \to K^+\pi^-$, as shown in Section 4.2.1, using the Stripping containers `StdLoosePions` with their identification ensured

Table 5.6.: Summary of preselections on all decay modes. In this table these selections are in addition to those described in Section 3.4

	Variable	Requirement
$\pi^\pm$	$\mathcal{P}_\pi$	> 0.1
	$\mathcal{P}_\pi(1-\mathcal{P}_K)$	> 0.2
$\eta \to \pi^+\pi^-\gamma$	$\chi^2_{\text{vtx}}/\text{ndf}$	< 25
	$p_{\text{T}}(\gamma)$	$> 500\,\text{MeV}$
	IsNotH	> 0.05
	$p_{\text{T}}(\eta)$	$> 1.5\,\text{GeV}$
	$\|m(\pi^+\pi^-\gamma) - m(\eta)\|$	$< 100\,\text{MeV}$
$\eta' \to \rho^0\gamma$	$p_{\text{T}}(\gamma)$	$> 500\,\text{MeV}$
	IsNotH	> 0.05
	$p_{\text{T}}(\eta')$	$> 1.5\,\text{GeV}$
	$\|m(\pi^+\pi^-\gamma) - m(\eta')\|$	$< 100\,\text{MeV}$
$\rho^0 \to \pi^+\pi^-$	$\chi^2_{\text{vtx}}/\text{ndf}$	< 25
	$m(\rho^0)$	$\in [600, 900]\,\text{MeV}$
$\eta \to \pi^+\pi^-\pi^0$	$\chi^2_{\text{vtx}}/\text{ndf}$	< 25
	$p_{\text{T}}(\pi^0)$	$> 1\,\text{GeV}$
	$p_{\text{T}}(\eta)$	$> 1.5\,\text{GeV}$
	$\|m(\pi^+\pi^-\gamma\gamma) - m(\eta)\|$	$< 100\,\text{MeV}$
$\pi^0 \to \gamma\gamma$	$p_{\text{T}}(\gamma)$	$> 200\,\text{MeV}$
	Min. IsNotH	> 0.05
	$\|m(\gamma\gamma) - m(\pi^0)\|$	$< 60\,\text{MeV}$
$\eta' \to \pi^+\pi^-\eta$	$\chi^2_{\text{vtx}}/\text{ndf}$	< 25
	$p_{\text{T}}(\eta)$	$> 1\,\text{GeV}$
	$p_{\text{T}}(\eta')$	$> 1.5\,\text{GeV}$
	$\|m(\pi^+\pi^-\gamma\gamma) - m(\eta')\|$	$< 100\,\text{MeV}$
$\eta \to \gamma\gamma$	$p_{\text{T}}(\gamma)$	$> 200\,\text{MeV}$
	Min. IsNotH	> 0.05
	$\|m(\gamma\gamma) - m(\eta)\|$	$< 100\,\text{MeV}$

by a combination of two cuts on the artificial neural network variables (see Section 2.2.4) $\text{ProbNN}_\pi > 0.1$ and $\text{ProbNN}_\pi \times (1 - \text{ProbNN}_K) > 0.2$.

The selection of photons in all $\eta^{(\prime)}$ decays were done initially using the `StdLooseAllPhotons` stripping container. A minimum transverse momentum requirement of $p_{\mathrm{T}}^{\gamma} > 500\,\text{MeV}$ for single photon modes and $\eta \to \gamma\gamma$ and lower requirement of $p_{\mathrm{T}}^{\gamma} > 200\,\text{MeV}$ for $\pi^0 \to \gamma\gamma$ was used to initially reduce photon combinatorics. For identification the photons had a loose requirement determined by the ANN-based PID variable (see Section 2.3.2) $\text{IsNotH} > 0.05$.

The good vertex fit of the two pions was ensured with a requirement that $\chi^2_{\text{vtx}}/\text{ndf} < 25$ for $\eta^{(\prime)} \to \pi^+\pi^- X^0$ and $\rho^0 \to \pi^+\pi^-$. All intermediary resonances have initial mass requirements to have a loose agreement between their reconstructed mass and the mass of the desired parent decay. The mass requirements were such that the mass of the $\rho^0 \to \pi^+\pi^-$ were in the range $[600, 900]\,\text{MeV}$, the $\eta^{(\prime)}$ mesons were within $\pm 100\,\text{MeV}$ of their respective expected masses (from the Particle Data Group's latest averages in [41]) and the π^0 meson was within 60 MeV of its expected mass.

The decaying intermediary mesons also had reasonably high transverse momentum requirements in the early-stage selection requirements to further reduce combinatorial backgrounds. The requirement on the four $\eta^{(\prime)} \to \pi^+\pi^- X$ modes was $p_{\mathrm{T}}(\eta^{(\prime)}) > 1.5\,\text{GeV}$ and the two photon $(\eta/\pi^0 \to \gamma\gamma)$ modes was $p_{\mathrm{T}}(\eta/\pi^0) > 1\,\text{GeV}$.

5.2.2. Mass Vetoes

For the normalisation channel, $B^0 \to J/\psi\rho^0$ with $\rho^0 \to \pi^+\pi^-$, there were mass vetoes determined using the DTF 4-vectors in order to reconstruct different mass hypotheses for one of the pions in $\rho^0 \to \pi^+\pi^-$. This was done specifically to remove the backgrounds of $B^0 \to J/\psi K^{*0}$ with $K^{*0} \to K^+\pi^-$ and $B^+ \to J/\psi K^+$. Yet since there were two possible options for the π-K PID swap, the π with the highest PID probability of ProbNN_K was the one that was measured with the K mass hypothesis and then vetoed at 30 MeV from the B^0 or B^+ mass at about 5280 MeV.

5.3. Monte Carlo corrections

5.3.1. Gradient Boosted Reweighting

The GBR technique was used to improve the agreement between Monte Carlo simulated and real collision data. A control sample was needed to give good statistics for each individual data-taking period. This is particularly important for the exceptionally small data set of the

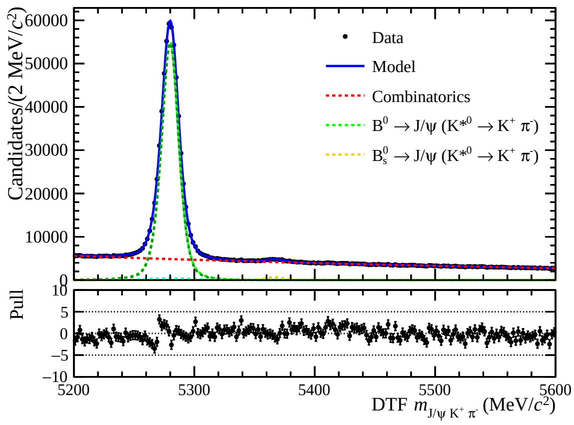

Figure 5.1.: Fit to the decay tree fitted B^0 mass distribution of the collision data sample of the reconstructed signal $B^0 \to J/\psi K^{*0}$ for 2016. This is the fit that was used in the sPlotting [115] for the background-subtracted data used in the training of the Gradient Boosted Reweighter.

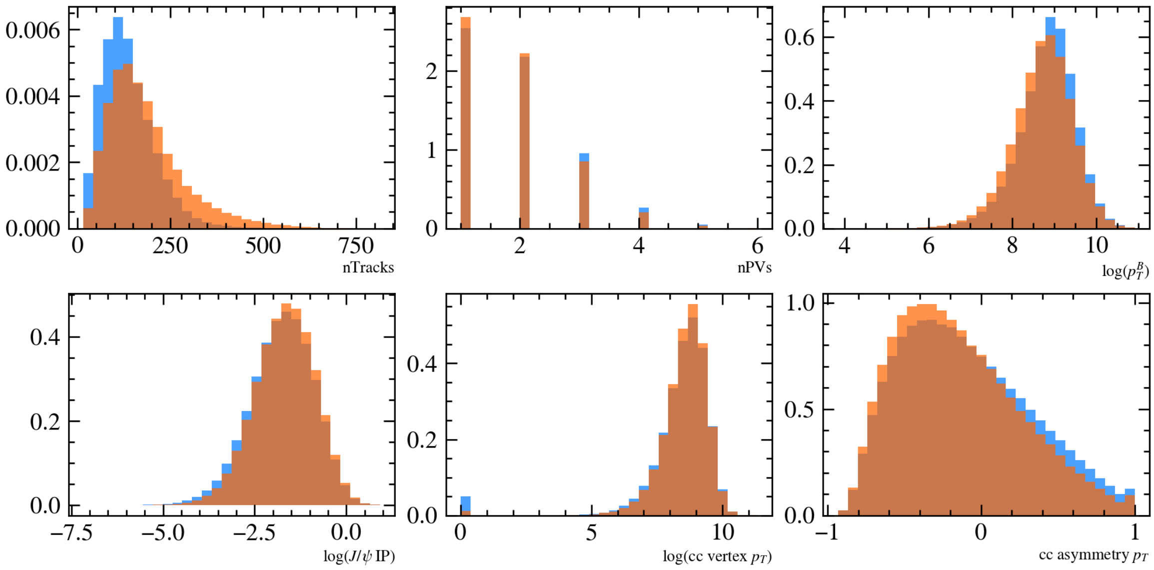

Figure 5.2.: The distributions of the input variables and expressions used for the training of the Gradient Boosted Reweighter. The orange distribution is the background-subtracted $B^0 \to J/\psi K^{*0}$ 2016 collision data used as a target. The blue distribution is the original $B^0 \to J/\psi K^{*0}$ 2016 MC data.

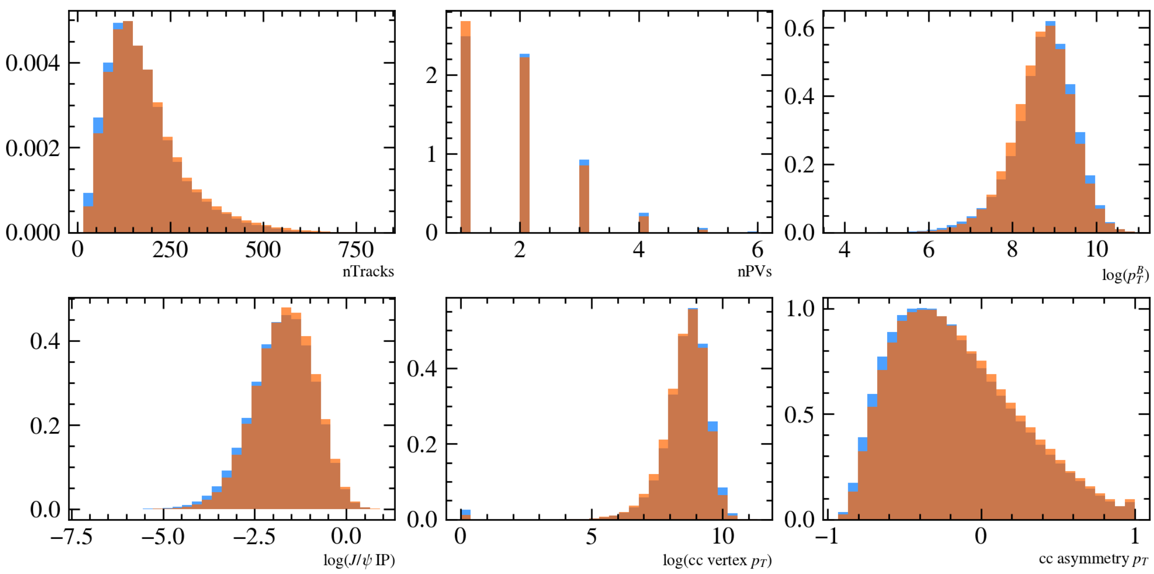

Figure 5.3.: The distributions of the input variables and expressions used for the training of the Gradient Boosted Reweighter. The orange distribution is the background-subtracted $B^0 \to J/\psi K^{*0}$ 2016 collision data used as a target. The blue distribution is the $B^0 \to J/\psi K^{*0}$ 2016 MC data after applying the event-by-event weights that were calculated by the reweighter.

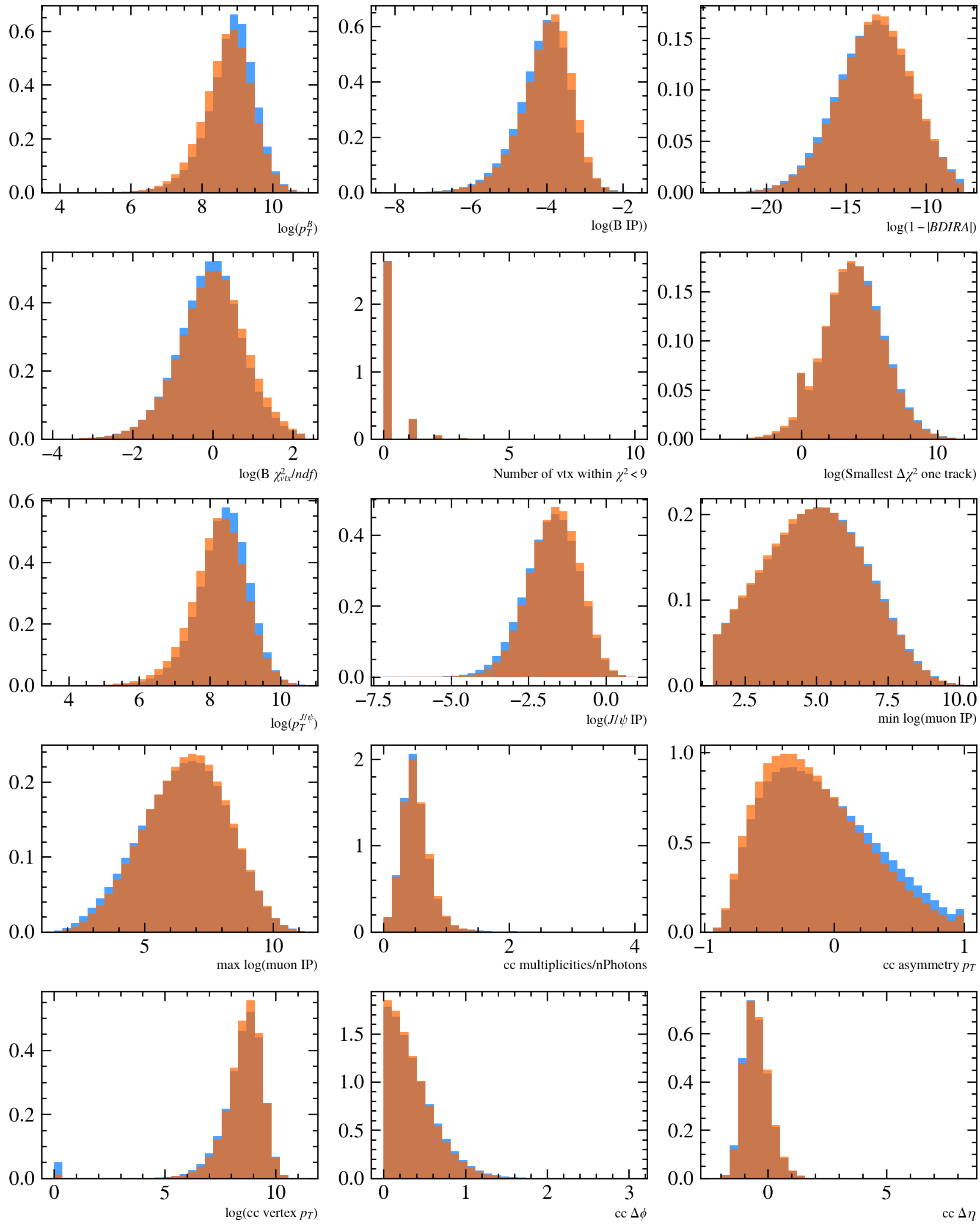

Figure 5.4.: The distributions of a subset of the variables and expressions used in the training of the MVA (omitting those unavailable to $B^0 \to J/\psi K^{*0}$ decays) as well as occupancy variables. The orange distribution is the background-subtracted $B^0 \to J/\psi K^{*0}$ 2016 collision data used as a target. The blue distribution is the original $B^0 \to J/\psi K^{*0}$ 2016 MC data.

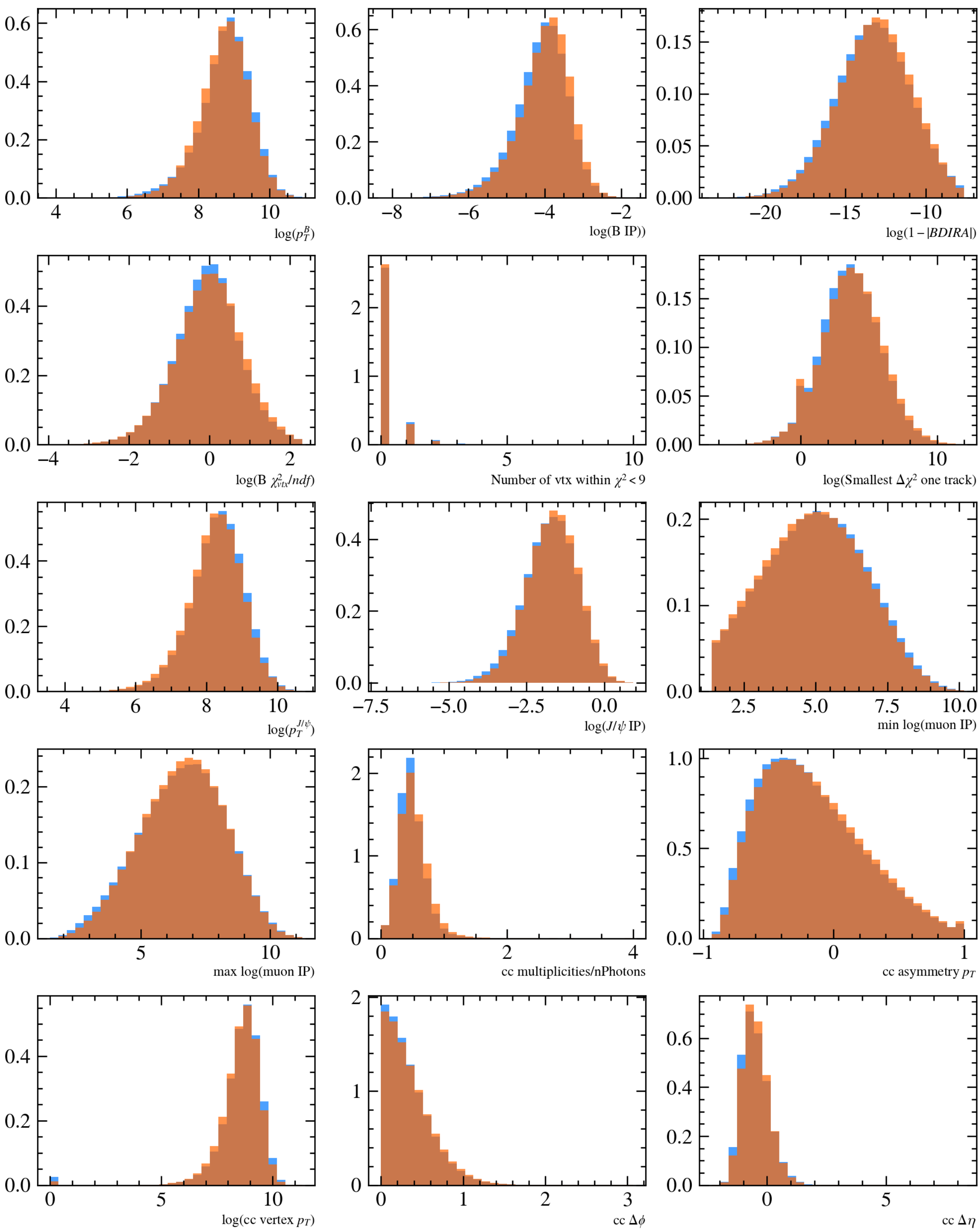

Figure 5.5.: The distributions of a subset of the variables and expressions used in the training of the MVA (omitting those unavailable to $B^0 \to J/\psi K^{*0}$ decays) as well as occupancy variables. The orange distribution is the background-subtracted $B^0 \to J/\psi K^{*0}$ 2016 collision data used as a target. The blue distribution is the $B^0 \to J/\psi K^{*0}$ 2016 MC data after applying weights calculated by the reweighter.

2015 data. Therefore the decay process $B^0 \to J/\psi K^{*0}$ where $J/\psi \to \mu^+\mu^-$ and $K^{*0} \to K^+\pi^-$ was employed for its similarity of many variables. The real collision data were background subtracted using the fit shown in Figure 5.1. Figure 5.2 shows the chosen input variables and expressions chosen for Monte Carlo and background-subtracted real data. After reweighting, these variables reached near-perfect agreement between the MC and real data, as seen in Figure 5.3. This yields similar agreement levels as the procedure described in Section 4.3.1, with excellent agreement in all variables but the charged cone multiplicities over the number of photons as can be seen in the comparison of Figures 5.4 and 5.5. Therefore there can be reasonable confidence that the BDT efficiencies were well described in Monte Carlo.

5.3.2. Particle identification corrections

As described in Section 3.5.2, the particle identification efficiencies were determined using calibration samples in replacement of the Monte Carlo efficiencies of the requirements that both π^+ and π^- in the signal and normalisation channels satisfy $\text{ProbNN}_\pi > 0.1$ and $\text{ProbNN}_\pi(1 - \text{ProbNN}_K) > 0.2$. The uncertainty due to statistics of the calibration samples are included in the uncertainties given in efficiency tables in Section 5.6 and the uncertainty due to the limited binning of the variables used in the method are given in Section 5.7.2.

5.3.3. L0 trigger efficiency corrections

Table 5.7.: The TIS and TOS efficiencies of the $B^+ \to J/\psi K^+$ simulated and real collision data reweighted to the muon kinematics and event occupancy of the signal and normalisation channels.

Channel	$\varepsilon^{MC}_{TISTOS}$ / %	$\varepsilon^{RD}_{TISTOS}$ / %	$\frac{\varepsilon^{RD}_{TISTOS}}{\varepsilon^{MC}_{TISTOS}}$ / %
$\eta \to \pi^+\pi^-\gamma$	86.78 ± 0.09	86.47 ± 0.12	99.65 ± 0.17
$\eta \to \pi^+\pi^-\pi^0$	87.90 ± 0.09	86.76 ± 0.12	98.70 ± 0.17
$\eta' \to \rho^0\gamma$	87.41 ± 0.09	87.00 ± 0.12	99.54 ± 0.17
$\eta' \to \pi^+\pi^-\eta$	87.99 ± 0.09	87.81 ± 0.12	99.79 ± 0.17
$\rho^0 \to \pi^+\pi^-$	86.81 ± 0.09	85.61 ± 0.12	98.62 ± 0.17

Similarly to the method of Section 4.3.4, the efficiencies of the trigger in Monte Carlo and real collision data needed to be determined so that corrections could be made to the measurements of the absolute branching ratios and the ratios of different final states used to determine φ_P and φ_G. Therefore the $B^+ \to J/\psi K^+$ samples were reweighted again with the signal and normalisation channels of this analysis in order to estimate the trigger efficiencies. The resulting efficiencies in data and MC are given in Table 5.7. The resulting corrections on the

Table 5.8.: The correction factors to the efficiency ratios used in the calculation of the branching ratios of $B^0_{(s)} \to J/\psi\eta^{(\prime)}$ and the ratios $\mathcal{R}_{d,s}$.

Channel	$\mathcal{R}^{cor}_{L0}$ / %
Single photon	
$\mathcal{B}\,(B^0_{(s)} \to J/\psi\eta)$	98.97 ± 0.24
$\mathcal{B}\,(B^0_{(s)} \to J/\psi\eta')$	99.08 ± 0.24
$\mathcal{R}_{d,s}$	100.11 ± 0.24
Two photon	
$\mathcal{B}\,(B^0_{(s)} \to J/\psi\eta)$	99.92 ± 0.24
$\mathcal{B}\,(B^0_{(s)} \to J/\psi\eta')$	98.82 ± 0.24
$\mathcal{R}_{d,s}$	98.91 ± 0.24

branching ratio fractions are then given in Table 5.8 with the associated statistical uncertainties assigned as the systematic uncertainty of the corrections.

5.4. Multivariate Analysis

5.4.1. Classification and training

The MVA classification process was performed using the methodology of Section 3.6. The Monte Carlo samples of the $B^0_s \to J/\psi\eta^{(\prime)}$ and $B^0 \to J/\psi\rho^0$ were used for the signal category. GBR weights were used to correct the BDT inputs as shown form Figure 5.4 to Figure 5.5 (in Section 5.3.1). Using the $\eta \to \pi^+\pi^-\gamma$ final state as an example, Figures (5.6) and (5.7) show normalised distributions of the training variables for the signal and background categories superimposed. Those figures show the separation of the two categories for the various distributions. The combination of information from the input variables led to the response shown in Figure 5.8. The BDTs trained on $B^0_s \to J/\psi\eta^{(\prime)}$ were then applied to $B^0 \to J/\psi\eta^{(\prime)}$.

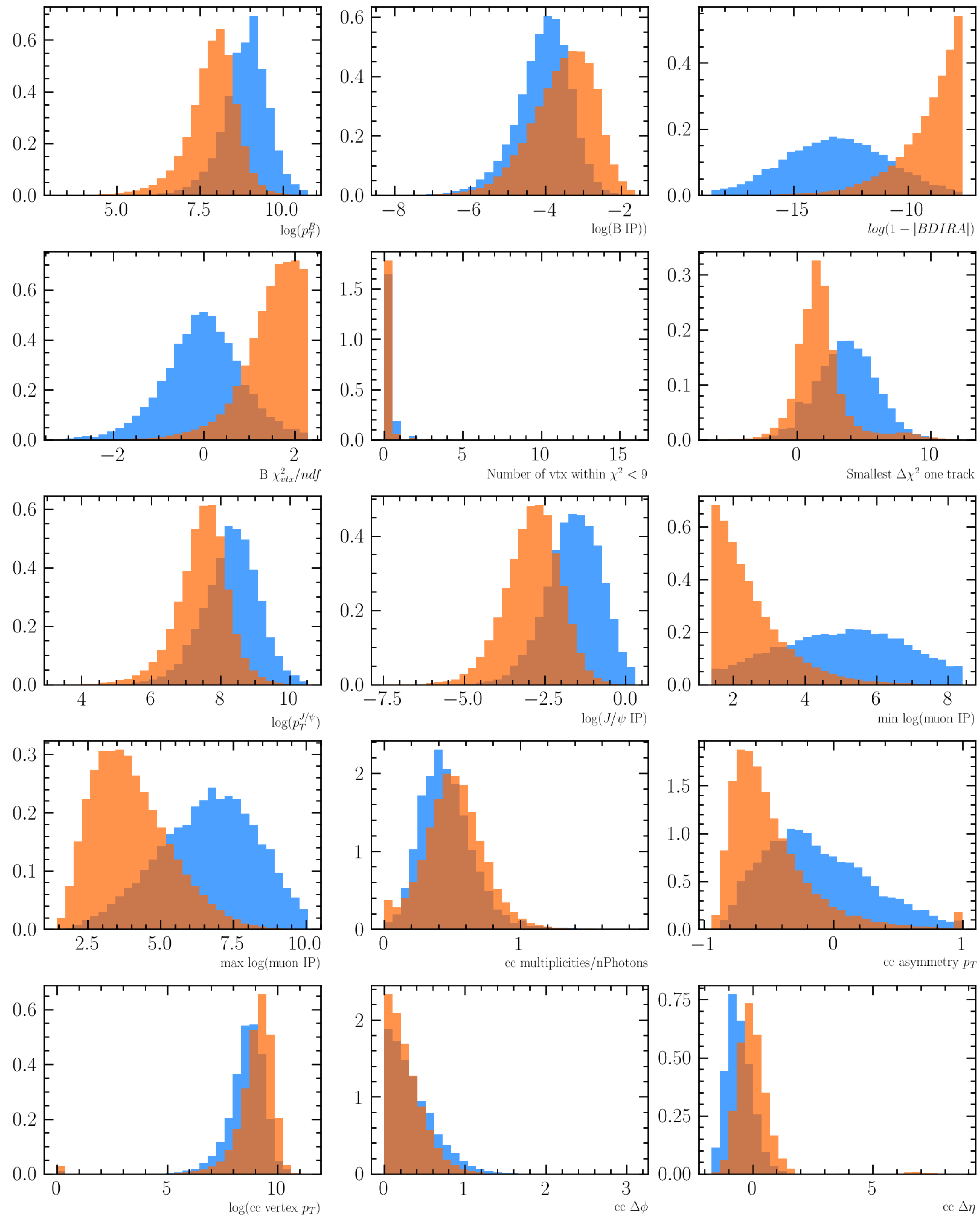

Figure 5.6.: Fifteen of the sixteen input variables used in the training of the Boosted Decision Trees. Theses distributions are of the $B^0_s \to J/\psi\eta$ where $\eta \to \pi^+\pi^-\gamma$ signal Monte Carlo (blue) and the combinatorics in the collison sample, where $|m(\mu^+\mu^-) - m(J/\psi)| > 60\,\text{MeV}$ (orange).

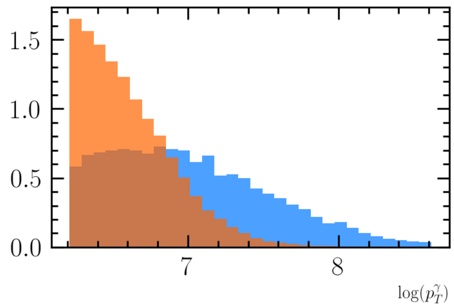

Figure 5.7.: The only input variable used in the training of the Boosted Decision Trees related to the photon. These distributions are of the $B^0_s \to J/\psi\eta$ where $\eta \to \pi^+\pi^-\gamma$ signal Monte Carlo (blue) and the combinatorics in the collision sample, where $|m(\mu^+\mu^-) - m(J/\psi)| > 60\,\text{MeV}$ (orange).

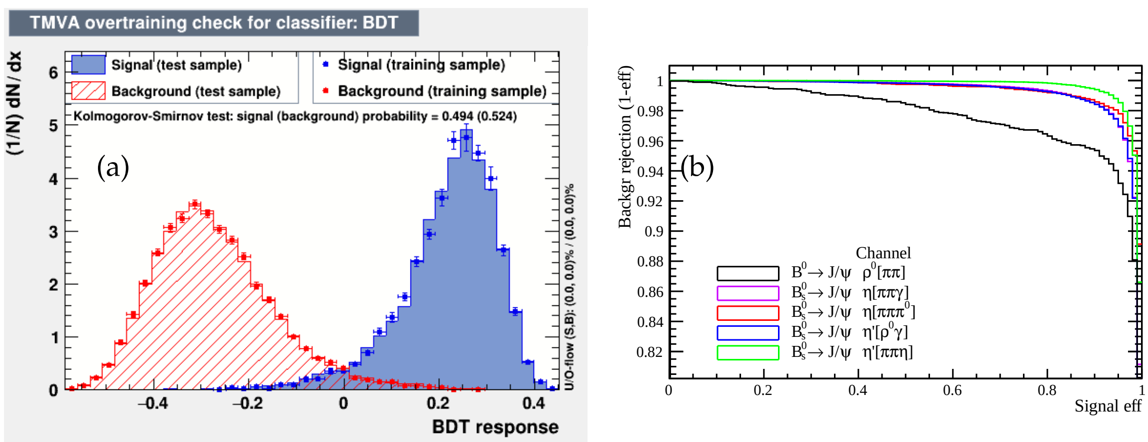

Figure 5.8.: a) The response of the BDT for $B^0_s \to J/\psi\eta$ where $\eta \to \pi^+\pi^-\gamma$. Showing the response of signal Monte Carlo (blue) and the combinatorics in the collision sample, where $|m(\mu^+\mu^-) - m(J/\psi)| > 60\,\text{MeV}$ (red). b) The overlaid background rejection verses signal efficiencies for the BDT responses of the signal and normalisation channels.

5.4.2. Optimisation of selections

The Cabibbo suppressed $B^0 \to J/\psi\eta^{(\prime)}$ decays require selections targeting not only the reduction of combinatorial backgrounds, which the BDTs were primarily trained to do, but also a separation from physics backgrounds and the $B^0_s \to J/\psi\eta^{(\prime)}$ signals. In this section the targeting of $B^0 \to J/\psi\eta^{(\prime)}$ was chosen specifically for the purpose of measuring the ratio $\mathcal{R}_d$ as precisely as possible. The relatively low yield of B^0 channels meanth that this particular ratio is the precision limiting factor of measuring both φ_P and φ_G and so ensuring the statistical uncertainty is as low as possible greatly improved the precision at which these angles were measured. This is a compromise that means the statistics of the $B^0_s \to J/\psi\eta^{(\prime)}$ are reduced in favour of better precision in the mixing measurements.

In the optimisation process it was important to have a complete model of the backgrounds that appear with the preselections. For the modelling of the combinatorial background a sample of collision data was used where the decays were reconstructed with the two pions having the same sign instead of opposite. Then this sample was scaled to the level expected by the high mass side band of the correct sign collision data to ensure that it is well describing the real background.

In the case of the single photon $\eta \to \pi^+\pi^-\gamma$ and $\eta' \to \rho^0\gamma$ final states, multiple physics backgrounds could limit the precision of the measurement of the $B^0 \to J/\psi\eta^{(\prime)}$ yields. For $\eta \to \pi^+\pi^-\gamma$ there were background contaminations from both of the two photon final states ($\eta \to \pi^+\pi^-\pi^0$ and $\eta' \to \pi^+\pi^-\eta$) arising from the partial reconstruction of these channels with only one of the two photons entering in the initial $\pi^+\pi^-\gamma$ mass window of $\pm100\,\text{MeV}$.

For $\to \rho^0\gamma$ there were two cases in which partially reconstructed backgrounds appear in the B mass fit range. One is $B^0_s \to J/\psi\phi$ with $\phi \to \pi^+\pi^-\pi^0$ which has a high enough invariant mass to produce pions from ρ^0 decays. The dominant case is therefore when a photon from the π^0 is lost and the pions decay via $\rho^0 \to \pi^+\pi^-$. The other background is from $B \to J/\psi K\pi\pi$ which appears similarly to this background in $B^0 \to J/\psi K^{*+}$, as described in Section 4.5.5, yet it is likely to dominantly decay via a ρ^0.

More information on these backgrounds is given in Sections 5.5.2 and 5.5.3. All of these backgrounds were modelled using Monte-Carlo samples of these decays reconstructed as $J/\psi\pi^+\pi^-\gamma$ with their yields estimated relative to the respective signal channels. The scaling of these yields were determined using the ratios of their efficiencies in MC and the averaged previous measurements of the branching ratios involved (from the Particle Data Group [41]).

Compared to measuring the single photon modes, the two photon modes require the reconstruction of an additional photon which gives a wider resonance in the $B^0_{(s)}$ mass distribution. Therefore the wider B^0_s and B^0 distributions overlap with each other and can be difficult to separate. To aid in the improvement of the significance of the $B^0 \to J/\psi\eta^{(\prime)}$ signal, tighter

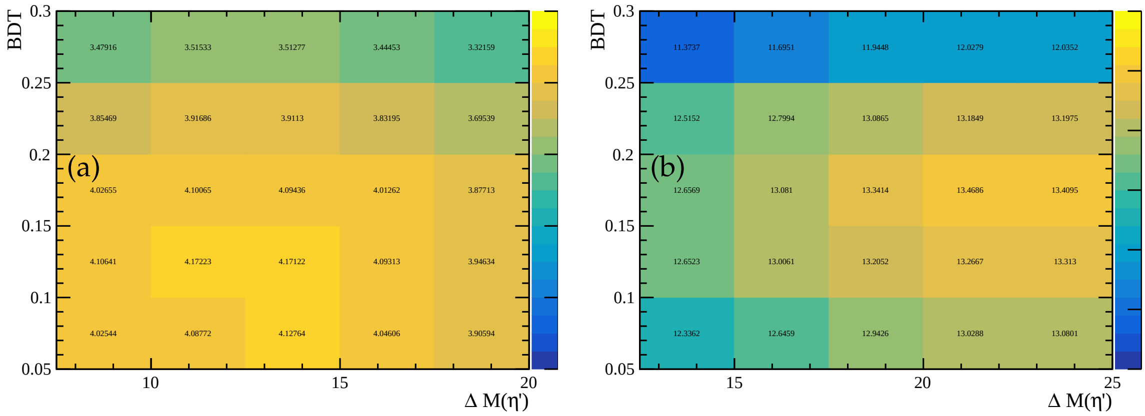

Figure 5.9.: The significance plots over different selections of the BDT and difference in the mass of the nominal $\eta^{(\prime)}$ and reconstructed $\pi^+\pi^-\gamma$ for $B^0 \to J/\psi\eta^{(\prime)}$ where a) $\eta \to \pi^+\pi^-\gamma$ and b) $\eta' \to \rho^0\gamma$. The lower bin boundaries for the y-axis are the BDT cuts BDT $>$ y and the upper bin boundaries for the x-axis are the mass windows $|\Delta M(\eta^{(\prime)})| < x$. The z-axis and numbers quoted in the bins are the average significance $(S/\sqrt{S+B})$ of the B^0 peak.

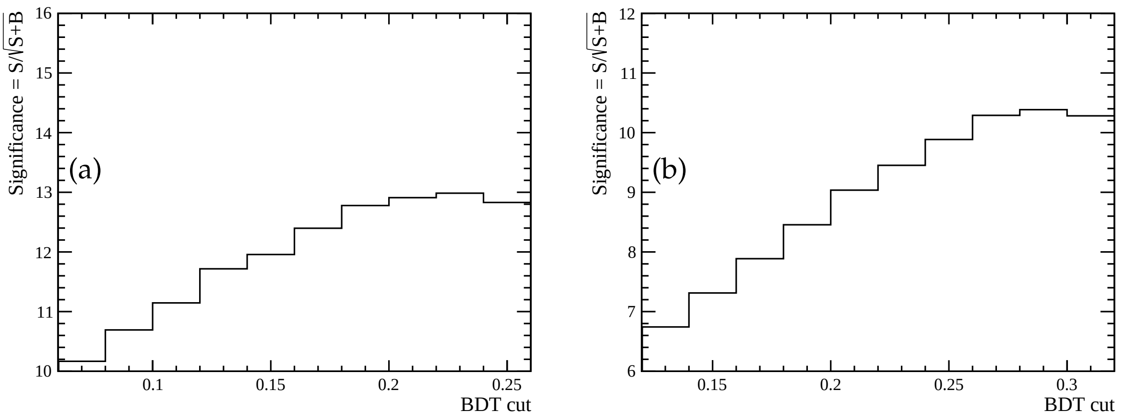

Figure 5.10.: The significance plots over different selections of the BDT and difference in the mass of the nominal $\eta^{(\prime)}$ and reconstructed $\pi^+\pi^-\gamma\gamma$ for $B^0 \to J/\psi\eta^{(\prime)}$ where a) $\eta \to \pi^+\pi^-\pi^0$ and b) $\eta' \to \pi^+\pi^-\eta$. The lower bin boundaries for the x-axis are the BDT cuts BDT $>$ x. The y-axis and numbers quoted in the bins are the average significance $(S/\sqrt{S+B})$ of the B^0 peak.

mass windows than those defined in the preselections were needed for the single photon channels. The selection of the DTF $\chi^2/\mathrm{ndf} < 2.5$ (as described in Section 3.4) led to narrower distributions in the DTF $B^0_{(s)}$ mass distributions and so good separation of the B^0 and B^0_s peaks. This meant that the need for tight mass windows in the two-photon channels was negated. Therefore the optimisation of the BDT selection was performed simultaneously with the selection of the mass windows of the single photon modes, and just the BDT selection for two-photon modes.

The figure of merit for the determination of the optimum selections was the significance of the $B^0 \to J/\psi\eta^{(\prime)}$ signal, estimated as $S/\sqrt{S+B}$ where S is the number of $B^0 \to J/\psi\eta^{(\prime)}$ and B is the combined yield of the combinatorial backgrounds, physics backgrounds and $B^0_s \to J/\psi\eta^{(\prime)}$ all measured within 3σ of the B^0 mass peak. These yields are estimated repeatedly using bootstrapped Monte Carlo. Bootstrapping is a statistical resampling method to simulate MC production and allows for greater certainty of the estimations for $S/\sqrt{S+B}$ by taking the mean value of $S/\sqrt{S+B}$ for resampled MC. This meant the reduction of the statistical fluctuations in these estimations from the limited MC sample sizes.

After performing a fit to the $B^0_{(s)}$ mass spectrum using the original Monte Carlo simulated data, the resulting parameters of the PDFs are used to generate the bootstrapped MC distributions. These samples were produced with the same statistics as the original Monte Carlo samples. Then new fits of these samples were performed where the yields of these fits were used to determine new efficiencies. These efficiencies were combined with the ratios of averaged branching fractions of the Particle Data Group [41] to determine the expected yields of each signal $B^0_{(s)} \to J/\psi\eta^{(\prime)}$ and their respective backgrounds. These yields were then used to estimate the $S/\sqrt{S+B}$ value of $B^0 \to J/\psi\eta^{(\prime)}$ for each set of toy Monte Carlo sample. This was repeated 100 times for each decay channel and each set of BDT and mass window selections which led to the averaged significance values shown in Figure 5.9 for single photons and Figure 5.10 for two photons. Therefore the chosen selections are $BDT > 0.1$ with $|M(\eta) - M(\pi^+\pi^-\gamma)| < 15\,\mathrm{MeV}$ for $\eta \to \pi^+\pi^-\gamma$, $BDT > 0.15$ with $|M(\eta') - M(\pi^+\pi^-\gamma)| < 22.5\,\mathrm{MeV}$ for $\eta' \to \rho^0\gamma$, $BDT > 0.22$ for $\eta \to \pi^+\pi^-\pi^0$ and $BDT > 0.28$ for $\eta' \to \pi^+\pi^-\eta$.

5.5. Mass fits and signal yields

5.5.1. Fit models

As described in Section 3.7, fit model of both the signal and background physics signatures (with the exception of the backgrounds of $B^0_{(s)} \to J/\psi\eta'$ with $\eta' \to \rho^0\gamma$) was a double-sided Crystal Ball function. This is two equally populated Crystal Ball functions used to model asymmetric tails with common means and widths. For the combinatorial backgrounds in real collision data, a free exponential function was used as the model. Unlike the previous analysis the background of a photon from the underlying event being combined with signal tracks was negligible for all channels. It seems that with the additional track (two pions instead of one kaon) the probability of this mis-match of the photons is reduced to the point where it could be neglected throughout this analysis.

5.5.2. Backgrounds impacting the $B^0_{(s)} \to J/\psi\eta$ with $\eta \to \pi^+\pi^-\gamma$ mode

- $B^0_{(s)} \to J/\psi\eta$ with $\eta \to \pi^+\pi^-\pi^0$: When a photon is lost in $\pi^0 \to \gamma\gamma$ there is the possibility that the invariant mass of the remaining $\pi^+\pi^-\gamma$ is still within the mass bounds of the $\eta \to \pi^+\pi^-\gamma$ at $|m(\pi^+\pi^-\gamma) - m(\eta)| < 15\,\text{MeV}$. Then as there is a mass constrain from the DTF the lower η mass contamination is skewed to the higher B mass region with a broad distribution. This is therefore included in the total fit model. The yield expectation is determined by the ratio of efficiencies in Monte Carlo and the branching ratios of $\eta \to \pi^+\pi^-\gamma$ and $\eta \to \pi^+\pi^-\pi^0$ times that of $\pi^0 \to \gamma\gamma$. The central value of the Gaussian constrain was set to the expectation relative to the signal of 66.2% with the width set to the uncertainty on this expectation at 2.0%.
- $B^0_{(s)} \to J/\psi\eta'$ with $\eta' \to \pi^+\pi^-\eta$: Similarly to $\eta \to \pi^+\pi^-\pi^0$, one photon can be lost in reconstruction and the $\pi^+\pi^-\gamma$ invariant mass is just within selections. Yet, it is only the extreme end of the tails of the $\pi^+\pi^-\gamma$ and so with the tighter requirements determined in the optimisation process it is able to be accounted for in the combinatorial model with the exponential PDF. The expected contribution relative to signal would be $(7.3 \pm 1.6)\%$.

5.5.3. Backgrounds impacting the $B^0_{(s)} \to J/\psi\eta'$ with $\eta' \to \rho^0\gamma$ mode

- $B^0_s \to J/\psi\phi$ with $\phi \to \pi^+\pi^-\pi^0$: There are a few ways that the ϕ can decay to the $\pi^+\pi^-\gamma$ final state to be mistakenly reconstructed and selected as $\eta' \to \rho^0\gamma$. The dominant case is when the $\phi \to \rho^0\pi^0$ where one photon is lost. The other cases involve both photons lost and one underlying event photon is combined with the true decay tracks or the ϕ can also decay to $(\rho^+ \to \pi^+\pi^0)\pi^-$, yet these other decays are less dominant. In the tight selections of this channel this background is reduced. This is a necessary consequence of the optimisation procedure as it did peak at a position near the $B^0 \to J/\psi\eta'$. Therefore maximising the B^0 signal significance necessarily meant the removal of this background. The expectation from the branching ratios and efficiencies would be $(9.2 \pm 1.4)\%$ of signal. Yet due to this being a broad shape in the low mass region, this had a negligible effect on the result.

- $B \to J/\psi K\pi\pi$: Similar to $B^+ \to J/\psi K^{*+}$ and $B^0 \to J/\psi K^{*0}$ in the previous analysis, there is the possibility of different partially reconstructed backgrounds to originate from different $K\pi\pi$ resonances. Section 4.5.3 highlights the most relevant case of $B^+ \to J/\psi K^{*+}$. Yet in this case it is less likely to originate from $K^+{}_1(1270) \to K^{*+}(892)\pi^0$, as the pions can also originate from a ρ^0 also. Therefore the use of the dedicated $B^+ \to J/\psi(K^+{}_1(1270) \to K^{*+}(892)\pi^0)$ MC sample of the previous analysis was less helpful. Instead, as shown in Table 5.5, two samples of $B^0 \to J/\psi X^0$ and $B^+ \to J/\psi X^+$ were used. Within these samples, there are inclusions of the different intermediary decays from $K_1(1270)$ to the $K\pi\pi$ final states. This was used in the optimisation process of the selections, but after applying the optimal selections the overall shape in the fit range was that of an exponential-like tail so was accounted for in the same model as the combinatorial background.

5.5.4. Backgrounds impacting the $B^0 \to J/\psi\rho^0$ mode

- $B^0_s \to J/\psi\eta'$ with $\eta' \to \rho^0\gamma$: This background is a partially reconstructed background where the photon is lost leading to a distribution underneath the signal which had to be fit for. The fitting strategy is the same as that used for $B \to J/\psi K\pi\pi$ within $B^+ \to J/\psi K^{*+}$ (see Section 4.5.3), as the dominant case for this background was the loss of one π^0, the overall shape is very similar. Therefore an Argus background PDF convoluted with a Normal distribution was added to a Crystal Ball function for this background.

5.5.5. Monte Carlo fits

For the fit of the signal channels, it was necessary to first perform fits to the MC simulated data to determine the tail-shape parameters (α_1 and n_1 for the left tail, or α_2 and n_2 for the right tail) of the double-sided Crystal Ball PDFs. These parameters are then fixed in the fits on collision data. This takes advantage of the large MC statistics while also limiting the number of floating parameters in the collision data fit. Both of these advantages enable the determination of the signal yields at good precision. Tables 5.9 and 5.10 contain the resulting fit parameters of the signal fits in Monte Carlo that are propagated to the real data fits. Interestingly the parameters of the left-hand tails are most similar between modes that include a $\rho^0 \to \pi^+\pi^-$ resonance or between modes that do not. For the right-hand tails, the parameters are more similar between the channels with photons, as the uncertainty on the right-handed tails are usually made more pronounced by photon pile-up.

Table 5.9.: The resulting tail parameters for $B^0_s \to J/\psi\eta^{(\prime)}$ and $B^0 \to J/\psi\rho^0$ from fits to full Run-1 and Run-2 MC simulated data. These parameters are fixed and used in the fits to Run-2 collision data.

Channel	α_R	n_R	α_L	n_L
$\eta \to \pi^+\pi^-\gamma$	-0.929 ± 0.008	8.51 ± 0.28	1.112 ± 0.010	7.11 ± 0.25
$\eta \to \pi^+\pi^-\pi^0$	-0.740 ± 0.013	25.4 ± 4.1	1.192 ± 0.018	7.3 ± 0.5
$\eta' \to \rho^0\gamma$	-1.129 ± 0.008	5.68 ± 0.13	1.452 ± 0.011	5.20 ± 0.15
$\eta' \to \pi^+\pi^-\eta$	-0.7698 ± 0.007	20.0 ± 1.4	0.8166 ± 0.010	130.954 ± 0.019
$\rho^0 \to \pi^+\pi^-$	-1.9223 ± 0.0027	6.9722 ± 0.0038	1.726 ± 0.006	9 ± 8

Table 5.10.: The resulting mass mean and width parameters for $B^0_{(s)} \to J/\psi\eta^{(\prime)}$ and $B^0 \to J/\psi\rho^0$ from fits to all available Run-1 and Run-2 MC simulated data.

	$B^0 \to J/\psi X$		$B^0_s \to J/\psi X$	
Channel	μ / MeV	σ / MeV	μ / MeV	σ / MeV
$\eta \to \pi^+\pi^-\gamma$	5279.58 ± 0.08	13.50 ± 0.08	5366.63 ± 0.04	13.406 ± 0.039
$\eta \to \pi^+\pi^-\pi^0$	5280.08 ± 0.25	12.98 ± 0.17	5366.67 ± 0.08	16.60 ± 0.08
$\eta' \to \rho^0\gamma$	5279.54 ± 0.06	8.93 ± 0.06	5366.74 ± 0.02	9.656 ± 0.020
$\eta' \to \pi^+\pi^-\eta$	5279.81 ± 0.17	14.26 ± 0.21	5366.75 ± 0.02	15.740 ± 0.018
$\rho^0 \to \pi^+\pi^-$	5283.42 ± 0.02	7.793 ± 0.012	-	-

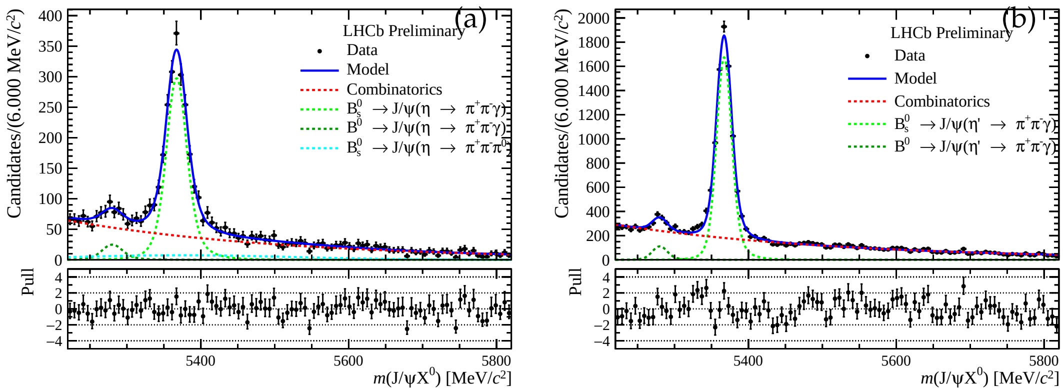

Figure 5.11.: Fit to the decay tree fitted B^0_s and B^0 mass distribution of the Run-1 and Run-2 collision data of the reconstructed signal $B^0_{(s)} \to J/\psi\eta^{(\prime)}$ with a) $\eta \to \pi^+\pi^-\gamma$ and b) $\eta' \to \rho^0\gamma$.

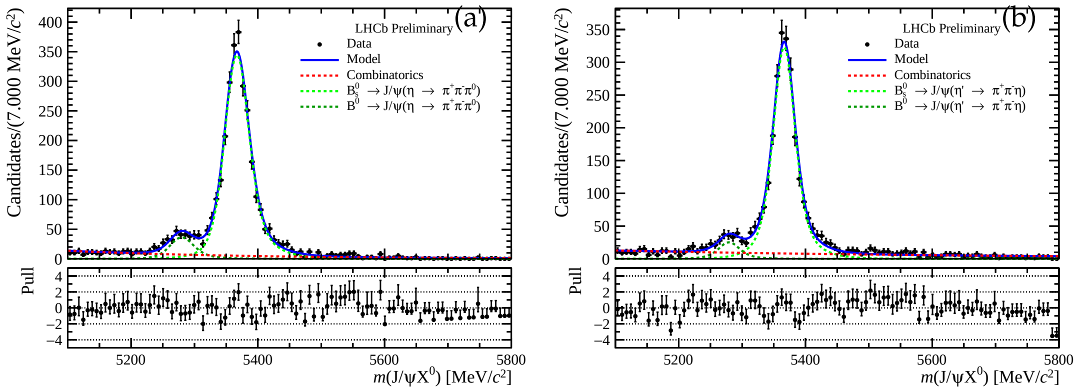

Figure 5.12.: Fit to the decay tree fitted B^0_s and B^0 mass distribution of the Run-1 and Run-2 collision data of the reconstructed signal $B^0_{(s)} \to J/\psi\eta^{(\prime)}$ with a) $\eta \to \pi^+\pi^-\pi^0$ and b) $\eta' \to \pi^+\pi^-\eta$.

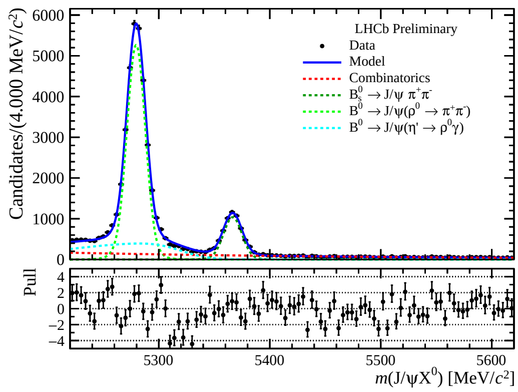

Figure 5.13.: Fit to the decay tree fitted B^0 mass distribution of the Run-1 and Run-2 collision data of the reconstructed signal $B^0 \to J/\psi\rho^0$.

Table 5.11.: The resulting signal yields for $B^0_{(s)} \to J/\psi\eta^{(\prime)}$ using the maximum-likelihood fit with Run-1 and Run-2 collision data.

Channel	$N(B^0_s)$	$N(B^0)$	$N(B^0)/N(B^0_s)$
$J/\psi\ (\eta \to \pi^+\pi^-\gamma)$	1938 ± 60	162 ± 36	0.083 ± 0.019
$J/\psi\ (\eta \to \pi^+\pi^-\pi^0)$	2695 ± 55	278 ± 23	0.103 ± 0.009
$J/\psi\ (\eta' \to \rho^0\gamma)$	7764 ± 107	515 ± 56	0.066 ± 0.007
$J/\psi\ (\eta' \to \pi^+\pi^-\eta)$	2305 ± 52	172 ± 20	0.075 ± 0.009
$J/\psi\ (\rho^0 \to \pi^+\pi^-)$	5498 ± 87	27884 ± 213	-

Table 5.12.: The fit parameters of the $B^0_{(s)} \to J/\psi\eta^{(\prime)}$ and $B^0 \to J/\psi\rho^0$ DTF $B^0_{(s)}$ mass fits to Run-1 and Run-2 collision data for each final state.

	$\Delta\mu$ / MeV	$f(\sigma)$	$p_0^{\text{exponential}}$
$\eta \to \pi^+\pi^-\gamma$	-0.6 ± 0.5	1.045 ± 0.039	$(3.32 \pm 0.15) \times 10^{-3}$
$\eta \to \pi^+\pi^-\pi^0$	0.3 ± 0.5	1.162 ± 0.026	$(-3.61 \pm 0.28) \times 10^{-3}$
$\eta' \to \rho^0\gamma$	0.35 ± 0.16	1.074 ± 0.017	$(-3.25 \pm 0.06) \times 10^{-3}$
$\eta' \to \pi^+\pi^-\eta$	-0.4 ± 0.5	1.151 ± 0.031	$(-1.66 \pm 0.19) \times 10^{-3}$
$\rho^0 \to \pi^+\pi^-$	-3.83 ± 0.06	1.070 ± 0.007	$(-3.49 \pm 0.24) \times 10^{-3}$

Table 5.13.: The background fractions or yields in the $B^0_{(s)} \to J/\psi\eta^{(\prime)}$ and $B^0 \to J/\psi\rho^0$ DTF $B^0_{(s)}$ mass fits to Run-1 and Run-2 collision data for each final state.

Channel	$f(\eta \to \pi^+\pi^-\pi^0)$	$N^b_{\eta' \to \rho^0\gamma}$	$N^b_{exponent}$
$\eta \to \pi^+\pi^-\gamma$	0.204 ± 0.006	-	$(2.79 \pm 0.09) \times 10^3$
$\eta \to \pi^+\pi^-\pi^0$	-	-	$(4.98 \pm 0.31) \times 10^2$
$\eta' \to \rho^0\gamma$	-	-	$(1.282 \pm 0.014) \times 10^4$
$\eta' \to \pi^+\pi^-\eta$	-	-	$(7.52 \pm 0.36) \times 10^2$
$\rho^0 \to \pi^+\pi^-$	-	$(9.39 \pm 0.31) \times 10^3$	$(8.99 \pm 0.28) \times 10^3$

5.5.6. Combined model fit to collision data

Every fit on collision data comes with combinatorial backgrounds that are well-modelled with an exponential PDF which has one free decay constant or slope parameter. The rest of the fit model is just the combination of the MC fitted signal and physics background PDFs with free parameters representing energy calibration and scaling of the detector resolution. These are a shift in PDF nominal means and multiplicative factors in model nominal widths respectively. The estimated yields of physics backgrounds are used in Gaussian constraining the measured yields with respect to the observed signal yields. The Gaussian mean is the central value of the calculated yield expectations and the Gaussian standard deviation is the combined uncertainty of the efficiencies and branching ratios used in the yield estimation.

The combined models fit to the full Run-1 and Run-2 collision data are shown in Figures 5.11-5.13. The models of the B^0_s and B^0 signal signatures are determined by their MC fits, where both take the tail parameters from $B^0_s \to J/\psi\eta^{(\prime)}$ fits (Table 5.9). The nominal B^0_s mass means are taken from the same fits, yet the nominal B^0 mass is fixed on the expected difference from that B^0_s mass ($5366.88 - 5279.65 = 87.23\,\text{MeV}$). In both the B^0 and B^0_s cases the nominal widths of the distributions are inherited from their fits to MC. The resulting signal yields determined by these fits are given in Table 5.11. The ratios of the B^0 and B^0_s yields are found to be consistent between the same $B^0_{(s)}$ decay modes of different final states. In the case of $B^0 \to J/\psi\rho^0$, the $B^0_s \to J/\psi\pi^+\pi^-$ peak used the same fit model shape parameters as the $B^0 \to J/\psi\rho^0$ model.

With the same fitting procedure as Section 4.5.6, the only free parameters were the signal and background yields, as well as the combinatorial background slope parameter and the common width scale factor and PDF mean position change. This led to six free parameters in the two-photon and the $\eta' \to \rho^0\gamma$ channels: the number of signal decays from B^0_s ($N^s(B^0_s)$), the number of B^0 signal decays ($N^s(B^0)$), the combinatorial background yield ($N(\text{exponent})$), the difference between the collision data and simulation mean position ($\Delta\mu$), the scaling factor for physics shape widths $f(\sigma)$ and the decay constant of the exponential used to model the combinatorics ($p_0^{\text{exponential}}$). The $\eta \to \pi^+\pi^-\gamma$ final state also includes the Gaussian constrained yield of the partially reconstructed $\eta \to \pi^+\pi^-\pi^0$ background. The normalisation channel has the additional background yields of $B^0_s \to J/\psi\pi^+\pi^-$ and $B^0_s \to J/\psi\eta'$ (where $\eta' \to \rho^0\gamma$). All of the parameters related to the model shapes are in Table 5.12 and the background yields or fractions of signal are in Table 5.13.

5.5.7. Correction to the yield of the normalisation channel $B^0 \to J/\psi\rho^0$

In this analysis the normalisation channel has the resonance specific branching fraction and Monte Carlo samples of $B^0 \to J/\psi\rho^0$ with $\rho^0 \to \pi^+\pi^-$. There are contributions to the measured signal yield in the DTF mass spectrum of $J/\psi\pi^+\pi^-$ originating from decays of $B^0 \to J/\psi\pi^+\pi^-$

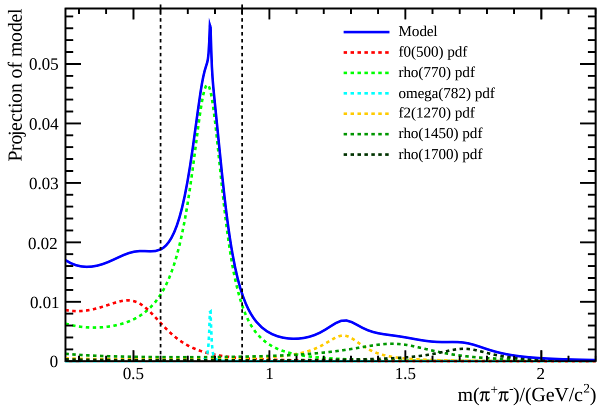

Figure 5.14.: The PDFs from [126] projected to the $\pi^+\pi^-$ mass. The vertical dashed line highlights the range used in this analysis.

that pass through other resonances of $X \to \pi^+\pi^-$. These contribution must be accounted for by measuring the amplitude of $\rho^0 \to \pi^+\pi^-$ within the mass range of $[600, 900]$ MeV.

In the previous studies of the $B^0 \to J/\psi\rho^0$ at LHCb an amplitude analysis had to be performed in order to determine the branching ratio of this decay. Hence, the non-ρ^0 contributions in a larger $m(\pi^+\pi^-)$ fit range were already calculated in [126]. To determine this fraction for the relatively narrow fit range of $[600, 900]$ MeV, the fit parameters for all of the multi-dimensional $\pi^+\pi^-$ resonances' PDFs were taken from [126] and the PDFs were projected to $m(\pi^+\pi^-)$, as shown in Figure 5.14. The ratio of the integral in $[600, 900]$ MeV of the $\rho^0(770)$ PDF over the sum of the integrals of all the PDFs was multiplied by the $\rho^0(770)$ fit fraction to obtain the correction of $(87.0 \pm 4.3)\%$. The uncertainty on this correction is already accounted for in the branching ratio of $B^0 \to J/\psi\rho^0$ so can be omitted in the uncertainty budget of the analysis of this thesis.

5.6. Monte Carlo efficiencies

The efficiencies were estimated by Monte Carlo samples as the sum of GBR weights and, as shown in Table 5.14, and are broken down by analysis step. These efficiencies were estimated as a weighted average based on the expected statistics of each year calculated by the product of the energy dependent cross section and integrated luminosity, see Table 2.1 in Section 2.1 for a summary of this. The efficiencies of $B^0_s \to J/\psi\eta^{(\prime)}$ and $B^0 \to J/\psi\eta^{(\prime)}$ were particularly similar for the acceptance, trigger and PID selections, other differences are likely to arise from the difference in available phase-space for the decays and therefore subtly different kinematics can be expected. Generally the efficiencies were more similar between channels with the same number of photons. It can be assumed that these similarities in efficiencies would imply that, in the use of the ratios in the calculations of $\mathcal{R}_s$, $\mathcal{R}_d$, $\mathcal{R}_\eta$ and $\mathcal{R}_{\eta'}$, there would be cancellation

Table 5.14.: The weighted average reconstruction and selection efficiencies for the signal $B^0_{(s)} \to J/\psi\eta^{(\prime)}$ and $B^0 \to J/\psi\rho^0$ Monte-Carlo simulated data. The weights in the average were determined year-by-year as proportional to the product of expected cross-sections and integrated luminosity.

Channel	$\varepsilon^{MC}(B^0_s)/\%$	$\varepsilon^{MC}(B^0)/\%$
	Acceptance	
$\eta \to \pi^+\pi^-\gamma$	11.59 ± 0.17	15.63 ± 0.28
$\eta \to \pi^+\pi^-\pi^0$	13.37 ± 0.08	15.52 ± 0.04
$\eta' \to \rho^0\gamma$	15.442 ± 0.09	15.93 ± 0.29
$\eta' \to \pi^+\pi^-\eta$	10.34 ± 0.14	14.68 ± 0.27
$\rho^0 \to \pi^+\pi^-$	-	15.908 ± 0.035
	Reconstruction and preselection	
$\eta \to \pi^+\pi^-\gamma$	3.724 ± 0.016	2.514 ± 0.016
$\eta \to \pi^+\pi^-\pi^0$	1.281 ± 0.009	0.960 ± 0.007
$\eta' \to \rho^0\gamma$	2.116 ± 0.009	1.887 ± 0.014
$\eta' \to \pi^+\pi^-\eta$	2.275 ± 0.013	1.388 ± 0.012
$\rho^0 \to \pi^+\pi^-$	-	7.209 ± 0.011
	Trigger	
$\eta \to \pi^+\pi^-\gamma$	85.24 ± 0.40	83.9 ± 0.6
$\eta \to \pi^+\pi^-\pi^0$	86.3 ± 0.6	85.4 ± 0.7
$\eta' \to \rho^0\gamma$	85.59 ± 0.37	84.5 ± 0.7
$\eta' \to \pi^+\pi^-\eta$	87.2 ± 0.5	86.8 ± 0.8
$\rho^0 \to \pi^+\pi^-$	-	83.59 ± 0.15
	BDT selection	
$\eta \to \pi^+\pi^-\gamma$	89.88 ± 0.45	88.6 ± 0.6
$\eta \to \pi^+\pi^-\pi^0$	72.0 ± 0.6	69.7 ± 0.6
$\eta' \to \rho^0\gamma$	84.41 ± 0.40	83.5 ± 0.7
$\eta' \to \pi^+\pi^-\eta$	71.5 ± 0.5	69.2 ± 0.8
$\rho^0 \to \pi^+\pi^-$	-	80.09 ± 0.16
	PID selection	
$\eta \to \pi^+\pi^-\gamma$	95.32 ± 0.08	94.85 ± 0.07
$\eta \to \pi^+\pi^-\pi^0$	95.32 ± 0.06	95.266 ± 0.035
$\eta' \to \rho^0\gamma$	94.69 ± 0.08	94.05 ± 0.07
$\eta' \to \pi^+\pi^-\eta$	96.18 ± 0.11	95.94 ± 0.09
$\rho^0 \to \pi^+\pi^-$	-	93.07 ± 0.09
	Total	
$\eta \to \pi^+\pi^-\gamma$	0.3110 ± 0.0016	0.2769 ± 0.0020
$\eta \to \pi^+\pi^-\pi^0$	0.0912 ± 0.0008	0.0845 ± 0.0008
$\eta' \to \rho^0\gamma$	0.2203 ± 0.0011	0.1997 ± 0.0017
$\eta' \to \pi^+\pi^-\eta$	0.1339 ± 0.0010	0.1176 ± 0.0013
$\rho^0 \to \pi^+\pi^-$	-	0.7144 ± 0.0016

of biases and Monte Carlo mis-modelling effects on the final results. Although it is worth noting that in the case of the single photon channels it appears there is a higher reconstruction efficiency for $\eta \to \pi^+\pi^-\gamma$ as opposed to $\eta' \to \rho^0\gamma$, due to the higher transverse momentum of the photon it is more likely to pass the $p_{\mathrm{T}}^{\gamma} > 500\,\mathrm{MeV}$ requirement.

5.7. Systematic uncertainties

5.7.1. Fit model choice

Table 5.15.: The systematic uncertainties on the measured yields of the binned maximum likelihood fits due to the choice of signal PDF.

Channel	Uncertainty on $N(B^0_s)/\%$	Uncertainty on $N(B^0)/\%$
$\eta \to \pi^+\pi^-\gamma$	0.75%	0.10%
$\eta \to \pi^+\pi^-\pi^0$	1.7%	2.7%
$\eta' \to \rho^0\gamma$	0.20%	1.1%
$\eta' \to \pi^+\pi^-\eta$	0.020%	3.4%
$\rho^0 \to \pi^+\pi^-$	-	2.24%

Table 5.16.: The systematic uncertainties on the measured yields of the binned maximum likelihood fits due to the choice of combinatorial background PDF.

Channel	Uncertainty on $N(B^0_s)/\%$	Uncertainty on $N(B^0)/\%$
$\eta \to \pi^+\pi^-\gamma$	1.3%	0.11%
$\eta \to \pi^+\pi^-\pi^0$	1.9%	4.0%
$\eta' \to \rho^0\gamma$	1.1%	0.99%
$\eta' \to \pi^+\pi^-\eta$	0.68%	3.6%
$\rho^0 \to \pi^+\pi^-$	-	0.40%

The same method to study this systematic uncertainty is applied as shown in Section 4.7.1 The chosen alternative model in this occasion was the double-sided Hypatia function [120]. This is a Crystal Ball-like function with a hyperbolic core and asymmetric tails, the uncertainties are determined as the relative difference in the signal yields between the two methods and are shown in Table 5.15. In the case of the background model the same alternatives were used as described previously giving the RMS uncertainty on the different measured signal yields as the systematic uncertainties in Table 5.16.

5.7.2. PID calibration binning scheme

As described in Section 4.7.2, there are a certain number of events in the Monte Carlo samples that are either in bins that give negative sWeights in the calibration samples or are outside of the binning range altogether. These events therefore do not give an efficiency of the PID

Table 5.17.: The systematic uncertainties on the binning of the PID calibration samples.

Channel	Uncertainty on $\varepsilon^{MC}(B^0_s)/\%$	Uncertainty on $\varepsilon^{MC}(B^0)/\%$
$\eta \to \pi^+\pi^-\gamma$	0.26%	0.21%
$\eta \to \pi^+\pi^-\pi^0$	0.04%	0.02%
$\eta' \to \rho^0\gamma$	0.48%	0.29%
$\eta' \to \pi^+\pi^-\eta$	0.05%	0.05%
$\rho^0 \to \pi^+\pi^-$	-	0.49%

requirements and must be accounted for a small systematic on the overall PID efficiencies. The fraction of events, *i.e.* the systematic uncertainty, are given in Table 5.17. The number of events with exceptionally high pion p_{T} is increased in the case of the two photon channels as there is higher available phase-space for these pions. This causes the larger uncertainties as they are more likely to be outside of the upper bound of that binning variable.

5.7.3. Varying B DTF mass fit boundaries

Table 5.18.: The systematic uncertainties on the measured yields of the binned maximum likelihood fits due to the fitting boundaries.

Channel	Uncertainty on $N(B^0_s)/\%$	Uncertainty on $N(B^0)/\%$
$\eta \to \pi^+\pi^-\gamma$	1.2%	5.2%
$\eta \to \pi^+\pi^-\pi^0$	1.0%	3.8%
$\eta' \to \rho^0\gamma$	0.56%	5.2%
$\eta' \to \pi^+\pi^-\eta$	0.78%	2.6%
$\rho^0 \to \pi^+\pi^-$	-	0.65%

Varying the chosen boundaries for fitting can impact the measured yields due to the variation in the combinatorial background fitted yield and slope. The variation chosen was symmetrically $\pm 50\,\mathrm{MeV}$, the same as described in Section 4.7.3. The RMS uncertainty of the three signal yields with nominal, narrower and wider boundaries are shown in Table 5.18. It is clear that these effects were particularly important to the low yield B^0 peak which was closer to the boundary and very sensitive to these changes. There is another factor leading to the increase in this systematic, in the single photon modes, there were the backgrounds that appeared in the low mass region. These backgrounds were included in the optimisation of the cuts for the BDT and mass windows but were neglected in the final fit. These were neglected because the tails of these backgrounds were able to be accounted for in the combinatorial fit. Therefore the larger systematic uncertainties that arise in the single photon case, as these backgrounds have a larger effect in the wider fitting range and therefore count the extra uncertainty that comes from the decision to neglect these backgrounds.

5.7.4. Varying intermediary decay mass window boundaries

Table 5.19.: The systematic uncertainties on the ratio of measured yields of the binned maximum likelihood fits over the Monte Carlo efficiencies due to the mass windows.

Channel	Uncertainty on $\left(\frac{N^s}{\varepsilon^{MC}}\right)(B^0_s)/\%$	Uncertainty on $\left(\frac{N^s}{\varepsilon^{MC}}\right)(B^0)/\%$
$\eta \to \pi^+\pi^-\gamma$	2.2%	2.1%
$\eta \to \pi^+\pi^-\pi^0$	1.1%	3.3%
$\pi^0 \to \gamma\gamma$	2.6%	6.5%
$\eta' \to \rho^0\gamma$	1.8%	1.6%
$\eta' \to \pi^+\pi^-\eta$	0.79%	4.1%
$\eta \to \gamma\gamma$	0.57%	3.9%
$\rho^0 \to \pi^+\pi^-$	-	1.7%

An important source of uncertainty would arise from the measured efficiencies of the selections on the intermediary particle masses. These mass windows are unique to each decay channel and therefore any discrepancy in the efficiencies from Monte Carlo and real data remains in the final result of the branching ratio measurements and $\mathcal{R}_{d,s}$ but not $\mathcal{R}_{\eta,\eta'}$. The systematic uncertainties shown in Table 5.19 are calculated by varying the mass windows of $\eta^{(\prime)} \to \pi^+\pi^-X^0$ to be wider or narrower by a few MeV and taking the RMS uncertainty of the ratio of signal yield over Monte Carlo efficiency for the nominal, wider and narrow selections. The RMS uncertainty is then assigned as a systematic on these ratios. The particular variations for the two photon modes which had $\pm 3\sigma$ mass windows were $\pm 0.5\sigma = 6\,\text{MeV}$ from the nominal mass difference for $\eta \to \pi^+\pi^-\pi^0$ and $\pm 0.5\sigma = 14\,\text{MeV}$ for $\eta' \to \pi^+\pi^-\eta$. In the single photon cases there were already tight mass windows so smaller variations sufficed. For $\eta \to \pi^+\pi^-\gamma$ this was $\pm 0.5\,\text{MeV}$ and $\pm 2.5\,\text{MeV}$ for $\eta' \to \rho^0\gamma$. A similar test is performed on the loosely selected $\pi^0 \to \gamma\gamma$ and $\eta \to \gamma\gamma$ and $\rho^0 \to \pi^+\pi^-$ where the mass windows are reduced to $\pm 3\sigma$ and $\pm 2.5\sigma$ and the RMS uncertainty is again used.

5.7.5. BDT efficiencies

The method to determine the uncertainty on the BDT efficiencies was used as that shown in Section 4.7.5. Table 5.20 shows that the resulting uncertainties were all at the sub-percent level for this analysis. It appears that, by using the B^0 transverse momentum in the control channel

Table 5.20.: The systematic uncertainties on the BDT efficiencies.

Channel	Uncertainty on $\varepsilon^{MC}(B^0_s)/\%$	Uncertainty on $\varepsilon^{MC}(B^0)/\%$
$\eta \to \pi^+\pi^-\gamma$	0.92%	0.10%
$\eta \to \pi^+\pi^-\pi^0$	0.40%	0.08%
$\eta' \to \rho^0\gamma$	0.11%	0.81%
$\eta' \to \pi^+\pi^-\eta$	0.62%	0.04%
$\rho^0 \to \pi^+\pi^-$	-	0.71%

as an input in the training of the GBR, the weights typically caused greater differences to the B^0_s channels efficiencies that of the B^0 channels. This could be increasing the uncertainty quoted here for the B^0_s modes.

5.7.6. Total of systematic uncertainties

The combination of all of the systematic uncertainties was done by adding in quadrature the relevant uncertainties for each ratio of branching fractions. These are shown in Table 5.21 with uncertainties on the weighted average. The largest uncertainties arise in the $B^0 \to J/\psi\eta^{(\prime)}$ measurements which were particularly sensitive to changes in the fit models, fit boundaries, and the mass windows.

Table 5.21.: The sources of systematic uncertainty for the measurement of each of the ratios of Branching fractions and their contributions as a percentage.

	Single photon							
Channel	$\mathcal{R}_d$	$\mathcal{R}_s$	$\mathcal{R}_\eta$	$\mathcal{R}_{\eta'}$	$\mathcal{B}^\eta_d$	$\mathcal{B}^\eta_s$	$\mathcal{B}^{\eta'}_d$	$\mathcal{B}^{\eta'}_s$
Signal model	1.1	0.8	0.8	1.1	2.2	2.4	2.5	2.2
Background model	1.0	1.7	1.3	1.5	0.4	1.4	1.1	1.2
PID calibration	0.4	0.6	0.3	0.6	0.5	0.6	0.6	0.7
Fit boundaries	7.4	1.3	5.3	5.2	5.2	1.4	5.2	0.9
Mass windows	2.6	2.8	3.0	2.4	2.7	2.8	2.3	2.5
Trigger efficiency	0.2	0.2	0	0	0.2	0.2	0.2	0.2
BDT efficiency	0.8	0.9	0.9	0.8	0.7	1.2	1.1	0.7
Total	8.0	3.8	6.3	6.1	6.3	4.4	6.4	3.8
	Two photon							
Channel	$\mathcal{R}_d$	$\mathcal{R}_s$	$\mathcal{R}_\eta$	$\mathcal{R}_{\eta'}$	$\mathcal{B}^\eta_d$	$\mathcal{B}^\eta_s$	$\mathcal{B}^{\eta'}_d$	$\mathcal{B}^{\eta'}_s$
Signal model	4.3	1.7	3.2	3.4	3.5	2.8	4.1	2.2
Background model	6.5	2.0	5.8	3.7	4.0	1.9	3.6	0.8
PID calibration	0.1	0.1	0.0	0.1	0.5	0.5	0.5	0.5
Fit boundaries	4.6	1.3	3.9	2.7	3.9	1.2	2.7	1.0
Mass windows	9.2	3.0	7.8	5.7	7.5	3.3	5.9	2.0
Trigger efficiency	0.2	0.2	0	0	0.2	0.2	0.2	0.2
BDT efficiency	0.1	0.7	0.4	0.6	0.7	0.8	0.7	0.9
Total	12.9	4.3	11.0	8.1	10.0	5.0	8.5	3.4
	Average							
Channel	$\mathcal{R}_d$	$\mathcal{R}_s$	$\mathcal{R}_\eta$	$\mathcal{R}_{\eta'}$	$\mathcal{B}^\eta_d$	$\mathcal{B}^\eta_s$	$\mathcal{B}^{\eta'}_d$	$\mathcal{B}^{\eta'}_s$
Total	6.8	2.8	5.5	4.9	5.3	3.3	5.1	2.5

5.8. Branching ratio and η-η' mixing results

5.8.1. Calculating $\mathcal{R}_{\eta^{(\prime)},d,s}$

The four ratios $\mathcal{R}_\eta$, $\mathcal{R}_{\eta'}$, $\mathcal{R}_s$ and $\mathcal{R}_d$ can each be calculated twice: one ($\mathcal{R}^{\gamma}_{\eta^{(\prime)},d,s}$) with the single photon final states $\eta \to \pi^+\pi^-\gamma$ and $\eta' \to \rho^0\gamma$ and the other ($\mathcal{R}^{\gamma\gamma}_{\eta^{(\prime)},d,s}$) with the two photon final states $\eta \to \pi^+\pi^-\pi^0$ and $\eta' \to \pi^+\pi^-\eta$. The calculation of these ratios are done by the double ratio of the signal yields (from Section 5.5.6) and efficiencies (from Section 5.6). In the case of $\mathcal{R}_s$ and $\mathcal{R}_d$ the calculation requires the ratio of intermediary branching ratios as the ratios are

Table 5.22.: The absolute measurements of φ_P and φ_G and the ratios or combination of ratios used to measure them.

	Single photon	
	$\varphi_P(^\circ)$	$\varphi_G(^\circ)$
$\mathcal{R}_\eta$	$46.5 \pm 4.3\,(\text{stat}) \pm 1.4\,(\text{syst}) \pm 0.6(f_s/f_d)$	-
$\mathcal{R}'_\eta$	$40.2 \pm 2.0\,(\text{stat}) \pm 2.1\,(\text{syst}) \pm 0.6(f_s/f_d)$	-
$\mathcal{R}_s$&$\mathcal{R}_d$	$43.4 \pm 1.9\,(\text{stat}) \pm 0.6\,(\text{syst})$	$18.8 \pm 10.7\,(\text{stat}) \pm 3.6\,(\text{syst}) \pm 1.4(\mathcal{B})$
	Two photons	
	$\varphi_P(^\circ)$	$\varphi_G(^\circ)$
$\mathcal{R}_\eta$	$44.0 \pm 1.7\,(\text{stat}) \pm 2.1\,(\text{syst}) \pm 0.6(f_s/f_d)$	-
$\mathcal{R}'_\eta$	$42.4 \pm 2.2\,(\text{stat}) \pm 1.5\,(\text{syst}) \pm 0.6(f_s/f_d)$	-
$\mathcal{R}_s$ and $\mathcal{R}_d$	$43.2 \pm 1.1\,(\text{stat}) \pm 1.0\,(\text{syst})$	$21.6 \pm 5.3\,(\text{stat}) \pm 4.9\,(\text{syst}) \pm 0.9(\mathcal{B})$

between two different final states; and in the case of the $\mathcal{R}_\eta$ and $\mathcal{R}_{\eta'}$ fractions this involves f_s/f_d as these are between B^0 and B^0_s initial states with the same final state.

So $\mathcal{R}^\gamma_d$ and $\mathcal{R}^\gamma_s$ are calculated as

$$\mathcal{R}^\gamma_d = \left(\frac{\Phi^\eta_d}{\Phi^{\eta'}_d}\right)^3 \frac{\mathcal{B}_{B^0\to J/\psi\eta'}}{\mathcal{B}_{B^0\to J/\psi\eta}} = \frac{N_{B^0\to J/\psi\eta'}}{N_{B^0\to J/\psi\eta}} \frac{\varepsilon_{B^0\to J/\psi\eta}}{\varepsilon_{B^0\to J/\psi\eta'}} \frac{\mathcal{B}_{\eta\to\pi^+\pi^-\gamma}}{\mathcal{B}_{\eta'\to\rho^0\gamma}} \tag{5.1}$$

$$\mathcal{R}^\gamma_s = \left(\frac{\Phi^\eta_s}{\Phi^{\eta'}_s}\right)^3 \frac{\mathcal{B}_{B^0_s\to J/\psi\eta'}}{\mathcal{B}_{B^0_s\to J/\psi\eta}} = \frac{N_{B^0_s\to J/\psi\eta'}}{N_{B^0_s\to J/\psi\eta}} \frac{\varepsilon_{B^0_s\to J/\psi\eta}}{\varepsilon_{B^0_s\to J/\psi\eta'}} \frac{\mathcal{B}_{\eta\to\pi^+\pi^-\gamma}}{\mathcal{B}_{\eta'\to\rho^0\gamma}}, \tag{5.2}$$

and $\mathcal{R}^{\gamma\gamma}_d$ and $\mathcal{R}^{\gamma\gamma}_s$ are calculated as

$$\mathcal{R}^{\gamma\gamma}_d = \left(\frac{\Phi^\eta_d}{\Phi^{\eta'}_d}\right)^3 \frac{\mathcal{B}_{B^0\to J/\psi\eta'}}{\mathcal{B}_{B^0\to J/\psi\eta}} = \frac{N_{B^0\to J/\psi\eta'}}{N_{B^0\to J/\psi\eta}} \frac{\varepsilon_{B^0\to J/\psi\eta}}{\varepsilon_{B^0\to J/\psi\eta'}} \frac{\mathcal{B}_{\eta\to\pi^+\pi^-\pi^0}\mathcal{B}_{\pi^0\to\gamma\gamma}}{\mathcal{B}_{\eta'\to\pi^+\pi^-\eta}\mathcal{B}_{\eta\to\gamma\gamma}} \tag{5.3}$$

$$\mathcal{R}^{\gamma\gamma}_s = \left(\frac{\Phi^\eta_s}{\Phi^{\eta'}_s}\right)^3 \frac{\mathcal{B}_{B^0_s\to J/\psi\eta'}}{\mathcal{B}_{B^0_s\to J/\psi\eta}} = \frac{N_{B^0_s\to J/\psi\eta'}}{N_{B^0_s\to J/\psi\eta}} \frac{\varepsilon_{B^0_s\to J/\psi\eta}}{\varepsilon_{B^0_s\to J/\psi\eta'}} \frac{\mathcal{B}_{\eta\to\pi^+\pi^-\pi^0}\mathcal{B}_{\pi^0\to\gamma\gamma}}{\mathcal{B}_{\eta'\to\pi^+\pi^-\eta}\mathcal{B}_{\eta\to\gamma\gamma}}. \tag{5.4}$$

$$\tag{5.5}$$

and for both single and two-photon channels, $\mathcal{R}_\eta$ and $\mathcal{R}_{\eta'}$ are calculated as

$$\mathcal{R}_\eta = \left(\frac{\Phi^\eta_s}{\Phi^\eta_d}\right)^3 \frac{\mathcal{B}_{B^0\to J/\psi\eta}}{\mathcal{B}_{B^0_s\to J/\psi\eta}} = \frac{N_{B^0\to J/\psi\eta}}{N_{B^0_s\to J/\psi\eta}} \frac{\varepsilon_{B^0_s\to J/\psi\eta}}{\varepsilon_{B^0\to J/\psi\eta}} \frac{f_s}{f_d}, \tag{5.6}$$

$$\mathcal{R}_{\eta'} = \left(\frac{\Phi^{\eta'}_s}{\Phi^{\eta'}_d}\right)^3 \frac{\mathcal{B}_{B^0\to J/\psi\eta'}}{\mathcal{B}_{B^0_s\to J/\psi\eta'}} = \frac{N_{B^0\to J/\psi\eta'}}{N_{B^0_s\to J/\psi\eta'}} \frac{\varepsilon_{B^0_s\to J/\psi\eta'}}{\varepsilon_{B^0\to J/\psi\eta'}} \frac{f_s}{f_d}. \tag{5.7}$$

This gives the resulting ratios as

$$\mathcal{R}^\gamma_d = 0.80 \pm 0.20\,(\text{stat}) \pm 0.06\,(\text{syst}) \pm 0.02(\mathcal{B}), \tag{5.8}$$
$$\mathcal{R}^\gamma_s = 1.004 \pm 0.035\,(\text{stat}) \pm 0.037\,(\text{syst}) \pm 0.023(\mathcal{B}), \tag{5.9}$$
$$\mathcal{R}^\gamma_\eta = 0.025 \pm 0.006\,(\text{stat}) \pm 0.002\,(\text{syst}) \pm 0.001(f_s/f_d), \tag{5.10}$$
$$\mathcal{R}^\gamma_{\eta'} = 0.0201 \pm 0.0022\,(\text{stat}) \pm 0.0014\,(\text{syst}) \pm 0.0006(f_s/f_d), \tag{5.11}$$

for one photon, and

$$\mathcal{R}^{\gamma\gamma}_d = 0.76 \pm 0.11\,(\text{stat}) \pm 0.10\,(\text{syst}) \pm 0.01(\mathcal{B}), \tag{5.12}$$
$$\mathcal{R}^{\gamma\gamma}_s = 0.98 \pm 0.03\,(\text{stat}) \pm 0.04\,(\text{syst}) \pm 0.02(\mathcal{B}), \tag{5.13}$$
$$\mathcal{R}^{\gamma\gamma}_\eta = 0.0300 \pm 0.0026\,(\text{stat}) \pm 0.0033\,(\text{syst}) \pm 0.0009(f_s/f_d), \tag{5.14}$$
$$\mathcal{R}^{\gamma\gamma}_{\eta'} = 0.0234 \pm 0.0028\,(\text{stat}) \pm 0.0019\,(\text{syst}) \pm 0.0007(f_s/f_d), \tag{5.15}$$

for two photon modes. By using equations (1.156), (1.157), (1.161) and (1.162), these ratio values give the absolute measurements of φ_P and φ_G and summarised in Table 5.22 as well as the exclusion plots in Figure 5.15.

5.8.2. Averaging of ratios over different final states

The resulting measurements of $R_{\eta^{(\prime)},s,d}$ are uncorrelated between the single and two photon channels as they originate form different data sets. Therefore an uncertainty-weighted average of the results can be made using the definitions

$$\overline{x} = \frac{\sum_i^n w_i x_i}{\sum_i^n w_i}, \tag{5.16}$$

where $w_i = 1/\sigma_i^2$ and each measurement is $x_i \pm \sigma_i$. The uncertainty is then propagated as

$$\sigma_{\overline{x}} = \frac{1}{\sqrt{\sum_i^n w_i}}, \tag{5.17}$$

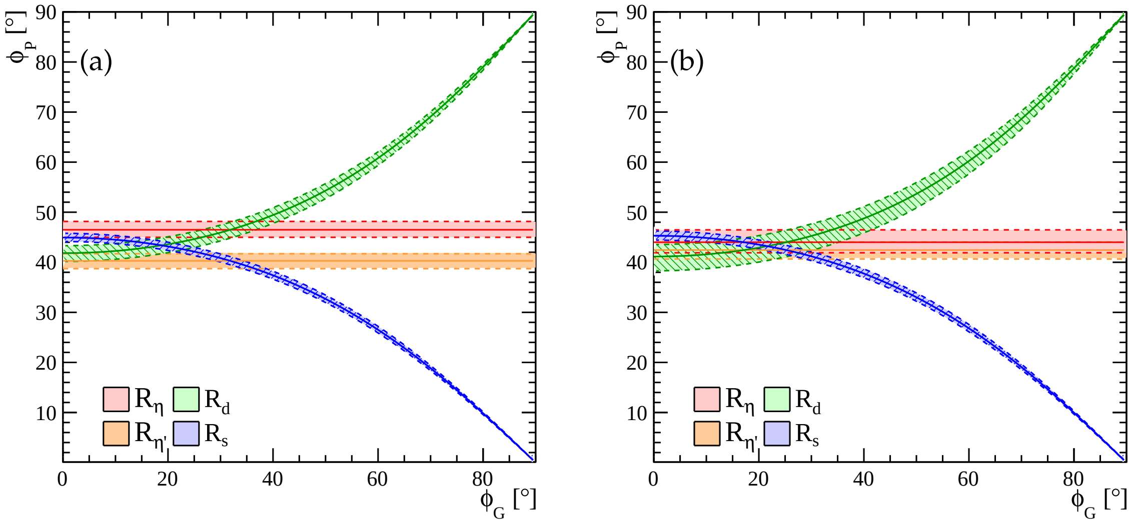

Figure 5.15.: The exclusion plot for the mixing angles φ_P and φ_G as measured by the relevant branching ratios substituted into the ratios $\mathcal{R}_{d,s}$ and $\mathcal{R}_\eta^{(\prime)}$ a) for the single photon channels ($\eta \to \pi^+\pi^-\gamma$ and $\eta' \to \rho^0\gamma$) and b) for the two photon channels ($\eta \to \pi^+\pi^-\pi^0$ and $\eta' \to \pi^+\pi^-\eta$).

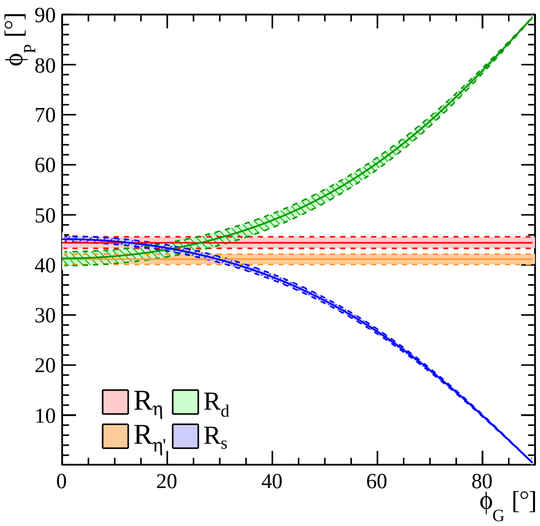

Figure 5.16.: The exclusion plot for the mixing angles φ_P and φ_G as measured by the relevant branching ratios substituted into the ratios $\mathcal{R}_{d,s}$ and $\mathcal{R}_\eta^{(\prime)}$ taking an average of single and two photon channels.

The results of this averaging are:

$$\mathcal{R}_d = 0.77 \pm 0.10\,(\text{stat}) \pm 0.05\,(\text{syst}) \pm 0.01(\mathcal{B}), \tag{5.18}$$

$$\mathcal{R}_s = 0.990 \pm 0.023\,(\text{stat}) \pm 0.028\,(\text{syst}) \pm 0.014(\mathcal{B}), \tag{5.19}$$

$$\mathcal{R}_\eta = 0.0291 \pm 0.0023\,(\text{stat}) \pm 0.0016\,(\text{syst}) \pm 0.0006(f_s/f_d), \tag{5.20}$$

$$\mathcal{R}_{\eta'} = 0.0213 \pm 0.0017\,(\text{stat}) \pm 0.0010\,(\text{syst}) \pm 0.0005(f_s/f_d). \tag{5.21}$$

Table 5.23.: The absolute measurements of the branching ratios and the final states used to measure them.

Channel	$\mathcal{B}(B^0_s \to J/\psi\eta)$
$\eta \to \pi^+\pi^-\gamma$	$17.03 \pm 0.55\,(\text{stat}) \pm 0.32(\mathcal{B}) \pm 1.10(\mathcal{R}_\gamma) \pm 0.53(f_s/f_d)$
$\eta \to \pi^+\pi^-\pi^0$	$18.99 \pm 0.45\,(\text{stat}) \pm 0.23(\mathcal{B}) \pm 1.29(\mathcal{R}_{\pi^0}) \pm 0.59(f_s/f_d)$
Channel	$\mathcal{B}(B^0 \to J/\psi\eta)$
$\eta \to \pi^+\pi^-\gamma$	$0.405 \pm 0.091\,(\text{stat}) \pm 0.008(\mathcal{B}) \pm 0.026(\mathcal{R}_\gamma)$
$\eta \to \pi^+\pi^-\pi^0$	$0.537 \pm 0.045\,(\text{stat}) \pm 0.007(\mathcal{B}) \pm 0.037(\mathcal{R}_\gamma)$
Channel	$\mathcal{B}(B^0_s \to J/\psi\eta')$
$\eta' \to \rho^0\gamma$	$13.77 \pm 0.23\,(\text{stat}) \pm 0.19(\mathcal{B}) \pm 0.89(\mathcal{R}_\gamma) \pm 0.43(f_s/f_d)$
$\eta' \to \pi^+\pi^-\eta$	$11.79 \pm 0.30\,(\text{stat}) \pm 0.15(\mathcal{B}) \pm 1.08(\mathcal{R}_\gamma) \pm 0.37(f_s/f_d)$
Channel	$\mathcal{B}(B^0 \to J/\psi\eta')$
$\eta' \to \rho^0\gamma$	$0.256 \pm 0.028\,(\text{stat}) \pm 0.003(\mathcal{B}) \pm 0.017(\mathcal{R}_\gamma)$
$\eta' \to \pi^+\pi^-\eta$	$0.255 \pm 0.030\,(\text{stat}) \pm 0.003(\mathcal{B}) \pm 0.023(\mathcal{R}_\gamma)$

The averaged ratios then give the complete exclusion plot summarising all of the results in Figure 5.16 which correspond to the averaged mixing angles

$$\varphi_P^{\mathcal{R}_d/\mathcal{R}_s} = (43.2 \pm 1.0\,(\text{stat}) \pm 0.5\,(\text{syst}))^\circ, \tag{5.22}$$
$$\varphi_G^{\mathcal{R}_d\times\mathcal{R}_s} = (20.8 \pm 4.8\,(\text{stat}) \pm 2.8\,(\text{syst}) \pm 0.8(\mathcal{B}))^\circ, \tag{5.23}$$

where the intermediary branching ratios cancel in the ratio of $\mathcal{R}_d/\mathcal{R}_s$ removing their contribution to the uncertainty of φ_P. Whereas, in the multiplication of $\mathcal{R}_d \times \mathcal{R}_s$, this contribution is increased. The other two averaged ratios are

$$\varphi_P^{\mathcal{R}_\eta} = (44.5 \pm 1.5\,(\text{stat}) \pm 1.1\,(\text{syst}) \pm 0.4(f_s/f_d))^\circ, \tag{5.24}$$
$$\varphi_P^{\mathcal{R}_{\eta'}} = (41.1 \pm 1.5\,(\text{stat}) \pm 0.9\,(\text{syst}) \pm 0.4(f_s/f_d))^\circ \tag{5.25}$$

where these calculations have assumed that the transition form factors $F_{B^0\to J/\psi d\bar{d}}$ and $F_{B^0_s\to J/\psi s\bar{s}}$ are equal. It is worth noting that these two measurements are not independent of the measurement in equation (5.22) and that measuring φ_P using the ratio $\mathcal{R}_{\eta'}/\mathcal{R}_\eta$ would be the exact same calculation as $\mathcal{R}_d/\mathcal{R}_s$ using ratios of the same signal yields, efficiencies and branching ratios.

5.8.3. Absolute branching ratios $\mathcal{B}$ ($B^0_{(s)} \to J/\psi\eta^{(\prime)}$)

This section gives the result of the branching ratios of the four decays $B^0_{(s)} \to J/\psi\eta^{(\prime)}$ with two results for each final state of η and η', and an average of the two. Combining the signal yields of Section 5.5.6 with the efficiencies of Section 5.6 into equations (3.2) and (3.3) gives the normalised ratio of branching ratios as shown in Table 5.23. The average of the results for single and two-photon final states gives

$$\frac{\mathcal{B}_{B^0_s\to J/\psi\eta}}{\mathcal{B}_{B^0\to J/\psi\rho^0}} = 18.08 \pm 0.35\,(\text{stat}) \pm 0.59\,(\text{syst}) \pm 0.19(\mathcal{B}) \pm 0.84(\mathcal{R}_\gamma) \pm 0.39(f_s/f_d), \tag{5.26}$$

$$\frac{\mathcal{B}_{B^0\to J/\psi\eta}}{\mathcal{B}_{B^0\to J/\psi\rho^0}} = 0.511 \pm 0.040\,(\text{stat}) \pm 0.023\,(\text{syst}) \pm 0.005(\mathcal{B}) \pm 0.021(\mathcal{R}_\gamma), \tag{5.27}$$

$$\frac{\mathcal{B}_{B^0_s\to J/\psi\eta'}}{\mathcal{B}_{B^0\to J/\psi\rho^0}} = 12.73 \pm 0.18\,(\text{stat}) \pm 0.32\,(\text{syst}) \pm 0.12(\mathcal{B}) \pm 0.69(\mathcal{R}_\gamma) \pm 0.28(f_s/f_d), \tag{5.28}$$

$$\frac{\mathcal{B}_{B^0\to J/\psi\eta'}}{\mathcal{B}_{B^0\to J/\psi\rho^0}} = 0.255 \pm 0.020\,(\text{stat}) \pm 0.013\,(\text{syst}) \pm 0.002(\mathcal{B}) \pm 0.014(\mathcal{R}_\gamma), \tag{5.29}$$

which, by multiplying by the known branching ratio $\mathcal{B}(B^0 \to J/\psi\rho^0) = (2.55^{+0.18}_{-0.16}) \times 10^{-5}$ [41] gives the average absolute branching ratios as

$$\mathcal{B}_{B^0_s\to J/\psi\eta} = \Big(4.61 \pm 0.09\,(\text{stat}) \pm 0.15\,(\text{syst}) \pm 0.05(\mathcal{B}) \pm 0.21(\mathcal{R}_\gamma) \pm 0.10(f_s/f_d)^{+0.33}_{-0.29}(\mathcal{B}_{B^0\to J/\psi\rho^0})\Big) \times 10^{-4}, \tag{5.30}$$

$$\mathcal{B}_{B^0\to J/\psi\eta} = \Big(1.30 \pm 0.10\,(\text{stat}) \pm 0.06\,(\text{syst}) \pm 0.13(\mathcal{B}) \pm 0.05(\mathcal{R}_\gamma)^{+0.09}_{-0.08}(\mathcal{B}_{B^0\to J/\psi\rho^0})\Big) \times 10^{-5}, \tag{5.31}$$

$$\mathcal{B}_{B^0_s\to J/\psi\eta'} = \Big(3.25 \pm 0.05\,(\text{stat}) \pm 0.08\,(\text{syst}) \pm 0.03(\mathcal{B}) \pm 0.18(\mathcal{R}_\gamma) \pm 0.07(f_s/f_d)^{+0.23}_{-0.20}(\mathcal{B}_{B^0\to J/\psi\rho^0})\Big) \times 10^{-4}, \tag{5.32}$$

$$\mathcal{B}_{B^0\to J/\psi\eta'} = \Big(6.51 \pm 0.52\,(\text{stat}) \pm 0.33\,(\text{syst}) \pm 0.06(\mathcal{B}) \pm 0.34(\mathcal{R}_\gamma)^{+0.46}_{-0.41}(\mathcal{B}_{B^0\to J/\psi\rho^0})\Big) \times 10^{-6}. \tag{5.33}$$

5.9. Discussion of results

5.9.1. Compatibility between single photon and two-photon results

In the case of both the branching ratio measurements and the mixing angles there was excellent agreement (less than one σ) between the results with one photon or two photons in the final state. This suggests that the selections and overall methodology for the two cases were performed in a consistent way. With the similar statistical uncertainty of the single and two-

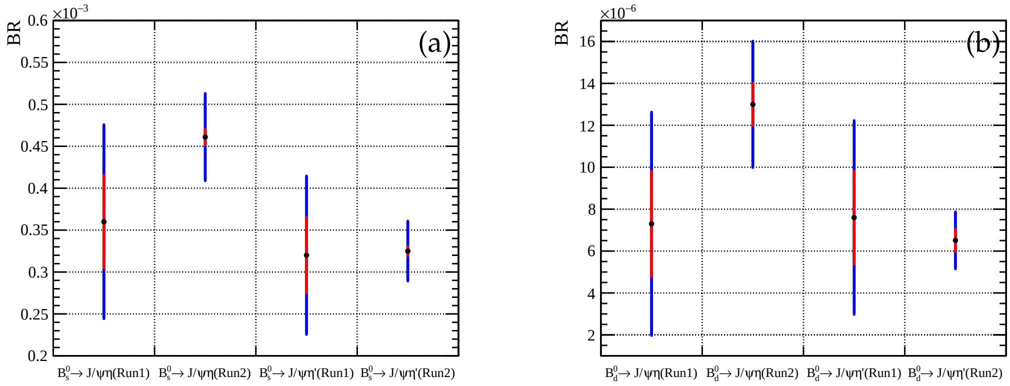

Figure 5.17.: Comparison of the average branching ratio measurements from the previous Run-1 result [77] and the current Run-1 and Run-2 result presented in this thesis. a) showing the results for the $B^0_s \to J/\psi\eta^{(\prime)}$ branching ratios and b) showing the results for the $B^0 \to J/\psi\eta^{(\prime)}$ branching ratios. The uncertainties shown are statistical in red and total in blue.

photon results, it has proven useful to perform these measurements with multiple final states to take advantage of the increased statistics, in contrast to the previous Run-1 analysis of η-η' mixing [77] which only used the results from the two-photon channels for that aim.

5.9.2. $\mathrm{SU}(3)_F$ symmetry

There were calculations of the mixing angle φ_P, given in Table 5.22 or averaged as equations (5.24) and (5.25), that relied on the assumption that $\mathrm{SU}(3)_F$ symmetry is not broken, *i.e.* that the form factors $F_{B^0 \to J/\psi d\bar{d}} \approx F_{B^0_s \to J/\psi s\bar{s}}$. If this were not the case then the measurements of φ_P using $\mathcal{R}_\eta$ and $\mathcal{R}_{\eta'}$ would not have agreed with each other or the results from $\mathcal{R}_d/\mathcal{R}_s$. Yet, at the precision of these studies, this seemed to be the case. This implies that future studies with these decay channels may need increased statistics in order to be sensitive to $\mathrm{SU}(3)_F$ symmetry breaking effects.

5.9.3. Previous measurements at LHCb: $\mathcal{B}$ measurement

There were two previous analyses of these decays at LHCb. One using only 2011 data studied the absolute branching ratios of only $B^0_s \to J/\psi\eta^{(\prime)}$ with the same number of final states as this thesis (only using $\eta \to \gamma\gamma$ instead of $\eta \to \pi^+\pi^-\gamma$) of the $\eta^{(\prime)}$ [76]. As this data set is particularly small, that analysis could not measure the $B^0 \to J/\psi\eta^{(\prime)}$ precisely enough. The results with external factors at the time were

$$\mathcal{B}(B^0_s \to J/\psi\eta) = \left(3.79 \pm 0.31\,(\mathrm{stat})^{+0.20}_{-0.41}\,(\mathrm{syst})^{+0.29}_{-0.27}(f_s/f_d) \pm 0.56(\mathcal{B})\right) \times 10^{-4}, \tag{5.34}$$

$$\mathcal{B}(B^0_s \to J/\psi\eta') = \left(3.42 \pm 0.30\,(\mathrm{stat})^{+0.14}_{-0.35}\,(\mathrm{syst})^{+0.26}_{-0.25}(f_s/f_d) \pm 0.51(\mathcal{B})\right) \times 10^{-4}, \tag{5.35}$$

which are both compatible with the results of this thesis. From Table 2.1 in Section 2.2 it can be seen that, due to the luminosity and cross-section, there should be $(850 \pm 120) \times 10^9$ $b\bar{b}$ pairs in the full Run-1 and Run-2 data set and $(80 \pm 8) \times 10^9$ in 2011. Therefore the improvement on the statistical uncertainty should be by a factor of 3.3 with the same analysis strategy, yet with the strategy of this thesis, especially with the use of a multivariate analysis, the statistical uncertainty has actually improved by a factor of 3.9 for $B^0_s \to J/\psi\eta$ and 6 for $B^0_s \to J/\psi\eta'$.

In Figure 5.17 a comparison of these results are made where the ratio of $\frac{\mathcal{B}_{B^0_s \to J/\psi\eta^{(\prime)}}}{\mathcal{B}_{B^0 \to J/\psi\rho^0}}$ and the previous measurements of $\mathcal{R}_{\eta^{(\prime)}}$ [77] are multiplied with the current PDG average of the branching ratio of $B^0 \to J/\psi\rho^0$ to get the most up to date measurements.

5.9.4. Previous measurements at LHCb: η-η' mixing measurement

Another analysis performed at the LHCb experiment aimed to measure the same mixing angles of this thesis [77]. This previous study was performed on 2011 and 2012 data (*i.e.* Run-1 with $(255 \pm 22) \times 10^9$ $b\bar{b}$ pairs) and looked solely at the two-photon channels. The measured ratios of $\mathcal{R}_d$, $\mathcal{R}_s$, $\mathcal{R}_\eta$ and $\mathcal{R}_{\eta'}$ are all compatible between the Run-1 and Run-2 result of this thesis and the previous Run-1 result. Therefore the same can be said for the mixing angles themselves. The four ratios were quoted at the time as

$$\mathcal{R}_d = 1.111 \pm 0.475\,(\text{stat}) \pm 0.058\,(\text{syst}) \pm 0.023(\mathcal{B}), \tag{5.36}$$

$$\mathcal{R}_s = 0.902 \pm 0.072\,(\text{stat}) \pm 0.041\,(\text{syst}) \pm 0.019(\mathcal{B}), \tag{5.37}$$

$$\mathcal{R}_\eta = 0.0185 \pm 0.0061\,(\text{stat}) \pm 0.0009\,(\text{syst}) \pm 0.0011(f_s/f_d), \tag{5.38}$$

$$\mathcal{R}_{\eta'} = 0.0228 \pm 0.0065\,(\text{stat}) \pm 0.0010\,(\text{syst}) \pm 0.0013(f_s/f_d). \tag{5.39}$$

With the increased statistics of Run-1 and Run-2 there should be an improvement in statistical uncertainty of a factor of 1.8. For $\mathcal{R}_d$ using the same two photon channels (equation (5.12)) the improvement was by a factor of 2.8, and with the additional single photon channels it becomes a factor of 3.2. In Section 5.4 the expressed purpose of the BDT cut choice selections method was to improve the precision of measuring $B^0 \to J/\psi\eta^{(\prime)}$ and therefore $\mathcal{R}_d$. For the fraction of $\mathcal{R}_s$ the improvement using the same channels was a factor of 2.7 and with all channels was 3, so overall there was a similar improvement in the result.

The previous results of φ_P were $\varphi_P = (43.5^{+1.4}_{-2.8})^\circ$ using $\mathcal{R}_d$ and $\mathcal{R}_s$, well within one σ of the result of this thesis. Under the same assumption of $\text{SU}(3)_F$ symmetry their results were $\varphi_P = (43.8^{+3.9}_{-5.4})^\circ$ and $\varphi_P = (49.4^{+6.5}_{-4.5})^\circ$ using $\mathcal{R}_{\eta'}$ and $\mathcal{R}_\eta$, again in agreement with this thesis. The mixing angle related to the mixing between η' and a gluonium state was measured as $\varphi_G = (0 \pm 24.6)^\circ$ in Run-1, which is compatible with the full Run-1 and Run-2 result of $\varphi_G = (20.2 \pm 5.3\,(\text{stat}) \pm 0.8(\mathcal{B}))$. The major difference is that the central value of the mixing angle φ_G is 3.7σ from zero and provides evidence that there could be mixing between the η' and a non-$q\bar{q}$ bound gluonium state.

5.9.5. The bound gluon states

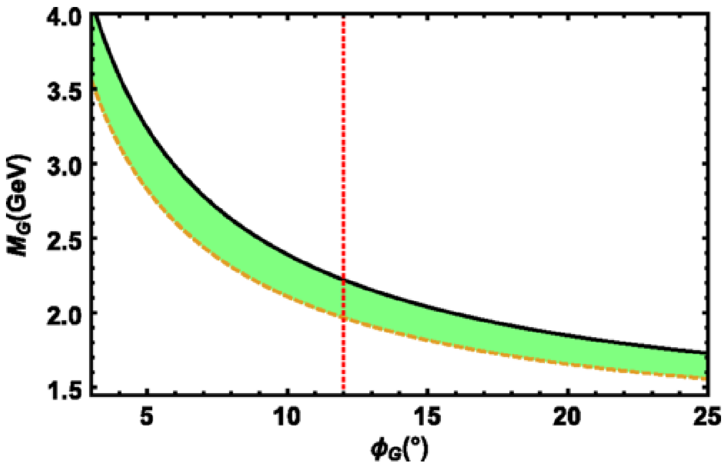

Figure 5.18.: The exclusion plot of the mass of a pseudoscalar gluonium, m_G, versus the mixing angle, φ_G produced in [127]. This is produced in a η-η'-η_G-η_c mixing scheme with assumed angles $\varphi_P = 43.7°$ and $\varphi_Q = 11.6°$ where φ_Q is the mixing angle between η_c and η_G. The green region is determined by uncertainty on the gluonic field strength. The red vertical dashed line shows the φ_G central value of a phenomenological analysis $\varphi_G = 12 \pm 13$ [128].

Providing evidence of the mixing between the η' meson and gluonium η_G with a measurement of φ_G can also suggest the mass that a gluonium pseudoscalar would have. In [127] they determine reasonable values of the physical mass of gluonium by studying the mixing between $\eta^{(\prime)}$ and gluonium, namely as a function of φ_G with other parameters constrained. This produces the plot given in Figure 5.18. With the resulting measurement of this thesis and that correlation with the mass, the mass range of the gluonium state should be about 1.5 GeV to 2.1 GeV, in agreement with the suggestions of [42], and as discussed in more depth in Section 1.3.5. This thesis therefore provides further evidence that the identification of a physical gluonium state could be done through the study of resonances around this range. Although studies of gluonium are still in their infancy, there are two good candidates ($\eta(1760)$ and $X(1835)$) that fit well within the range suggested in this thesis.

The $\eta(1760)$ was first observed in $J/\psi \to \gamma\rho^0\rho^0$ decays as a resonance in $\rho^0\rho^0$ by the DM2 Collaboration [129]. A partial wave analysis was later performed by the BES Collaboration which found this meson in $J/\psi \to \gamma\eta(1760)[\omega\omega]$ decays [130] and shows that it may have a large gluonic component and so is a good candidate. The Belle Collaboration also reported the presence of $\eta(1760)$ decays in $\gamma\gamma$ production to $\pi^+\pi^-\ \eta'$ [131] which is analgous to the $\eta' \to \pi^+\pi^-\eta$ channel of this thesis. The $\gamma\gamma$ production of $\eta(1760)$ in would be expected to be very low if $\eta(1760)$ was indeed mostly gluonium, which has been estimated to be as low as (1.4 ± 0.7) keV [132].

$X(1835)$ has previously been suggested as a good gluonium candidate by [133] after it was first seen decaying to $\pi^+\pi^-\ \eta'$ by BES-II and has been reported many times again by BES-II, CLEO and BES-III [134–142]. In the latest BES-III study of this meson it was determined that it is likely to have a sizeable $s\bar{s}$ component as it decays to $\phi\gamma$. Today, there is still need for further studies of the gluonic and $q\bar{q}$ component of both $\eta(1760)$ and $X(1835)$ before a conclusive rejection or acceptance of these mesons as mostly bound gluon states can be made.

Chapter 6.

Conclusions

This thesis has highlighted the latest results in studies of the decay rates of $B^0_{(s)} \to J/\psi\eta^{(\prime)}$ at the LHCb experiment. Chapter 1 showed why these decays are interesting to understand both conventional and non-conventional meson spectroscopy, as well as highlighting the possibility of future measurements of ϕ_s. It covered how decays of $B^0_s \to J/\psi\eta^{(\prime)}$ could be used in measurement of the time-dependent CP asymmetries of B^0_s decays. Described the quark model and the mixing schemes of the η and η' mesons, with predictions from phenomenology. It then described the extended mixing scheme with the inclusion of gluonium and how we could determine the contributions with new measurements of the branching ratios.

In Chapter 2 a brief overview of the LHCb experimental apparatus and its performance was shown in order to aid the reader in understanding the origin of data samples used, along with the source of their associated variables and the environment at which data was collected. There was then some focus on the methods on the reconstruction and identification of neutrals as this was particularly relevant to the performance analysis of this thesis and the process of measuring neutrals in the final states of the physics analysis.

Chapter 3 concerned the analysis strategies of both analyses and the commonalities in their methodology. Covering the selections for $B \to J/\psi X$ decays used, the strategy for correcting simulation occupancy and kinematics variables using the Gradient Boosted Reweighting method, the use of particle identification calibration samples for determining what the real data particle identification efficiencies are, and the strategy for measuring the signal yields by fitting signal and background models to data.

In Chapter 4, the efficiencies of reconstructing individual photons and $\pi^0 \to \gamma\gamma$ were determined for both simulated and real data for the purpose of determining corrections for the simulation efficiencies to be applied in the physics analysis. By effectively controlling other factors, the corrections for neutrals were determined as a ratio of the signal yields efficiencies and branching ratios for either $B^+ \to \chi_{c1}K^+$ or $B^+ \to J/\psi K^{*+}$ over $B^+ \to J/\psi K^+$, the normalisation channel. The corrections were determined to be

$$\begin{aligned}
\mathcal{R}_{\gamma}^{\text{corr}}(2011) &= (105.3 \pm 1.5(stat) \pm 4.8(syst) \pm 6.1(\mathcal{B}))\%\,, \\
\mathcal{R}_{\gamma}^{\text{corr}}(2012) &= (104.5 \pm 1.0(stat) \pm 3.7(syst) \pm 6.0(\mathcal{B}))\%\,, \\
\mathcal{R}_{\gamma}^{\text{corr}}(2016) &= (99.2 \pm 0.7(stat) \pm 2.0(syst) \pm 5.7(\mathcal{B}))\%\,, \\
\mathcal{R}_{\gamma}^{\text{corr}}(2017) &= (100.7 \pm 0.7(stat) \pm 1.9(syst) \pm 5.8(\mathcal{B}))\%\,, \\
\mathcal{R}_{\gamma}^{\text{corr}}(2018) &= (98.3 \pm 0.6(stat) \pm 3.1(syst) \pm 5.7(\mathcal{B}))\%\,,
\end{aligned}$$

for single photons, where the corrections were consistent between 2011 and 2012 (Run-1) and also consistent between 2016 to 2018 (Run-2) but not between Run-1 and Run-2. The corrections for photons originating from π^0 mesons were

$$\mathcal{R}_{\pi^0}^{\text{corr}}(2011) = (88.8 \pm 3.5(stat) \pm 3.0(syst) \pm 5.2(\mathcal{B}))\%\,, \tag{6.1}$$
$$\mathcal{R}_{\pi^0}^{\text{corr}}(2012) = (75.8 \pm 1.8(stat) \pm 2.5(syst) \pm 4.5(\mathcal{B}))\%\,, \tag{6.2}$$
$$\mathcal{R}_{\pi^0}^{\text{corr}}(2016) = (79.9 \pm 1.5(stat) \pm 2.1(syst) \pm 4.7(\mathcal{B}))\%\,, \tag{6.3}$$
$$\mathcal{R}_{\pi^0}^{\text{corr}}(2017) = (80.2 \pm 1.6(stat) \pm 1.9(syst) \pm 4.7(\mathcal{B}))\%\,, \tag{6.4}$$
$$\mathcal{R}_{\pi^0}^{\text{corr}}(2018) = (78.6 \pm 1.6(stat) \pm 1.6(syst) \pm 4.6(\mathcal{B}))\%\,, \tag{6.5}$$

where the Run-2 corrections were consistent with each other but the Run-1 corrections were not.

Chapter 5 was the final chapter that gave the specifics of the physics analysis and its results. This chapter follows the same structure as the preceding one due to the similarities in the overall analysis strategy: calculating a ratio of signal yields, efficiencies and branching ratios to produce various ratios of two branching ratios, whether it be signal and normalisation or two different signal channels. The resulting ratios of the various $B^0_{(s)} \to J/\psi\eta^{(\prime)}$ channels averaged between $\eta^{(\prime)} \to \pi^+\pi^-\gamma$ and $\eta^{(\prime)} \to \pi^+\pi^-\gamma\gamma$ final states were

$$\begin{aligned}
\mathcal{R}_d &= \left(\frac{\Phi_d^{\eta}}{\Phi_d^{\eta'}}\right)^3 \frac{\mathcal{B}_{B^0\to J/\psi\eta'}}{\mathcal{B}_{B^0\to J/\psi\eta}} = 0.77 \pm 0.10\,(\text{stat}) \pm 0.05\,(\text{syst}) \pm 0.01(\mathcal{B}), \\
\mathcal{R}_s &= \left(\frac{\Phi_s^{\eta}}{\Phi_s^{\eta'}}\right)^3 \frac{\mathcal{B}_{B^0_s\to J/\psi\eta'}}{\mathcal{B}_{B^0_s\to J/\psi\eta}} = 0.990 \pm 0.023\,(\text{stat}) \pm 0.028\,(\text{syst}) \pm 0.014(\mathcal{B}), \\
\mathcal{R}_\eta &= \left(\frac{\Phi_s^{\eta}}{\Phi_d^{\eta}}\right)^3 \frac{\mathcal{B}_{B^0\to J/\psi\eta}}{\mathcal{B}_{B^0_s\to J/\psi\eta}} = 0.0291 \pm 0.0023\,(\text{stat}) \pm 0.0016\,(\text{syst}) \pm 0.0006(f_s/f_d), \\
\mathcal{R}_{\eta'} &= \left(\frac{\Phi_s^{\eta'}}{\Phi_d^{\eta'}}\right)^3 \frac{\mathcal{B}_{B^0\to J/\psi\eta'}}{\mathcal{B}_{B^0_s\to J/\psi\eta'}} = 0.0213 \pm 0.0017\,(\text{stat}) \pm 0.0010\,(\text{syst}) \pm 0.0005(f_s/f_d).
\end{aligned}$$

where $\Phi_{d,s}^{\eta'}$ are phase-space factors for the $B^0_{(s)} \to J/\psi\eta^{(\prime)}$ decays. The quark and gluonium content of the η and η' mesons were discerned from these results to be

$$
\begin{aligned}
|\eta\rangle &= (0.729 \pm 0.012 \pm 0.006)|\eta_q\rangle - (0.69 \pm 0.06 \pm 0.04)|\eta_s\rangle, \\
|\eta'\rangle &= (0.64 \pm 0.24 \pm 0.01)|\eta_q\rangle + (0.68 \pm 0.24 \pm 0.01)|\eta_s\rangle - (0.355 \pm 0.030 \pm 0.017)|\eta_G\rangle,
\end{aligned}
$$

where the gluonium component of η is assumed to be negligible. Alongside these results were updates to the branching ratios of $B^0_{(s)} \to J/\psi\eta^{(\prime)}$ decays normalised to the branching ratio of $B^0 \to J/\psi\rho^0$:

$$
\begin{aligned}
\frac{\mathcal{B}_{B^0_s \to J/\psi\eta}}{\mathcal{B}_{B^0 \to J/\psi\rho^0}} &= 18.08 \pm 0.35\,(\text{stat}) \pm 0.59\,(\text{syst}) \pm 0.19(\mathcal{B}) \pm 0.84(\mathcal{R}_\gamma) \pm 0.39(f_s/f_d), \\
\frac{\mathcal{B}_{B^0 \to J/\psi\eta}}{\mathcal{B}_{B^0 \to J/\psi\rho^0}} &= 0.511 \pm 0.040\,(\text{stat}) \pm 0.023\,(\text{syst}) \pm 0.005(\mathcal{B}) \pm 0.021(\mathcal{R}_\gamma), \\
\frac{\mathcal{B}_{B^0_s \to J/\psi\eta'}}{\mathcal{B}_{B^0 \to J/\psi\rho^0}} &= 12.73 \pm 0.18\,(\text{stat}) \pm 0.32\,(\text{syst}) \pm 0.12(\mathcal{B}) \pm 0.69(\mathcal{R}_\gamma) \pm 0.28(f_s/f_d), \\
\frac{\mathcal{B}_{B^0 \to J/\psi\eta'}}{\mathcal{B}_{B^0 \to J/\psi\rho^0}} &= 0.255 \pm 0.020\,(\text{stat}) \pm 0.013\,(\text{syst}) \pm 0.002(\mathcal{B}) \pm 0.014(\mathcal{R}_\gamma).
\end{aligned}
$$

Together these results were the most precise measurements of branching ratios of these decays, and the mixing between η and η' using these decays, to date.

Appendix A.

Supplementary material for Chapter 4

A.1. Gradient Boosted Reweighting plots for all years

In Section 4.3.1, only 2018 Monte Carlo and collision data for the $B^+ \to J/\psi K^+$ decays were shown as examples for the performance of the reweighting with Gradient Boosted Decision Trees. Yet, this was performed on data from all data-taking periods, so this section displays all of these as supplementary material.

A.2. Kolmogorov-Smirnov distances for all variables used in GBR and BDT training

Table A.1.: The Kolmogorov-Smirnov distances for each variable used in the training of the Gradient Boosted Reweighter or the Multivariate Analysis for the $B^+ \to J/\psi K^+$ 2011 MC sample.

Variable	KS distance	
	Before reweighting	After reweighting
	GBR inputs	
nTracks	0.1310	0.0114
nPVs	0.0533	0.0095
$\log(B\ p_{\mathrm{T}})$	0.0176	0.0117
$\log(J/\psi\ \mathrm{IP})$	0.0065	0.0039
log(cc vector p_{T})	0.0602	0.0075
cc asymmetry p_z	0.0499	0.0102
	BDT inputs	
$\log(B\ p_{\mathrm{T}})$	0.0176	0.0117
$\log(B\ \mathrm{IP})$	0.0443	0.0545
$\log(1 - \lvert DIRA \rvert)$	0.0091	0.0068
$\log(B\ \chi^2_{\mathrm{vtx}})$	0.0234	0.0193
Number of vtx with $\chi^2 < 9$	0.0266	0.0564
log(Smallest $\Delta\chi^2$ one track)	0.0242	0.0149
$\log(J/\psi\ p_{\mathrm{T}})$	0.0265	0.0281
$\log(J/\psi\ \mathrm{IP})$	0.0065	0.0039
min $\log(\mu\ \mathrm{IP})$	0.0100	0.0100
max $\log(\mu\ \chi^2_{\mathrm{IP}})$	0.0203	0.0233
cc multiplicities/nPhotons	0.0271	0.0202
cc asymmetry p_z	0.0499	0.0102
log(cc vector p_{T})	0.0602	0.0075
cc $\Delta\phi$	0.0195	0.0067
cc $\Delta\eta$	0.0300	0.0257

Table A.2.: The Kolmogorov-Smirnov distances for each variable used in the training of the Gradient Boosted Reweighter or the Multivariate Analysis for the $B^+ \to J/\psi K^+$ 2012 MC sample.

Variable	KS distance	
	Before reweighting	After reweighting
	GBR inputs	
nTracks	0.1281	0.0131
nPVs	0.0249	0.0132
$\log(B\ p_{\mathrm{T}})$	0.0148	0.0145
$\log(J/\psi\ \mathrm{IP})$	0.0047	0.0036
$\log(\mathrm{cc\ vector}\ p_{\mathrm{T}})$	0.0777	0.0138
cc asymmetry p_z	0.0532	0.0162
	BDT inputs	
$\log(B\ p_{\mathrm{T}})$	0.0148	0.0145
$\log(B\ \mathrm{IP})$	0.0176	0.0380
$\log(1 - \lvert DIRA \rvert)$	0.0110	0.0063
$\log(B\ \chi^2_{\mathrm{vtx}})$	0.0179	0.0142
Number of vtx with $\chi^2 < 9$	0.0327	0.0691
log(Smallest $\Delta\chi^2$ one track)	0.0221	0.0189
$\log(J/\psi\ p_{\mathrm{T}})$	0.0424	0.0370
$\log(J/\psi\ \mathrm{IP})$	0.0047	0.0036
min $\log(\mu\ \mathrm{IP})$	0.0100	0.0080
max $\log(\mu\ \chi^2_{\mathrm{IP}})$	0.0045	0.0150
cc multiplicities/nPhotons	0.0365	0.0184
cc asymmetry p_z	0.0532	0.0162
$\log(\mathrm{cc\ vector}\ p_{\mathrm{T}})$	0.0777	0.0138
cc $\Delta\phi$	0.0082	0.0114
cc $\Delta\eta$	0.0305	0.0284

Table A.3.: The Kolmogorov-Smirnov distances for each variable used in the training of the Gradient Boosted Reweighter or the Multivariate Analysis for the $B^+ \to J/\psi K^+$ 2016 MC sample.

Variable	KS distance	
	Before reweighting	After reweighting
	GBR inputs	
nTracks	0.1949	0.0262
nPVs	0.0263	0.0280
$\log(B\ p_{\mathrm{T}})$	0.0199	0.0241
$\log(J/\psi$ IP)	0.0101	0.0043
log(cc vector p_{T})	0.0232	0.0286
cc asymmetry p_z	0.0286	0.0284
	BDT inputs	
$\log(B\ p_{\mathrm{T}})$	0.0199	0.0241
$\log(B$ IP)	0.0325	0.0518
$\log(1 - \lvert DIRA \rvert)$	0.0116	0.0310
$\log(B\ \chi^2_{\mathrm{vtx}})$	0.0258	0.0196
Number of vtx with $\chi^2 < 9$	0.0042	0.0134
log(Smallest $\Delta\chi^2$ one track)	0.0105	0.0232
$\log(J/\psi\ p_{\mathrm{T}})$	0.0277	0.0345
$\log(J/\psi$ IP)	0.0101	0.0043
min $\log(\mu$ IP)	0.0069	0.0107
max $\log(\mu\ \chi^2_{\mathrm{IP}})$	0.0161	0.0245
cc multiplicities/nPhotons	0.0113	0.0748
cc asymmetry p_z	0.0286	0.0284
log(cc vector p_{T})	0.0232	0.0286
cc $\Delta\phi$	0.0169	0.0191
cc $\Delta\eta$	0.0081	0.0286

Table A.4.: The Kolmogorov-Smirnov distances for each variable used in the training of the Gradient Boosted Reweighter or the Multivariate Analysis for the $B^+ \to J/\psi K^+$ 2017 MC sample.

Variable	KS distance	
	Before reweighting	After reweighting
	GBR inputs	
nTracks	0.1585	0.0256
nPVs	0.0352	0.0229
log(B p_{T})	0.0145	0.0218
log(J/ψ IP)	0.0214	0.0154
log(cc vector p_{T})	0.0220	0.0226
cc asymmetry p_z	0.0257	0.0264
	BDT inputs	
log(B p_{T})	0.0145	0.0218
log(B IP)	0.0087	0.0201
$\log(1 - \lvert DIRA \rvert)$	0.0014	0.0184
log(B χ^2_{vtx})	0.0424	0.0349
Number of vtx with $\chi^2 < 9$	0.0013	0.0151
log(Smallest $\Delta\chi^2$ one track)	0.0048	0.0286
log(J/ψ p_{T})	0.0320	0.0355
log(J/ψ IP)	0.0214	0.0154
min log(μ IP)	0.0147	0.0110
max log(μ χ^2_{IP})	0.0090	0.0162
cc multiplicities/nPhotons	0.0151	0.0686
cc asymmetry p_z	0.0257	0.0264
log(cc vector p_{T})	0.0220	0.0226
cc $\Delta\phi$	0.0174	0.0119
cc $\Delta\eta$	0.0075	0.0252

Table A.5.: The Kolmogorov-Smirnov distances for each variable used in the training of the Gradient Boosted Reweighter or the Multivariate Analysis for the $B^+ \to J/\psi K^+$ 2018 MC sample.

Variable	KS distance	
	Before reweighting	After reweighting
	GBR inputs	
nTracks	0.1752	0.0290
nPVs	0.0384	0.0256
$\log(B\ p_{\mathrm{T}})$	0.0220	0.0204
$\log(J/\psi$ IP)	0.0244	0.0170
log(cc vector p_{T})	0.0247	0.0233
cc asymmetry p_z	0.0240	0.0266
	BDT inputs	
$\log(B\ p_{\mathrm{T}})$	0.0220	0.0204
$\log(B$ IP)	0.0170	0.0114
$\log(1 - \lvert DIRA \rvert)$	0.0089	0.0163
$\log(B\ \chi^2_{\mathrm{vtx}})$	0.0364	0.0285
Number of vtx with $\chi^2 < 9$	0.0026	0.0158
log(Smallest $\Delta\chi^2$ one track)	0.0085	0.0317
$\log(J/\psi\ p_{\mathrm{T}})$	0.0566	0.0480
$\log(J/\psi$ IP)	0.0244	0.0170
min $\log(\mu$ IP)	0.0177	0.0130
max $\log(\mu\ \chi^2_{\mathrm{IP}})$	0.0077	0.0161
cc multiplicities/nPhotons	0.0148	0.0735
cc asymmetry p_z	0.0240	0.0266
log(cc vector p_{T})	0.0247	0.0233
cc $\Delta\phi$	0.0174	0.0153
cc $\Delta\eta$	0.0165	0.0257

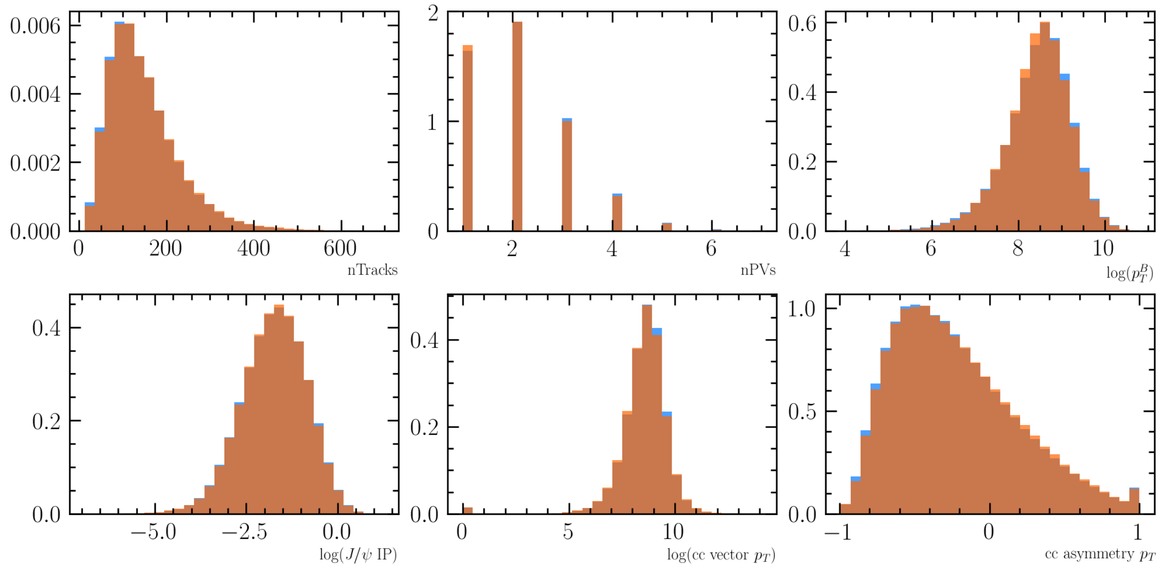

Figure A.1.: The distributions of the input variables and expressions used for the training of the Gradient Boosted Reweighter. The orange distribution is the background-subtracted $B^+ \to J/\psi K^+$ 2011 collision data used as a target. The blue distribution is the original $B^+ \to J/\psi K^+$ 2011 MC data.

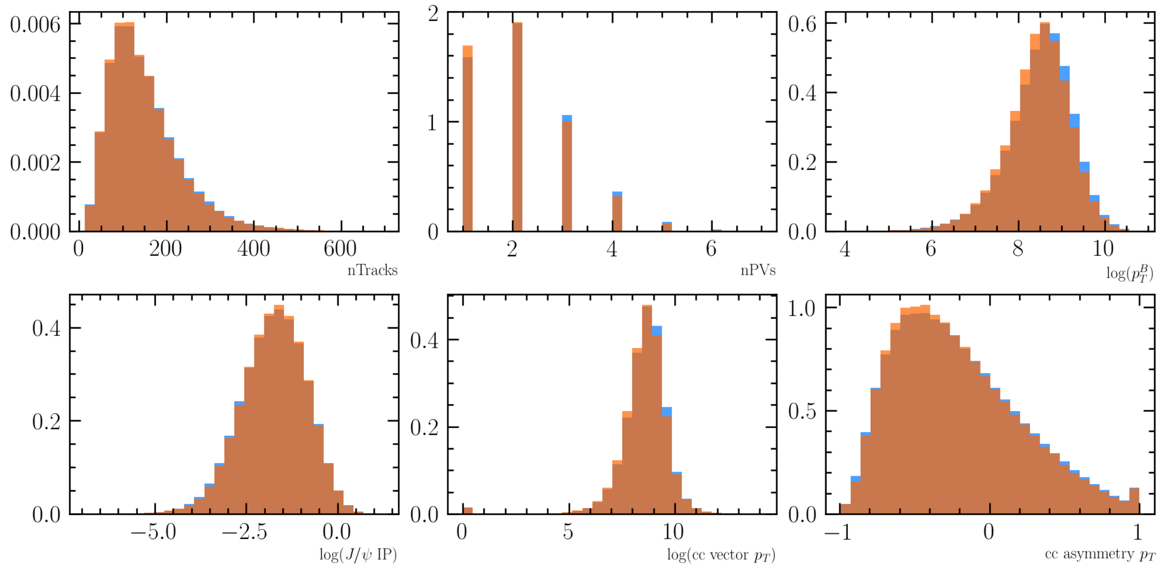

Figure A.2.: The distributions of the input variables and expressions used for the training of the Gradient Boosted Reweighter. The orange distribution is the background-subtracted $B^+ \to J/\psi K^+$ 2011 collision data used as a target. The blue distribution is the $B^+ \to J/\psi K^+$ 2011 MC data after applying the event-by-event weights that were calculated by the reweighter.

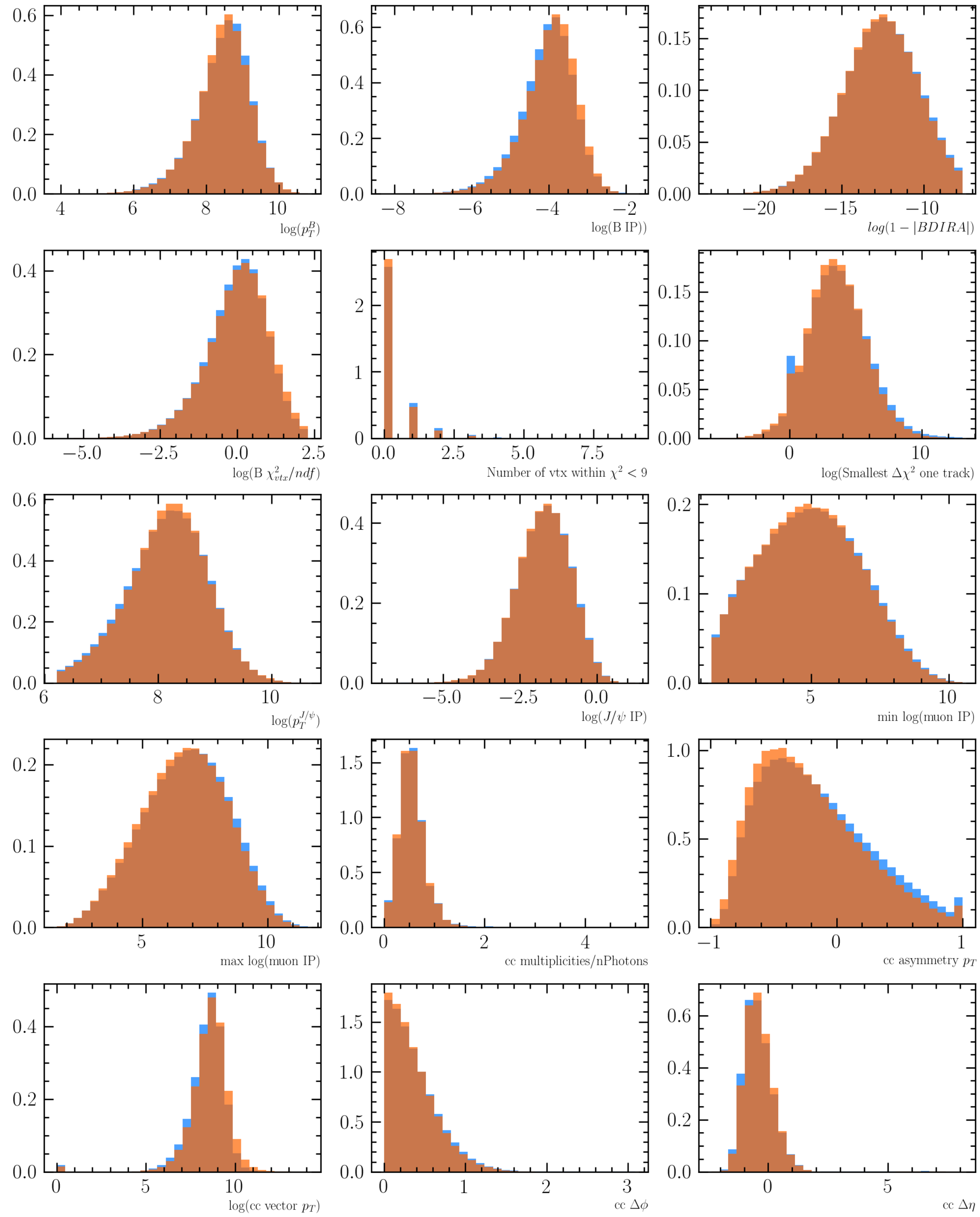

Figure A.3.: The distributions of a subset of the variables and expressions used in the training of the MVA (omitting those unavailable to $B^+ \to J/\psi K^+$ decays) as well as occupancy variables. The orange distribution is the background-subtracted $B^+ \to J/\psi K^+$ 2011 collision data used as a target. The blue distribution is the original $B^+ \to J/\psi K^+$ 2011 MC data.

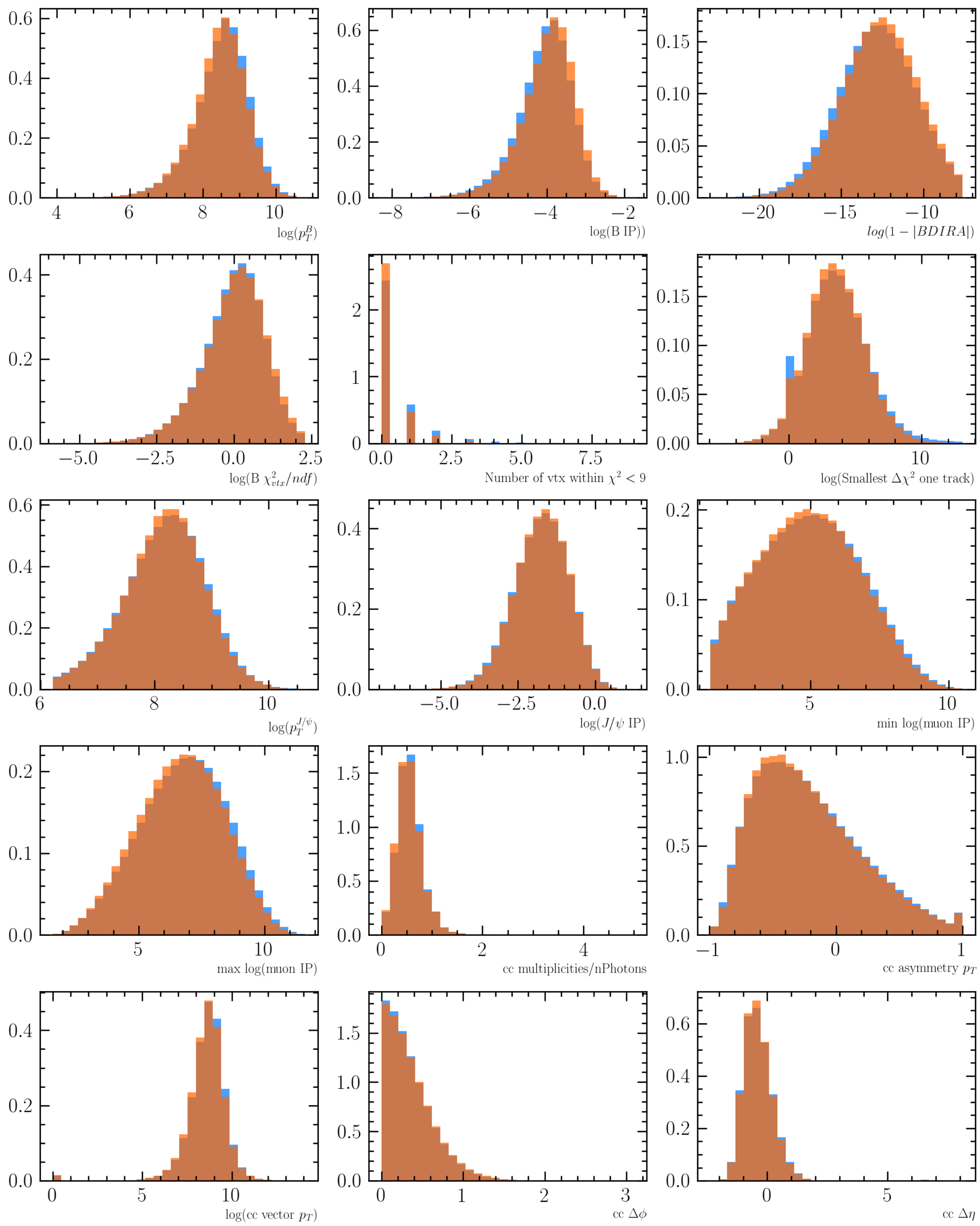

Figure A.4.: The distributions of a subset of the variables and expressions used in the training of the MVA (omitting those unavailable to $B^+ \to J/\psi K^+$ decays) as well as occupancy variables. The orange distribution is the background-subtracted $B^+ \to J/\psi K^+$ 2011 collision data used as a target. The blue distribution is the $B^+ \to J/\psi K^+$ 2011 MC data after applying weights calculated by the reweighter.

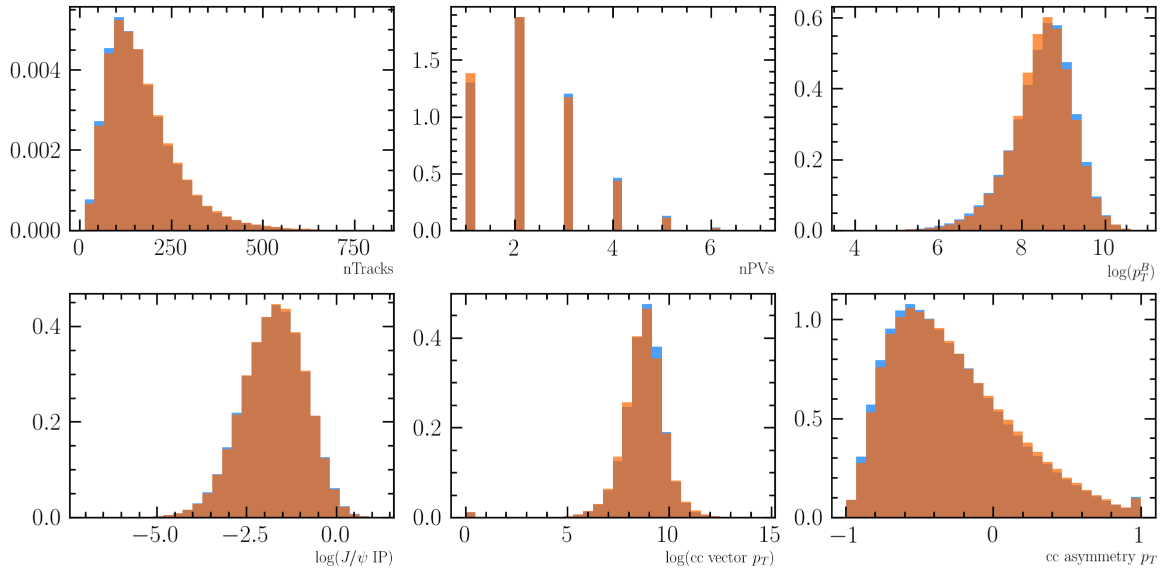

Figure A.5.: The distributions of the input variables and expressions used for the training of the Gradient Boosted Reweighter. The orange distribution is the background-subtracted $B^+ \to J/\psi K^+$ 2012 collision data used as a target. The blue distribution is the original $B^+ \to J/\psi K^+$ 2012 MC data.

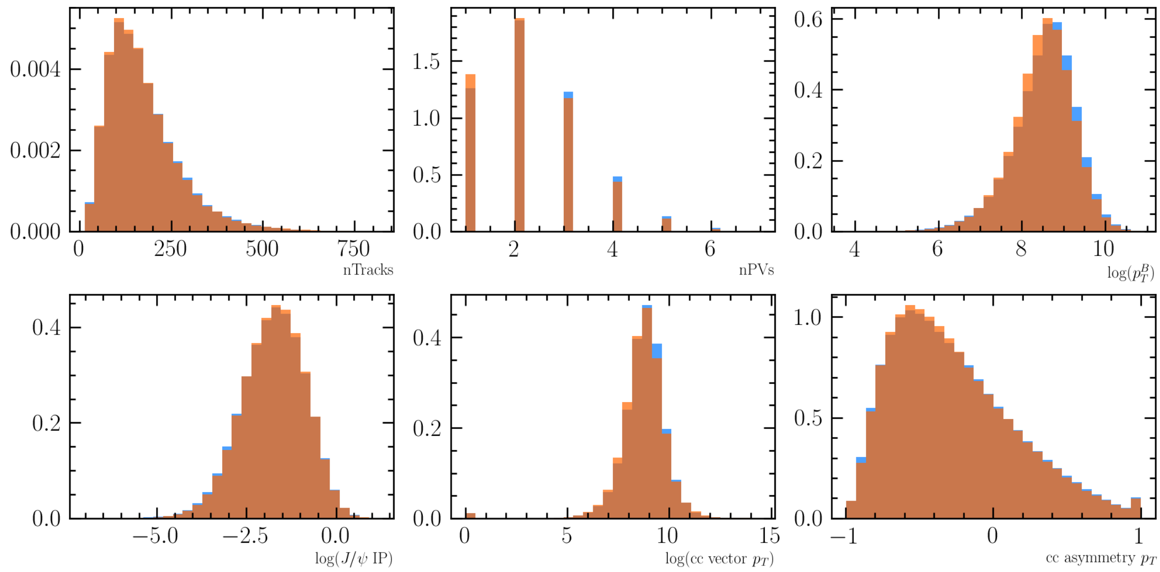

Figure A.6.: The distributions of the input variables and expressions used for the training of the Gradient Boosted Reweighter. The orange distribution is the background-subtracted $B^+ \to J/\psi K^+$ 2012 collision data used as a target. The blue distribution is the $B^+ \to J/\psi K^+$ 2012 MC data after applying the event-by-event weights that were calculated by the reweighter.

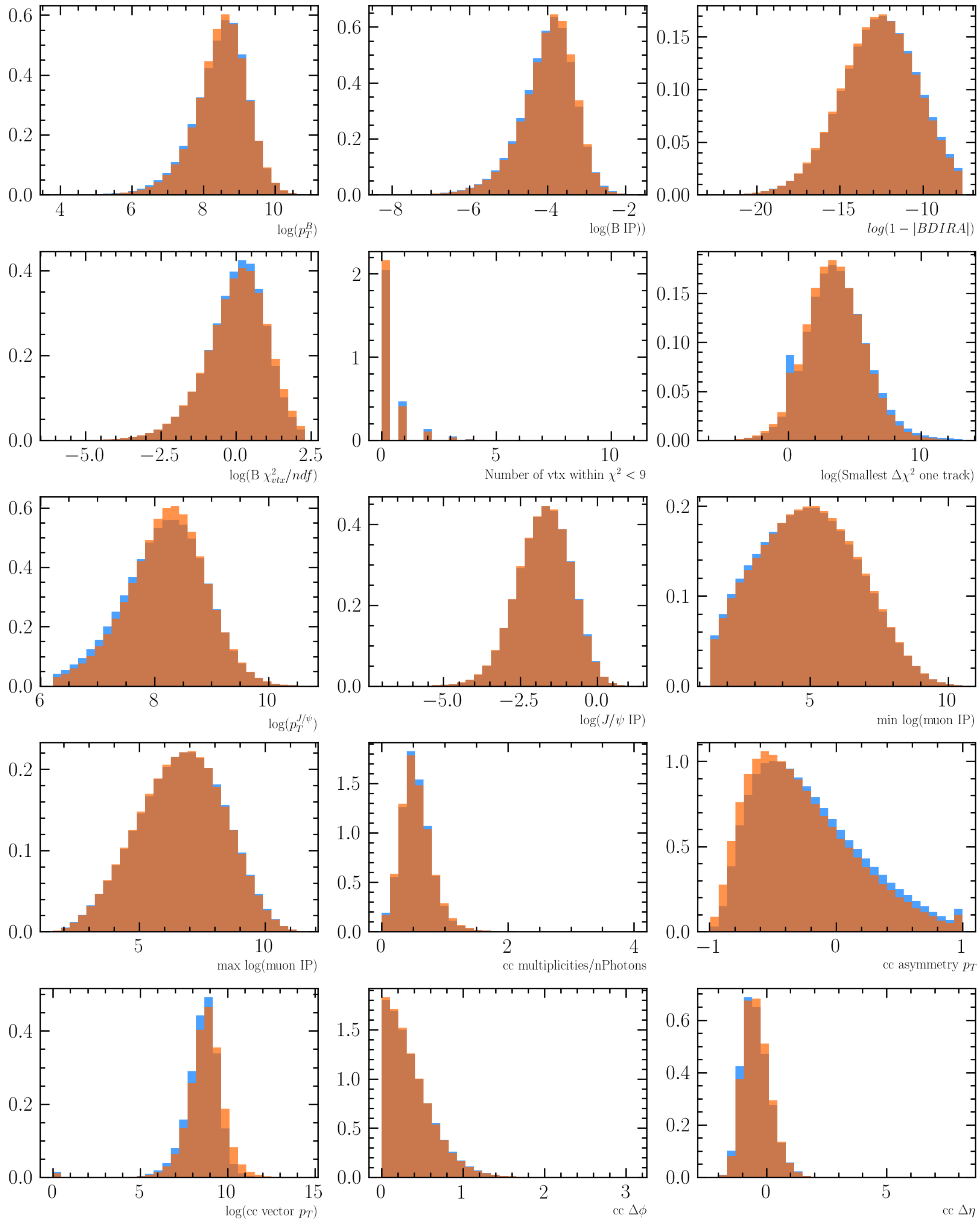

Figure A.7.: The distributions of a subset of the variables and expressions used in the training of the MVA (omitting those unavailable to $B^+ \to J/\psi K^+$ decays) as well as occupancy variables. The orange distribution is the background-subtracted $B^+ \to J/\psi K^+$ 2012 collision data used as a target. The blue distribution is the original $B^+ \to J/\psi K^+$ 2012 MC data.

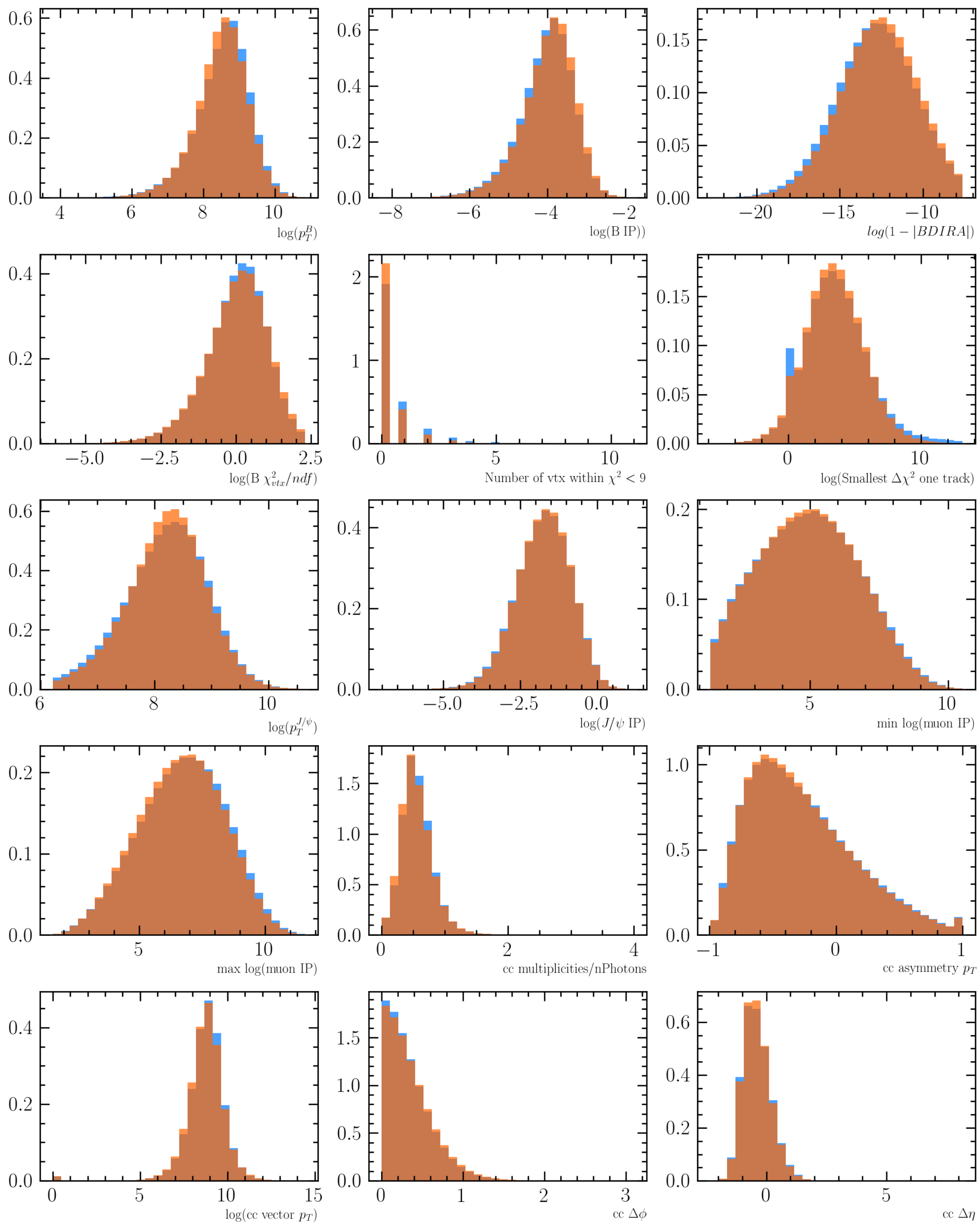

Figure A.8.: The distributions of a subset of the variables and expressions used in the training of the MVA (omitting those unavailable to $B^+ \to J/\psi K^+$ decays) as well as occupancy variables. The orange distribution is the background-subtracted $B^+ \to J/\psi K^+$ 2012 collision data used as a target. The blue distribution is the $B^+ \to J/\psi K^+$ 2012 MC data after applying weights calculated by the reweighter.

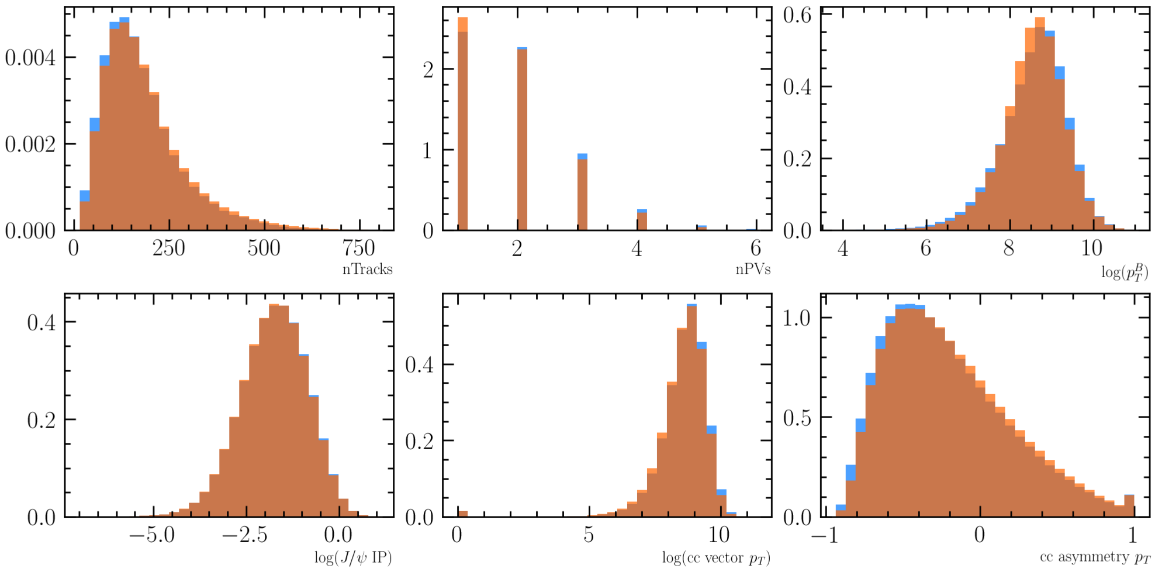

Figure A.9.: The distributions of the input variables and expressions used for the training of the Gradient Boosted Reweighter. The orange distribution is the background-subtracted $B^+ \to J/\psi K^+$ 2016 collision data used as a target. The blue distribution is the original $B^+ \to J/\psi K^+$ 2016 MC data.

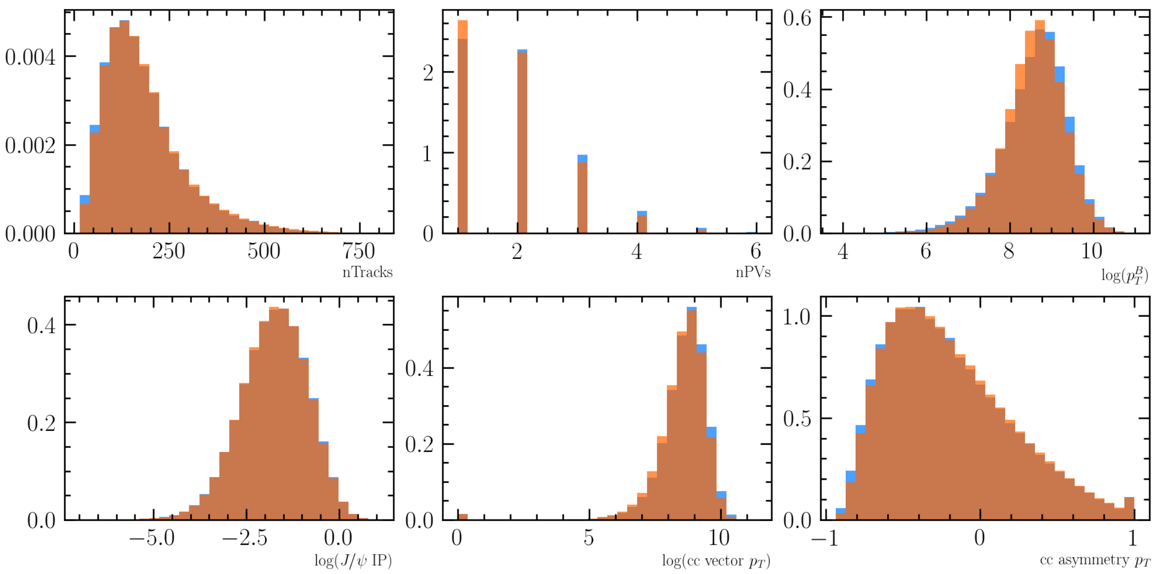

Figure A.10.: The distributions of the input variables and expressions used for the training of the Gradient Boosted Reweighter. The orange distribution is the background-subtracted $B^+ \to J/\psi K^+$ 2016 collision data used as a target. The blue distribution is the $B^+ \to J/\psi K^+$ 2016 MC data after applying the event-by-event weights that were calculated by the reweighter.

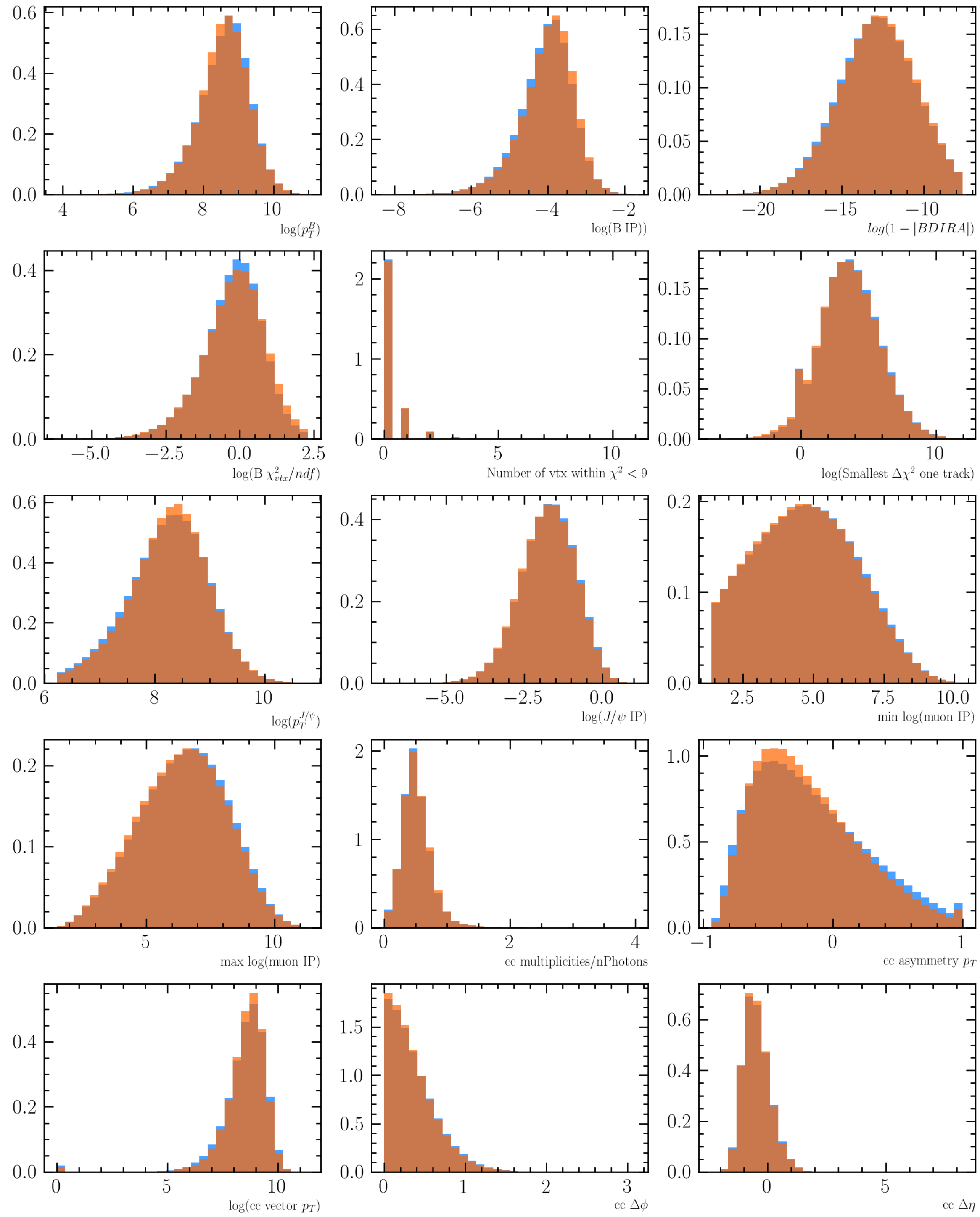

Figure A.11.: The distributions of a subset of the variables and expressions used in the training of the MVA (omitting those unavailable to $B^+ \to J/\psi K^+$ decays) as well as occupancy variables. The orange distribution is the background-subtracted $B^+ \to J/\psi K^+$ 2016 collision data used as a target. The blue distribution is the original $B^+ \to J/\psi K^+$ 2016 MC data.

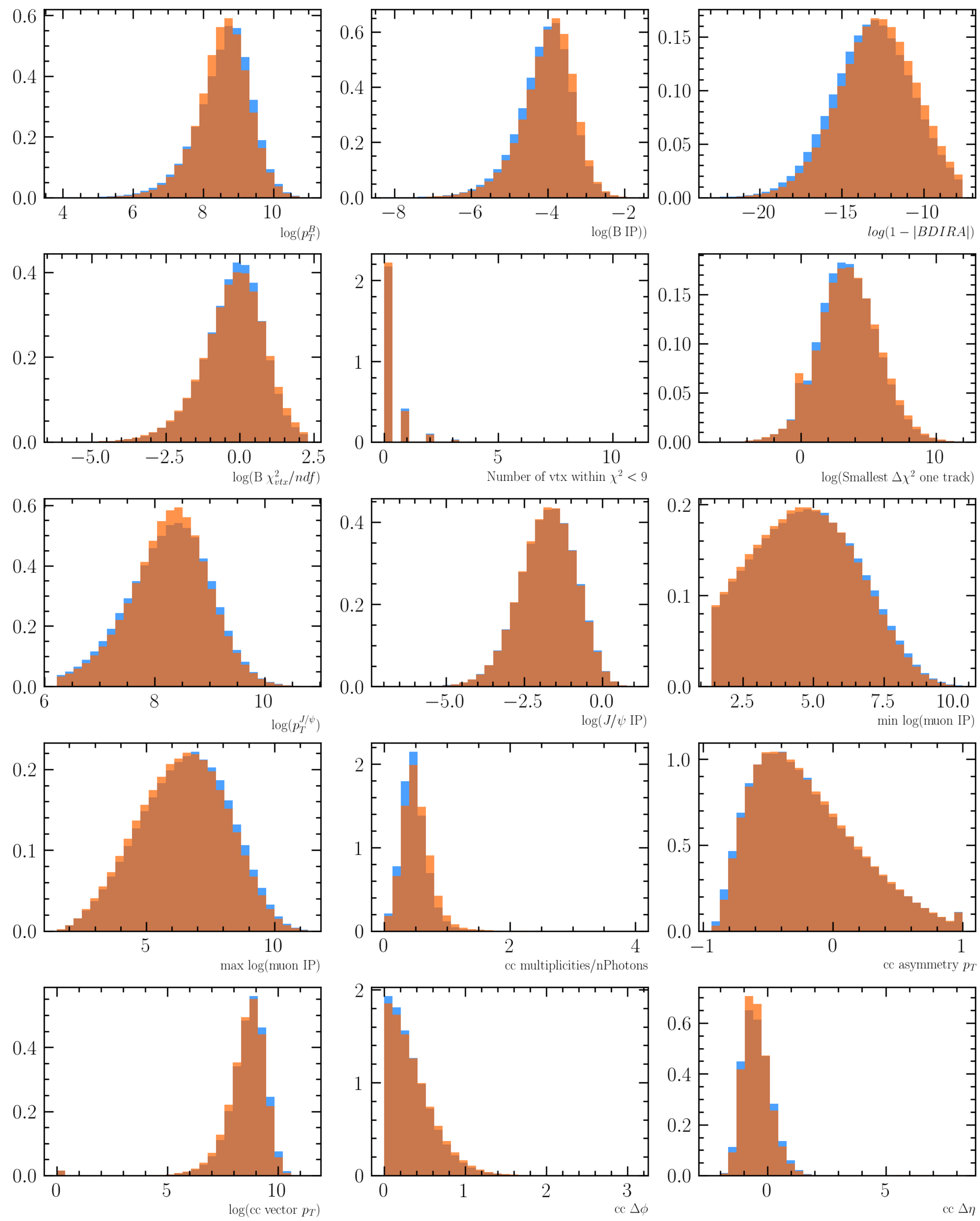

Figure A.12.: The distributions of a subset of the variables and expressions used in the training of the MVA (omitting those unavailable to $B^+ \to J/\psi K^+$ decays) as well as occupancy variables. The orange distribution is the background-subtracted $B^+ \to J/\psi K^+$ 2016 collision data used as a target. The blue distribution is the $B^+ \to J/\psi K^+$ 2016 MC data after applying weights calculated by the reweighter.

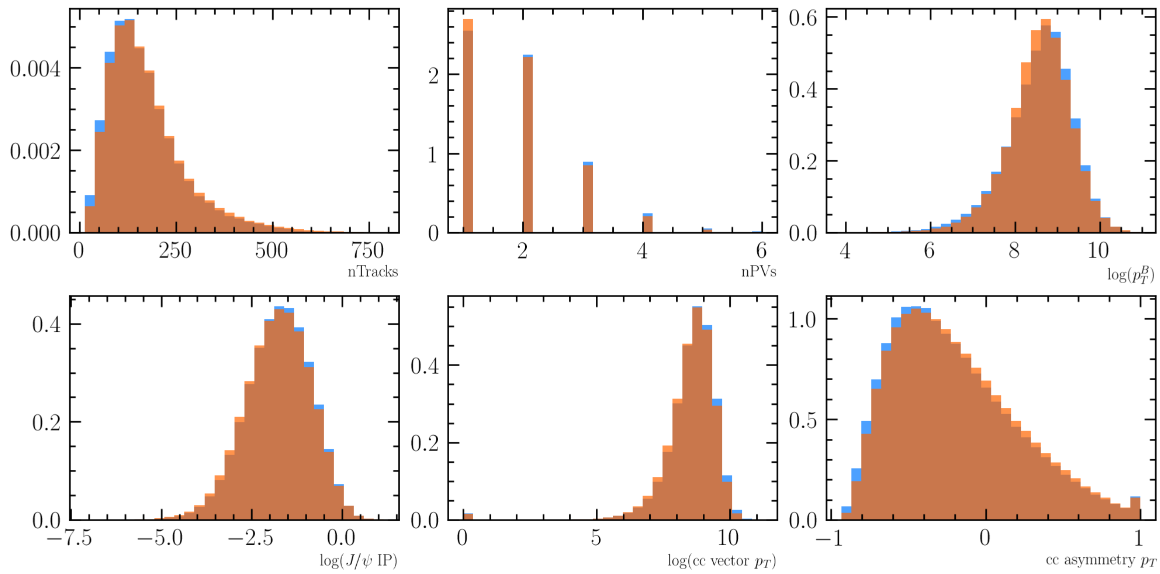

Figure A.13.: The distributions of the input variables and expressions used for the training of the Gradient Boosted Reweighter. The orange distribution is the background-subtracted $B^+ \to J/\psi K^+$ 2017 collision data used as a target. The blue distribution is the original $B^+ \to J/\psi K^+$ 2017 MC data.

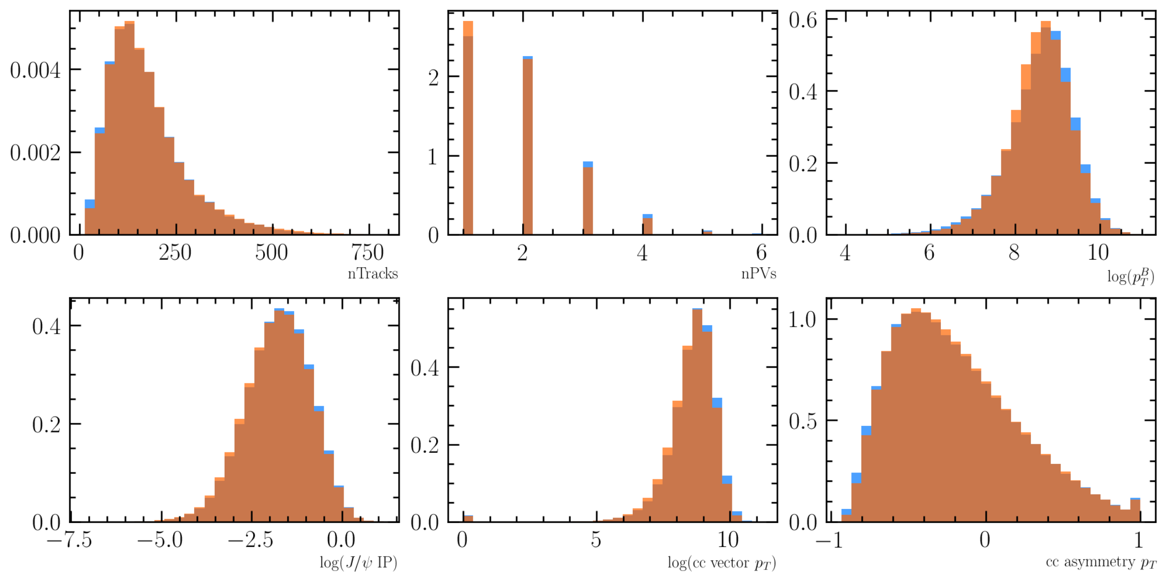

Figure A.14.: The distributions of the input variables and expressions used for the training of the Gradient Boosted Reweighter. The orange distribution is the background-subtracted $B^+ \to J/\psi K^+$ 2017 collision data used as a target. The blue distribution is the $B^+ \to J/\psi K^+$ 2017 MC data after applying the event-by-event weights that were calculated by the reweighter.

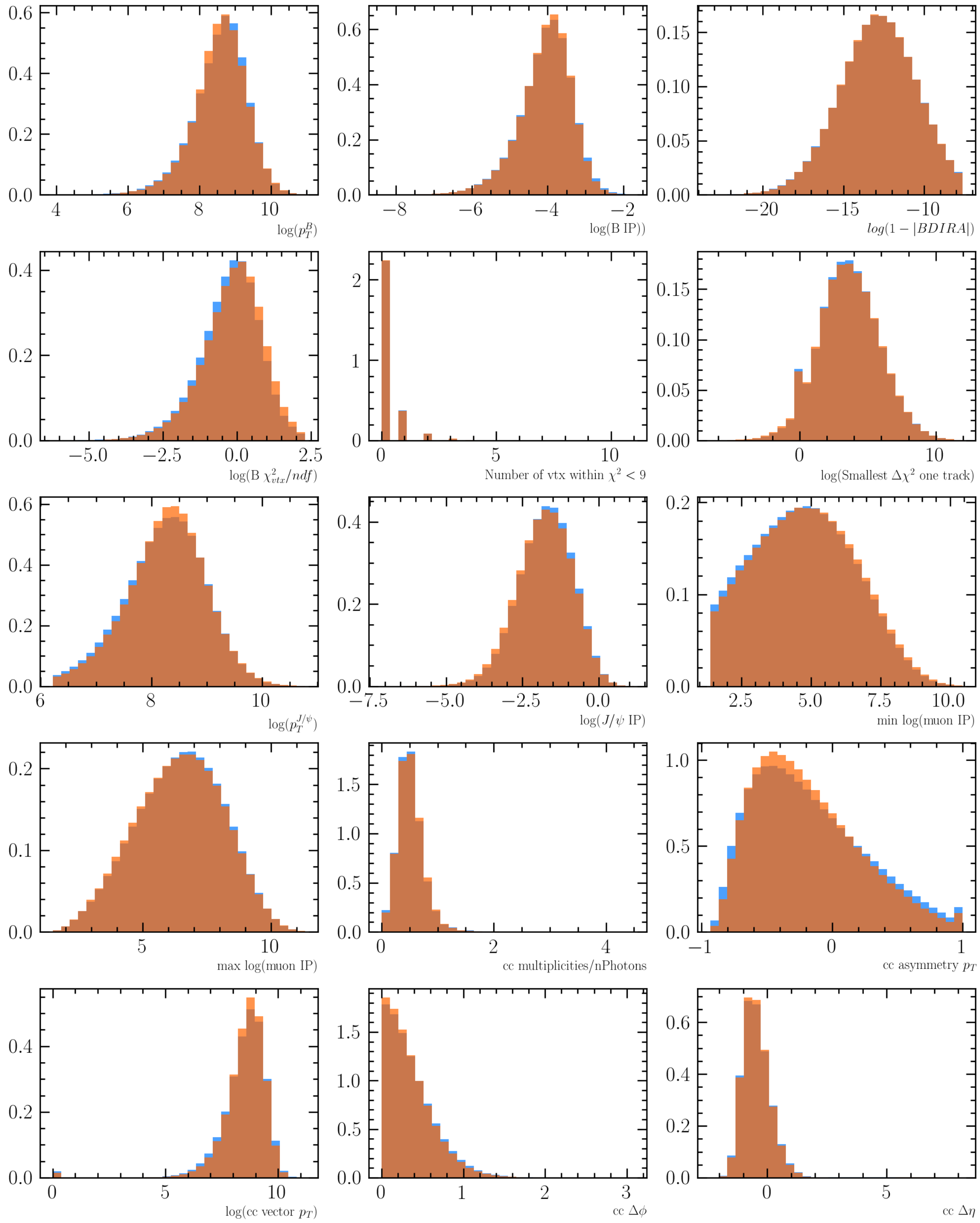

Figure A.15.: The distributions of a subset of the variables and expressions used in the training of the MVA (omitting those unavailable to $B^+ \to J/\psi K^+$ decays) as well as occupancy variables. The orange distribution is the background-subtracted $B^+ \to J/\psi K^+$ 2017 collision data used as a target. The blue distribution is the original $B^+ \to J/\psi K^+$ 2017 MC data.

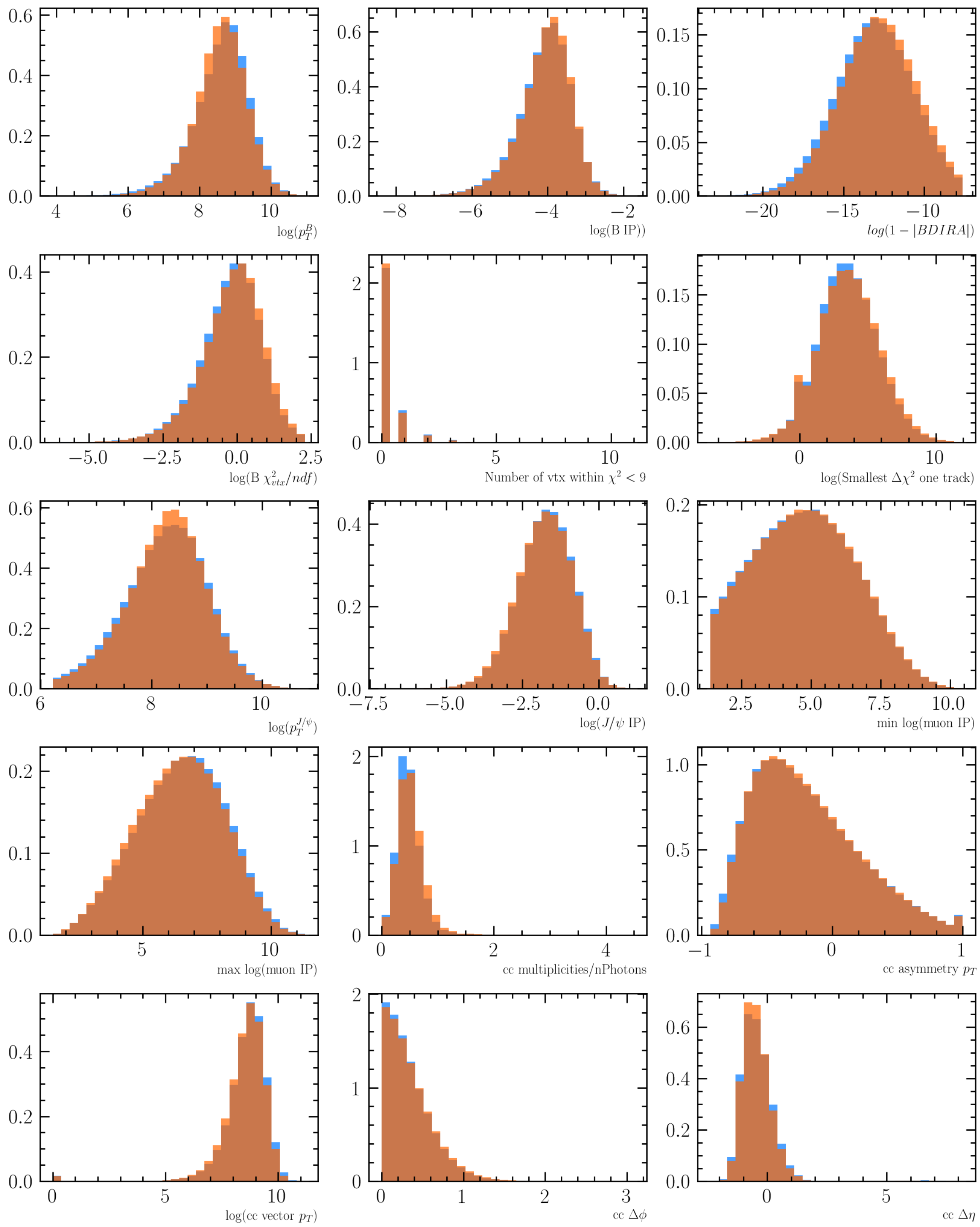

Figure A.16.: The distributions of a subset of the variables and expressions used in the training of the MVA (omitting those unavailable to $B^+ \to J/\psi K^+$ decays) as well as occupancy variables. The orange distribution is the background-subtracted $B^+ \to J/\psi K^+$ 2017 collision data used as a target. The blue distribution is the $B^+ \to J/\psi K^+$ 2017 MC data after applying weights calculated by the reweighter.

A.3. The trigger configuration keys for each data set

Table A.6.: The trigger configuration keys for $B^+ \to J/\psi K^+$ 2011 data. This includes the associated minima for muon momentum and number of SPD hits, as well as the fraction of the data set with certain configurations. Red highlights the configuration key used in the MC samples.

				Muon		DiMuon	
Mag	dec	hex	contr./%	$p_T^{L0}(\mu)$	SPD(mult)	$p_T^{L0}(\mu_1) p_T^{L0}(\mu_2)$	SPD(mult)
Up	0050	0032	7.44 ± 0.04	37	600	1050	900
	0051	0033	0.329 ± 0.008	20	600	1050	900
	0053	0035	31.53 ± 0.08	37	600	1050	900
	0054	0036	1.031 ± 0.014	40	500	2500	900
	0055	0037	32.97 ± 0.08	37	600	1050	900
	0056	0038	26.70 ± 0.07	37	600	1050	900
Down	0050	0032	22.72 ± 0.05	37	600	1050	900
	0051	0033	0.379 ± 0.007	20	600	1050	900
	0052	0034	0.209 ± 0.005	37	600	1050	900
	0053	0035	11.05 ± 0.04	37	600	1050	900
	0055	0037	32.84 ± 0.06	37	600	1050	900
	0056	0038	32.80 ± 0.06	37	600	1050	900

Table A.7.: The trigger configuration keys for $B^+ \to J/\psi K^+$ 2012 data. This includes the associated minima for muon momentum and number of SPD hits, as well as the fraction of the data set with certain configurations. Red highlights the configuration key used in the MC samples.

				Muon		DiMuon	
Mag	dec	hex	contr./%	$p_{\mathrm{T}}^{L0}(\mu)$	SPD(mult)	$p_{\mathrm{T}}^{L0}(\mu_1)p_{\mathrm{T}}^{L0}(\mu_2)$	SPD(mult)
Up	0061	003D	28.69 ± 0.04	44	600	1600	900
	0066	0042	35.51 ± 0.05	44	600	1600	900
	0067	0043	0.254 ± 0.04	44	600	1600	900
	0068	0044	22.81 ± 0.04	44	600	1600	900
	0069	0045	9.950 ± 0.024	44	600	1600	900
	0070	0046	2.789 ± 0.013	44	600	1600	900
Down	0061	003D	25.64 ± 0.04	44	600	1600	900
	0064	0040	6.582 ± 0.020	37	600	1050	900
	0066	0042	18.825 ± 0.034	44	600	1600	900
	0068	0044	25.37 ± 0.04	44	600	1600	900
	0070	0046	23.57 ± 0.04	44	600	1600	900

Table A.8.: The trigger configuration keys for $B^+ \to J/\psi K^+$ 2016 data. This includes the associated minima for muon momentum and number of SPD hits, as well as the fraction of the data set with certain configurations. Red highlights the configuration key used in the MC samples.

				Muon		DiMuon	
Mag	dec	hex	contr./%	$p_{\mathrm{T}}^{L0}(\mu)$	SPD(mult)	$p_{\mathrm{T}}^{L0}(\mu_1)p_{\mathrm{T}}^{L0}(\mu_2)$	SPD(mult)
Up	5641	1609	84.24 ± 0.05	26	450	676	900
	5649	1611	5.496 ± 0.013	30	450	784	900
	5650	1612	10.269 ± 0.018	32	450	900	900
Down	5635	1603	4.591 ± 0.012	22	450	400	900
	5636	1604	3.298 ± 0.010	26	450	576	900
	5637	1605	10.152 ± 0.018	30	450	676	900
	5641	1609	8.317 ± 0.016	26	450	676	900
	5646	160E	6.631 ± 0.015	30	450	676	900
	5647	160F	67.01 ± 0.05	36	450	900	900

Table A.9.: The trigger configuration keys for $B^+ \to J/\psi K^+$ 2017 data. This includes the associated minima for muon momentum and number of SPD hits, as well as the fraction of the data set with certain configurations. Red highlights the configuration key used in the MC samples.

				Muon		DiMuon	
Mag	dec	hex	contr./%	$p_{\mathrm{T}}^{L0}(\mu)$	SPD(mult)	$p_{\mathrm{T}}^{L0}(\mu_1)p_{\mathrm{T}}^{L0}(\mu_2)$	SPD(mult)
Up	5890	1702	0.367 ± 0.004	14	450	324	900
	5891	1703	3.051 ± 0.011	22	450	400	900
	5892	1704	3.264 ± 0.011	26	450	576	900
	5893	1705	15.515 ± 0.024	30	450	676	900
	5894	1706	3.059 ± 0.011	38	450	1296	900
	5895	1707	23.537 ± 0.029	34	450	1296	900
	5896	1708	13.171 ± 0.022	22	450	400	900
	5897	1709	38.04 ± 0.04	28	450	676	900
Down	5895	1707	49.06 ± 0.04	34	450	1296	900
	5896	1708	17.143 ± 0.024	22	450	400	900
	5897	1709	33.748 ± 0.034	28	450	676	900
	6055	17A7	0.0538 ± 0.0014	34	450	1296	900

Table A.10.: The trigger configuration keys for $B^+ \to J/\psi K^+$ 2018 data. This includes the associated minima for muon momentum and number of SPD hits, as well as the fraction of the data set with certain configurations. Red highlights the configuration key used in the MC samples.

				Muon		DiMuon	
Mag	dec	hex	contr./%	$p_{\mathrm{T}}^{L0}(\mu)$	SPD(mult)	$p_{\mathrm{T}}^{L0}(\mu_1)p_{\mathrm{T}}^{L0}(\mu_2)$	SPD(mult)
Up	6145	1801	38.311 ± 0.034	35	450	1296	900
	6306	18A2	53.13 ± 0.04	35	450	1296	900
	6308	18A4	8.562 ± 0.016	35	450	1296	900
Down	6145	1801	45.20 ± 0.04	35	450	1296	900
	6306	18A2	27.990 ± 0.028	35	450	1296	900
	6308	18A4	26.766 ± 0.028	35	450	1296	900

Appendix B.

Supplementary material for Chapter 5

B.1. Kolmogorov-Smirnov distances for all variables used in GBR and BDT training

Table B.1.: The Kolmogorov-Smirnov distances for each variable used in the training of the Gradient Boosted Reweighter or the Multivariate Analysis for the $B^+ \to J/\psi K^{*0}$ 2011 MC sample.

Variable	KS distance	
	Before reweighting	After reweighting
	GBR inputs	
nTracks	0.1185	0.0109
nPVs	0.0459	0.0087
$\log(B\ p_\mathrm{T})$	0.0209	0.0095
$\log(J/\psi$ IP)	0.0152	0.0108
log(cc vector p_T)	0.0594	0.0072
cc asymmetry p_z	0.0565	0.0100
	BDT inputs	
$\log(B\ p_\mathrm{T})$	0.0209	0.0095
$\log(B$ IP)	0.0472	0.0551
$\log(1 - \lvert DIRA \rvert)$	0.0073	0.0159
$\log(B\ \chi^2_\mathrm{vtx})$	0.0396	0.0344
Number of vtx with $\chi^2 < 9$	0.0348	0.0601
log(Smallest $\Delta\chi^2$ one track)	0.0276	0.0176
$\log(J/\psi\ p_\mathrm{T})$	0.0176	0.0089
$\log(J/\psi$ IP)	0.0152	0.0108
min $\log(\mu$ IP)	0.0110	0.0098
max $\log(\mu\ \chi^2_\mathrm{IP})$	0.0112	0.0172
cc multiplicities/nPhotons	0.0070	0.0256
cc asymmetry p_z	0.0565	0.0100
log(cc vector p_T)	0.0594	0.0072
cc $\Delta\phi$	0.0182	0.0072
cc $\Delta\eta$	0.0263	0.0217

Table B.2.: The Kolmogorov-Smirnov distances for each variable used in the training of the Gradient Boosted Reweighter or the Multivariate Analysis for the $B^+ \to J/\psi K^{*0}$ 2012 MC sample.

Variable	KS distance	
	Before reweighting	After reweighting
	GBR inputs	
nTracks	0.1215	0.0137
nPVs	0.0308	0.0116
$\log(B\ p_\mathrm{T})$	0.0110	0.0112
$\log(J/\psi$ IP)	0.0123	0.0138
log(cc vector p_T)	0.0783	0.0090
cc asymmetry p_z	0.0594	0.0111
	BDT inputs	
$\log(B\ p_\mathrm{T})$	0.0110	0.0112
$\log(B$ IP)	0.0177	0.0375
$\log(1 - \lvert DIRA \rvert)$	0.0052	0.0170
$\log(B\ \chi^2_\mathrm{vtx})$	0.0323	0.0267
Number of vtx with $\chi^2 < 9$	0.0410	0.0701
log(Smallest $\Delta\chi^2$ one track)	0.0286	0.0213
$\log(J/\psi\ p_\mathrm{T})$	0.0191	0.0165
$\log(J/\psi$ IP)	0.0123	0.0138
min $\log(\mu$ IP)	0.0219	0.0145
max $\log(\mu\ \chi^2_\mathrm{IP})$	0.0099	0.0073
cc multiplicities/nPhotons	0.0128	0.0323
cc asymmetry p_z	0.0594	0.0111
log(cc vector p_T)	0.0783	0.0090
cc $\Delta\phi$	0.0086	0.0103
cc $\Delta\eta$	0.0233	0.0221

Table B.3.: The Kolmogorov-Smirnov distances for each variable used in the training of the Gradient Boosted Reweighter or the Multivariate Analysis for the $B^+ \to J/\psi K^{*0}$ 2015 MC sample.

Variable	KS distance	
	Before reweighting	After reweighting
	GBR inputs	
nTracks	0.1997	0.0275
nPVs	0.0274	0.0266
$\log(B\ p_{\mathrm{T}})$	0.0128	0.0185
$\log(J/\psi\ \mathrm{IP})$	0.0065	0.0067
log(cc vector p_{T})	0.0381	0.0247
cc asymmetry p_z	0.0338	0.0248
	BDT inputs	
$\log(B\ p_{\mathrm{T}})$	0.0128	0.0185
$\log(B\ \mathrm{IP})$	0.0312	0.0554
$\log(1 - \lvert DIRA \rvert)$	0.0130	0.0377
$\log(B\ \chi^2_{\mathrm{vtx}})$	0.0438	0.0324
Number of vtx with $\chi^2 < 9$	0.0021	0.0074
log(Smallest $\Delta\chi^2$ one track)	0.0108	0.0206
$\log(J/\psi\ p_{\mathrm{T}})$	0.0342	0.0276
$\log(J/\psi\ \mathrm{IP})$	0.0065	0.0067
min $\log(\mu\ \mathrm{IP})$	0.0050	0.0088
max $\log(\mu\ \chi^2_{\mathrm{IP}})$	0.0122	0.0221
cc multiplicities/nPhotons	0.0170	0.0478
cc asymmetry p_z	0.0338	0.0248
log(cc vector p_{T})	0.0381	0.0247
cc $\Delta\phi$	0.0250	0.0148
cc $\Delta\eta$	0.0184	0.0251

Table B.4.: The Kolmogorov-Smirnov distances for each variable used in the training of the Gradient Boosted Reweighter or the Multivariate Analysis for the $B^+ \to J/\psi K^{*0}$ 2016 MC sample.

Variable	KS distance	
	Before reweighting	After reweighting
	GBR inputs	
nTracks	0.1848	0.0259
nPVs	0.0333	0.0258
$\log(B\ p_\mathrm{T})$	0.0332	0.0280
$\log(J/\psi\ \mathrm{IP})$	0.0050	0.0109
log(cc vector p_T)	0.0326	0.0250
cc asymmetry p_z	0.0328	0.0258
	BDT inputs	
$\log(B\ p_\mathrm{T})$	0.0332	0.0280
$\log(B\ \mathrm{IP})$	0.0377	0.0557
$\log(1-\lvert DIRA\rvert)$	0.0228	0.0403
$\log(B\ \chi^2_\mathrm{vtx})$	0.0375	0.0281
Number of vtx with $\chi^2 < 9$	0.0027	0.0078
log(Smallest $\Delta\chi^2$ one track)	0.0160	0.0183
$\log(J/\psi\ p_\mathrm{T})$	0.0208	0.0202
$\log(J/\psi\ \mathrm{IP})$	0.0050	0.0109
min $\log(\mu\ \mathrm{IP})$	0.0029	0.0074
max $\log(\mu\ \chi^2_\mathrm{IP})$	0.0086	0.0180
cc multiplicities/nPhotons	0.0157	0.0750
cc asymmetry p_z	0.0328	0.0258
log(cc vector p_T)	0.0326	0.0250
cc $\Delta\phi$	0.0137	0.0207
cc $\Delta\eta$	0.0065	0.0307

Table B.5.: The Kolmogorov-Smirnov distances for each variable used in the training of the Gradient Boosted Reweighter or the Multivariate Analysis for the $B^+ \to J/\psi K^{*0}$ 2017 MC sample.

Variable	KS distance	
	Before reweighting	After reweighting
	GBR inputs	
nTracks	0.1502	0.0239
nPVs	0.0397	0.0213
$\log(B\ p_\mathrm{T})$	0.0262	0.0242
$\log(J/\psi$ IP)	0.0072	0.0019
log(cc vector p_T)	0.0293	0.0213
cc asymmetry p_z	0.0300	0.0229
	BDT inputs	
$\log(B\ p_\mathrm{T})$	0.0262	0.0242
$\log(B$ IP)	0.0100	0.0255
$\log(1-\lvert DIRA\rvert)$	0.0122	0.0278
$\log(B\ \chi^2_\mathrm{vtx})$	0.0425	0.0346
Number of vtx with $\chi^2 < 9$	0.0010	0.0100
log(Smallest $\Delta\chi^2$ one track)	0.0068	0.0238
$\log(J/\psi\ p_\mathrm{T})$	0.0146	0.0158
$\log(J/\psi$ IP)	0.0072	0.0019
min $\log(\mu$ IP)	0.0236	0.0195
max $\log(\mu\ \chi^2_\mathrm{IP})$	0.0041	0.0070
cc multiplicities/nPhotons	0.0180	0.0659
cc asymmetry p_z	0.0300	0.0229
log(cc vector p_T)	0.0293	0.0213
cc $\Delta\phi$	0.0136	0.0135
cc $\Delta\eta$	0.0069	0.0262

Table B.6.: The Kolmogorov-Smirnov distances for each variable used in the training of the Gradient Boosted Reweighter or the Multivariate Analysis for the $B^+ \to J/\psi K^{*0}$ 2018 MC sample.

Variable	KS distance	
	Before reweighting	After reweighting
	GBR inputs	
nTracks	0.1662	0.0263
nPVs	0.0437	0.0246
$\log(B\ p_{\mathrm{T}})$	0.0102	0.0206
$\log(J/\psi\ \mathrm{IP})$	0.0110	0.0040
log(cc vector p_{T})	0.0274	0.0232
cc asymmetry p_z	0.0265	0.0262
	BDT inputs	
$\log(B\ p_{\mathrm{T}})$	0.0102	0.0206
$\log(B\ \mathrm{IP})$	0.0134	0.0165
$\log(1 - \lvert DIRA \rvert)$	0.0047	0.0258
$\log(B\ \chi^2_{\mathrm{vtx}})$	0.0394	0.0302
Number of vtx with $\chi^2 < 9$	0.0023	0.0111
log(Smallest $\Delta\chi^2$ one track)	0.0045	0.0288
$\log(J/\psi\ p_{\mathrm{T}})$	0.0265	0.0267
$\log(J/\psi\ \mathrm{IP})$	0.0110	0.0040
min $\log(\mu\ \mathrm{IP})$	0.0278	0.0212
max $\log(\mu\ \chi^2_{\mathrm{IP}})$	0.0050	0.0067
cc multiplicities/nPhotons	0.0183	0.0697
cc asymmetry p_z	0.0265	0.0262
log(cc vector p_{T})	0.0274	0.0232
cc $\Delta\phi$	0.0147	0.0161
cc $\Delta\eta$	0.0141	0.0257

B.2. The Monte Carlo efficiencies separated by year

Table B.7.: The reconstruction and selection efficiencies for the signal $B^0_{(s)} \to J/\psi\eta^{(\prime)}$ and $B^0 \to J/\psi\rho^0$ 2011 Monte-Carlo simulated data.

Channel	$\varepsilon^{MC}(B^0_s)/\%$	$\varepsilon^{MC}(B^0)/\%$
	Acceptance	
$\eta \to \pi^+\pi^-\gamma$	9.61 ± 0.21	-
$\eta \to \pi^+\pi^-\pi^0$	6.09 ± 0.16	-
$\eta' \to \rho^0\gamma$	9.34 ± 0.20	-
$\eta' \to \pi^+\pi^-\eta$	8.06 ± 0.17	-
$\rho^0 \to \pi^+\pi^-$	-	14.798 ± 0.024
	Reconstruction and preselection	
$\eta \to \pi^+\pi^-\gamma$	3.984 ± 0.023	-
$\eta \to \pi^+\pi^-\pi^0$	2.302 ± 0.021	-
$\eta' \to \rho^0\gamma$	3.116 ± 0.020	-
$\eta' \to \pi^+\pi^-\eta$	2.421 ± 0.018	-
$\rho^0 \to \pi^+\pi^-$	-	7.166 ± 0.019
	Trigger	
$\eta \to \pi^+\pi^-\gamma$	90.7 ± 0.5	-
$\eta \to \pi^+\pi^-\pi^0$	91.9 ± 0.9	-
$\eta' \to \rho^0\gamma$	91.8 ± 0.6	-
$\eta' \to \pi^+\pi^-\eta$	92.4 ± 0.7	-
$\rho^0 \to \pi^+\pi^-$	-	90.81 ± 0.25
	BDT selection	
$\eta \to \pi^+\pi^-\gamma$	89.2 ± 0.6	-
$\eta \to \pi^+\pi^-\pi^0$	74.0 ± 0.8	-
$\eta' \to \rho^0\gamma$	84.9 ± 0.6	-
$\eta' \to \pi^+\pi^-\eta$	72.6 ± 0.7	-
$\rho^0 \to \pi^+\pi^-$	-	80.99 ± 0.25
	PID selection	
$\eta \to \pi^+\pi^-\gamma$	92.84 ± 0.35	-
$\eta \to \pi^+\pi^-\pi^0$	92.77 ± 0.23	-
$\eta' \to \rho^0\gamma$	92.61 ± 0.34	-
$\eta' \to \pi^+\pi^-\eta$	93.12 ± 0.55	-
$\rho^0 \to \pi^+\pi^-$	-	91.51 ± 0.37
	Total	
$\eta \to \pi^+\pi^-\gamma$	0.2878 ± 0.0021	-
$\eta \to \pi^+\pi^-\pi^0$	0.0884 ± 0.0010	-
$\eta' \to \rho^0\gamma$	0.2102 ± 0.0017	-
$\eta' \to \pi^+\pi^-\eta$	0.1219 ± 0.0013	-
$\rho^0 \to \pi^+\pi^-$	-	0.7137 ± 0.0037

Table B.8.: The reconstruction and selection efficiencies for the signal $B^0_{(s)} \to J/\psi\eta^{(\prime)}$ and $B^0 \to J/\psi\rho^0$ 2012 Monte-Carlo simulated data.

Channel	$\varepsilon^{MC}(B^0_s)/\%$	$\varepsilon^{MC}(B^0)/\%$
	Acceptance	
$\eta \to \pi^+\pi^-\gamma$	12.91 ± 0.25	14.95 ± 0.27
$\eta \to \pi^+\pi^-\pi^0$	6.22 ± 0.12	-
$\eta' \to \rho^0\gamma$	15.18 ± 0.15	15.02 ± 0.27
$\eta' \to \pi^+\pi^-\eta$	8.17 ± 0.14	14.00 ± 0.26
$\rho^0 \to \pi^+\pi^-$	-	15.115 ± 0.026
	Reconstruction and preselection	
$\eta \to \pi^+\pi^-\gamma$	3.007 ± 0.013	2.34525 ± 0.015
$\eta \to \pi^+\pi^-\pi^0$	1.966 ± 0.014	-
$\eta' \to \rho^0\gamma$	1.836 ± 0.008	1.685 ± 0.013
$\eta' \to \pi^+\pi^-\eta$	2.133 ± 0.013	1.143 ± 0.011
$\rho^0 \to \pi^+\pi^-$	-	6.699 ± 0.018
	Trigger	
$\eta \to \pi^+\pi^-\gamma$	87.42 ± 0.41	87.4 ± 0.6
$\eta \to \pi^+\pi^-\pi^0$	88.3 ± 0.7	-
$\eta' \to \rho^0\gamma$	87.36 ± 0.39	87.5 ± 0.7
$\eta' \to \pi^+\pi^-\eta$	88.6 ± 0.7	89.1 ± 0.9
$\rho^0 \to \pi^+\pi^-$	-	86.23 ± 0.24
	BDT selection	
$\eta \to \pi^+\pi^-\gamma$	89.32 ± 0.44	87.7893 ± 0.7
$\eta \to \pi^+\pi^-\pi^0$	72.0 ± 0.6	-
$\eta' \to \rho^0\gamma$	84.18 ± 0.41	82.6251 ± 0.7
$\eta' \to \pi^+\pi^-\eta$	72.0 ± 0.6	69.1988 ± 0.8
$\rho^0 \to \pi^+\pi^-$	-	79.34 ± 0.25
	PID selection	
$\eta \to \pi^+\pi^-\gamma$	93.72 ± 0.15	93.73 ± 0.15
$\eta \to \pi^+\pi^-\pi^0$	93.56 ± 0.10	-
$\eta' \to \rho^0\gamma$	93.35 ± 0.15	93.29 ± 0.16
$\eta' \to \pi^+\pi^-\eta$	94.50 ± 0.22	94.37 ± 0.24
$\rho^0 \to \pi^+\pi^-$	-	92.17 ± 0.17
	Total	
$\eta \to \pi^+\pi^-\gamma$	0.2841 ± 0.0015	0.2521 ± 0.0019
$\eta \to \pi^+\pi^-\pi^0$	0.0728 ± 0.0007	-
$\eta' \to \rho^0\gamma$	0.1913 ± 0.0010	0.1708 ± 0.0016
$\eta' \to \pi^+\pi^-\eta$	0.1050 ± 0.0008	0.0931 ± 0.0011
$\rho^0 \to \pi^+\pi^-$	-	0.6385 ± 0.0024

Table B.9.: The reconstruction and selection efficiencies for the signal $B^0_{(s)} \to J/\psi\eta^{(\prime)}$ and $B^0 \to J/\psi\rho^0$ 2015 Monte-Carlo simulated data.

Channel	$\varepsilon^{MC}(B^0_s)/\%$	$\varepsilon^{MC}(B^0)/\%$
	Acceptance	
$\eta \to \pi^+\pi^-\gamma$	10.31 ± 0.26	-
$\eta \to \pi^+\pi^-\pi^0$	15.534 ± 0.038	-
$\eta' \to \rho^0\gamma$	16.125 ± 0.040	-
$\eta' \to \pi^+\pi^-\eta$	15.129 ± 0.037	-
$\rho^0 \to \pi^+\pi^-$	-	16.204 ± 0.034
	Reconstruction and preselection	
$\eta \to \pi^+\pi^-\gamma$	3.980 ± 0.027	-
$\eta \to \pi^+\pi^-\pi^0$	1.039 ± 0.010	-
$\eta' \to \rho^0\gamma$	2.001 ± 0.014	-
$\eta' \to \pi^+\pi^-\eta$	1.540 ± 0.012	-
$\rho^0 \to \pi^+\pi^-$	-	7.170 ± 0.027
	Trigger	
$\eta \to \pi^+\pi^-\gamma$	76.1 ± 0.6	-
$\eta \to \pi^+\pi^-\pi^0$	78.0 ± 0.8	-
$\eta' \to \rho^0\gamma$	76.2 ± 0.6	-
$\eta' \to \pi^+\pi^-\eta$	79.3 ± 0.7	-
$\rho^0 \to \pi^+\pi^-$	-	74.60 ± 0.32
	BDT selection	
$\eta \to \pi^+\pi^-\gamma$	90.9 ± 0.7	-
$\eta \to \pi^+\pi^-\pi^0$	73.2 ± 0.9	-
$\eta' \to \rho^0\gamma$	85.6 ± 0.7	-
$\eta' \to \pi^+\pi^-\eta$	73.2 ± 0.7	-
$\rho^0 \to \pi^+\pi^-$	-	80.8569 ± 0.39
	PID selection	
$\eta \to \pi^+\pi^-\gamma$	94.94 ± 0.10	-
$\eta \to \pi^+\pi^-\pi^0$	95.03 ± 0.09	-
$\eta' \to \rho^0\gamma$	93.79 ± 0.10	-
$\eta' \to \pi^+\pi^-\eta$	96.15 ± 0.11	-
$\rho^0 \to \pi^+\pi^-$	-	91.49 ± 0.11
	Total	
$\eta \to \pi^+\pi^-\gamma$	0.2696 ± 0.0022	-
$\eta \to \pi^+\pi^-\pi^0$	0.0875 ± 0.0011	-
$\eta' \to \rho^0\gamma$	0.1973 ± 0.0017	-
$\eta' \to \pi^+\pi^-\eta$	0.1299 ± 0.0013	-
$\rho^0 \to \pi^+\pi^-$	-	0.6412 ± 0.0033

Table B.10.: The reconstruction and selection efficiencies for the signal $B^0_{(s)} \to J/\psi\eta^{(\prime)}$ and $B^0 \to J/\psi\rho^0$ 2016 Monte-Carlo simulated data.

Channel	$\varepsilon^{MC}(B^0_s)/\%$	$\varepsilon^{MC}(B^0)/\%$
	Acceptance	
$\eta \to \pi^+\pi^-\gamma$	13.68 ± 0.26	15.83 ± 0.29
$\eta \to \pi^+\pi^-\pi^0$	15.48 ± 0.12	15.5205 ± 0.04
$\eta' \to \rho^0\gamma$	16.05 ± 0.15	16.205 ± 0.29
$\eta' \to \pi^+\pi^-\eta$	15.13 ± 0.14	14.885 ± 0.28
$\rho^0 \to \pi^+\pi^-$	-	16.186 ± 0.036
	Reconstruction and preselection	
$\eta \to \pi^+\pi^-\gamma$	3.275 ± 0.014	2.565 ± 0.016
$\eta \to \pi^+\pi^-\pi^0$	1.038 ± 0.005	0.960 ± 0.007
$\eta' \to \rho^0\gamma$	2.071 ± 0.008	1.948 ± 0.014
$\eta' \to \pi^+\pi^-\eta$	1.550 ± 0.007	1.461 ± 0.012
$\rho^0 \to \pi^+\pi^-$	-	7.303 ± 0.009
	Trigger	
$\eta \to \pi^+\pi^-\gamma$	82.96 ± 0.38	82.9 ± 0.6
$\eta \to \pi^+\pi^-\pi^0$	84.39 ± 0.45	85.46 ± 0.7
$\eta' \to \rho^0\gamma$	83.58 ± 0.37	83.6 ± 0.7
$\eta' \to \pi^+\pi^-\eta$	85.11 ± 0.43	86.0 ± 0.8
$\rho^0 \to \pi^+\pi^-$	-	81.32 ± 0.11
	BDT selection	
$\eta \to \pi^+\pi^-\gamma$	89.80 ± 0.43	88.8 ± 0.6
$\eta \to \pi^+\pi^-\pi^0$	72.03 ± 0.45	69.7 ± 0.6
$\eta' \to \rho^0\gamma$	84.24 ± 0.40	83.8 ± 0.7
$\eta' \to \pi^+\pi^-\eta$	71.49 ± 0.42	69.2 ± 0.7
$\rho^0 \to \pi^+\pi^-$	-	80.2017 ± 0.12
	PID selection	
$\eta \to \pi^+\pi^-\gamma$	95.241 ± 0.040	95.188 ± 0.041
$\eta \to \pi^+\pi^-\pi^0$	95.240 ± 0.035	95.266 ± 0.035
$\eta' \to \rho^0\gamma$	94.190 ± 0.041	94.278 ± 0.044
$\eta' \to \pi^+\pi^-\eta$	96.293 ± 0.048	96.416 ± 0.047
$\rho^0 \to \pi^+\pi^-$	-	91.940 ± 0.046
	Total	
$\eta \to \pi^+\pi^-\gamma$	0.3179 ± 0.0015	0.2844 ± 0.0021
$\eta \to \pi^+\pi^-\pi^0$	0.0930 ± 0.0006	0.0845 ± 0.0008
$\eta' \to \rho^0\gamma$	0.2205 ± 0.0011	0.2084 ± 0.0018
$\eta' \to \pi^+\pi^-\eta$	0.1374 ± 0.0008	0.1249 ± 0.0013
$\rho^0 \to \pi^+\pi^-$	- 0.7087 ± 0.0011	

Table B.11.: The reconstruction and selection efficiencies for the signal $B^0_{(s)} \to J/\psi \eta^{(\prime)}$ and $B^0 \to J/\psi \rho^0$ 2017 Monte-Carlo simulated data.

Channel	$\varepsilon^{MC}(B^0_s)/\%$	$\varepsilon^{MC}(B^0)/\%$
	Acceptance	
$\eta \to \pi^+\pi^-\gamma$	10.64 ± 0.16	-
$\eta \to \pi^+\pi^-\pi^0$	15.535 ± 0.037	-
$\eta' \to \rho^0\gamma$	16.101 ± 0.041	-
$\eta' \to \pi^+\pi^-\eta$	8.95 ± 0.15	-
$\rho^0 \to \pi^+\pi^-$	-	16.134 ± 0.038
	Reconstruction and preselection	
$\eta \to \pi^+\pi^-\gamma$	4.131 ± 0.017	-
$\eta \to \pi^+\pi^-\pi^0$	1.056 ± 0.007	-
$\eta' \to \rho^0\gamma$	2.106 ± 0.007	-
$\eta' \to \pi^+\pi^-\eta$	2.66 ± 0.014	-
$\rho^0 \to \pi^+\pi^-$	-	7.325 ± 0.008
	Trigger	
$\eta \to \pi^+\pi^-\gamma$	87.98 ± 0.38	-
$\eta \to \pi^+\pi^-\pi^0$	88.3 ± 0.6	-
$\eta' \to \rho^0\gamma$	88.10 ± 0.32	-
$\eta' \to \pi^+\pi^-\eta$	89.3 ± 0.5	-
$\rho^0 \to \pi^+\pi^-$	-	86.13 ± 0.10
	BDT selection	
$\eta \to \pi^+\pi^-\gamma$	89.78 ± 0.41	-
$\eta \to \pi^+\pi^-\pi^0$	71.36 ± 0.6	-
$\eta' \to \rho^0\gamma$	84.06 ± 0.34	-
$\eta' \to \pi^+\pi^-\eta$	71.71 ± 0.49	-
$\rho^0 \to \pi^+\pi^-$	-	79.83 ± 0.11
	PID selection	
$\eta \to \pi^+\pi^-\gamma$	96.560 ± 0.036	-
$\eta \to \pi^+\pi^-\pi^0$	96.538 ± 0.032	-
$\eta' \to \rho^0\gamma$	95.966 ± 0.038	-
$\eta' \to \pi^+\pi^-\eta$	97.269 ± 0.042	-
$\rho^0 \to \pi^+\pi^-$	-	94.509 ± 0.042
	Total	
$\eta \to \pi^+\pi^-\gamma$	0.3352 ± 0.0015	-
$\eta \to \pi^+\pi^-\pi^0$	0.0997 ± 0.0008	-
$\eta' \to \rho^0\gamma$	0.2409 ± 0.0010	-
$\eta' \to \pi^+\pi^-\eta$	0.1486 ± 0.0010	-
$\rho^0 \to \pi^+\pi^-$	-	0.7680 ± 0.0011

Table B.12.: The reconstruction and selection efficiencies for the signal $B^0_{(s)} \to J/\psi\eta^{(\prime)}$ and $B^0 \to J/\psi\rho^0$ 2018 Monte-Carlo simulated data.

Channel	$\varepsilon^{MC}(B^0_s)/\%$	$\varepsilon^{MC}(B^0)/\%$
	Acceptance	
$\eta \to \pi^+\pi^-\gamma$	10.71 ± 0.16	-
$\eta \to \pi^+\pi^-\pi^0$	15.542 ± 0.033	-
$\eta' \to \rho^0\gamma$	16.050 ± 0.041	-
$\eta' \to \pi^+\pi^-\eta$	8.84 ± 0.15	-
$\rho^0 \to \pi^+\pi^-$	-	16.19 ± 0.04
	Reconstruction and preselection	
$\eta \to \pi^+\pi^-\gamma$	4.040 ± 0.016	-
$\eta \to \pi^+\pi^-\pi^0$	1.040 ± 0.007	-
$\eta' \to \rho^0\gamma$	2.076 ± 0.007	-
$\eta' \to \pi^+\pi^-\eta$	2.679 ± 0.015	-
$\rho^0 \to \pi^+\pi^-$	-	7.347 ± 0.008
	Trigger	
$\eta \to \pi^+\pi^-\gamma$	83.63 ± 0.37	-
$\eta \to \pi^+\pi^-\pi^0$	85.0 ± 0.6	-
$\eta' \to \rho^0\gamma$	84.02 ± 0.31	-
$\eta' \to \pi^+\pi^-\eta$	86.1 ± 0.5	-
$\rho^0 \to \pi^+\pi^-$	-	81.39 ± 0.10
	BDT selection	
$\eta \to \pi^+\pi^-\gamma$	90.35 ± 0.42	-
$\eta \to \pi^+\pi^-\pi^0$	71.8 ± 0.6	-
$\eta' \to \rho^0\gamma$	84.64 ± 0.34	-
$\eta' \to \pi^+\pi^-\eta$	70.51 ± 0.49	-
$\rho^0 \to \pi^+\pi^-$	-	80.26 ± 0.11
	PID selection	
$\eta \to \pi^+\pi^-\gamma$	96.004 ± 0.033	-
$\eta \to \pi^+\pi^-\pi^0$	96.109 ± 0.030	-
$\eta' \to \rho^0\gamma$	95.474 ± 0.034	-
$\eta' \to \pi^+\pi^-\eta$	96.962 ± 0.038	-
$\rho^0 \to \pi^+\pi^-$	-	93.953 ± 0.037
	Total	
$\eta \to \pi^+\pi^-\gamma$	0.3137 ± 0.0015	-
$\eta \to \pi^+\pi^-\pi^0$	0.0948 ± 0.0008	-
$\eta' \to \rho^0\gamma$	0.2263 ± 0.0009	-
$\eta' \to \pi^+\pi^-\eta$	0.1395 ± 0.0010	-
$\rho^0 \to \pi^+\pi^-$	-	0.7302 ± 0.0011

Bibliography

[1] F. Halzen and A. D. Martin, *Quarks and Leptons: An Introductory Course In Modern Particle Physics*, 1984.

[2] Belle collaboration, S. K. Choi *et al.*, *Observation of a narrow charmonium-like state in exclusive $B^{\pm} \to K^{\pm}\pi^{+}\pi^{-}J/\psi$ decays*, Phys. Rev. Lett. **91** (2003) 262001, arXiv:hep-ex/0309032.

[3] LHCb collaboration, R. Aaij *et al.*, *Quantum numbers of the $X(3872)$ state and orbital angular momentum in its $\rho^0 J/\psi$ decays*, Phys. Rev. **D92** (2015) 011102(R), arXiv:1504.06339.

[4] Belle collaboration, S. K. Choi *et al.*, *Observation of a resonance-like structure in the $pi^{\pm}\psi'$ mass distribution in exclusive $B \to K\pi^{\pm}\psi'$ decays*, Phys. Rev. Lett. **100** (2008) 142001, arXiv:0708.1790.

[5] LHCb collaboration, R. Aaij *et al.*, *Observation of the resonant character of the $Z(4430)^-$ state*, Phys. Rev. Lett. **112** (2014) 222002, arXiv:1404.1903.

[6] D0 collaboration, V. M. Abazov *et al.*, *Evidence for a $B_s^0\pi^{\pm}$ state*, Phys. Rev. Lett. **117** (2016) 022003, arXiv:1602.07588.

[7] LHCb collaboration, R. Aaij *et al.*, *Search for structure in the $B_s^0\pi^{\pm}$ invariant mass spectrum*, Phys. Rev. Lett. **117** (2016) 152003, arXiv:1608.00435.

[8] D. Griffiths, *Introduction to elementary particles*, 2008.

[9] S. L. Glashow, *Partial Symmetries of Weak Interactions*, Nucl. Phys. **22** (1961) 579.

[10] P. Kooijman and N. Tuning, *Lectures on CP violation (or: The Physics of Anti-matter)*, https://www.nikhef.nl/ h71/Lectures/2015/ppII-cpviolation-19032018.pdf. Accessed: January 5, 2023.

[11] Heavy Flavor Averaging Group, Y. Amhis *et al.*, *Averages of b-hadron, c-hadron, and τ-lepton properties as of summer 2014*, arXiv:1412.7515.

[12] C. Amsler, *Nuclear and particle physics*, IOPP, 2015.

[13] T. D. Lee and C.-N. Yang, *Question of Parity Conservation in Weak Interactions*, Phys. Rev.

104 (1956) 254.

[14] C. S. Wu *et al.*, *Experimental Test of Parity Conservation in β Decay*, Phys. Rev. **105** (1957) 1413.

[15] M. Goldhaber, L. Grodzins, and A. W. Sunyar, *Helicity of Neutrinos*, Phys. Rev. **109** (1958) 1015.

[16] J. H. Christenson, J. W. Cronin, V. L. Fitch, and R. Turlay, *Evidence for the 2π Decay of the K_2^0 Meson*, Phys. Rev. Lett. **13** (1964) 138.

[17] J. S. Schwinger, *The Theory of quantized fields. 1.*, Phys. Rev. **82** (1951) 914.

[18] G. Luders, *On the Equivalence of Invariance under Time Reversal and under Particle-Antiparticle Conjugation for Relativistic Field Theories*, Kong. Dan. Vid. Sel. Mat. Fys. Med. **28N5** (1954) 1.

[19] W. Pauli, L. Rosenfeld, and V. Weisskopf, *Niels bohr and the development of physics*, British Journal for the Philosophy of Science **7** (1957) 357.

[20] Particle Data Group, J. Beringer *et al.*, *Review of particle physics*, Phys. Rev. **D86** (2012) 010001, and 2013 partial update for the 2014 edition.

[21] N. Cabibbo, *Unitary symmetry and leptonic decays*, Phys. Rev. Lett. **10** (1963) 531.

[22] M. Kobayashi and T. Maskawa, *CP-violation in the renormalizable theory of weak interaction*, Prog. Theor. Phys. **49** (1973) 652.

[23] J. P. Silva, *Phenomenological aspects of CP violation*, in *Central European School in Particle Physics*, 2004, `arXiv:hep-ph/0410351`.

[24] L.-L. Chau and W.-Y. Keung, *Comments on the Parametrization of the Kobayashi-Maskawa Matrix*, Phys. Rev. Lett. **53** (1984) 1802.

[25] L. Wolfenstein, *Parametrization of the Kobayashi-Maskawa Matrix*, Phys. Rev. Lett. **51** (1983) 1945.

[26] CKMfitter group, J. Charles *et al.*, *CP violation and the CKM matrix: Assessing the impact of the asymmetric B factories*, Eur. Phys. J. **C41** (2005) 1, `arXiv:hep-ph/0406184`, updated results and plots available at `http://ckmfitter.in2p3.fr/`.

[27] Heavy Flavor Averaging Group, Y. Amhis *et al.*, *Averages of b-hadron, c-hadron, and τ-lepton properties as of 2018*, Eur. Phys. J. **C81** (2021) 226, `arXiv:1909.12524`, updated results and plots available at `https://hflav.web.cern.ch`.

[28] CKMfitter group, J. Charles *et al.*, *Current status of the standard model CKM fit and constraints*

on $\Delta F = 2$ new physics, Phys. Rev. **D91** (2015) 073007, arXiv:1501.05013, updated results and plots available at http://ckmfitter.in2p3.fr/.

[29] LHCb collaboration, R. Aaij *et al.*, *Precision measurement of CP violation in $B_s^0 \to J/\psi K^+K^-$ decays*, Phys. Rev. Lett. **114** (2015) 041801, arXiv:1411.3104.

[30] LHCb collaboration, R. Aaij *et al.*, *Updated measurement of time-dependent CP-violating observables in $B_s^0 \to J/\psi K^+K^-$ decays*, Eur. Phys. J. **C79** (2019) 706, Erratum ibid. **C80** (2020) 601, arXiv:1906.08356.

[31] LHCb collaboration, R. Aaij *et al.*, *Measurement of the CP-violating phase ϕ_s in $\overline{B}_s^0 \to J/\psi\pi^+\pi^-$ decays*, Phys. Lett. **B736** (2014) 186, arXiv:1405.4140.

[32] LHCb collaboration, R. Aaij *et al.*, *Resonances and CP-violation in B_s^0 and $\overline{B}_s^0 \to J/\psi K^+K^-$ decays in the mass region above the $\phi(1020)$*, JHEP **08** (2017) 037, arXiv:1704.08217.

[33] LHCb collaboration, R. Aaij *et al.*, *Measurement of the CP violating phase and decay-width difference in $B_s^0 \to \psi(2S)\phi$ decays*, Phys. Lett. **B762** (2016) 253, arXiv:1608.04855.

[34] LHCb collaboration, R. Aaij *et al.*, *Measurement of the CP-violating phase ϕ_s in $\overline{B}_s^0 \to D_s^+D_s^-$ decays*, Phys. Rev. Lett. **113** (2014) 211801, arXiv:1409.4619.

[35] LHCb collaboration, R. Aaij *et al.*, *Measurement of the CP-violating phase ϕ_s from $B_s^0 \to J/\psi\pi^+\pi^-$ decays in 13 TeV pp collisions*, Phys. Lett. **B797** (2019) 134789, arXiv:1903.05530.

[36] BaBar collaboration, B. Aubert *et al.*, *Observation of CP violation in $B^0 \to K^+\pi^-$ and $B^0 \to \pi^+\pi^-$*, Phys. Rev. Lett. **99** (2007) 021603, arXiv:hep-ex/0703016.

[37] Belle collaboration, S. W. Lin *et al.*, *Difference in direct charge-parity violation between charged and neutral B meson decays*, Nature **452** (2008) 332.

[38] CDF collaboration, T. Aaltonen *et al.*, *Measurements of Direct CP Violating Asymmetries in Charmless Decays of Strange Bottom Mesons and Bottom Baryons*, Phys. Rev. Lett. **106** (2011) 181802, arXiv:1103.5762.

[39] LHCb collaboration, R. Aaij *et al.*, *First evidence of direct CP violation in charmless two-body decays of B_s^0 mesons*, Phys. Rev. Lett. **108** (2012) 201601, arXiv:1202.6251.

[40] LHCb collaboration, R. Aaij *et al.*, *Observation of CP violation in $B^\pm \to DK^\pm$ decays*, Phys. Lett. **B712** (2012) 203, Erratum ibid. **B713** (2012) 351, arXiv:1203.3662.

[41] Particle Data Group, P. A. Zyla *et al.*, *Review of particle physics*, Prog. Theor. Exp. Phys. **2020** (2020) 083C01.

[42] C. Amsler, *The Quark Structure of Hadrons: An Introduction to the Phenomenology and*

Spectroscopy, vol. 949, Springer, Cham, 2018.

[43] L. D. Landau, *On the angular momentum of a system of two photons*, Dokl. Akad. Nauk SSSR **60** (1948) 207.

[44] C.-N. Yang, *Selection Rules for the Dematerialization of a Particle Into Two Photons*, Phys. Rev. **77** (1950) 242.

[45] S. Okubo, *Phi meson and unitary symmetry model*, Phys. Lett. **5** (1963) 165.

[46] G. Zweig, in *An SU(3) model for strong interaction symmetry and its breaking. Version 2*, D. B. Lichtenberg and S. P. Rosen, eds., pp. 22–101, 1964.

[47] J. Iizuka, *Systematics and phenomenology of meson family*, Prog. Theor. Phys. Suppl. **37** (1966) 21.

[48] L. Gan, B. Kubis, E. Passemar, and S. Tulin, *Precision tests of fundamental physics with η and η' mesons*, Phys. Rept. **945** (2022) 1, `arXiv:2007.00664`.

[49] T. Feldmann, *Quark structure of pseudoscalar mesons*, Int. J. Mod. Phys. A **15** (2000) 159, `arXiv:hep-ph/9907491`.

[50] ETM collaboration, K. Ottnad and C. Urbach, *Flavor-singlet meson decay constants from $N_f = 2+1+1$ twisted mass lattice QCD*, Phys. Rev. D **97** (2018) 054508, `arXiv:1710.07986`.

[51] H. Leutwyler, *On the 1/N expansion in chiral perturbation theory*, Nucl. Phys. B Proc. Suppl. **64** (1998) 223, `arXiv:hep-ph/9709408`.

[52] T. Feldmann, P. Kroll, and B. Stech, *Mixing and decay constants of pseudoscalar mesons*, Phys. Rev. D **58** (1998) 114006, `arXiv:hep-ph/9802409`.

[53] R. Escribano and J.-M. Frere, *Study of the eta - eta-prime system in the two mixing angle scheme*, JHEP **06** (2005) 029, `arXiv:hep-ph/0501072`.

[54] R. Escribano, P. Masjuan, and P. Sanchez-Puertas, *\eta and \eta' transition form factors from rational approximants*, Phys. Rev. D **89** (2014) 034014, `arXiv:1307.2061`.

[55] P. Bickert, P. Masjuan, and S. Scherer, *η-η' Mixing in Large-N_c Chiral Perturbation Theory*, Phys. Rev. D **95** (2017) 054023, `arXiv:1612.05473`.

[56] Particle Data Group, S. Eidelman *et al.*, *Review of particle physics. Particle Data Group*, Phys. Lett. B **592** (2004) 1.

[57] S. D. Bass and P. Moskal, *η and η mesons with connection to anomalous glue*, Rev. Mod. Phys. **91** (2019) 015003, `arXiv:1810.12290`.

[58] C. Amsler and F. E. Close, *Is f0 (1500) a scalar glueball?*, Phys. Rev. D **53** (1996) 295, arXiv:hep-ph/9507326.

[59] F. E. Close and A. Kirk, *The Mixing of the f(0)(1370), f(0)(1500) and f(0)(1710) and the search for the scalar glueball*, Phys. Lett. B **483** (2000) 345, arXiv:hep-ph/0004241.

[60] F. E. Close and A. Kirk, *Scalar glueball q anti-q mixing above 1-GeV and implications for lattice QCD*, Eur. Phys. J. C **21** (2001) 531, arXiv:hep-ph/0103173.

[61] C. Amsler *et al.*, *High statistics study of f0 (1500) decay into pi0 pi0*, Phys. Lett. B **342** (1995) 433.

[62] Crystal Barrel collaboration, C. Amsler *et al.*, *High statistics study of f0 (1500) decay into eta eta*, Phys. Lett. B **353** (1995) 571.

[63] Crystal Barrel collaboration, A. Abele *et al.*, *Observation of f(0)(1500) decay into K(L) K(L)*, Phys. Lett. B **385** (1996) 425.

[64] WA102 collaboration, D. Barberis *et al.*, *A Coupled channel analysis of the centrally produced K+ K- and pi+ pi- final states in p p interactions at 450-GeV/c*, Phys. Lett. B **462** (1999) 462, arXiv:hep-ex/9907055.

[65] F. E. Close and Q. Zhao, *Production of f0(1710), f0(1500), and f0(1370) in j/psi hadronic decays*, Phys. Rev. D **71** (2005) 094022, arXiv:hep-ph/0504043.

[66] BESIII collaboration, M. Ablikim *et al.*, *Partial wave analysis of $J/\psi \to \gamma\eta\eta'$*, arXiv:2202.00623.

[67] H.-X. Chen *et al.*, *An updated review of the new hadron states*, arXiv:2204.02649.

[68] M. J. Teper, *Physics from the lattice: Glueballs in QCD: Topology: SU(N) for all N*, in *NATO Advanced Study Institute on Confinement, Duality and Nonperturbative Aspects of QCD*, 43–74, 1997, arXiv:hep-lat/9711011.

[69] C. J. Morningstar and M. J. Peardon, *The Glueball spectrum from an anisotropic lattice study*, Phys. Rev. D **60** (1999) 034509, arXiv:hep-lat/9901004.

[70] Y. Chen *et al.*, *Glueball spectrum and matrix elements on anisotropic lattices*, Phys. Rev. D **73** (2006) 014516, arXiv:hep-lat/0510074.

[71] W. Sun *et al.*, *Glueball spectrum from $N_f = 2$ lattice QCD study on anisotropic lattices*, Chin. Phys. C **42** (2018) 093103, arXiv:1702.08174.

[72] A. Athenodorou and M. Teper, *The glueball spectrum of SU(3) gauge theory in 3 + 1 dimensions*, JHEP **11** (2020) 172, arXiv:2007.06422.

[73] N. Wu, T.-N. Ruan, and Z.-P. Zheng, *New meson mass relation and lowest pseudoscalar glueball mass*, Chin. Phys. **10** (2001) 611, arXiv:hep-ph/0011338.

[74] R. Fleischer, R. Knegjens, and G. Ricciardi, *Exploring CP Violation and η-η' Mixing with the $B^0_{s,d} \to J/\psi\eta^{(\prime)}$ Systems*, Eur. Phys. J. C **71** (2011) 1798, arXiv:1110.5490.

[75] C. E. Thomas, *Composition of the Pseudoscalar Eta and Eta' Mesons*, JHEP **10** (2007) 026, arXiv:0705.1500.

[76] LHCb collaboration, R. Aaij *et al.*, *Evidence for the decay $B^0 \to J/\psi\omega$ and measurement of the relative branching fractions of B^0_s meson decays to $J/\psi\eta$ and $J/\psi\eta'$*, Nucl. Phys. **B867** (2013) 547, arXiv:1210.2631.

[77] LHCb collaboration, R. Aaij *et al.*, *Study of η–η' mixing from measurement of $B^0_{(s)} \to J/\psi\eta^{(\prime)}$ decay rates*, JHEP **01** (2015) 024, arXiv:1411.0943.

[78] L. R. Evans and P. Bryant, *LHC Machine*, JINST **3** (2008) S08001. 164 p, This report is an abridged version of the LHC Design Report (CERN-2004-003).

[79] LHCb collaboration, R. Aaij *et al.*, *Measurement of the b-quark production cross-section in 7 and 13 TeV pp collisions*, Phys. Rev. Lett. **118** (2017) 052002, Erratum ibid. **119** (2017) 169901, arXiv:1612.05140.

[80] LHCb collaboration, R. Aaij *et al.*, *LHCb detector performance*, Int. J. Mod. Phys. **A30** (2015) 1530022, arXiv:1412.6352.

[81] LHCb collaboration, F. Alessio, R. Jacobsson, and R. Le Gac, *Lhcb operations plots*, https://lbgroups.cern.ch/online/OperationsPlots/index.htm. Accessed: January 5, 2023.

[82] LHCb collaboration, C. Elsässer, *$\bar{b}b$ production angle plots*, https://lhcb.web.cern.ch/lhcb/speakersbureau/html/bb_ProductionAngles.html. Accessed: January 5, 2023.

[83] LHCb collaboration, A. A. Alves Jr. *et al.*, *The LHCb detector at the LHC*, JINST **3** (2008) S08005.

[84] LHCb collaboration, *LHCb reoptimized detector design and performance: Technical Design Report*, CERN-LHCC-2003-030, 2003.

[85] C. Abellan Beteta *et al.*, *Calibration and performance of the LHCb calorimeters in Run 1 and 2 at the LHC*, arXiv:2008.11556, submitted to JINST.

[86] A. Arefev *et al.*, *Beam test results of the LHCb electromagnetic calorimeter*, CERN-LHCB-2007-149, 2008.

[87] C. Coca *et al.*, *The hadron calorimeter prototype beam-test results*, LHCb-2000-036, 2000.

[88] C. A. Beteta *et al.*, *Time alignment of the front end electronics of the LHCb calorimeters*, Journal of Instrumentation **7** (2012) P08020.

[89] LHCb collaboration, R. Quagliani, *Novel real-time alignment and calibration of LHCb detector for Run II and tracking for the upgrade.*, J. Phys. Conf. Ser. **762** (2016) 012046.

[90] R. Aaij *et al.*, *Performance of the LHCb trigger and full real-time reconstruction in Run 2 of the LHC*, JINST **14** (2019) P04013, arXiv:1812.10790.

[91] M. Adinolfi *et al.*, *Performance of the LHCb RICH detector at the LHC*, Eur. Phys. J. **C73** (2013) 2431, arXiv:1211.6759.

[92] F. Archilli *et al.*, *Performance of the muon identification at LHCb*, JINST **8** (2013) P10020, arXiv:1306.0249.

[93] G. Barrand *et al.*, *GAUDI - A software architecture and framework for building HEP data processing applications*, Comput. Phys. Commun. **140** (2001) 45.

[94] T. Sjöstrand, S. Mrenna, and P. Skands, *PYTHIA 6.4 physics and manual*, JHEP **05** (2006) 026, arXiv:hep-ph/0603175.

[95] T. Sjöstrand, S. Mrenna, and P. Skands, *A brief introduction to PYTHIA 8.1*, Comput. Phys. Commun. **178** (2008) 852, arXiv:0710.3820.

[96] D. J. Lange, *The EvtGen particle decay simulation package*, Nucl. Instrum. Meth. **A462** (2001) 152.

[97] E. Barberio and Z. Was, *PHOTOS: A Universal Monte Carlo for QED radiative corrections. Version 2.0*, Comput. Phys. Commun. **79** (1994) 291.

[98] I. Belyaev *et al.*, *Handling of the generation of primary events in Gauss, the LHCb simulation framework*, J. Phys. Conf. Ser. **331** (2011) 032047.

[99] LHCb collaboration, I. Belyaev *et al.*, *Handling of the generation of primary events in Gauss, the LHCb simulation framework*, J. Phys. Conf. Ser. **331** (2011) 032047.

[100] LHCb collaboration, *LHCb computing: Technical Design Report*, CERN-LHCC-2005-019, 2005.

[101] G. Corti *et al.*, *Software for the LHCb experiment*, IEEE Trans. Nucl. Sci. **53** (2006) 1323.

[102] V. Breton, N. Brun, and P. Perret, *A clustering algorithm for the LHCb electromagnetic calorimeter using a cellular automaton* , CERN, Geneva, 2001.

[103] O. Deschamps *et al.*, *Photon and neutral pion reconstruction*, LHCb-2003-091, 2003.

[104] M. Chefdeville *et al.*, *Calibration samples of γ and π^0 for particle identification at LHCb in 2017 and 2018* , CERN, Geneva, 2021.

[105] M. Hoballah, *Measurement of the photon polarization using $B_s^0 \to \phi\gamma$ at LHCb.*, PhD thesis, Clermont-Ferrand U., 2015.

[106] M. Calvo Gomez *et al.*, *A tool for γ/π^0 separation at high energies* , CERN, Geneva, 2015.

[107] LHCb collaboration, R. Aaij *et al.*, *Precise measurement of the f_s/f_d ratio of fragmentation fractions and of B_s^0 decay branching fractions*, Phys. Rev. **D104** (2021) 032005, arXiv:2103.06810.

[108] Particle Data Group, R. L. Workman *et al.*, *Review of Particle Physics*, , to be published (2022).

[109] LHCb collaboration, R. Aaij *et al.*, *Search for the $B_s^0 \to \eta'\phi$ decay*, JHEP **05** (2017) 158, arXiv:1612.08110.

[110] LHCb collaboration, R. Aaij *et al.*, *Observation of the decays $\Lambda_b^0 \to \chi_{c1} p K^-$ and $\Lambda_b^0 \to \chi_{c2} p K^-$*, Phys. Rev. Lett. **119** (2017) 062001, arXiv:1704.07900.

[111] A. Hoecker *et al.*, *TMVA 4 — Toolkit for Multivariate Data Analysis with ROOT. Users Guide.*, arXiv:physics/0703039.

[112] W. D. Hulsbergen, *Decay chain fitting with a Kalman filter*, Nucl. Instrum. Meth. A **552** (2005) 566, arXiv:physics/0503191.

[113] A. Rogozhnikov, *Reweighting with Boosted Decision Trees*, J. Phys. Conf. Ser. **762** (2016) 012036, arXiv:1608.05806.

[114] R. Aaij *et al.*, *Selection and processing of calibration samples to measure the particle identification performance of the LHCb experiment in Run 2*, Eur. Phys. J. Tech. Instr. **6** (2019) 1, arXiv:1803.00824.

[115] M. Pivk and F. R. Le Diberder, *SPlot: A Statistical tool to unfold data distributions*, Nucl. Instrum. Meth. A **555** (2005) 356, arXiv:physics/0402083.

[116] H. Voss, A. Hoecker, J. Stelzer, and F. Tegenfeldt, *TMVA - Toolkit for Multivariate Data Analysis with ROOT*, PoS **ACAT** (2007) 040.

[117] W. Verkerke and D. P. Kirkby, *The RooFit toolkit for data modeling*, eConf **C0303241** (2003) MOLT007, arXiv:physics/0306116.

[118] I. Antcheva *et al.*, *ROOT: A C++ framework for petabyte data storage, statistical analysis and visualization*, Comput. Phys. Commun. **180** (2009) 2499, arXiv:1508.07749.

[119] T. Skwarnicki, *A study of the radiative CASCADE transitions between the Upsilon-Prime and*

Upsilon resonances, PhD thesis, Cracow, INP, 1986.

[120] D. Martínez Santos and F. Dupertuis, *Mass distributions marginalized over per-event errors*, Nucl. Instrum. Meth. **A764** (2014) 150, arXiv:1312.5000.

[121] S. Tolk, J. Albrecht, F. Dettori, and A. Pellegrino, *Data driven trigger efficiency determination at LHCb* , CERN, Geneva, 2014.

[122] N. D. Gagunashvili, *Comparison of weighted and unweighted histograms*, PoS **ACAT** (2007) 054, arXiv:physics/0605123.

[123] E. Govorkova, V. Egorychev, D. Savrina, and I. Belyaev, *Study for π^0/γ reconstruction efficiency* , CERN, Geneva, 2014.

[124] BaBar collaboration, B. Aubert *et al.*, *Evidence for $X(3872) \to \psi_{2S}\gamma$ in $B^{\pm} \to X_{3872}K^{\pm}$ decays, and a study of $B \to c\bar{c}\gamma K$*, Phys. Rev. Lett. **102** (2009) 132001, arXiv:0809.0042.

[125] Belle collaboration, V. Bhardwaj *et al.*, *Observation of $X(3872) \to J/\psi\gamma$ and search for $X(3872) \to \psi'\gamma$ in B decays*, Phys. Rev. Lett. **107** (2011) 091803, arXiv:1105.0177.

[126] LHCb collaboration, R. Aaij *et al.*, *Measurement of the resonant and CP components in $\bar{B}^0 \to J/\psi\pi^+\pi^-$ decays*, Phys. Rev. **D90** (2014) 012003, arXiv:1404.5673.

[127] W. Qin, Q. Zhao, and X.-H. Zhong, *Revisiting the pseudoscalar meson and glueball mixing and key issues in the search for a pseudoscalar glueball state*, Phys. Rev. D **97** (2018) 096002, arXiv:1712.02550.

[128] R. Escribano and J. Nadal, *On the gluon content of the eta and eta-prime mesons*, JHEP **05** (2007) 006, arXiv:hep-ph/0703187.

[129] DM2 collaboration, D. Bisello *et al.*, *First Observation of Three Pseudoscalar States in the $J/\psi \to \gamma\rho\rho$ Decay*, Phys. Rev. D **39** (1989) 701.

[130] BES collaboration, M. Ablikim *et al.*, *Pseudoscalar production at omega omega threshold in J/psi —> gamma omega omega*, Phys. Rev. D **73** (2006) 112007, arXiv:hep-ex/0604045.

[131] Belle collaboration, C. C. Zhang *et al.*, *First study of η_c, $\eta(1760)$ and $X(1835)$ production via $\eta'\pi^+\pi^-$ final states in two-photon collisions*, Phys. Rev. D **86** (2012) 052002, arXiv:1206.5087.

[132] P. R. Page and X.-Q. Li, *Gluonic mesons in J / psi radiative decay*, Eur. Phys. J. C **1** (1998) 579, arXiv:hep-ph/9610250.

[133] N. Kochelev and D.-P. Min, *Eta(c): Glueball mixing and resonance X(1835)*, Phys. Rev. D **72** (2005) 097502, arXiv:hep-ph/0510016.

[134] BES collaboration, J. Z. Bai *et al.*, *Observation of a near threshold enhancement in th p anti-p mass spectrum from radiative J / psi —> gamma p anti-p decays*, Phys. Rev. Lett. **91** (2003) 022001, arXiv:hep-ex/0303006.

[135] CLEO collaboration, J. P. Alexander *et al.*, *Study of $\psi(2S)$ Decays to $\gamma p\bar{p}$, $\pi^0 p\bar{p}$ and $\eta p\bar{p}$ and Search for $p\bar{p}$ Threshold Enhancements*, Phys. Rev. D **82** (2010) 092002, arXiv:1007.2886.

[136] BESIII collaboration, M. Ablikim *et al.*, *$\eta\pi^+\pi^-$ Resonant Structure around 1.8 GeV/c^2 and $\eta(1405)$ in $J/psi \to \omega\eta\pi^+\pi^-$*, Phys. Rev. Lett. **107** (2011) 182001, arXiv:1107.1806.

[137] BESIII collaboration, M. Ablikim *et al.*, *Confirmation of the $X(1835)$ and observation of the resonances $X(2120)$ and $X(2370)$ in $J/\psi \to \gamma\pi^+\pi^-\eta'$*, Phys. Rev. Lett. **106** (2011) 072002, arXiv:1012.3510.

[138] BESIII collaboration, M. Ablikim *et al.*, *Spin-Parity Analysis of $p\bar{p}$ Mass Threshold Structure in J/ψ and ψ' Radiative Decays*, Phys. Rev. Lett. **108** (2012) 112003, arXiv:1112.0942.

[139] BESIII collaboration, M. Ablikim *et al.*, *Observation of a structure at 1.84 GeV/c^2 in the 3$(^{+-})$ mass spectrum in J/$\psi\to\gamma$3$(^{+-})$ decays*, Phys. Rev. D **88** (2013) 091502, arXiv:1305.5333.

[140] BESIII collaboration, M. Ablikim *et al.*, *Observation and Spin-Parity Determination of the X(1835) in J/$\psi \to \gamma K^0_S K^0_S$*, Phys. Rev. Lett. **115** (2015) 091803, arXiv:1506.04807.

[141] BESIII collaboration, M. Ablikim *et al.*, *Observation of an anomalous line shape of the $\eta'\pi^+\pi^-$ mass spectrum near the $p\bar{p}$ mass threshold in $J/\psi \to \gamma\eta'\pi^+\pi^-$*, Phys. Rev. Lett. **117** (2016) 042002, arXiv:1603.09653.

[142] BESIII collaboration, M. Ablikim *et al.*, *Study of $\eta(1475)$ and $X(1835)$ in radiative J/ψ decays to $\gamma\phi$*, Phys. Rev. D **97** (2018) 051101, arXiv:1801.02127.

List of figures

List of tables